

**In-vivo Short Echo Hydrogen Spectroscopy:  
Precise Quantification and Application to Mental Illness**

by

Robert Bartha

Department of Medical Biophysics

Submitted in partial fulfillment  
of the requirements for the degree of  
Doctor of Philosophy

Faculty of Graduate Studies  
The University of Western Ontario  
London, Ontario  
November 1998

©Robert Bartha 1998



National Library  
of Canada

Acquisitions and  
Bibliographic Services

395 Wellington Street  
Ottawa ON K1A 0N4  
Canada

Bibliothèque nationale  
du Canada

Acquisitions et  
services bibliographiques

395, rue Wellington  
Ottawa ON K1A 0N4  
Canada

*Your file Votre référence*

*Our file Notre référence*

The author has granted a non-exclusive licence allowing the National Library of Canada to reproduce, loan, distribute or sell copies of this thesis in microform, paper or electronic formats.

The author retains ownership of the copyright in this thesis. Neither the thesis nor substantial extracts from it may be printed or otherwise reproduced without the author's permission.

L'auteur a accordé une licence non exclusive permettant à la Bibliothèque nationale du Canada de reproduire, prêter, distribuer ou vendre des copies de cette thèse sous la forme de microfiche/film, de reproduction sur papier ou sur format électronique.

L'auteur conserve la propriété du droit d'auteur qui protège cette thèse. Ni la thèse ni des extraits substantiels de celle-ci ne doivent être imprimés ou autrement reproduits sans son autorisation.

0-612-40240-1

**Canada**

## **Abstract**

Clinical investigation into the causes of mental illness would benefit from the precise determination of in-vivo cerebral metabolite levels. Short echo  $^1\text{H}$  magnetic resonance spectroscopy may be used to measure in-vivo levels of twelve metabolites. However, precise quantification of these spectra remains problematic at 1.5 Tesla (T) due to low signal to noise ratio, low resolution, and a variable spectral baseline from uncharacterized macromolecule resonances.

The object of this work was to increase the measurement precision associated with in-vivo short echo  $^1\text{H}$  spectroscopy. New software was developed for the non-interactive quantification of spectra in the time domain. Using this software, an approach to spectral quantification was developed at 1.5 T that optimized measurement precision. This optimized technique was applied in clinical studies of schizophrenia and obsessive-compulsive disorder at 1.5 T. The effect of field strength on quantification precision was also determined using data acquired at 1.5 T and 4.0 T.

The modeling of macromolecule resonances, the fitting of resonances adjacent to the spectral region of interest, and the elimination of time domain filtering, were all components of a quantification strategy that lead to increased in-vivo measurement precision. The acquisition of data at 4.0 T also increased measurement precision due to the increased signal to noise ratio and chemical shift dispersion compared to 1.5 T. The quantification strategy developed was used to obtain reliable measures of *N*-acetylaspartate, glutamate, glutamine, phosphocreatine and creatine, and choline containing compounds from 4.5 cm<sup>3</sup>

voxels at 1.5 T and from 1.5 cm<sup>3</sup> voxels at 4.0 T. The reduction of voxel volume to 1.5 cm<sup>3</sup> at 4.0 T significantly reduced partial volume sampling.

Clinical studies at 1.5 T using this technique found increased levels of glutamine in the left medial prefrontal cortex of never treated schizophrenic patients compared to controls, and decreased levels of *N*-acetylaspartate in the left corpus striatum of obsessive compulsive patients compared to controls.

These findings illustrate that short echo <sup>1</sup>H magnetic resonance spectroscopy is a valuable technique for clinical research. Future improvements in measurement precision, especially at higher field strengths, will enable the detection of subtle metabolite level differences in small patient groups.

## **Co-Authorship**

The following thesis contains material from two previously published manuscripts (Chapters 5 and 6), a third manuscript that has been accepted for publication (Chapter 2), and a fourth manuscript that is in preparation for submission (Chapter 3).

All of the experimental work presented within this thesis was performed by Robert Bartha, with the exception of the volumetric analysis of tissue content reported in Chapter 6, which was performed by Maria Densmore. All clinical assessments were performed by Peter Williamson and Gita Canaran (Chapter 5), and Murray Stein and Peter Williamson (Chapter 6).

Original manuscripts, versions of which appear in Chapters 2, 3, 5, 6, were written by Robert Bartha (Chapters 2, 3, 5, 6), Dick Drost (Chapters 2, 3, 5, 6), Peter Williamson (Chapters 2, 3, 5, 6), Murray Stein (Chapter 6), and Richard Neufeld (Chapters 5, 6).

For copyright releases, see Appendix G.

## **Acknowledgements**

I would like to thank my supervisors Dr. Dick Drost and Dr. Peter Williamson for their expertise, enthusiasm, assistance, and advice during the last five years.

To my wife Charlene, thank you for your love and understanding. Thank you for spending time with me at the lab when I had to work long hours, and most importantly thank you for letting me scan you whenever I needed a subject.

To the rest of my family, my father, Peter, my mother, Regina, and my sister, Christina, thank you for your interest and support while I pursued this degree.

Dr. Terry Thompson and Dr. Steve Karlik for helpful discussions and suggestions regarding this work. Dr. Murray Stein for thoughtful insights regarding the obsessive-compulsive study.

John Potwarka for teaching me a little of what you know about programming. Gita Canaran and Betsy Schaefer for organizing the clinical studies. Maria Densmore, for analyzing all the volumetric data. Dr. Ravi Menon and Joe Gati for help with data collection at 4.0 Tesla.

Finally, to all the staff and students in the Imaging Division of the Lawson Research Institute, thank-you for making the last five years so enjoyable, entertaining, and educational.

# Table of Contents

CERTIFICATE OF EXAMINATION.....	II
ABSTRACT.....	III
CO-AUTHORSHIP.....	V
ACKNOWLEDGEMENTS.....	VI
TABLE OF CONTENTS.....	VII
LIST OF TABLES .....	XII
LIST OF FIGURES .....	XIII
LIST OF APPENDICES.....	XV
LIST OF ABBREVIATIONS, SYMBOLS, NOMENCLATURE.....	XVI
CHAPTER 1 .....	1
INTRODUCTION.....	1
1.0 INTRODUCTION TO IN-VIVO MR SPECTROSCOPY QUANTIFICATION AND THESIS OUTLINE .....	1
1.0.1 <i>Introduction to In-Vivo MR Spectroscopy in Mental Illness</i> .....	1
1.0.2 <i>Acquisition of MR Spectroscopy Data</i> .....	4
1.0.3 <i>Spin Echoes and Stimulated Echoes</i> .....	9
1.0.4 <i>A Short History of In-Vivo Quantification Strategies and Data Acquisition</i> .....	13
1.0.5 <i>Thesis Objectives</i> .....	17
1.0.6 <i>Hypotheses</i> .....	18
1.0.7 <i>Thesis Outline</i> .....	18
1.1 IN-VIVO SPECTROSCOPY .....	22
1.1.1 <i>The In-Vitro Short Echo <sup>1</sup>H Spectrum</i> .....	22
1.1.2 <i>The In-Vivo Short Echo <sup>1</sup>H Spectrum</i> .....	28

1.1.3	<i>In-Vivo Spectroscopy: The Problems</i> .....	29
1.1.4	<i>Field Strength Considerations</i> .....	32
1.2	DATA ACQUISITION.....	34
1.2.1	<i>Introduction to Data Acquisition and Localization</i> .....	34
1.2.2	<i>Stimulated Echo Acquisition Mode (STEAM) Localized Spectroscopy</i> .....	35
1.2.3	<i>Typical Experimental Protocol</i> .....	38
1.3	DATA QUANTIFICATION .....	39
1.3.1	<i>Lineshape Distortion</i> .....	39
1.3.2	<i>Post-Processing using Eddy Current Correction (ECC)</i> .....	43
1.3.3	<i>Post-Processing using QUALITY Deconvolution</i> .....	45
1.3.4	<i>Combined ECC and QUALITY Deconvolution</i> .....	48
1.3.5	<i>Subtraction of Residual Water</i> .....	49
1.3.6	<i>Metabolite Quantification</i> .....	52
1.3.7	<i>Metabolite Prior-Knowledge</i> .....	53
1.3.8	<i>Macromolecule and Baseline Prior-Knowledge</i> .....	55
1.3.9	<i>Prior-Knowledge Constraints</i> .....	57
1.3.10	<i>Absolute Metabolite Quantification</i> .....	57
1.4	REFERENCES.....	59
 <b>CHAPTER 2</b> .....		<b>68</b>
 <b>FACTORS AFFECTING THE QUANTIFICATION OF SHORT ECHO IN-VIVO <sup>1</sup>H SPECTRA: PRIOR-KNOWLEDGE, PEAK ELIMINATION, FILTERING</b> .....		<b>68</b>
2.0	INTRODUCTION .....	68
2.1	EXPERIMENTAL .....	72
2.1.1	<i>Data Acquisition</i> .....	72
2.1.2	<i>Spectral Processing and Fitting</i> .....	75
2.1.3	<i>Prior Knowledge</i> .....	77
2.1.4	<i>Optimization of Fitting Strategy</i> .....	80
2.2	RESULTS .....	82
2.3	DISCUSSION .....	93



2.3.1 <i>Limitations</i> .....	98
2.4 CONCLUSION .....	98
2.5 REFERENCES .....	99
<b>CHAPTER 3</b> .....	<b>105</b>
<b>QUANTIFICATION AND PRECISION OF SHORT ECHO <sup>1</sup>H SPECTRA AT 1.5 AND 4.0 TESLA</b> .....	<b>105</b>
3.0 INTRODUCTION .....	105
3.1 EXPERIMENTAL .....	109
3.1.0 <i>Data Acquisition</i> .....	109
3.1.1 <i>Spectral Post Processing</i> .....	111
3.1.2 <i>Spectral Fitting and Prior Knowledge</i> .....	114
3.1.3 <i>Statistical Analysis</i> .....	116
3.2 RESULTS .....	117
3.3 DISCUSSION .....	125
3.3.0 <i>Limitations</i> .....	128
3.4 CONCLUSION .....	130
3.5 REFERENCES .....	130
<b>CHAPTER 4</b> .....	<b>135</b>
<b><sup>1</sup>H MAGNETIC RESONANCE SPECTROSCOPY IN MENTAL ILLNESS</b> .....	<b>135</b>
4.0 CLINICAL APPLICATION OF SHORT ECHO <sup>1</sup> H MRS TO MENTAL ILLNESS .....	135
4.0.1 <i>A Neurochemical Basis for Mental Illness?</i> .....	135
4.0.2 <i>The Basal-Ganglia Thalamocortical Pathway</i> .....	136
4.1 PHYSIOLOGICAL INTERPRETATION OF <sup>1</sup> H MAGNETIC RESONANCE SPECTROSCOPY .....	139
4.1.1 <i>Physiological Interpretation of Measured Metabolites</i> .....	139
4.2 REFERENCES .....	142
<b>CHAPTER 5</b> .....	<b>147</b>

<b>MEASUREMENT OF GLUTAMATE AND GLUTAMINE IN THE MEDIAL PREFRONTAL CORTEX OF NEVER TREATED SCHIZOPHRENIC PATIENTS AND HEALTHY CONTROLS BY PROTON MAGNETIC RESONANCE SPECTROSCOPY.....</b>	<b>147</b>
5.0 INTRODUCTION .....	147
5.1 METHOD .....	149
5.1.1 <i>Subjects</i> .....	149
5.1.2 <i><sup>1</sup>H MR Spectroscopy</i> .....	153
5.1.3 <i>Spectral Processing</i> .....	154
5.1.4 <i>Statistical Analysis</i> .....	156
5.2 RESULTS .....	157
5.3 COMMENT.....	162
5.3.1 <i>Limitations</i> .....	166
5.4 CONCLUSION.....	167
5.5 REFERENCES .....	168
<b>CHAPTER 6.....</b>	<b>176</b>
<b>A SHORT ECHO <sup>1</sup>H SPECTROSCOPY AND VOLUMETRIC MR IMAGING STUDY OF THE CORPUS STRIATUM IN PATIENTS WITH OBSESSIVE-COMPULSIVE DISORDER AND COMPARISON SUBJECTS.....</b>	<b>176</b>
6.0 INTRODUCTION .....	176
6.1 METHOD .....	179
6.1.1 <i>Subjects</i> .....	179
6.1.2 <i><sup>1</sup>H MR Spectroscopy</i> .....	182
6.1.3 <i>Spectral Processing</i> .....	182
6.1.4 <i>Volumetric Imaging</i> .....	184
6.1.5 <i>Statistical Analysis</i> .....	184
6.2 RESULTS .....	186
6.2.1 <i>Spectroscopy Results</i> .....	188
6.2.2 <i>Volumetric Imaging Results</i> .....	190
6.2.3 <i>Bivariate Correlations</i> .....	190

6.3 DISCUSSION .....	191
6.3.1 <i>Limitations</i> .....	193
6.4 CONCLUSION.....	194
6.5 REFERENCE.....	194
<b>CHAPTER 7.....</b>	<b>203</b>
<b>SUMMARY AND FUTURE WORK .....</b>	<b>203</b>
7.0 SUMMARY.....	203
7.0.1 <i>Acquisition, Processing, and Quantification</i> .....	203
7.0.2 <i>In-Vivo Application to Schizophrenia</i> .....	205
7.0.3 <i>In-Vivo Application to Obsessive-Compulsive Disorder</i> .....	205
7.1 LIMITATIONS.....	206
7.1.1 <i>Quantification Limitations</i> .....	206
7.1.2 <i>In-Vivo Application Limitations</i> .....	207
7.2 FUTURE WORK.....	208
7.2.1 <i>Future Work in Short Echo <sup>1</sup>H Quantification</i> .....	208
7.2.2 <i>Future Applications to Schizophrenia and Obsessive-Compulsive Disorder</i> .....	209
7.3 REFERENCE.....	210
<b>APPENDIX A: POST PROCESSING BY EDDY CURRENT CORRECTION .....</b>	<b>212</b>
<b>APPENDIX B: POST PROCESSING BY QUALITY DECONVOLUTION .....</b>	<b>214</b>
<b>APPENDIX C: SINGULAR VALUE DECOMPOSITION OF MR SPECTRA.....</b>	<b>216</b>
<b>APPENDIX D: NON-LINEAR MINIMIZATION.....</b>	<b>219</b>
<b>APPENDIX E: QUANTIFICATION OF SIMULATED <sup>1</sup>H SHORT ECHO SPECTRA .....</b>	<b>222</b>
<b>APPENDIX F: ETHICS APPROVAL FOR STUDIES INVOLVING HUMAN SUBJECTS .....</b>	<b>230</b>
<b>APPENDIX G: COPYRIGHT RELEASE INFORMATION .....</b>	<b>233</b>
<b>CURRICULUM VITAE.....</b>	<b>235</b>

## List of Tables

TABLE 2-1 : METABOLITE LEVELS FOLLOWING QUALITY DECONVOLUTION AND ECC CORRECTION .....	83
TABLE 2-2 : EFFECT OF MODEL FUNCTIONS FOR REGION OUTSIDE THE SPECTRAL REGION OF INTEREST ....	86
TABLE 2-3 : MODELING OF MACROMOLECULE RESONANCES IN THE IN-VIVO SPECTRUM TEMPLATE .....	88
TABLE 3-1: SIGNAL TO NOISE AND RESOLUTION AT 1.5 AND 4.0 TESLA .....	119
TABLE 3-2: QUANTIFIED METABOLITE LEVELS AND PRECISION AT 1.5 AND 4.0 TESLA .....	121
TABLE 3-3: CINGULATE TEST-RETEST RELIABILITY AT 4.0 TESLA .....	123
TABLE 3-4: THALAMUS TEST-RETEST RELIABILITY AT 4.0 TESLA .....	124
TABLE 5-1: SUBJECT CHARACTERISTICS .....	151
TABLE 5-2: METABOLITE CORRELATIONS WITH SYMPTOM SCORES .....	162
TABLE 6-1: SUBJECT DEMOGRAPHICS .....	180

## List of Figures

FIGURE 1-1: ORIENTATION OF RF COIL.....	6
FIGURE 1-2: NUTATION OF $M_0$ INTO THE TRANSVERSE PLANE .....	7
FIGURE 1-3: TIME DOMAIN NMR SIGNAL.....	8
FIGURE 1-4: FREQUENCY DOMAIN NMR SIGNAL.....	9
FIGURE 1-5: SPIN ECHO FORMATION .....	10
FIGURE 1-6: SPIN ECHO FORMATION WITH SCALAR COUPLING.....	12
FIGURE 1-7: 4.0 TESLA IN-VIVO SPECTRUM.....	14
FIGURE 1-8: SHORT ECHO $^1\text{H}$ MR SPECTRUM OF TWO DIFFERENT NUCLEI .....	24
FIGURE 1-9: SHORT ECHO $^1\text{H}$ MR SPECTRUM OF TWO DIFFERENT NUCLEI WITH J-COUPLING .....	26
FIGURE 1-10: SHORT ECHO $^1\text{H}$ MR IN-VITRO SPECTRUM OF GLUTAMATE AT 1.5 TESLA AND 4.0 TESLA .....	27
FIGURE 1-11: SHORT ECHO $^1\text{H}$ MR IN-VIVO SPECTRUM AT 1.5 TESLA .....	29
FIGURE 1-12: VOLUME SELECTION.....	36
FIGURE 1-13: SCHEMATIC OF STEAM SEQUENCE USED AT 4.0 TESLA.....	37
FIGURE 1-14: IN-VIVO EXPERIMENTAL TIMELINE.....	39
FIGURE 1-15: EDDY CURRENT LINESHAPE DISTORTION.....	42
FIGURE 1-16: GRADIENT COIL VIBRATION LINESHAPE DISTORTION .....	42
FIGURE 1-17: COMBINED EDDY CURRENT AND GRADIENT COIL VIBRATION LINESHAPE DISTORTION .....	43
FIGURE 1-18: IN-VITRO SPECTRUM WITH EDDY CURRENTS AT 4.0 TESLA.....	44
FIGURE 1-19: IN-VITRO SPECTRUM FOLLOWING EDDY CURRENT CORRECTION AT 4.0 TESLA.....	45
FIGURE 1-20: IN-VIVO TIME DOMAIN SIGNAL FOLLOWING QUALITY DECONVOLUTION AT 4.0 TESLA .....	47
FIGURE 1-21: IN-VIVO TIME DOMAIN SIGNAL FOLLOWING EDDY CURRENT CORRECTION AT 4.0 TESLA .....	47
FIGURE 1-22: TIME DOMAIN SIGNAL AFTER COMBINED QUALITY DECONVOLUTION AND EDDY CURRENT CORRECTION .....	49
FIGURE 1-23: IN-VIVO RESIDUAL WATER AT 4.0 TESLA .....	51
FIGURE 1-24: IN-VIVO RESIDUAL WATER REMOVED AT 4.0 TESLA .....	51
FIGURE 1-25: IN-VITRO SPECTRA OF GLUTAMINE (GLN) AT 1.5 AND 4.0 TESLA.....	55
FIGURE 2-1: IN-VITRO SPECTRUM OF NAA AND TEMPLATE OF PRIOR KNOWLEDGE .....	74
FIGURE 2-2: IN-VIVO 1.5 TESLA SPECTRA AND FIT RESULTS .....	84
FIGURE 2-3: EFFECT OF EXPONENTIAL DAMPING ON METABOLITE QUANTIFICATION.....	90

FIGURE 2-4: EFFECT OF RECTANGULAR FILTER ON METABOLITE QUANTIFICATION .....	92
FIGURE 3-1: ANATOMICAL REGIONS USED FOR 4.0 T REPRODUCIBILITY TESTING.....	111
FIGURE 3-2: 4.0 T AND 1.5 T PARIETAL LOBE DATA USED FOR S/N COMPARISON .....	118
FIGURE 3-3: 4.0 T SHORT ECHO <sup>1</sup> H SPECTRA FROM 1.5 CM <sup>3</sup> VOXELS .....	122
FIGURE 4-1: BASAL GANGLIA – THALAMOCORTICAL NEURONAL CIRCUIT.....	137
FIGURE 5-1: CORONAL AND SAGITTAL LOCALIZER IMAGES.....	154
FIGURE 5-2: IN-VIVO SPECTRUM AND COMPONENTS FROM LEFT MEDIAL PREFRONTAL CORTEX.....	158
FIGURE 5-3: MEAN METABOLITE LEVELS .....	160
FIGURE 6-1: LOCATION OF VOLUME OF INTEREST IN LEFT CORPUS STRIATUM.....	183
FIGURE 6-2: IN-VIVO SPECTRUM AND COMPONENTS FROM LEFT CORPUS STRIATUM .....	187
FIGURE 6-3: QUANTIFIED METABOLITE LEVELS FROM LEFT CORPUS STRIATUM.....	189
FIGURE E-1: THE CREATION OF IN-VIVO SIMULATED SPECTRA .....	223
FIGURE E-2: RESULTS FROM THE QUANTIFICATION OF IN-VIVO SIMULATIONS.....	229

## List of Appendices

APPENDIX A: POST PROCESSING BY EDDY CURRENT CORRECTION .....	212
APPENDIX B: POST PROCESSING BY QUALITY DECONVOLUTION .....	214
APPENDIX C: SINGULAR VALUE DECOMPOSITION OF MR SPECTRA.....	216
APPENDIX D: NON-LINEAR MINIMIZATION.....	219
APPENDIX E: QUANTIFICATION OF SIMULATED <sup>1</sup> H SHORT ECHO SPECTRA .....	222
APPENDIX F: ETHICS APPROVAL FOR STUDIES INVOLVING HUMAN SUBJECTS .....	230
APPENDIX G: COPYRIGHT RELEASE INFORMATION .....	233

## List of Abbreviations, Symbols, Nomenclature

$\omega$	- angular precession frequency
$\nu$	- chemical shift in Hz
$\delta$	- chemical shift in ppm
$\alpha$	- exponential decay constant
$\beta$	- Gaussian decay constant
$\gamma$	- gyromagnetic ratio
$\sigma$	- shielding constant
$^{15}\text{N}$	- nitrogen
$^1\text{H}$	- hydrogen (proton)
$^{31}\text{P}$	- phosphorus
Asp	- aspartate
ATP	- adenosine triphosphate
B	- magnetic field
$B_0$	- main magnetic field
$B_1$	- alternating magnetic field in the transverse plane
c	- amplitude
CGI	- clinical global impression scale
Cho	- choline containing compounds
CV	- coefficient of variation
D	- exponential filter damping
dB/dt	- magnetic gradient slew rate
ECC	- eddy current correction technique
f	- frequency
$f_V$	- frequency of $B_0$ vibration



FWHM	- full width at half maximum
GABA	- $\gamma$ -aminobutyric acid
Glc	- glucose
Gln	- glutamine
Glu	- glutamate
ISIS	- image selective spectroscopy
J	- scalar coupling constant
K	- maximum number of peaks
LB	- exponential line broadening constant
M 2.05	- macromolecule at 2.05 ppm
M 2.29	- macromolecule at 2.29 ppm
M 3.00	- macromolecule at 3.00 ppm
$M_0$	- net magnetization
MP	- mobile phospholipids
MR	- magnetic resonance
Myo	- myo-inositol
N	- maximum number of discrete samples
NAA	- <i>N</i> -acetylaspartate
NAAG	- <i>N</i> -acetylaspartyl glutamate
NIMH-OCS	- National Institute of Mental Health obsessive-compulsive scale
NMR	- nuclear magnetic resonance
OCD	- obsessive compulsive disorder
PCr + Cr	- phosphocreatine and creatine
PCr	- phosphocreatine
PCR/Cr	- phosphocreatine and creatine
PDE	-phosphodiesterases

$\phi$	-phase
Pi	- inorganic phosphate
PME	- phosphomonoesters
ppm	- parts per million
PRESS	- point resolved spectroscopy
QUALITY	- lineshape correction technique
r	- position
S/N	- signal to noise ratio
SANS	- scale for the assessment of negative symptoms
SAPS	- scale for the assessment of positive symptoms
SCID	- structured clinical interview for DSM-IV
SRI	- spectral region of interest
STEAM	- stimulated echo acquisition mode
Syl	- scyllo-inositol
T	- tesla
t	- time
$t_0$	- delay time
$T_1$	- longitudinal relaxation time constant
$T_2$	- transverse relaxation time constant
$T_2^*$	- transverse relaxation time constant including effects of magnetic field inhomogeneities
Tau	- taurine
TE	-echo time
TM	- mixing time
TSP	- trimethyl-silyl propionic acid
VOI	- volume of interest

$x, y, z$	- laboratory frame of reference
$x', y', z'$	- rotating frame of reference
YBOCS	- Yale-Brown obsessive-compulsive scale
$\Delta B_{0,D}$	- $B_0$ drift
$\Delta B_{0,S}$	- $B_0$ spatial dependence
$\Delta B_{0,V}$	- $B_0$ vibration
$\Delta t$	- dwell line
$\alpha_D$	- $B_0$ drift decay constant
$\alpha_V$	- $B_0$ vibration decay constant
$\phi_V$	- phase offset of $B_0$ vibration
$\omega_0$	- Larmor precession frequency

## Chapter 1

### Introduction

#### ***1.0 Introduction to In-Vivo MR Spectroscopy Quantification and Thesis Outline***

##### 1.0.1 Introduction to In-Vivo MR Spectroscopy in Mental Illness

Since the early experiments in nuclear magnetic resonance (NMR) in the late 1940's by Bloembergen, Purcell, and Pound (1), the use of NMR for in-vivo imaging and spectroscopy has achieved wide usage for the investigation of many different illnesses (2). In-vivo magnetic resonance (MR) spectroscopy is the only investigational technique that can be used to gain quantitative in-vivo chemical information non-invasively with no known significant long term or short term side effects (3). Since the observed NMR signal from a particular nucleus is directly proportional to the concentration of that nucleus within the sample, NMR spectroscopy can be used to measure in-vivo metabolite concentrations. Therefore NMR spectroscopy can be used to study in-vivo metabolic changes which occur following drug treatments or as a result of disease states in muscles, internal organs (for example liver and heart), and the brain.

The study of mental illness by NMR spectroscopy is appealing due to the high incidence rate and the lack of knowledge about these diseases. For example, the lifetime risk of developing schizophrenia is ~1% (4). Most patients live long

lives, despite the onset of mental illness in early adulthood. Often these patients require medical attention including hospitalization for extended periods of time. Therefore, these illnesses cost North Americans billions of dollars annually in direct health care costs and lost productivity (5, 6). Unfortunately, current medications are only partially successful in treating the symptoms of these illnesses and may have severe side effects. In an effort to improve current medications and develop a cure for these illnesses more research is needed.

Both  $^{31}\text{P}$  and  $^1\text{H}$  NMR spectroscopy have been used in the past to study patients with various mental illnesses, including schizophrenia (7, 8, 9, 10) and obsessive-compulsive disorder (OCD, 11), although significant findings have been variable with respect to location and metabolite changes.  $^{31}\text{P}$  spectroscopy measures levels of adenosine triphosphate (ATP), phosphocreatine (PCr), and inorganic phosphate (Pi), as well as components of membrane metabolism such as mobile phospholipids (MP), phosphomonoesters (PME) and phosphodiester (PDE) (7). Unfortunately, due to the low sensitivity of the  $^{31}\text{P}$  nucleus (6.6% that of  $^1\text{H}$ ), volumes studied using this technique must be quite large ( $27\text{ cm}^3$ ) to obtain data with sufficient signal to noise for reliable quantification in a reasonable amount of time. Long echo  $^1\text{H}$  spectroscopy measures levels of *N*-acetylaspartate (NAA), phosphocreatine and creatine (PCr/Cr), and choline containing compounds (Cho). The high sensitivity of the  $^1\text{H}$  nucleus and simplicity of the long echo spectrum have made this technique popular; especially for metabolic imaging studies (12). Short echo ( $\leq 30\text{ ms}$ )  $^1\text{H}$  MR spectroscopy (13) has been used less extensively due to the complexity of the acquired spectrum and resulting quantification difficulty. However, short echo  $^1\text{H}$  MR spectroscopy is ideally suited for the study of mental illness due to the variety

of interesting cerebral metabolites that can be measured (14, 15). Measurable metabolites include *N*-acetyl-aspartate (NAA), glutamate (Glu), glutamine (Gln),  $\gamma$ -amino-butyric acid (GABA), aspartate (Asp), *N*-acetyl-aspartyl-glutamate (NAAG), taurine (Tau), glucose (Glc), choline containing compounds(Cho), phosphocreatine and creatine (PCr/Cr), scyllo-inositol (Syl), myo-inositol (Myo), and macromolecules at 3.00 ppm (M 3.00), 2.29 ppm (M 2.29), and 2.05 ppm (M 2.05) (16). The amino acids glutamate and glutamine are particularly important because glutamate is the principle excitatory neurotransmitter in the brain (17), and glutamine its precursor (18). Therefore, monitoring the levels of these amino acids may provide important information regarding the pathophysiology of mental illness.

Previous long and short echo  $^1\text{H}$  MR spectroscopy studies (8, 9, 10, 12, 13) of schizophrenia have not yielded reproducible results or shown expected differences in metabolite levels. There are several possible explanations for this. First, mental illnesses such as schizophrenia and obsessive-compulsive disorder likely involve several regions of the brain which have yet to be positively identified and may vary slightly between individuals. Second, the metabolic changes that may be present and responsible for these illnesses are likely small compared with the normal biological variation present between subjects. Third, the acquisition and quantification of spectroscopic data is limited by several factors (which are discussed in detail in chapters 1-3) that effect the accuracy and precision of metabolite measures. To investigate mental illnesses such as schizophrenia and obsessive-compulsive disorder data must be collected from small (less than  $5\text{ cm}^3$ ) volumes of interest (such as the anterior cingulate and striatum) to limit the partial volume effect associated with sampling multiple brain

regions that are involved in different functions. Since the time for data acquisition must be limited to 10-12 minutes per spectrum to reduce patient motion artifacts, and since many regions of the brain likely involved in mental illnesses have poor magnetic field homogeneity (near the skull), spectra are acquired with low signal to noise ratio and resolution. These limitations ultimately determine the sensitivity of the NMR experiment. Unfortunately, due to the limited quality of short echo  $^1\text{H}$  in-vivo MR spectra, the measurement precision of many metabolites has been low in the past, meaning that subtle metabolite level differences which may exist between normal and diseased tissue have not been observed. Therefore, to improve the sensitivity of in-vivo short echo  $^1\text{H}$  spectroscopy experiments to study small metabolite level changes, improvements to the acquisition and quantification of spectroscopic data were necessary.

### 1.0.2 Acquisition of MR Spectroscopy Data

Nuclei that possess angular momentum (i.e.  $^1\text{H}$ ,  $^{31}\text{P}$ ,  $^{15}\text{N}$ ) have an associated magnetic dipole moment (19). When placed within a magnetic field these dipole moments tend to align either parallel or anti-parallel to the magnetic field (19). Due to quantum mechanical restrictions, the magnetic moments can not align perfectly with the direction of the field, instead they orient at an angle (dependent on the angular momentum of the nucleus) with respect to it (19). Therefore, the main magnetic field ( $B_0$ ) exerts a torque on each dipole moment causing this moment to precess about the main field at a frequency given by the Larmor relation (19) as shown by equation 1-1.

$$\omega = \gamma \cdot B \quad [1-1]$$

Where:  $\omega$   $\equiv$  the angular frequency  
 $\gamma$   $\equiv$  the gyromagnetic ratio  
 $B$   $\equiv$  the magnetic field experienced by the nucleus

Since spins that are aligned parallel to the magnetic field are at a lower energy than spins aligned anti-parallel to  $B_0$ , there will be an excess of spins aligned in the parallel state causing a net magnetization  $M_0$  in the direction of  $B_0$  as shown in Figure 1-1 ( $B_0$  is along the z-axis).

In the NMR experiment, a radio frequency coil is placed around the sample in the magnet. For the current discussion we will assume a linear coil oriented along the y-direction as shown in Figure 1-1.



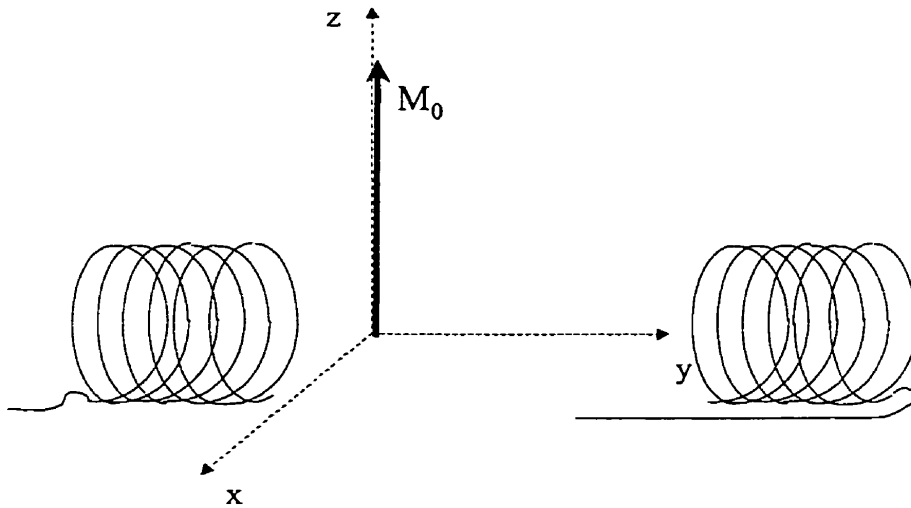


**Figure 1-1: Orientation of RF Coil**

A linear RF coil may be placed along the y-axis to produce a magnetic field  $B_1$  which perturbs the net magnetization  $M_0$  and to detect the component of the net magnetization  $M_0$  which exists in the transverse ( $xy$ ) plane. In the situation depicted above, no signal is induced in the coil since the magnetization is pointing along the z-axis and has no component in the transverse plane.

Using this coil a temporary magnetic field  $B_1$  can be generated which oscillates at the precession frequency of the individual magnetic moments. This oscillating  $B_1$  field can be represented as two rotating vectors; one rotating at the frequency  $\omega_0$ , and the other rotating at the frequency  $-\omega_0$ . The  $B_1$  vector which rotates at  $-\omega_0$  has a negligible effect on the spin system. The  $B_1$  vector which rotates at  $\omega_0$  is rotating at the same frequency as the individual magnetic moments.

Therefore, it appears stationary from the frame of reference of the spins ( $x'$ ,  $y'$ ,  $z'$ , called the rotating frame) (19). This  $B_1$  field exerts a torque on the net magnetization causing this vector to nutate away from the z-axis (Figure 1-2) at a frequency  $\omega_1 = \gamma B_1$  (analogous to equation 1-1).

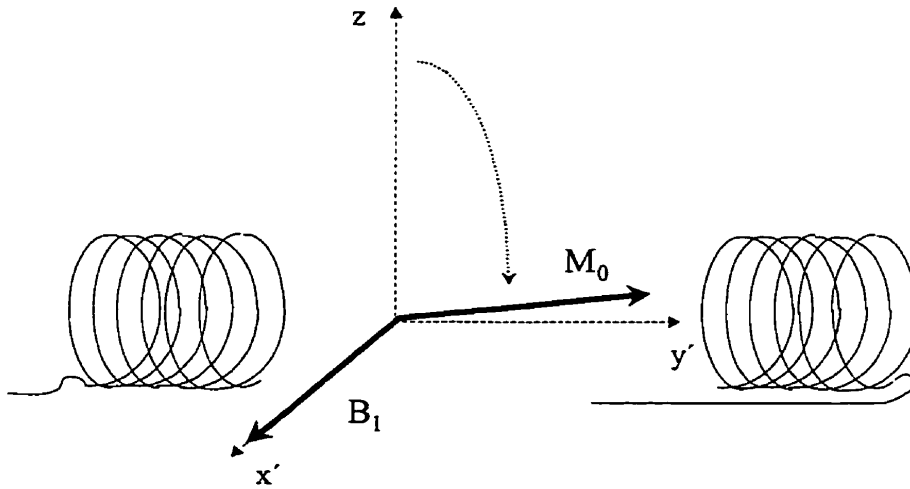


### Figure 1-2: Nutation of $M_0$ into the Transverse Plane

In the rotating frame ( $x'$ ,  $y'$ ,  $z'$ ) a constant  $B_1$  magnetic field is applied which causes  $M_0$  to nutate. After some time  $\tau$ , the net magnetization  $M_0$  will lie along the positive  $y'$ -axis. In this figure, only the component of  $B_1$  rotating with frequency  $\omega_0$  is shown.

Following the application of the  $B_1$  magnetic field for the appropriate time  $\tau$ , the  $M_0$  vector will lie along the  $y'$ -axis (90 degree pulse). If we now move back to the laboratory reference frame ( $x$ ,  $y$ ,  $z$ ), we see that the vector  $M_0$  is only influenced by the main magnetic field  $B_0$  after  $B_1$  has been turned off. Therefore,  $M_0$  will precess about  $B_0$  at approximately the Larmor frequency  $\omega_0$  (its exact frequency is determined by the chemical environment of the nucleus). This rotating magnetization vector  $M_0$  will induce a sinusoidally varying voltage in the linear RF coil (Figure 1-3) that will decay in the  $xy$ -plane with time constant  $T_2$  (assuming a perfectly homogeneous sample) due to a loss of coherence, and regrow along the  $z$ -axis with a time constant  $T_1$  (1). In-vivo, the  $T_2$  of water and measured metabolites is less than the  $T_1$ (20, 21). In practice, the signal induced in the RF

coil decays with relaxation time constants  $T_1$  and  $T_2^*$ . The time constant  $T_2^*$  includes the effect of signal loss due to spin dephasing as a result of  $B_0$  field inhomogeneities. The vector  $M_0$  oscillates at a frequency on the order of 64 MHz at 1.5 Tesla. However, it is common practice to demodulate this signal using a standard reference frequency. In the case of  $^1\text{H}$  spectroscopy, this reference frequency is set to the precession frequency of water ( $\text{H}_2\text{O}$ ) within the sample.

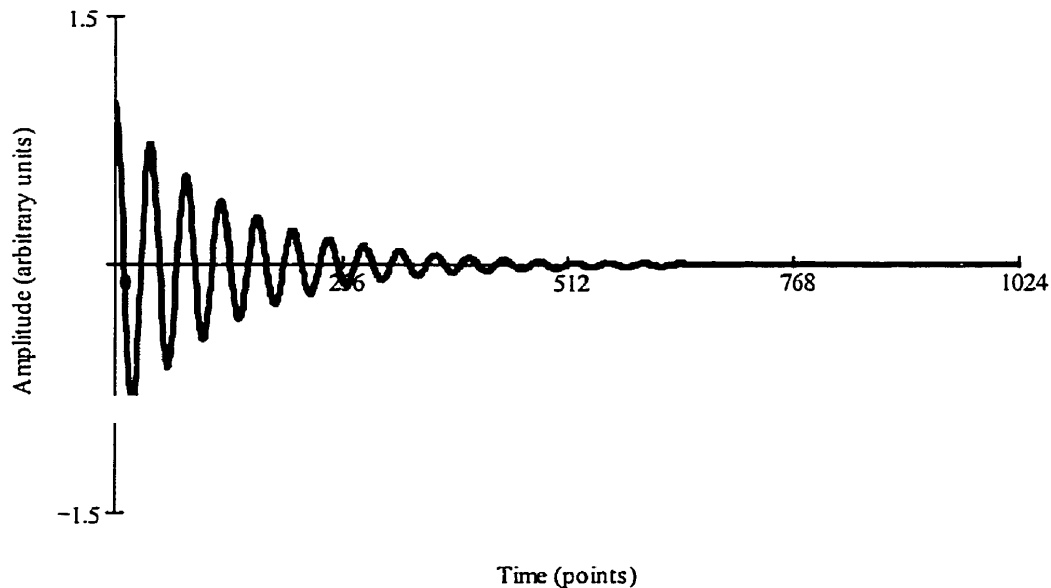


**Figure 1-3: Time Domain NMR Signal**

The NMR signal induced by the net magnetization in the receiver coil following demodulation with the reference frequency. In this example, the signal amplitude is unity, and the signal is oscillating at a frequency of 5 Hz. There is no phase offset or time delay between the instant when the  $B_1$  field is turned off ( $M_0$  reaches the  $y'$ -axis) and the acquisition of data. The signal decays with time constants  $T_1$  and  $T_2$ .

The fast Fourier transform (22) of this signal produces a single peak at a frequency of 5 Hz.

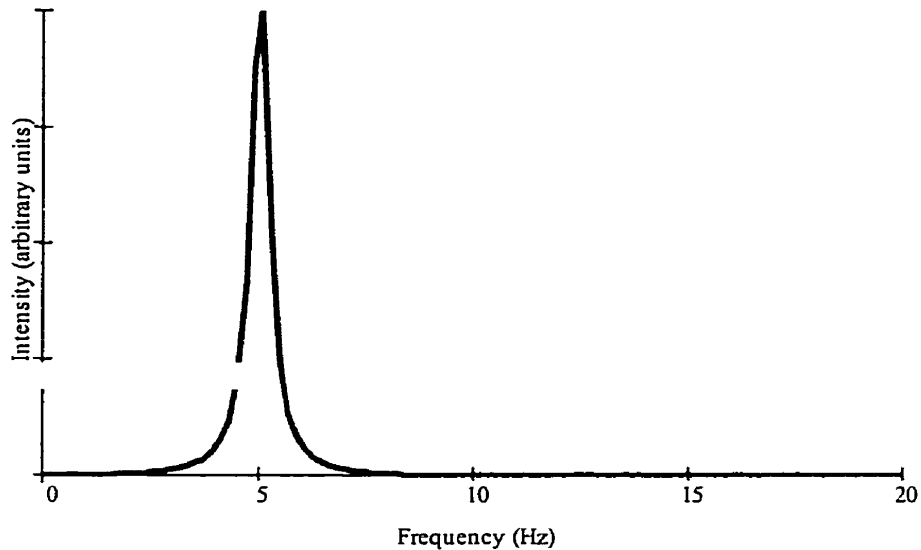


### Figure 1-4: Frequency Domain NMR Signal

The signal shown in Figure 1-3 following fast Fourier transform.

Although seemingly different, the data displayed in Figures 1-3 and 1-4 contain the same information. Historically, NMR data of this type has been Fourier transformed prior to quantification because spectral information is more intuitively visualized in the frequency domain. In the frequency domain, the area under the spectral peak is proportional to the concentration of the nucleus under investigation (this is equal to the value of the point at time 0 in Figure 1-3). Similarly the full width at half maximum (FWHM) of the peak in Figure 1-4 is related to the rate of signal damping in Figure 1-3, and the position of the peak in Figure 1-4 is related to the oscillation frequency of the signal in Figure 1-3.

#### 1.0.3 Spin Echoes and Stimulated Echoes

The formation of echoes (23) is another means of observing the NMR signal.

Echo generation can be used in conjunction with localization techniques to obtain

spectra from small localized tissue volumes, as described in Section 1.2.2. An echo is formed when spins which have lost phase coherence, due to differences in precession frequency and constant  $B_0$  variations within the sample, are refocused and regain phase coherence. One method of generating a spin echo is to apply a 90 degree excitation pulse, allow the spins to dephase, and then apply a 180 degree refocus pulse as illustrated in Figure 1-5.

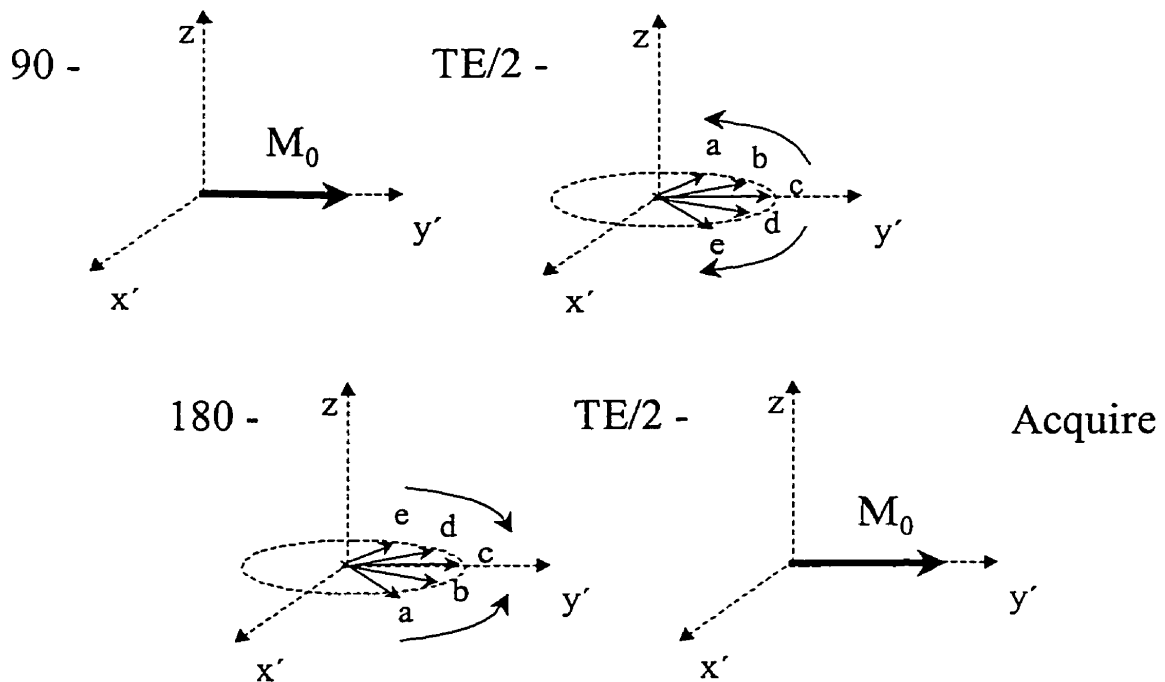


**Figure 1-5: Spin Echo Formation**

Following the application of a 90 degree excitation pulse, the net magnetization vector is nutated to the  $x'y'$  plane. Spin vectors begin dephasing due to differences in precession frequency, and magnetic field inhomogeneities. A 180 degree pulse flips the spins so that they begin to refocus. Spins a and e, which were precessing fast relative to spin c, will continue to precess fast and in the same direction as prior to the 180 degree refocusing pulse. Therefore, all spins will realign at the time TE (echo time) and form a spin echo.

Additional 180 degree pulses can be added to generate more echoes. For example, a spin echo is also generated following a  $90 - TE/4 - 180 - TE/2 - 180 - TE/4 - \text{Acquire}$  sequence. Another type of echo, called a stimulated echo can be generated by applying a  $90 - TE/2 - 90 - TM$  (mixing time)  $- 90 - TE/2 - \text{Acquire}$  sequence which is described in more detail within the context of spatial localization in Section 1.2.2. The difference between spin echoes and stimulated echoes is in how magnetization information is stored prior to echo formation. In the case of spin echoes, information is stored in the transverse plane, while information leading to stimulated echoes is stored partly in the transverse plane (during  $TE/2$  periods) and partly along the z-axis (during the  $TM$  period). Therefore, the intensity of the echo maximum is determined by the transverse relaxation time,  $T_2$ , for spin echoes and by  $T_1$  and  $T_2$  for stimulated echoes. Consequently, echoes that are formed in a short echo time (i.e. 0-20 ms) suffer little attenuation due to  $T_2$  losses, while echoes formed at later times (i.e. 270 ms) are more severely attenuated.  $T_1$  losses during the stimulated echo  $TM$  period are usually negligible. One disadvantage of stimulated echoes is that they only have half the signal to noise ratio of spin echoes, although stimulated echoes generally have shorter echo times.

Another important consideration in the formation of echoes is the effect of homonuclear scalar coupling. Scalar coupling is described in more detail in section 1.1.1. Homonuclear scalar coupling prevents complete refocusing of the NMR signal during echo formation and results in spectral peaks that have different phase (Figure 1-6). The degree of phase discrepancy is proportional to the scalar coupling constant and the amount of time elapsed prior to echo formation (echo time). Therefore resonances from metabolites with coupled

nuclei become significantly reduced and distorted due to scalar coupling at long echo times. In this study the echo time of 20 ms reduced the effect of scalar coupling and  $T_2$  relaxation losses.

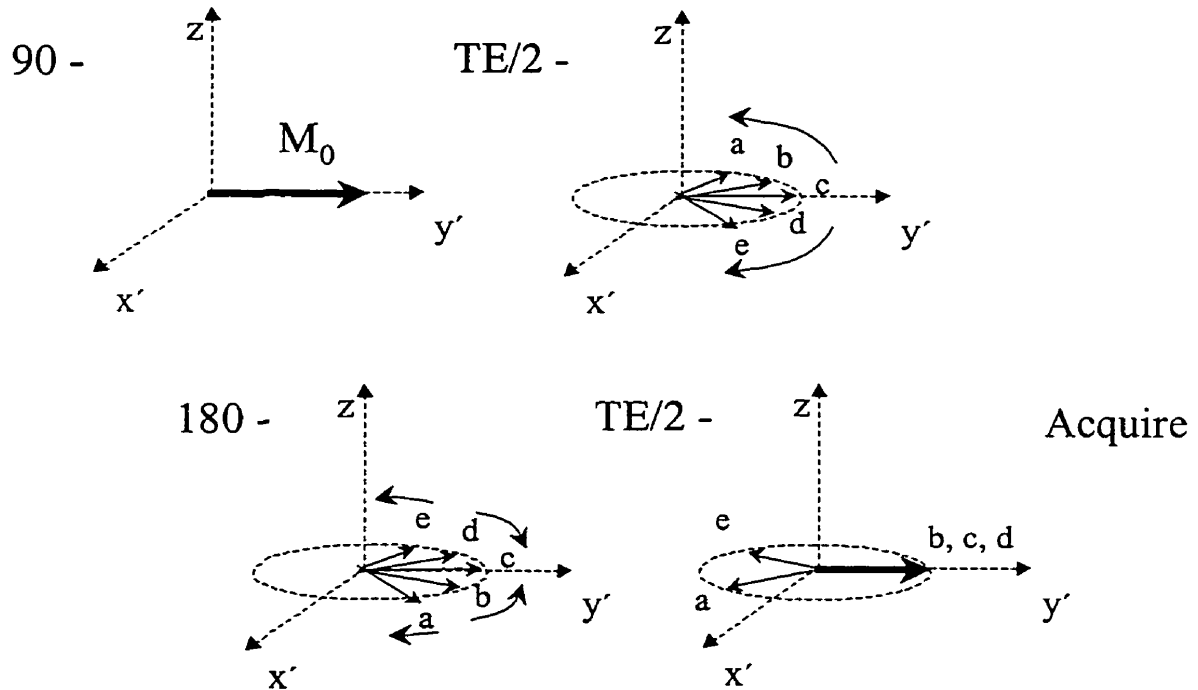


### Figure 1-6: Spin Echo Formation with Scalar Coupling

In this example, spins  $b$ ,  $c$ , and  $d$  are dephased due to differences in precession frequency and magnetic field inhomogeneities as shown in Figure 1-5. Spins  $a$  and  $e$  are coupled. Following the 180 degree refocus pulse, the precession direction of coupled spins is inverted so that these spins continue to dephase.

Discussions regarding spectroscopic quantification apply equally to NMR data collected immediately following a 90 degree excitation pulse or following echo formation. The entire problem of spectroscopic quantification can be simplified to the accurate and precise determination of the peak area for all peaks that may be

present in a spectrum. This is a trivial problem for a spectrum such as the one shown in Figures 1-3 and 1-4. However, in-vivo spectra are more complex and contain overlapping components making it difficult to resolve individual metabolites.

#### 1.0.4 A Short History of In-Vivo Quantification Strategies and Data Acquisition

Methods of analysis for in-vivo spectra have changed over the past 20 years to manage data of increasing complexity. The fundamental goal of MR spectral quantification is to accurately and precisely determine the area under each spectral peak. This area is directly proportional to the concentration of the nucleus from which the peak arose. When spectra are acquired from in-vitro solutions, spectral peaks are well resolved (Figure 1-4 or 1-8) and it is sufficient to measure peak height to determine concentrations (24) assuming all peaks have the same linewidth. A variation of this method, which accounts for differences in peak linewidth, is to calculate peak area using computer integration (24). Although peak integration is still occasionally used today for the quantification of in-vivo spectra, this method is generally not useful for short echo  $^1\text{H}$  MR spectra because it requires a large degree of user interaction and can only be used for well resolved resonances. Figure 1-7 shows a typical 4.0 T in-vivo brain spectrum and illustrates the degree of overlap of many components. Simple peak integration will not produce accurate or precise metabolite levels estimates from such a spectrum.



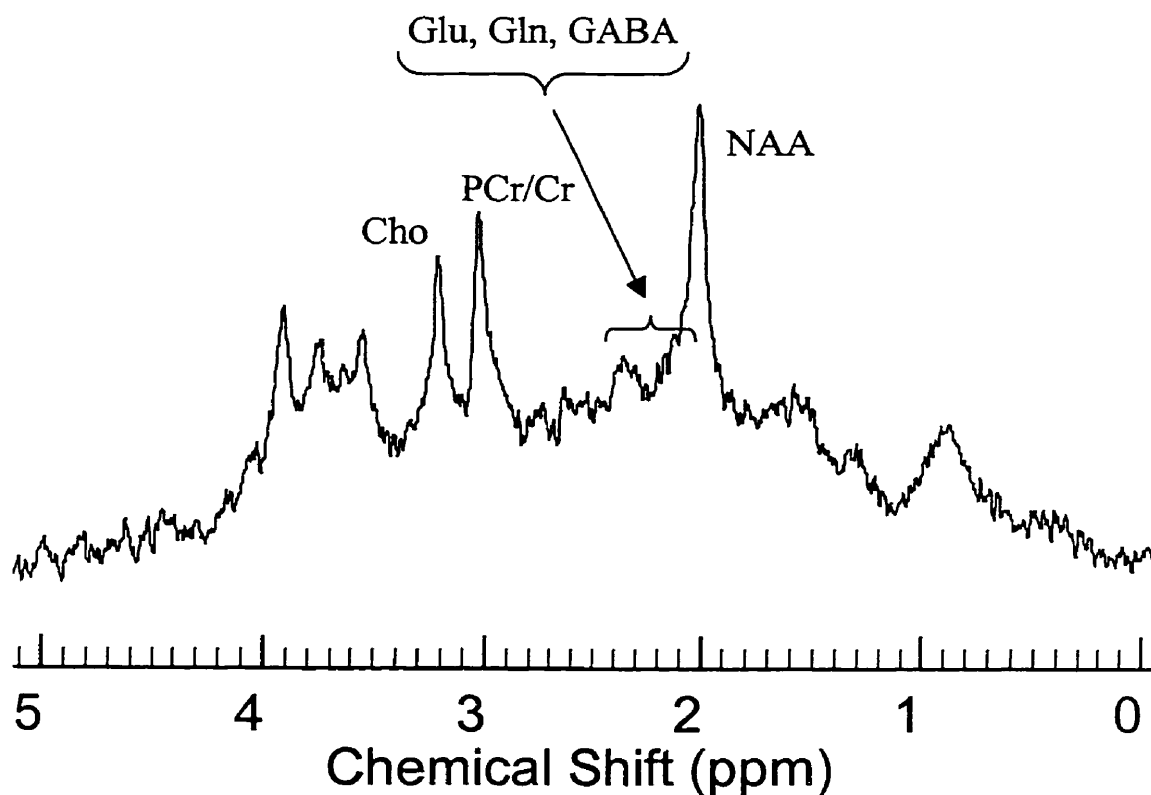


**Figure 1-7: 4.0 Tesla In-Vivo Spectrum**

A typical 4.0 Tesla in-vivo brain spectrum is shown to illustrate the overlap of resonance information. The metabolites Glu, Gln, and GABA all have resonances in the range 2.0-2.4 ppm, (the ppm scale is explained in section 1.10) however it is impossible to isolate individual peaks from each metabolite. NAA, PCr/Cr, and Cho produce more distinct spectral components.

Spectral overlap can be avoided, if data acquisition is limited to a single metabolite by employing one of the many spectral editing techniques described in the literature (25, 26, 27, 28). These techniques select only the metabolite of interest, thereby simplifying quantification since it is possible to use integration to determine metabolite levels. However, some of these techniques suffer from low signal to noise ratio in-vivo due to the method of editing, which necessitates data

collection from large volumes. Therefore, these techniques can only be used when looking for changes in a specific metabolite from a large volume.

When information regarding multiple metabolites is desired, computer peak fitting can be used as the means of extracting spectral peak areas with increased precision. Many approaches to computer fitting have been attempted including lineshape modeling using linear (29) and non-linear (in the time (30) or frequency (14) domain) fitting techniques (31), principle component analysis (32), Prony method (33), and wavelet analysis (34). The two most commonly used techniques for spectral fitting incorporate lineshape modeling with linear or nonlinear minimization (14, 15, 29, 30). Both of these techniques are discussed in detail in Section 1.3 and Appendices C and D. Spectral fitting based on linear minimization is performed in the time domain and does not include prior knowledge about the metabolites contained within the spectrum. On the other hand spectral fitting using non-linear minimization, which can be performed in either the time or frequency domain, does include prior knowledge regarding signals within the spectrum. Both techniques have been applied to in-vivo spectroscopy with some success. However, the complexity of short echo  $^1\text{H}$  spectra necessitates the use of prior knowledge about metabolites within the spectrum in order to obtain physiologically meaningful results. Several groups (14, 15) have incorporated prior knowledge with non-linear fitting for the quantification of short echo  $^1\text{H}$  spectra. One recent approach by Provencher (15) in the frequency domain utilized digitized metabolite spectra as prior knowledge, and handled baseline macromolecules (discussed in detail in Section 1.3.8) by fitting a smooth lineshape to the baseline that was also consistent with the data. The advantage of this approach is that prior knowledge regarding metabolite

spectra are digitized, not parameterized, therefore no lineshape is assumed a priori. The disadvantage relates to the method of baseline modeling, which always produces good looking fits but may not be correct. Stanley et al (14) also proposed a method of data analysis in the frequency domain which utilized parameterized prior knowledge. The main disadvantage of this approach was the model function used was limited in that it did not incorporate phase or delay time as parameters to be fit. Therefore, user interactive phasing of data was required prior to analysis.

When attempting complex spectral analysis utilizing prior knowledge, several important factors must be considered which ultimately determine the amount of user interaction employed. These factors include the domain used for fitting, the method of prior knowledge modeling, the amount of prior knowledge incorporated into the model, the method of handling the signal from a largely unknown and variable spectral baseline (16), and the method of handling spectral components other than the metabolites of interest (including residual water signal). These issues are considered in more detail in Chapters 2 and 3.

The magnetic field strength used for data collection also affects in-vivo spectral quantification. The acquisition of in-vivo spectroscopic data has traditionally occurred at low field strength (0.5 – 1.5 Tesla) due to the availability of these types of clinical MR scanners, the technical limitations and costs involved in producing higher field MR scanners, and the unknown risks associated with magnetic field exposure at higher fields. Recently however, research systems have been built for human use at fields of up to and surpassing 4.0 Tesla. The acquisition of human in-vivo data at high field strengths (i.e. 4.0 T vs. 1.5 T) may

increase the precision and accuracy of metabolite measures from in-vivo spectra due to the increase in signal to noise ratio and chemical shift dispersion with field strength. These issues are described in more detail in Section 1.1.4.

#### 1.0.5 Thesis Objectives

The acquisition of short echo  $^1\text{H}$  spectra with low S/N and resolution has resulted in low measurement precision for a number of metabolites using past quantification strategies. Therefore, subtle metabolite level differences between patients with mental illnesses and controls which may be present within the brain may go undetected. Therefore, the objectives of this thesis were to:

- 1) Develop a quantification strategy for short echo  $^1\text{H}$  MR spectroscopy data that would increase the quantification precision of all measured metabolites. This included the following specific goals:
  - a) To develop non-interactive software for the quantification of spectroscopic data in the time domain and frequency domain.
  - b) To develop a feasible quantification strategy accounting for spectral baseline contributions and other resonances within the spectrum
  - c) To determine whether quantification precision increases for data acquired at high field strength (4.0 T) compared to low field strength (1.5 T).
- 2) To apply the optimized quantification strategy to the measurement of metabolite levels from in-vivo data with low S/N and resolution. Data were collected from schizophrenic patients, obsessive compulsive patients, and

healthy control subjects to determine if metabolite level differences were detectable between these groups.

#### 1.0.6 Hypotheses

The following hypotheses were made:

- 1) The use of fully automated software in the time domain would improve the quantification precision of metabolites such as glutamate and glutamine by removing user bias.
- 2) That accurate information regarding macromolecule signals and resonances outside the spectral region of interest must be included as prior knowledge for optimal quantification precision.
- 3) The acquisition of data at 4.0 Tesla would lead to increased quantification precision compared to 1.5 Tesla due to increased S/N and chemical shift dispersion.
- 4) Metabolite level differences would be detectable in the medial prefrontal cortex of schizophrenic patients indicating abnormal glutamatergic neurotransmission.
- 5) Metabolite level differences would be detectable in the striatum of obsessive-compulsive patients indicating reduced neuronal density in this region.

#### 1.0.7 Thesis Outline

The remainder of Chapter 1 contains important background information for material discussed in Chapters 2 and 3 regarding in-vivo spectroscopy, data acquisition, spectral processing, and metabolite quantification.

Chapter 2 contains a manuscript written by Robert Bartha entitled, "Factors Affecting the Quantification of Short Echo In-Vivo  $^1\text{H}$  Spectra: Prior-Knowledge, Peak Elimination, Filtering." This manuscript was co-authored by Dick J. Drost and Peter C. Williamson and has been accepted for publication in NMR in Biomedicine. This manuscript outlines a strategy for the quantification of short echo  $^1\text{H}$  MR spectra in the time domain that optimizes metabolite measurement precision. The quantification software used for data analysis was written and developed by John Potwarka and myself. I developed the quantification strategy and prior knowledge template described within this paper, as well as collected, processed, and analyzed (including statistical comparisons) all the data presented.

Chapter 3 contains a manuscript written by Robert Bartha entitled, "Quantification and Precision of Short Echo  $^1\text{H}$  Spectra at 1.5 and 4.0 Tesla." This manuscript was co-authored by Dick J. Drost, Peter C. Williamson, and Ravi S. Menon and is in preparation for submission to NMR in Biomedicine. This manuscript outlines the advantages and disadvantages of high field in-vivo short echo  $^1\text{H}$  spectroscopy. Metabolite measurement precision is compared between spectra acquired at 1.5 and 4.0 Tesla. In addition overall experimental reproducibility at 4.0 Tesla is determined. I optimized the sequence used for data collection at 4.0 Tesla (originally written by Ravi Menon) to achieve optimal water suppression and minimal eddy current distortion. I collected, processed, and analyzed (including statistical comparisons) all data presented within this paper.

Chapter 4 contains a brief introduction to the in-vivo applications presented in Chapters 5 and 6. Specifically, the illnesses of schizophrenia and obsessive-

compulsive disorder are discussed in relation to the basal-ganglia-thalamocortical neuronal circuit. This neuronal circuit may be involved in both mental illnesses.

Chapter 5 contains a manuscript written by Robert Bartha entitled, "Measurement of Glutamate and Glutamine in the Medial Prefrontal Cortex of Never Treated Schizophrenic Patients and Healthy Controls by Proton Magnetic Resonance Spectroscopy." This manuscript was co-authored by Peter C. Williamson, Dick J. Drost, Ashok Malla, Tom J. Carr, Len Cortese, Gita Canaran, Jane Rylett, and Richard W.J. Neufeld, and is published in the Archives of General Psychiatry / Volume 54, October 1997. In this study, spectra from the left medial prefrontal cortex were acquired and quantified from a group of never-treated schizophrenic patients and matched control subjects. I collected, processed, and analyzed (including statistical comparisons) all spectroscopic data presented within this paper.

Chapter 6 contains a manuscript written by Robert Bartha entitled, "A Short Echo  $^1\text{H}$  Spectroscopy and Volumetric MR Imaging Study of the Corpus Striatum in Patients with Obsessive-Compulsive Disorder and Healthy Comparison Subjects." This manuscript was co-authored by Murray B. Stein, Peter C. Williamson, Dick J. Drost, Richard W. J. Neufeld, Tom J. Carr, Gita Canaran, Maria Densmore, Geri Anderson, and Abdur R. Siddiqui, and is published in the American Journal of Psychiatry / Volume 155, November 1998. In this study, spectra from the left striatum were acquired and quantified from a group of obsessive-compulsive patients and matched control subjects. I collected, processed, and analyzed (including statistical comparisons) all spectroscopic

data presented within this paper. The volumetric measurements reported in this study were made by Maria Densmore.

Chapter 7 contains a general summary and discussion of future work.

Appendix A contains a detailed description of a post-processing technique (ECC correction) that corrects temporal phase distortions.

Appendix B contains a detailed description of a post processing technique (QUALITY deconvolution) that corrects temporal and spatial phase distortions and restores the Lorentzian lineshape.

Appendix C contains a detailed description of the use of singular value decomposition for the removal of residual water signal.

Appendix D contains a detailed description of the Levenberg-Marquardt Algorithm used in the spectral quantification.

Appendix E describes the quantification of a series of simulated in-vivo  $^1\text{H}$  short echo spectra over a range of signal to noise ratios.

Appendix F contains proof of ethics approval for the studies involving human subjects.

Appendix G contains copyright release information.



## 1.1 In-Vivo Spectroscopy

To describe the improvements made to the quantification of short echo in-vivo  $^1\text{H}$  MR spectra a few basic concepts must be introduced which describe a typical MR spectrum of this type. This section outlines the important features of a spectrum and why they occur.

### 1.1.1 The In-Vitro Short Echo $^1\text{H}$ Spectrum

Typically the frequency of a spectral peak is measured relative to a reference peak (35). Throughout this thesis trimethyl-silyl propionic acid (TSP) was used as the chemical shift reference when in-vitro spectra were acquired, and defined as 0 Hz frequency. Therefore, all in-vitro resonance frequencies were measured relative to this reference. Another common practice is the normalization of the frequency scale by the absolute frequency of the reference (usually approximated by the spectrometer reference frequency) to the  $\delta$  scale. The  $\delta$  scale has units of parts per million (ppm) and facilitates the comparison of spectra acquired at different field strengths (19).

$$\delta_i = 10^6 \cdot \frac{(\nu_i - \nu_{TSP})}{\nu_{TSP}} \quad [1-2]$$

Where:

- $\delta$          $\equiv$  the chemical shift in ppm
- $\nu_i$        $\equiv$  the chemical shift of resonance  $i$  in Hz
- $\nu_{TSP}$      $\equiv$  the chemical shift of the TSP reference in Hz

The essential features of a spectrum were described in Section 1.0.2 (Figure 1-4). That spectrum consisted of a single peak arising from a single species of

magnetically equivalent  $^1\text{H}$  nuclei. Most molecules however contain more than one magnetically distinct hydrogen nucleus, each resonating at a slightly different frequency. Equation 1-1 states that the precession frequency of a particular group of spins depends on the strength of the magnetic field experienced by the nucleus. However, the local field experienced by the nucleus will be different from the main magnetic field  $B_0$  due to the effect of the surrounding electrons. This effect is known as electronic shielding (19). The presence of the static magnetic field  $B_0$  causes the electron cloud surrounding the nucleus to circulate in such a way as to reduce the magnetic field seen by the nucleus (diamagnetic effect) (36). This electronic shielding is dependant on the electronic structure and symmetry of a particular nucleus and is therefore characteristic for nuclei within different molecules (19). Therefore the magnetic field seen by the nucleus can be written as equation 1-3.

$$B = B_0(1 - \sigma) \quad [1-3]$$

Where  $\sigma \equiv$  shielding constant

Therefore equation 1-1 can be modified to equation 1-4.

$$\omega = \gamma \cdot B_0(1 - \sigma) \quad [1-4]$$

This implies that nuclei from different molecules, or even within the same molecule, but at different positions will precess about  $B_0$  at a characteristic frequency. Consider a molecule that contains two magnetically distinct hydrogen nuclei  $H_B$  and  $H_A$  as shown at the top of Figure 1-8.

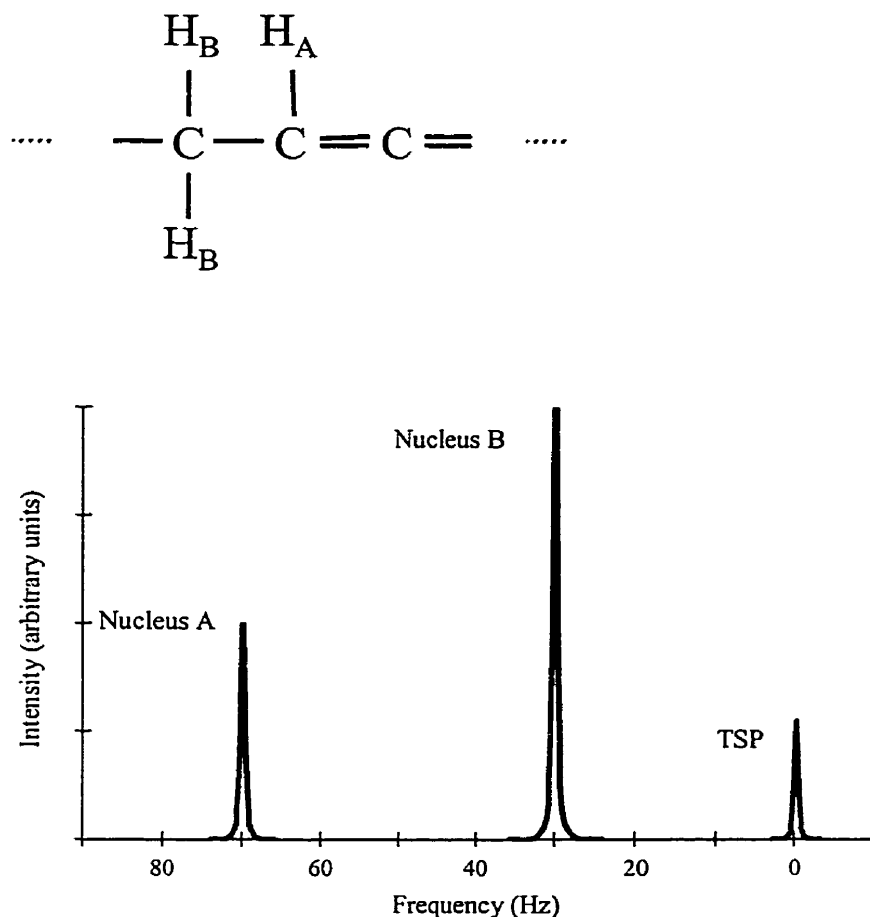


**Figure 1-8: Short Echo  $^1\text{H}$  MR Spectrum of Two Different Nuclei**

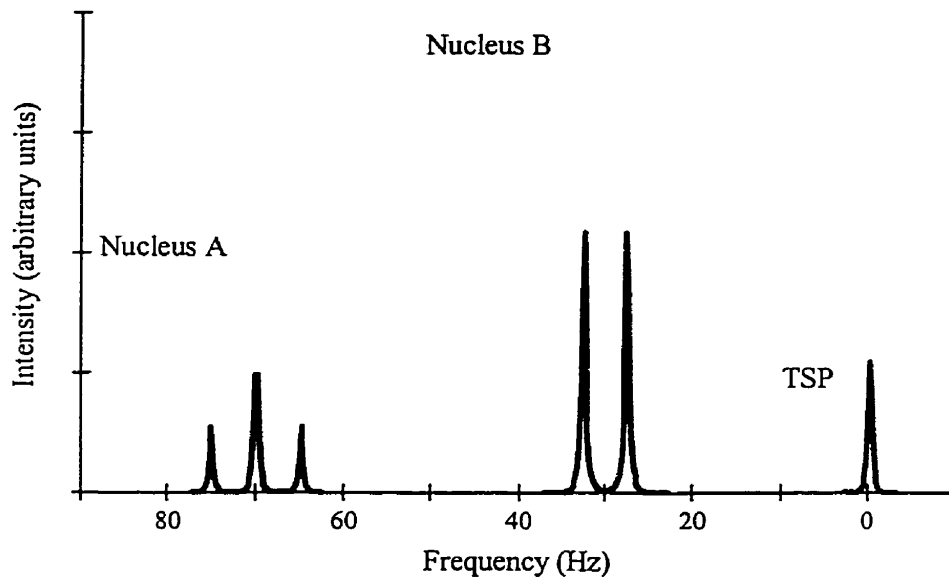
The spectrum obtained following demodulation when the molecule shown above (with two different spin groups: nucleus A ( $\text{H}_A$ ) and nucleus B ( $\text{H}_B$ )) is dissolved in water along with the chemical shift reference TSP (arbitrarily defined as 0 frequency). For the purpose of this illustration we will assume that both nuclei labeled  $\text{H}_B$  are equivalent. The resonance line due to  $\text{H}_B$  has twice the area as that due to  $\text{H}_A$  since it is a signal induced by two nuclei rather than one ( $\text{H}_A$ ).

Figure 1-8 illustrates how nuclei with different shielding constants ( $\sigma$ ) appear as lines at different positions in the NMR spectrum (assuming no scalar coupling

interaction between nuclei). Therefore, nuclei from different regions within a molecule may be identified.

The NMR spectrum is further complicated by the interaction which occurs between spin  $\frac{1}{2}$  nuclei in the same molecule, provided these nuclei are separated by three bonds or less (19). The term used to describe this through bond interaction is scalar coupling or J-coupling. J-coupling also exists between nuclei separated by more than three bonds, however the effect of this is not visible except in very high resolution spectroscopy. This interaction is mediated through the electron cloud surrounding both nuclei. J-coupling is dependent only on the structure of the molecule, therefore, it is independent of the molecular orientation or the field strength at which the NMR experiment is performed.

In the example shown above, nucleus A would be J-coupled to nuclei B and vice-versa. If nuclei A and B are aligned anti-parallel with respect to one another, then the overall energy of the system is lower than if they are aligned parallel. In an ensemble of spins, both situations will arise in an equal number of molecules. This leads to a splitting of the spectral line from nucleus A by an amount  $J_{AB}$ . Typical values for J are in the 2-10 Hz range for homonuclear proton coupling (19). Consider again the molecule shown in Figure 1-8, except now, we will introduce the effect of J-coupling on peak splitting assuming  $J_{AB} = 5$  Hz. This would give rise to the spectrum shown in Figure 1-9. Peak phase modulation due to J-coupling is not shown in Figure 1-9, however this effect can be seen in Figure 1-10. This type of phase modulation is dependent on echo time and the magnitude of the J-coupling constant.



**Figure 1-9: Short Echo  $^1\text{H}$  MR Spectrum of Two Different Nuclei with J-Coupling**

The spectrum obtained from the molecule shown in Figure 1-8 with two different spin groups, nucleus A ( $\text{H}_\text{A}$ ) and nucleus B ( $\text{H}_\text{B}$ ). For the purpose of this illustration we will assume that both nuclei labeled  $\text{H}_\text{B}$  are equivalent. The line from nucleus A is split into a triplet due to J-coupling with nucleus B, while the line from nucleus B is split into a doublet due to J-coupling with nucleus A. In both cases,  $J_{\text{AB}} = 5$  Hz. J-coupling phase modulation effects are not shown.

The resonance line from  $\text{H}_\text{A}$  is split twice; once from the first  $\text{H}_\text{B}$ , each resulting line is then split again by the second  $\text{H}_\text{B}$ . This results in a triplet with area ratios 1:2:1. Similarly, the resonance line from  $\text{H}_\text{B}$  is split once by  $\text{H}_\text{A}$  to form a doublet with area ratios 1:1. The total area under the peaks is preserved. If we imagine that noise is also present on the spectral baseline, peaks which are split due to J-coupling become more difficult to observe relative to the noise. The high degree of J-coupling in the  $^1\text{H}$  NMR spectrum of molecules such as glutamate (Figure 1-10) and glutamine make these metabolites difficult to quantify in-vivo.

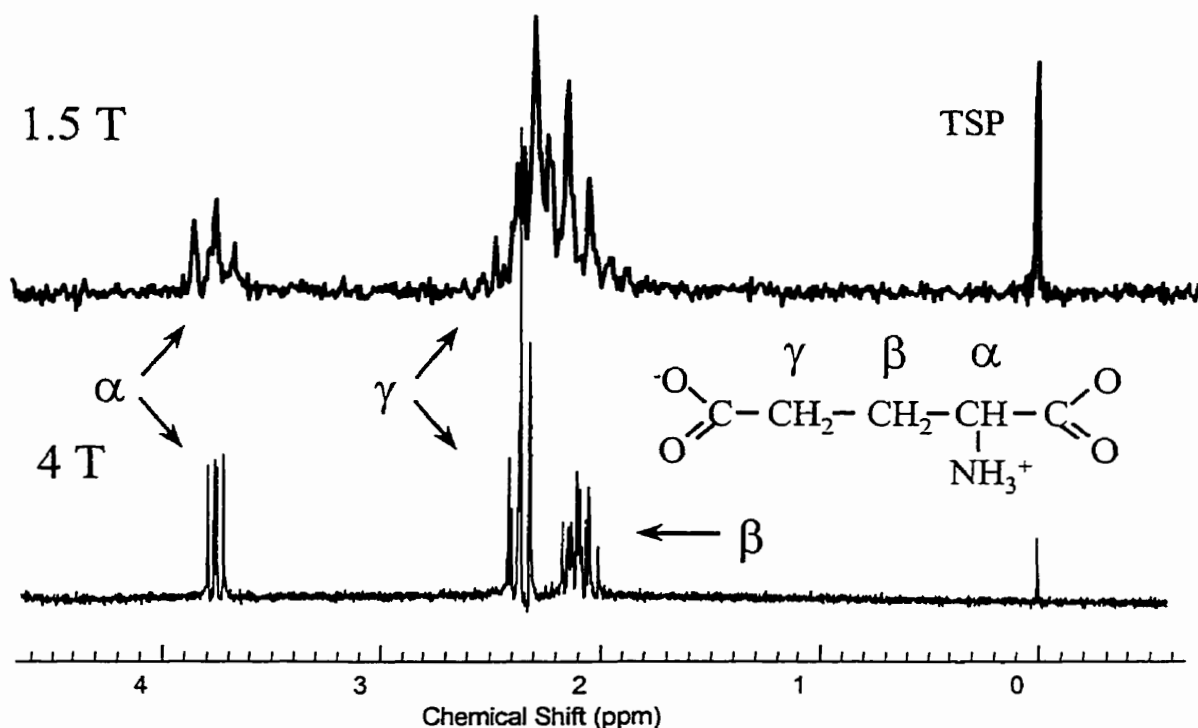


**Figure 1-10: Short Echo  $^1\text{H}$  MR In-vitro Spectrum of glutamate at 1.5 Tesla and 4.0 Tesla**

The in-vitro spectrum of glutamate is shown at 1.5 Tesla and 4.0 Tesla illustrating the effects of J-coupling. The TSP reference standard is visible on the right side of both spectra. The splitting of the  $\alpha$ ,  $\beta$ , and  $\gamma$  multiplet structures is due to J-coupling. The molecular structure of this amino acid is shown between the two spectra. The  $\beta$  multiplet has the most peaks since it is coupled to both the  $\alpha$ , and  $\gamma$  protons. Phase modulation effects are visible, especially in the  $\gamma$ -multiplet resonances.

It is interesting to note the increased chemical shift dispersion of the  $\gamma$  and  $\beta$  multiplet structures at 4.0 T compared to 1.5 T (Figure 1-10). However, peaks within each multiplet retain the same splitting at both field strengths since they arise due to J-coupling. It is also possible to observe the phase modulation of

peaks within a multiplet ( $\gamma$  multiplet) due to homonuclear J-coupling. This phase modulation arises because the data in Figure 1-10 was acquired from an echo. Phase modulation is field strength independent although it is more visible on the 4.0 T spectrum in Figure 1-10 because this spectrum has higher resolution. Figure 1-10 illustrates that the in-vitro spectra of individual metabolites are easy to interpret at either field strength because of good signal to noise ratio and good resolution yielding visually separated peaks. The excellent resolution obtained in-vitro is due to the homogeneity of the in-vitro sample. Unfortunately, this homogeneity is significantly reduced when the data acquisition is repeated in-vivo.

### 1.1.2 The In-Vivo Short Echo $^1\text{H}$ Spectrum

The in-vivo spectrum is complicated by several factors. First, the magnetic field homogeneity within the body is reduced compared to a phantom or in-vitro sample due to the presence of structures with different magnetic susceptibility (soft tissue, bone, air). Therefore, the resolution of an in-vivo spectrum is decreased (usually on the order of 500-1000%) compared to an in-vitro spectrum (comparing the full width at half maximum of the water resonance). Second, the in-vitro spectrum is composed of resonances from multiple metabolites, many of which overlap (there are at least twelve detectable metabolites in a short echo  $^1\text{H}$  MR spectrum). Third, unknown components on the spectral baseline (likely arising from macromolecules) overlap with metabolite resonances. And fourth, since it typically takes 10-15 minutes to acquire adequate signal to noise ratio for reliable quantification of in-vivo spectra, spectra are susceptible to further distortion due to subject motion. These factors make the quantification of short

echo  $^1\text{H}$  spectra difficult at best, and have resulted in a high level of uncertainty for many quantified metabolites.

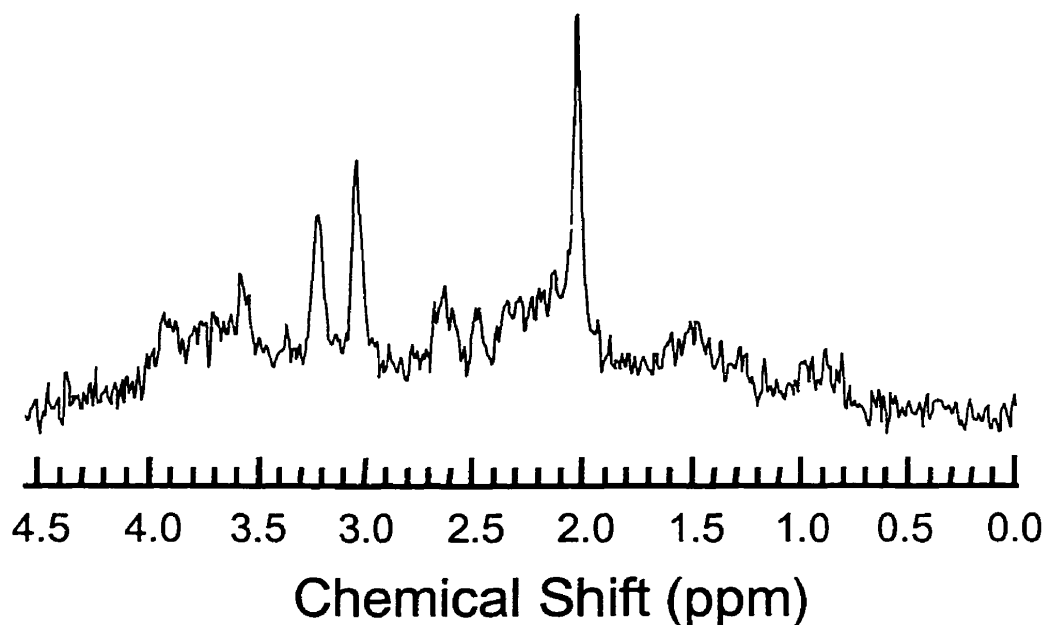


**Figure 1-11: Short Echo  $^1\text{H}$  MR In-vivo Spectrum at 1.5 Tesla**

The short echo in-vivo  $^1\text{H}$  spectrum at 1.5 Tesla shows several distinct peaks including NAA at 2.0 ppm, PCr/Cr at 3.0 ppm and Cho at 3.2 ppm. Metabolic information relating to Glu and Gln is mostly contained within the range 2.0-2.4 ppm, although no distinct peaks are present. Distinct peaks from glutamate and glutamine are not visible due to severe J-coupling within, and overlap between, these metabolites

### 1.1.3 In-Vivo Spectroscopy: The Problems

Unlike  $^1\text{H}$  MR in-vitro chemistry, human  $^1\text{H}$  MR in-vivo studies suffer from several problems related to the nature of the experiment. Ultimately, each problem complicates the acquired data and results in a loss of quantification precision. There are three distinct problems which are encountered when doing human in-



vivo experiments: low signal to noise ratio (S/N), low spectral resolution, and the presence of spectral artifacts caused by the use of magnetic field gradients for localization.

Three factors contribute to the low S/N typical of human in-vivo spectroscopy studies. First, due to safety regulations (and technical/financial problems in building high field whole body magnets), human experiments must be conducted at low field strength compared to chemical or animal studies. Typical experiments are performed at 1.5 Tesla (T) (37, 38, 39, 40) although 4.0 T is now used for clinical research (41, 42). This contrasts with field strengths in excess of 10 T (43, 44) available for in-vitro chemical and biochemical studies. As the S/N of the in-vivo NMR experiment is approximately linearly proportional to the magnetic field strength (45), in-vivo spectroscopy is at an immediate disadvantage. Second, in-vivo studies must be kept short to reduce the effects of patient motion and discomfort. Typical in-vivo spectra are acquired in 6-15 minutes (13, 37, 38, 39) depending on the volume from which data is acquired. Spectra acquired for longer periods suffer a loss of resolution due to subject motion. This contrasts with in-vitro studies that can be run indefinitely to take advantage of signal averaging until the desired S/N is achieved. Third, due to large in-vivo sample sizes (head, body) large volume coils are used to acquire data. Since thermal noise from within the subject is the dominant factor contributing to noise in an in-vivo spectrum (45), the noise seen by the coil comes from a much larger volume than that from which spectroscopic data is collected. Therefore, the large coils necessary for in-vivo spectroscopy immediately increase the noise content of the spectrum compared to small in-vitro coils. Also, in-vivo studies must be done at body temperature, while in-vitro

chemistry studies can be done at lower temperatures (using liquid nitrogen to cool the sample) to reduce thermal noise. In these in-vitro studies noise from the coil and other electronics become the dominant noise source rather than the sample studied.

Two factors contribute to the low resolution of in-vivo spectroscopy studies. First, due to the size of the magnet bore required to accommodate human subjects, magnetic field homogeneity is significantly less than that found in high resolution spectrometers. Typical optimized magnetic field homogeneity (using room temperature shim sets) for a 1.5 T whole body magnet is 5 Hz FWHM across a 20 cm spherical phantom. Second, magnetic field homogeneity decreases when a living subject is studied due to differences in magnetic susceptibility between substances within the organism (i.e. bone, soft tissue, air). In contrast, chemical studies are conducted on homogeneous samples and use spectrometers that have many room temperature shims that can be adjusted for an indefinite length of time to achieve optimal magnetic field homogeneity within the sample. Regardless of the reason, the decreased resolution of in-vivo spectra compared to in-vitro spectra results in the severe overlap of spectral components to the point where individual resonances can not be resolved. This has necessitated the development of quantification strategies specifically for in-vivo data.

The presence of spectra artifacts is discussed in more detail in section 1.3. Generally, because in-vivo subjects are large, spectroscopic data is only acquired from a specific tissue volume (usually 5-30 cm<sup>3</sup>) (13, 37, 38, 39, 40). The acquisition of data from localized regions within the sample requires using pulsed magnetic field gradients (46) which are described in Section 1.2.2.

Although necessary for localization, pulsed magnetic field gradients produce spectral artifacts. These artifacts are described in detail in Sections 1.3.1-1.3.4. In contrast, high resolution in-vitro spectroscopy requires no localization since samples are typically only a few milliliters in volume (43).

Despite these limitations, in-vivo spectroscopy is an invaluable research tool since it can be used to non-invasively measure many important metabolites.

#### 1.1.4 Field Strength Considerations

As already mentioned, in-vivo spectroscopic data can be acquired at a variety of field strengths (0.5 T – 4.0 T) (41, 42, 47). Each field strength has advantages and disadvantages as described in detail in Chapter 3. Generally speaking higher field strengths are advantageous because S/N scales proportional to field strength (45) and Larmor precession frequency (equation 1-1) is directly proportional to field strength resulting in increased chemical shift dispersion (peak separation).

The signal to noise ratio of a spectroscopy experiment scales directly proportional to field strength and sample size (48, 49). Therefore, the increased signal to noise ratio at higher field strengths can be traded for a reduced sample size while still maintaining adequate signal to noise ratio for reliable quantification. Since partial volume effects (gray/white matter) are a concern in neuro-spectroscopy, any reduction in volume size reduces partial volume contamination and may lead to more precise results.

The second advantage to high field spectroscopy relates to the increase in chemical shift dispersion. This is due to the increased absolute frequency difference between resonances as field strength increases (equation 1-1). However, this increase in peak separation does not apply to peaks that arise due to J-coupling (which is field strength independent). Therefore, the separation of multiplet structures increases (Figure 1-10) on an absolute scale while the same is not true for the lines within a multiplet structure. This may lead to an increase in quantification precision because multiplets from different molecules (glutamate and glutamine) which are overlapped at low field strengths may now be resolved.

There are also several disadvantages to high field spectroscopy that will only be briefly mentioned. First, the increase in field strength will cause an increase in magnetic field distortion at boundaries between substances with different magnetic susceptibilities (air, bone, tissue). Increased field distortion may even occur at the microscopic level within tissue leading to an overall decrease in magnetic field homogeneity within the volume studied (50). Reduced magnetic field homogeneity results in reduced spectral resolution (line broadening), although this effect may be partially offset by increased chemical shift dispersion and reduced sample sized at the higher field strength.

The second major disadvantage is related to eddy current effects (51, 52) induced by gradient coil vibration (Section 1.3) caused by the application of magnetic field gradients for spectral localization. These eddy current effects which lead to spectral distortions and an overall reduction in S/N are described in detail in Section 1.3 and Chapter 3.

## **1.2 Data Acquisition**

### 1.2.1 Introduction to Data Acquisition and Localization

Data for the studies described in this thesis were acquired on either a Siemens 1.5 Tesla SP4000 magnetom (Chapters 2, 5, and 6), a Siemens 1.5 Tesla Vision (Chapter 3), or a Siemens/Varian 4.0 Tesla hybrid (Chapter 3). Data acquisition parameters are given in each chapter as required. The study of specific brain structures required the localization of data acquisition to within particular cerebral volumes. There are a number of different methods available for spectral localization, for example, surface coil methods (53), image selective spectroscopy (ISIS) (54), projection presaturation (55), point resolved spectroscopy (PRESS) (56), and stimulated echo acquisition mode (STEAM) (57). Surface coil methods have been used to study cerebral tissue near the skull; however they are not effective for the localization of structures deep within the brain. ISIS has been used mainly for  $^{31}\text{P}$  spectroscopy since there is very little delay time between excitation and data collection. This is important for  $^{31}\text{P}$  spectroscopy where signal decay times are much less than that seen in  $^1\text{H}$  spectroscopy ( $T_2^* \sim 15\text{-}20$  ms for  $^{31}\text{P}$  metabolites versus  $T_2^* \sim 45\text{-}60$  ms for  $^1\text{H}$  metabolites). ISIS is a subtraction technique and thus is more sensitive to motion artifacts than either PRESS or STEAM. PRESS and STEAM are both used extensively for localized proton spectroscopy. Both have advantages and disadvantages, although as will be explained in the next section, STEAM localized spectroscopy may have advantages over PRESS, especially at high fields.

### 1.2.2 Stimulated Echo Acquisition Mode (STEAM) Localized Spectroscopy

In order to localize data collection to a particular volume within the brain, the spins within that volume must be uniquely excited compared with spins outside the volume of interest. This can be achieved using magnetic field gradients combined with frequency limited radio frequency (RF) pulses. The combined action of a magnetic field gradient and frequency limited RF pulse excites a slice of spins within the sample – slice selective excitation (48). Typically sinc shaped RF pulses are used giving an approximately rectangular excitation frequency range (48).

When placed within the static magnetic field  $B_0$ , all spins within the sample experience the same magnetic field, assuming a perfectly homogeneous  $B_0$  field throughout the sample and no electronic shielding. A magnetic field gradient may be applied along any direction within the sample using gradient coils causing spins within the sample to precess at frequencies determined by their spatial localization. Therefore, a frequency selective RF pulse can be used to excite a slice whose thickness is determined by the strength of the magnetic field gradient and the bandwidth of the RF pulse (48).

A specific volume within the sample may be excited by repeating this slice selection three times in orthogonal directions. Only a cube at the intersection of all three slices will experience all three excitations (Figure 1-12). The selective excitations illustrated in Figure 1-12 are ideal. In practice, slice selection profiles are not perfectly rectangular resulting in selected volumes that are not exactly cubic (58).

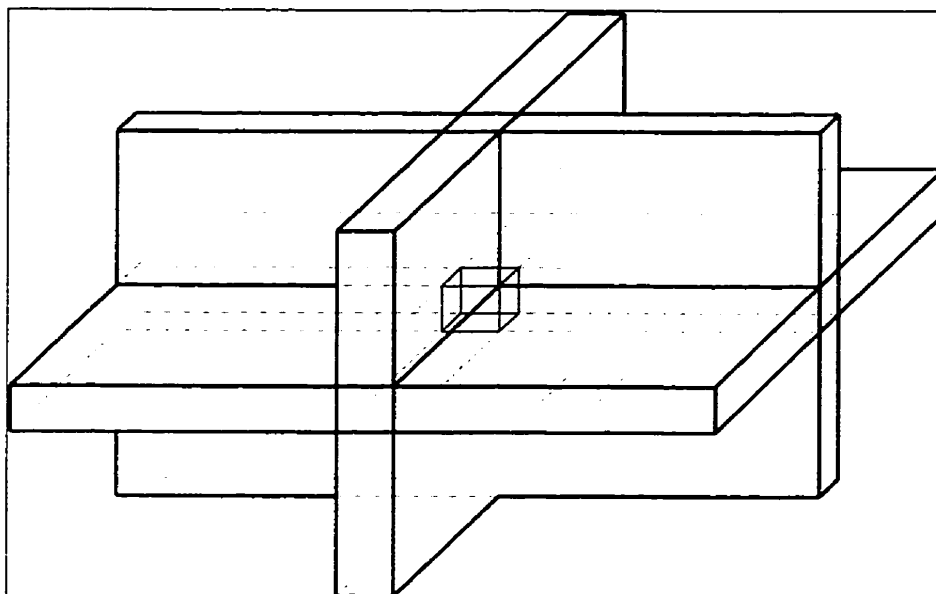


**Figure 1-12: Volume Selection**

A specific volume of tissue can be excited by repeated slice selection in three orthogonal directions. Following the third slice, only a cube at the intersection of all three slices experiences all RF pulses and is refocused.

Any sequence that uses three selective RF pulses to generate a measurable spin signal may be used in conjunction with slice select gradients to localize data acquisition. Both PRESS and STEAM sequences meet these requirements. PRESS consists of a  $90 - TE/4 - 180 - TE/2 - 180 - TE/4 - \text{Acquire}$  sequence which generates a spin-echo at time TE. STEAM consists of a  $90 - TE/2 - 90 - TM - 90 - TE/2 - \text{Acquire}$  sequence, which generates a stimulated echo at time TE. The values 90 and 180 in the above sequence descriptions represent the flip angle imparted to the irradiated spins.

Another complication of in-vivo  $^1\text{H}$  spectroscopy is the signal from water within the volume studied. Since the concentration of water in the sample is  $\sim 10000$  times the concentration of most metabolites, the water signal must be

suppressed to avoid problems associated with the dynamic range of the receiver and overlap of the water signal with metabolite signals. The method of water suppression used in this thesis is called CHESS (59). This method of suppression involves selective excitation of the water resonance (using a Gaussian shaped pulse) followed by crusher gradients to destroy the signal in the transverse plane. The process of selective excitation followed by gradient crushers can be repeated multiple times.

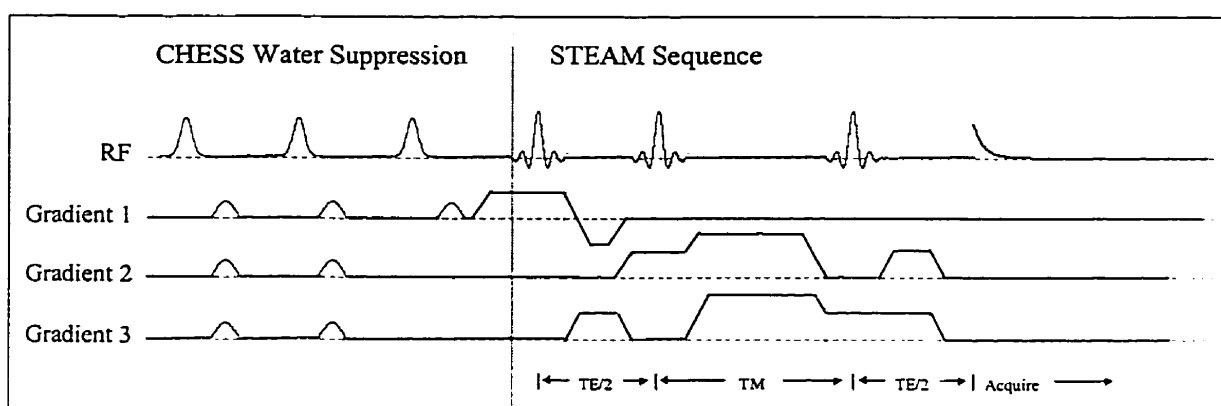


**Figure 1-13: Schematic of STEAM sequence used at 4.0 Tesla**

The STEAM sequence used for in-vivo data acquisition at 4.0 Tesla. The initial part of the sequence uses three frequency selective Gaussian pulses and half sine crusher gradients for water suppression. The second part uses three 7 lobe sinc frequency selective pulses for localization. TE was 20 ms and TM was 30 ms for studies conducted in this thesis.

Studies performed within this thesis used the STEAM method of localized spectroscopy. STEAM has several advantages over PRESS, although it also has one major disadvantage – a factor of two decrease in S/N (omitting relaxation effects). First, slice selection profiles are better with STEAM



compared to PRESS. This is because 90 degree excitation pulses are used for localization in STEAM, which produce less off resonance distortion (48) compared to the 180 degree pulses used in PRESS. Second, since 90 degree pulses and associated rewind gradients are typically shorter than 180 degree pulses, the echo times (TE) achievable using STEAM are less than those achievable using PRESS. This allows data collection with reduced  $T_2$  weighting and J-coupling phase modulation effects (Section 1.0.3).

### 1.2.3 Typical Experimental Protocol

Typical experimental protocols for in-vivo experiments involved the following general steps: global shim, acquisition of localizer images, local shim, and data acquisition. Localizer images were used to position the volume from which spectroscopic data were collected. A typical timeline is presented in Figure 1-14.

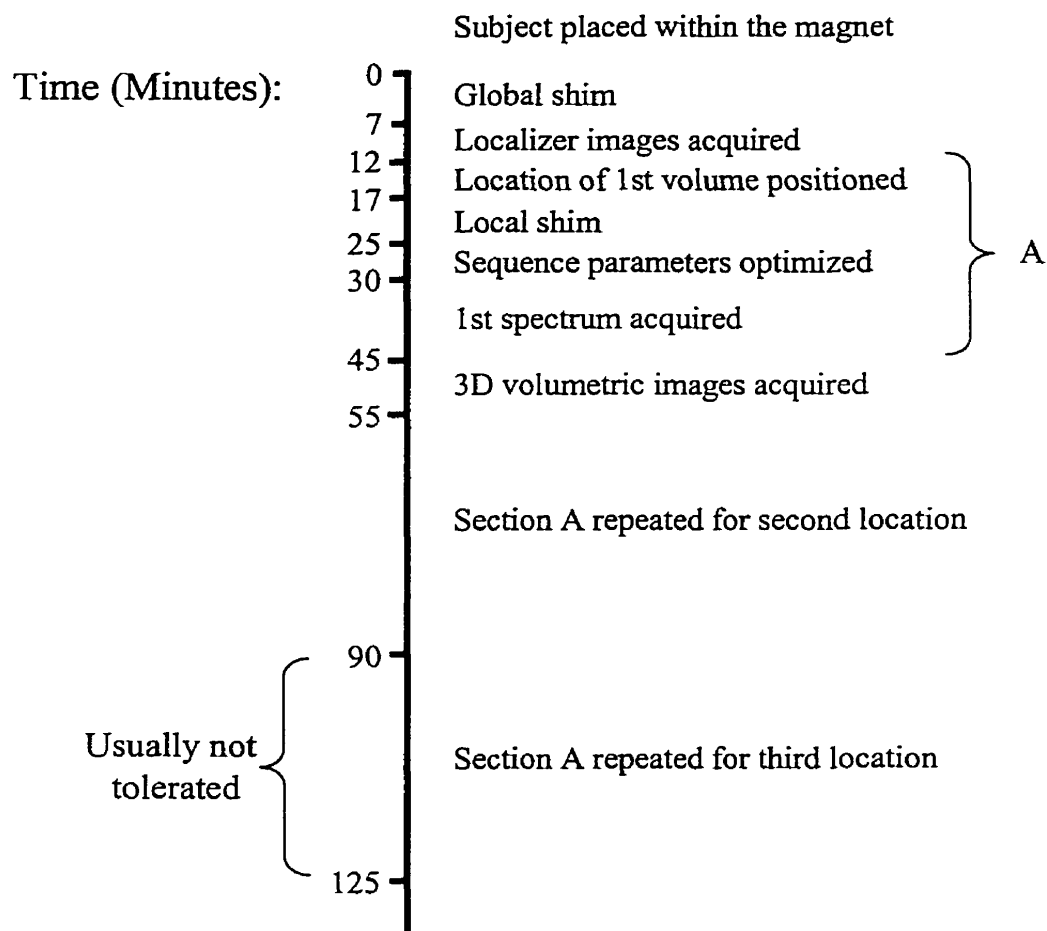


**Figure 1-14: In-vivo Experimental Timeline**

Timing requirements for a typical in-vivo experiment.

### **1.3 Data Quantification**

#### **1.3.1 Lineshape Distortion**

Spectroscopic data may contain lineshape distortions. These distortions are either caused by temporal or spatial fluctuations in  $B_0$  (52, 60, 61). This section describes artifacts that cause temporal  $B_0$  fluctuations. Artifacts caused by

spatial  $B_0$  fluctuations are described in section 1.3.2. Generally, the precession frequency of each resonance in a spectrum is given by equation 1-5.

$$\omega_j(r,t) = -\gamma \cdot B_{0,j}(r,t) \quad [1-5]$$

Where  $\omega_j(r,t)$   $\equiv$  frequency of resonance  $j$  at position  $r$  and time  $t$   
 $\gamma$   $\equiv$  the gyromagnetic ratio  
 $B_{0,j}(r,t)$   $\equiv$  magnetic field felt by resonance  $j$  at position  $r$  and time  $t$

The acquisition of data from localized brain regions in these studies was accomplished using a frequency selective localization technique: STEAM. Localization was achieved by combining frequency selective RF pulses with pulsed magnetic field gradients as described in section 1.2.1. One drawback of such a technique is that the rapid switching of magnetic field gradients induces eddy currents in conductive structures within the magnet (bore and cryostat) by induction (Lenz's Law) (36). Rapid switching of magnetic gradient pulses also leads to gradient coil vibration (due to the torque and thrust experienced by the gradient coil from the main magnetic field). Both induced eddy currents and gradient coil vibration are regionally specific and can last for more than several hundred milliseconds. Artifacts produced by gradient coil vibration increase with field strength as the forces on the gradient coil increase resulting in more vibration. Both induced eddy currents and gradient coil vibration produce characteristic artifacts which modulate the magnetic field term of equation 1-5 as described by equation 1-6.

$$B_{0,j}(r,t) = (B_0 + \Delta B_{0,D} \cdot e^{-(t\alpha_D)} + \Delta B_{0,V} \cdot \sin(t \cdot f_V + \phi_V) \cdot e^{-(t\alpha_V)} + \Delta B_{0,S}(r))(1 - \sigma_j) \quad [1-6]$$

Where	$B_0$	$\equiv$ average magnetic field strength across sample
	$\Delta B_{0,D}$	$\equiv B_0$ drift cause by eddy currents
	$\Delta B_{0,V}$	$\equiv B_0$ vibration caused by gradient coil motion
	$\Delta B_{0,S}$	$\equiv B_0$ spatial dependence (section 1.32)
	t	$\equiv$ time
	r	$\equiv$ position
	$\alpha_D$	$\equiv$ decay constant of $B_0$ drift
	$f_V$	$\equiv$ frequency of $B_0$ vibration
	$\phi_V$	$\equiv$ phase offset of $B_0$ vibration
	$\alpha_V$	$\equiv$ decay constant of $B_0$ vibration
	$\sigma_j$	$\equiv$ shielding constant of peak j

For the time being (until section 1.3.2) we will assume a homogeneous  $B_0$  field within the sample, therefore  $\Delta B_{0,S}(r) = 0$  in equation 1-6. The effects of  $\Delta B_{0,D}$  and  $\Delta B_{0,V}$  on spectral lineshape are shown in Figures 1-15, 1-16, and 1-17.

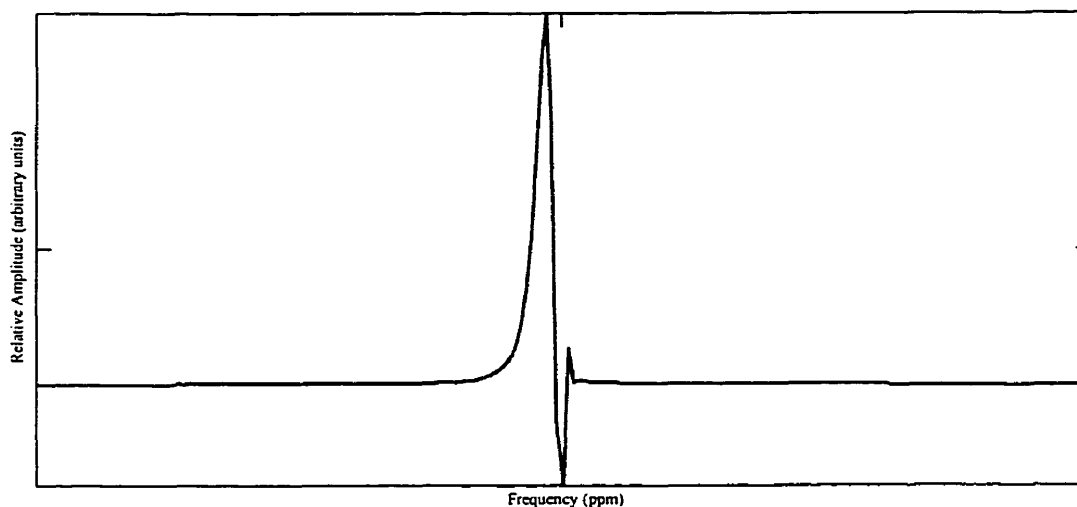


**Figure 1-15: Eddy Current Lineshape Distortion**

The effect of  $B_0$  drift on spectral lineshape. This is a simulated unsuppressed water peak with no noise. The distortion shown above is the result of a 10 Hz  $B_0$  drift with a decay constant of 5 Hz as described by equations [1-5] and [1-6].

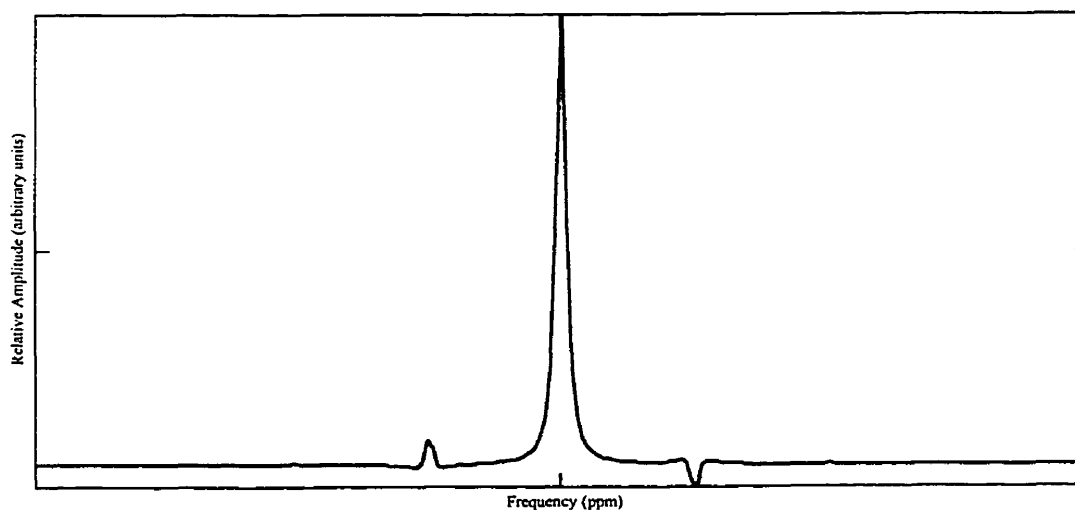


**Figure 1-16: Gradient Coil Vibration Lineshape Distortion**

The effect of gradient coil vibration on spectral lineshape. This is a simulated unsuppressed water peak with no noise. The distortion above is the result of a 100 Hz vibration with a decay constant of 5 Hz as described by equations [1-5] and [1-6].

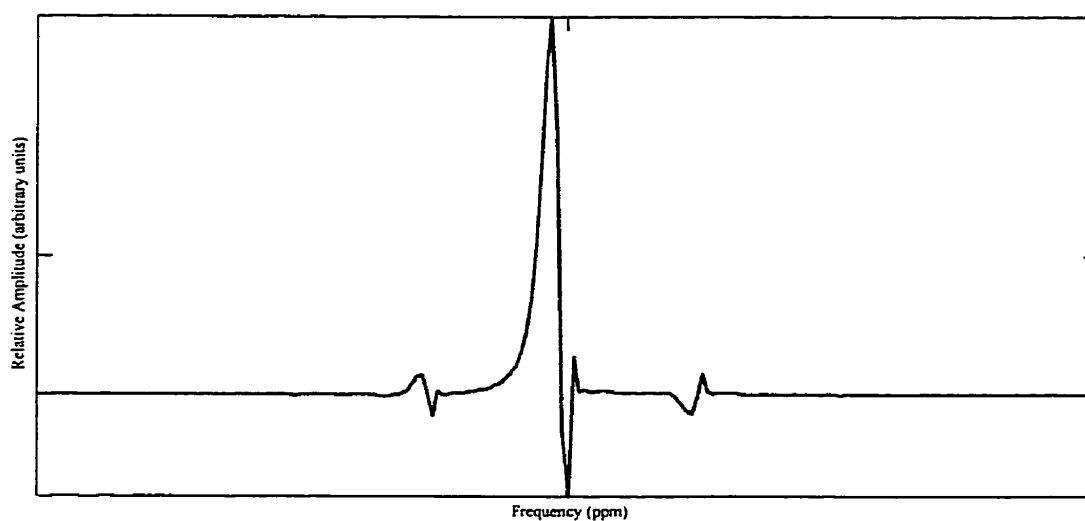


**Figure 1-17: Combined Eddy Current and Gradient Coil Vibration Lineshape Distortion**

The combined effect of  $B_0$  drift and gradient coil vibration as described in Figures 1-15 and 1-16 on a simulated unsuppressed water spectrum with no noise.

These artifacts are also present on the in-vitro creatine spectrum shown in Figure 1-18.

### 1.3.2 Post-Processing using Eddy Current Correction (ECC)

The spectral distortions described above are severe and if left uncorrected would render a typical spectrum unquantifiable. However, several groups have described eddy current correction techniques that can be used to remove the above artifacts (51, 52, 62, 63). All are based on the acquisition of a reference spectrum that contains a single peak on resonance. Therefore, any observed time dependent phase changes present within this reference signal can be attributed to eddy currents. Since the same eddy currents which cause distortion of the reference spectrum also cause distortion of the water suppressed data

spectrum, the phase of the reference peak can be subtracted from the phase of the data spectrum to remove any time dependent phase distortions. This process is described in detail in Appendix A.

Figures 1-18 and 1-19 show 4.0 Tesla in-vitro spectra of creatine before and after eddy current correction using the method described above.

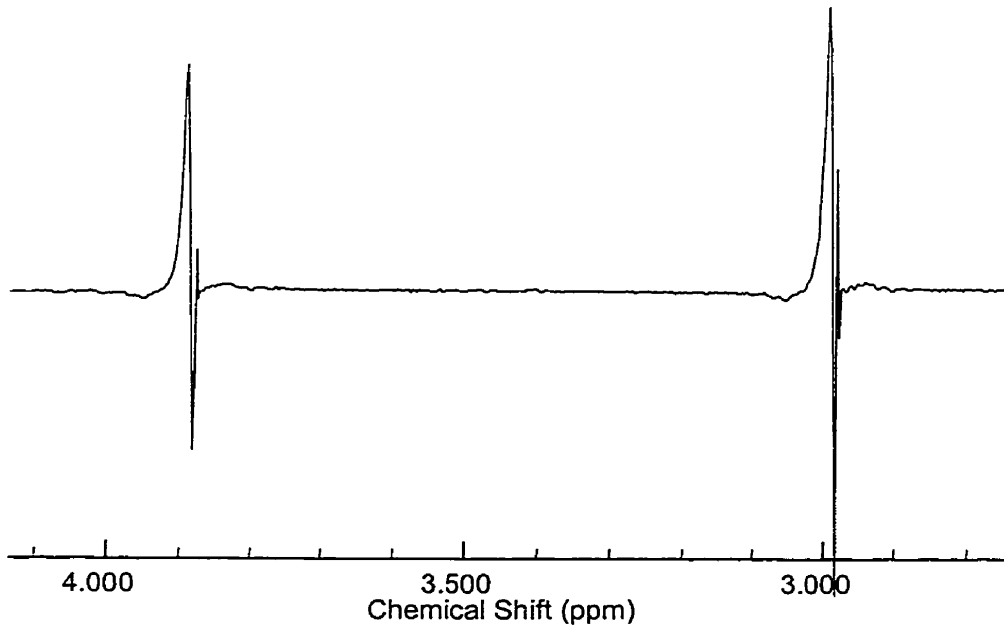


**Figure 1-18: In-Vitro Spectrum with Eddy Currents at 4.0 Tesla**

Creatine (Cr) in-vitro spectrum at 4.0 Tesla before eddy current correction. Both  $B_0$  drift and gradient coil vibration artifacts are visible on each peak.

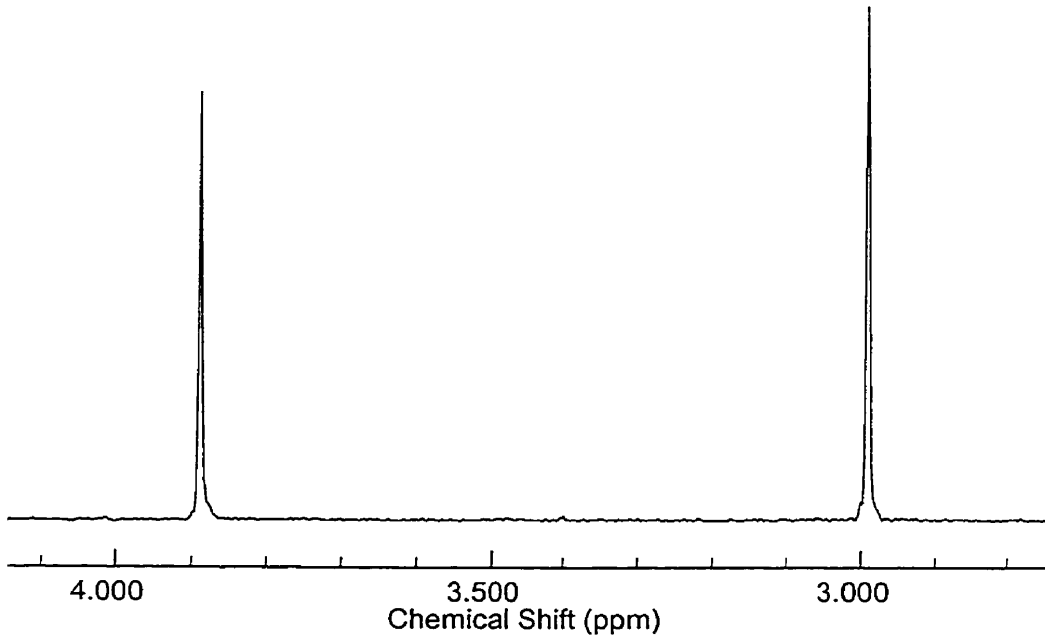


**Figure 1-19: In-vitro Spectrum Following Eddy Current Correction at 4.0 Tesla**

Creatine (Cr) in-vitro spectrum at 4.0 Tesla following eddy current correction. Both B<sub>0</sub> drift and gradient coil vibration artifacts have been removed.

### 1.3.3 Post-Processing using QUALITY Deconvolution

Although simple and effective, the eddy current correction described above removes only time dependant variations in offset frequency. Another source of lineshape distortion arises from spatially dependant variations in offset frequency  $\Delta B_{0,s}(r)$ . A simple method of removing spatially dependant (as well as time dependant) variations in offset frequency, called QUALITY deconvolution, has been developed by De Graaf *et al.* (60). Following this correction process, which is fully described in Appendix B, spectral lines are purely Lorentzian.



Restoration of the Lorentzian lineshape is important when processing spectra if Lorentzian functions are used to model peaks during quantification. Therefore, it would seem that the QUALITY deconvolution is the optimal method for correction of spectral artifacts. However, this method also suffers from one significant problem. Typically unsuppressed water is used as the reference spectrum for these corrections. However, the  $T_2$  of water is significantly shorter (~80 ms) (64, 65) than that of most metabolites (~200–400 ms) (21,66). Therefore the time domain reference data decays to noise prior to the water suppressed data which contains the metabolite information. Consequently, the application of the QUALITY deconvolution leads to a 'division by zero' near the end of the time domain data causing a corruption of these points. This is not usually a problem in-vitro where signals remain intact for > 1 second however is a considerable problem in-vivo as shown in Figure 1-20. To contrast this, Figure 1-21 shows the same data in the time domain following ECC correction.

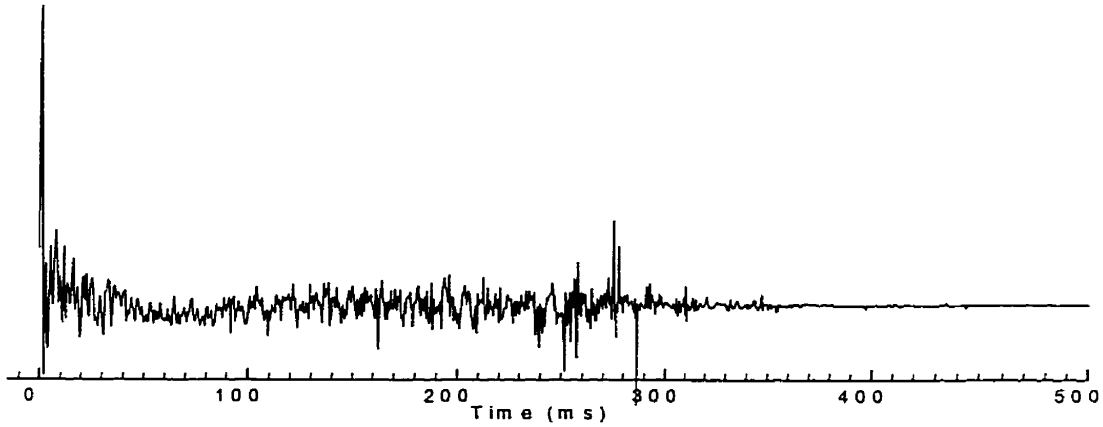


**Figure 1-20: In-vivo Time Domain Signal following QUALITY Deconvolution at 4.0 Tesla**

4.0 Tesla in-vivo time domain data showing the corruption of points near the end of the time domain signal following QUALITY deconvolution. Corrupted points occur between approximately 230-300 ms.

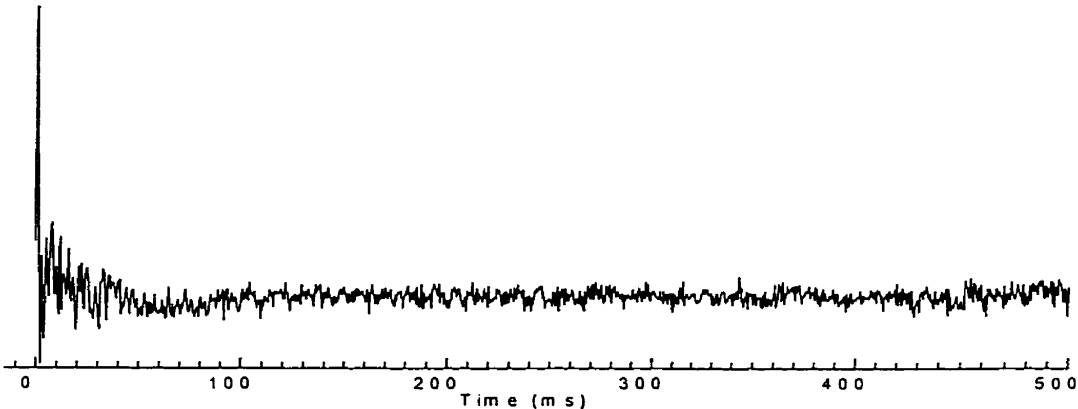


**Figure 1-21: In-vivo Time Domain Signal following Eddy Current Correction at 4.0 Tesla**

4.0 Tesla in-vivo time domain data following ECC correction. There is no evidence of corrupted data points similar to those shown in Figure 1-19 near the end of the time domain signal.

#### 1.3.4 Combined ECC and QUALITY Deconvolution

As described in section 1.3.6, spectroscopic data is modeled using a Lorentzian function. Therefore it is critical that all time and spatial dependent  $B_0$  fluctuation artifacts be removed from the data prior to quantification. For this purpose the QUALITY deconvolution is the superior technique. However as described in section 1.3.3, when this technique is applied to in-vivo data, often points near the end of the time domain signal become corrupted. This is not true of the eddy current correction technique described in section 1.3.2, although consequently, this technique does not correct spatially dependent  $B_0$  fluctuation artifacts.

A better approach is to combine these two techniques by applying a QUALITY deconvolution to the initial portion of the time domain signal, followed by a simple eddy current correction for the remaining points. In this way, data is partially restored to the Lorentzian lineshape and data at the end of the time domain signal is uncorrupted. The point at which the quality deconvolution ends and eddy current correction begins is somewhat arbitrary, although this point should be chosen to maximize the restoration of the Lorentzian lineshape while minimizing data corruption. Additional details regarding this technique are given in the Methods section of Chapter 3. The time domain signal shown in Figure 1-22 has been processed by combined QUALITY deconvolution and ECC correction:

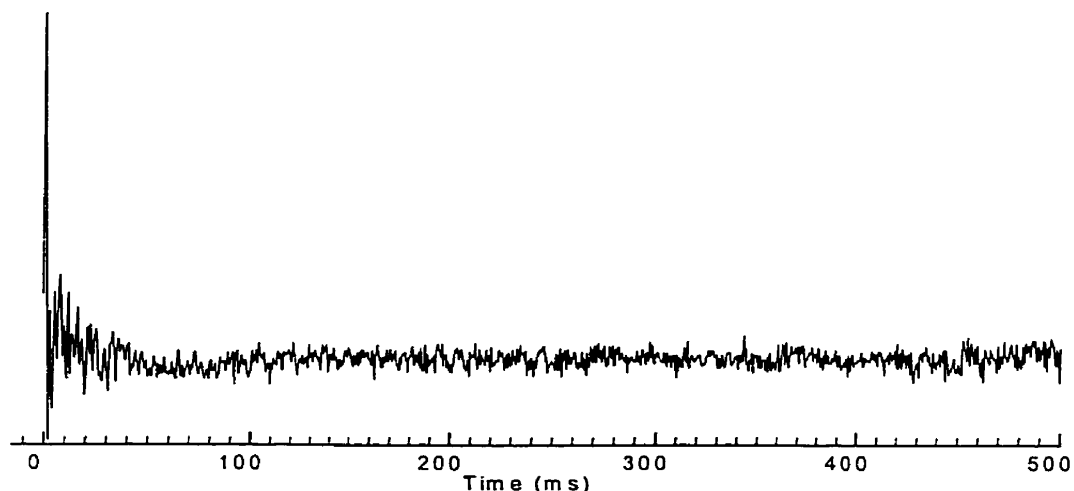


**Figure 1-22: Time Domain Signal after Combined QUALITY Deconvolution and Eddy Current Correction**

4.0 Tesla time domain data following the use of combined QUALITY deconvolution and ECC correction. QUALITY deconvolution was used for the initial 100 ms of signal followed by ECC correction for the remaining data.

### 1.3.5 Subtraction of Residual Water

Following the spectral post-processing described in sections 1.3.2-1.3.4, the residual water signal must be removed from the spectrum (67). This is important as the wings of the residual water signal can extend beneath the region of the spectrum that contains important metabolite information. If left within the spectrum and unaccounted for, this area from the water peak could cause metabolites that overlap with it to be overestimated. In the past, water has not always been removed prior to quantification. In these experiments spectra were manually phase corrected in the frequency domain to reduce the effect of the water wings (14). This process is highly user interactive and can reduce metabolite quantification precision. In an attempt to remove operator interaction from the fitting procedure, all spectra in these studies had residual water

removed using an automated linear fitting routine which required no prior knowledge (30, 29, 68). This automated procedure incorporates a singular value decomposition of the data as described in Appendix C.

Using this technique, each spectrum was fit to a series of damped exponential functions, each with independent amplitude, frequency, phase, and exponential damping. The residual water component was also fit since it is contained within the spectrum. Since no restrictions are imposed on peak parameters, multiple peaks can be used to fit the residual water peak resulting in excellent agreement between data and fit results (even in the case of irregular lineshapes). The results of this fit were used to subtract the residual water signal prior to metabolite quantification by subtracting resonances between 4.5-5.5 ppm (water ~ 4.7 ppm). The result was a spectrum without residual water as illustrated in Figures 1-23 and 1-24.

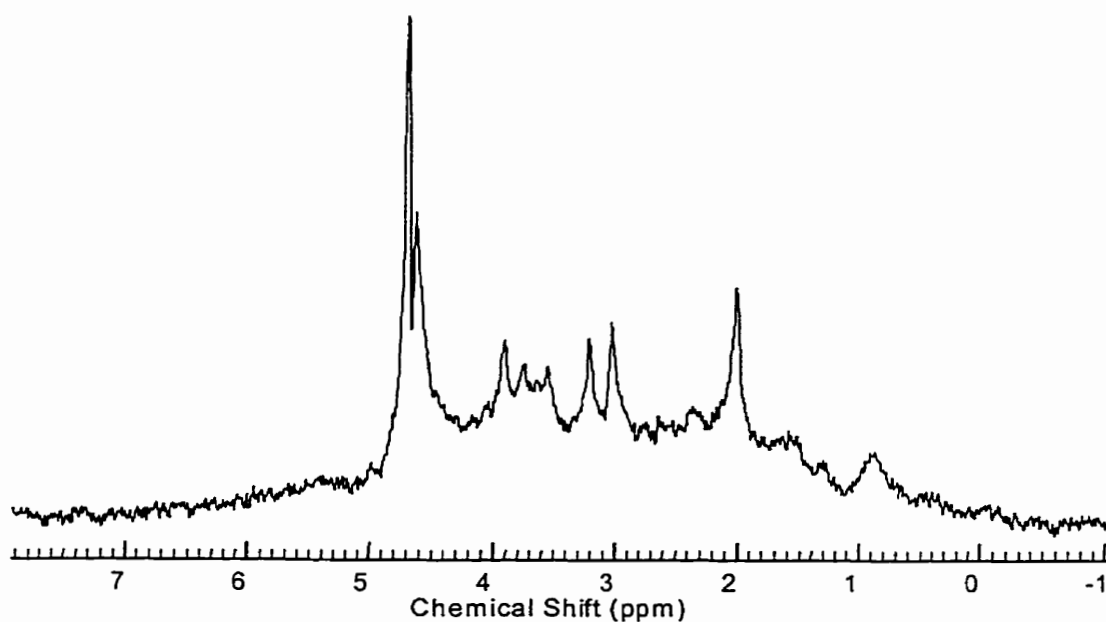


**Figure 1-23: In-vivo Residual Water at 4.0 Tesla**

4.0 Tesla in-vivo spectrum showing residual water peak at  $\sim 4.7$  ppm. This spectrum has been filtered with a 2 Hz exponential filter in the time domain prior to Fourier transform.

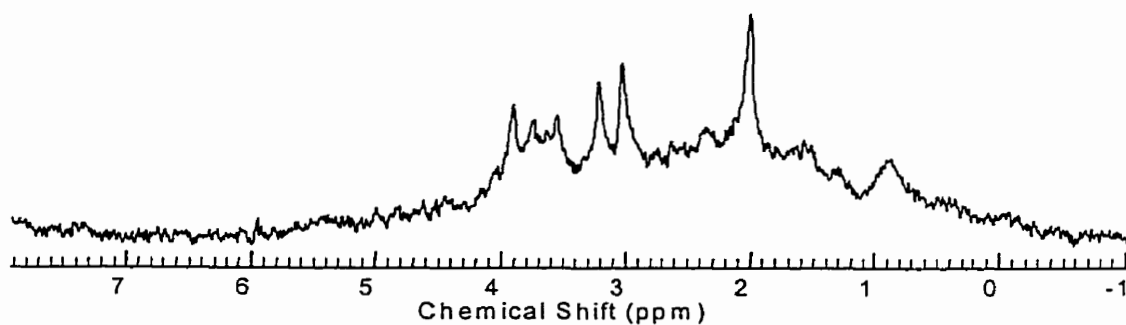


**Figure 1-24: In-vivo Residual Water Removed at 4.0 Tesla**

The 4.0 Tesla in-vivo spectrum shown in Figure 1-22 following the subtraction of residual water. This spectrum is also filtered by a 2 Hz exponential filter in the time domain prior to Fourier transform.

### 1.3.6 Metabolite Quantification

Following the subtraction of the residual water, metabolite levels were quantified using equation 2-1 in Chapter 2. As quantification was done in the time domain, the Fourier transform was never applied to the data except when viewing results, as it is more visually intuitive to view results in the frequency domain. The model function used contained both exponential and Gaussian damping terms, which may be exploited to obtain the best spectral fits. Gaussian damping was used to model macromolecule resonances as described in Section 1.3.8 and Chapter 2, despite the restoration of Lorentzian lineshapes following QUALITY deconvolution. The simplicity of the Gaussian model function in the time domain is perhaps the most compelling reason to quantify data in this domain. The Fourier transform of the Gaussian damping term has a closed form only when the function exists from negative infinity to positive infinity in the time domain (analogous to collecting the NMR signal from an entire echo). Usually, only a portion of an echo is sampled (i.e. the second half), or data is obtained as a FID. In this case, the shape of the Gaussian damping curve is easily modeled in the time domain by incorporating a parameter for delay time ( $t_0$ ) into the model function (see equation 2-1). However, when applying the Fourier transform to the Gaussian function, the incorporation of the parameter  $t_0$  is equivalent to integrating from  $t_0$  to infinity. The solution does not have a closed form and is solved numerically using the error function (69). This will increase the time required for fitting since the model function and its partial derivatives must be calculated numerically.

Quantification of metabolite levels was achieved using a Levenberg-Marquardt non-linear minimization algorithm (70) incorporating prior knowledge about

metabolite resonances (14, 15, 66). In contrast, the linear technique described in section 1.3.5 for water subtraction, which gives excellent looking fits, does not incorporate prior knowledge and yields physiologically meaningless results. This is due to the nature of the in-vivo spectrum which is composed of multiple overlapping resonances. Without the incorporation of prior knowledge into the fitting process, it would be impossible to resolve the contribution made by individual metabolites to the spectrum. The Levenberg-Marquardt minimization technique is described in detail in Appendix D.

Following the application of the Levenberg-Marquardt minimization, a set of parameter estimates were obtained which yielded the amplitudes, damping constants, phase, delay time, and frequencies of each metabolite in the spectrum. The values of the amplitude parameters are directly proportional to the concentration of the metabolite they represent.

Since initial values must be given for each parameter at the start of the fitting routine, the final outcome is somewhat dependant on the initial guesses. Therefore, it is wise to choose initial guesses which are reasonably close to the expected values, or else the fitting routine may become 'stuck' in a local minimum of parameter space and yield sub-optimal results.

### 1.3.7 Metabolite Prior-Knowledge

Due to the complexity and low resolution of in-vivo short echo  $^1\text{H}$  spectra, reliable metabolite quantification is only possible if prior-knowledge regarding individual metabolite lineshapes is utilized. Without such prior-knowledge it is impossible to



distinguish individual metabolites in the spectrum, which is necessary to determine the concentration of each metabolite. Prior-knowledge for quantification was obtained by acquiring a "high resolution" short echo  $^1\text{H}$  in-vitro spectrum of a solution of each metabolite using the same acquisition sequence that was used to collect in-vivo data. This was repeated at 1.5 Tesla and 4.0 Tesla. Each solution was adjusted to an in-vivo pH of 7.04 using HCl and NaOH and contained TSP as a reference for chemical shift and exponential damping.

Prior-knowledge was obtained regarding twelve metabolites which are observable in the short-echo in-vivo  $^1\text{H}$  spectrum. These included: *N*-acetylaspartate (NAA), glutamate (Glu), glutamine (Gln),  $\gamma$ -amino-butyric acid (GABA), aspartate (Asp), *N*-acetylaspartyl-glutamate (NAAG), taurine (Tau), glucose (Glc), choline (Cho), creatine (Cr), scyllo-inositol (Syl), and myo-inositol (Myo). Sample in-vitro spectra are shown in Figures 1-10 and 1-25 for glutamate and glutamine at 1.5 and 4.0 Tesla. Chapter 2 also contains the 1.5 Tesla in-vitro spectrum of *N*-acetylaspartate (Figure 2-1).

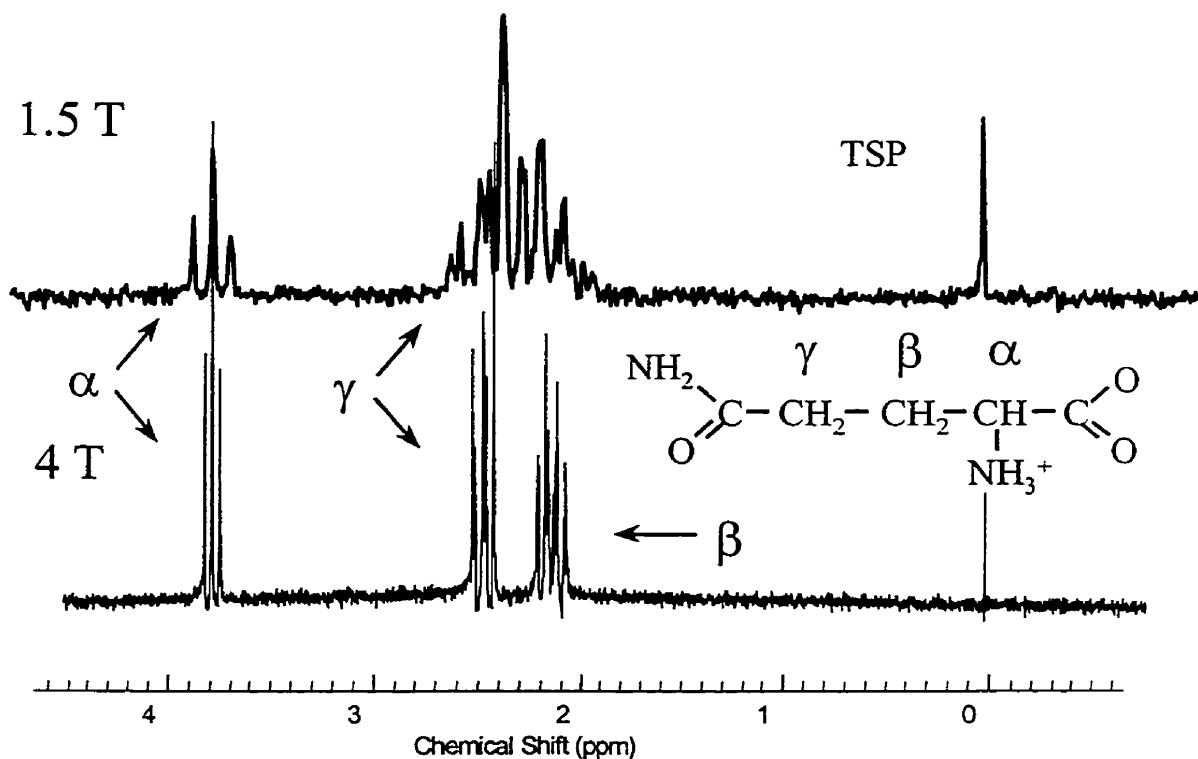


**Figure 1-25: In-vitro Spectra of glutamine (Gln) at 1.5 and 4.0 Tesla**

In-vitro spectrum of glutamine at 1.5 Tesla (top) and 4.0 Tesla (bottom). The chemical structure of glutamine is shown between the two spectra. The TSP reference standard is visible on the right side of both spectra. Resonances from the  $\alpha$ ,  $\beta$ , and  $\gamma$  multiplet structures are indicated.

### 1.3.8 Macromolecule and Baseline Prior-Knowledge

Uncharacterized resonances on the spectral baseline present the single most significant barrier to reliable quantification (16) of short echo  $^1\text{H}$  spectra. These resonances have been attributed to signals arising from macromolecules within the cell. Most likely, these signals come from amino acids (i.e. glutamate and glutamine) which have been incorporated into larger slow moving molecules such as proteins (16). Macromolecule resonances can vary largely between individuals and may contribute significant area to a spectrum. Therefore failing to

account for area they represent in a spectrum will lead to the overestimation of other metabolites.

Two approaches may be taken to account for macromolecule resonances: baseline fitting, or modeling. Baseline fitting has been attempted by Provencher (15) in the frequency domain with some success. However, this approach is somewhat arbitrary, and leads to fits which look good but may not be correct. Therefore modeling macromolecules was considered a more rigorous approach. When modeling macromolecules, two routes may be taken. The first consists of measuring the macromolecule contribution to a spectrum with a separate data acquisition. This method was proposed by Behar *et al* (16) and requires the addition of an inversion pulse prior to the acquisition sequence. When applied at an appropriate time prior to the sequence, the metabolite signal is nulled leaving only macromolecule signal. However, this experiment has three drawbacks. First, the longitudinal relaxation rates of each metabolite vary (1.15 s and 1.29 s for Cho at 1.5 T and 4.0 T respectively vs. 1.55 s and 1.72 s for Cr at 1.5 T and 4.0 T respectively (50, 57)). Therefore the time chosen to apply the inversion pulse will not result in the complete nulling of all metabolite signals. Second, the metabolite nulled spectrum requires an acquisition time at least equal to that of the original spectrum. This effectively doubles the data collection time (from approximately 10 minutes to 20 minutes). Third, because a subtraction of one spectrum from another is required, this technique is sensitive to patient motion.

Due to the above limitations another approach was attempted. This approach exploited the information obtained by Behar *et al* (16) regarding the chemical shifts of these broad metabolite resonances. These shifts were then used to

model the macromolecules using Gaussian lineshapes (as described in Chapter 2). Using this approach we were able to measure metabolite levels which were consistent with concentrations previously reported in the literature. Therefore, this approach was used to quantify in-vivo spectra for clinical applications (Chapters 5 and 6).

### 1.3.9 Prior-Knowledge Constraints

In-vitro metabolite spectra were modeled using Lorentzian lineshapes. These metabolite lineshape models were then used for in-vivo fitting. Metabolite shifts and widths were fixed relative to each other by relating them back to the TSP reference peak in each in-vitro spectrum. Only metabolite amplitudes were unconstrained. Two assumptions were made using this approach, first, the in-vitro chemical shifts, dampings, and amplitudes of metabolites are the same in-vitro and in-vivo, and second, that metabolite lineshapes are Lorentzian.

Therefore, the fitting routine varied the individual metabolite amplitudes, and the overall shift, width, phase, and delay time of the metabolite lineshapes to minimize the difference between the “estimated” spectrum and the original data. The constraining of metabolites and underlying assumptions are described in more detail in Chapters 2 and 3.

### 1.3.10 Absolute Metabolite Quantification

Rather than normalizing metabolite levels relative to a component of the spectrum (such as PCr/Cr and Cho), metabolite levels were normalized relative to the concentration of internal water from the same region studied (71, 72).

The use of PCr/Cr and/or Cho levels for normalization has two major disadvantages. First, there is no guarantee that the level of these metabolites is consistent between individuals, especially between individuals exhibiting symptoms of illness and control subjects. Second, there is always some uncertainty in the quantified level of these metabolites. This is especially true for short echo  $^1\text{H}$  spectroscopy which has ~10% coefficient of variation (CV) for PCr/Cr and Cho. Therefore, normalization of other metabolites to the levels of PCr/Cr or Cho increases the error in the ratio.

The use of internal water as a quantification standard is advantageous because the concentration of water is approximately 10000 times greater than that of most metabolites. Therefore it can be quantified with greater precision. However, the MR signal from water within a voxel may change between individuals due to partial volume of gray/white matter and CSF. Also, water relaxation times ( $T_1$  and  $T_2$ ) or concentration may change in some disease states and cause incorrect metabolite normalization. However, this would cause a systematic increase or decrease of all metabolite levels in a particular subject group. Therefore, such changes could be easily identified. Metabolite levels were not corrected for metabolite relaxation times ( $T_1$  and  $T_2$ ) or concentration differences in gray/white matter since the correction factors required are not known for all metabolites.

## 1.4 References

---

1. Bloembergen N, Purcell EM, Pound RV. Relaxation effects in Nuclear Magnetic Resonance Absorption. *Physical Review* 73, 679-712 (1948).
2. Ross B, Michaelis T. Clinical Applications of Magnetic Resonance Spectroscopy. *Magnetic Resonance Quarterly* 10, 191-247 (1994).
3. Guidelines on Exposure to Electromagnetic Fields from Magnetic Resonance Clinical Systems. Environmental Health Directorate Publication No. 87-EHD-127 (1987).
4. Roberts GW. Schizophrenia: The Cellular Biology of a Functional Psychosis. *TINS* 13, 207-211 (1990).
5. Wasylenki DA. The Cost of Schizophrenia. *Can. J. Psychiatry* 39, 65-69 (1995).
6. Davies LM, Drummond MF. Economics and Schizophrenia: The Real Cost. *British J. Psychiatry* 165, 18-21 (1994).
7. Pettegrew JW, Keshavan MS, Minshew NJ. <sup>31</sup>P Nuclear Magnetic Resonance Spectroscopy: Neurodevelopment and Schizophrenia. *Schiz. Bull.* 19, 35-53 (1993).
8. Buckley PF, Moore C, Long H, Larkin C, Thompson P, Mulvany F, Redmond O, Stack JP, Ennis JT, Waddington JL. <sup>1</sup>H-Magnetic Resonance Spectroscopy of the Left Temporal and Frontal Lobes in Schizophrenia: Clinical, Neurodevelopmental, and Cognitive Correlates. *Biol. Psychiatry* 36, 792-800 (1994).

- 
9. Renshaw PF, Yurgelun-Todd DA, Tohen M, Gruber S, Cohen BM. Temporal Lobe Proton Magnetic Resonance Spectroscopy of Patients with First-Episode Psychosis. *Am J Psychiatry* 152, 444-446 (1995).
  10. Bertolino A, Callicott JH, Elman I, Mattay VS, Tedeschi G, Frank JA, Breier A, Weinberger DR. Regionally Specific Neuronal Pathology in Untreated Patients with Schizophrenia: A Proton Magnetic Resonance Spectroscopic Imaging Study. *Biol. Psychiatry* 43, 641-648 (1998).
  11. Ebert D, Speck O, Konig A, Berger M, Hennig J, Hohagen F. <sup>1</sup>H-Magnetic Resonance Spectroscopy in Obsessive-Compulsive Disorder: Evidence for Neuronal Loss in the Cingulate Gyrus and the Right Striatum. *Psychiatry Res: Neuroimaging* 74, 173-176 (1997).
  12. Lim KO, Adalsteinsson E, Spielman D, Sullivan EV, Rosenbloom MJ, Pfefferbaum A. Proton Magnetic Resonance Spectroscopic Imaging of Cortical Gray and White Matter in Schizophrenia. *Arch. Gen. Psychiatry* 55, 346-352 (1998).
  13. Stanley JA, Williamson PC, Drost DJ, Rylett J, Carr T, Malla A, Thompson RT. An In-Vivo Proton Magnetic Resonance Spectroscopy Study of Schizophrenic Patients. *Schizophr. Bull.* 22, 597-609 (1996).
  14. Stanley JA, Drost DJ, Williamson PC, Thompson RT. The Use of *a Priori* Knowledge to Quantify Short Echo *in Vivo* <sup>1</sup>H MR Spectra. *Magn. Reson. Med.* 34, 17-24 (1995).
  15. Provencher SW. Estimation of Metabolite Concentrations from Localized *in-vivo* Proton NMR Spectra. *Magn. Reson. Med.* 30, 672-679 (1994).

- 
16. Behar KL, Rothman DL, Spencer DD, Petroff OAC. Analysis of Macromolecule Resonances in the  $^1\text{H}$  NMR Spectra of Human Brain. *Magn. Reson. Med.* 32, 294-302 (1994).
  17. Erecinska M, Silver IA. Metabolism and Role of Glutamate in Mammalian Brain. *Prog. Neurobiol.* 35, 245-296 (1990).
  18. Bradford HF, Ward HK, Thomas AJ. Glutamine: A Major Substrate for Nerve Endings. *J. Neurochem.* 30, 1453-1459 (1978).
  19. Harris RK. Nuclear Magnetic Resonance Spectroscopy: A Physiochemical View. New York, NY: John Wiley & Sons, Inc., 1991.
  20. Bottomley PA, Foster TH, Argersinger RE, Pfeifer LM. A Review of Normal Tissue Hydrogen NMR Relaxation Times and Relaxation Mechanisms from 1-100 MHz: Dependence on Tissue Type, NMR Frequency, Temperature, Species, Excision, and Age. *Med. Phys.* 11, 425-448 (1984).
  21. Kreis R, Ernst T, Ross BD. Absolute Quantitation of Water and Metabolites in the Human Brain. II. Metabolite Concentrations. *J. Mag. Res. Series B* 102, 9-19 (1993).
  22. Brigham EO. The Fast Fourier Transform. Englewood Cliffs, NJ: Prentice-Hall, Inc., 1974.
  23. Anderson AG, Garwin RL, Hahn EL, Horton JW, Tucker GL, Walker RM. Spin Echo Serial Storage Memory. *Journal of Applied Physics* 26, 1324-1338 (1955).
  24. Tofts PS, Wray S. A Critical Assessment of Methods of Measuring Metabolite Concentrations by NMR Spectroscopy. *NMR in Biomedicine* 1, 1-10 (1988).



- 
25. van Dijk JE, Mehlkopf AF, Bovee WMMJ. Comparison of Double and Zero Quantum NMR Editing Techniques for In Vivo Use. *NMR in Biomedicine* 5, 75-86 (1992).
  26. Rothman DL, Hanstock CC, Petroff OAC, Novotny EJ, Prichard JW, Shulman RG. Localized  $^1\text{H}$  NMR Spectra of Glutamate in the Human Brain. *Magn. Reson. Med.* 25, 94-106 (1992).
  27. Wilman AH, Allen PS. In Vivo NMR Detection Strategies for  $\gamma$ -Aminobutyric Acid, Utilizing Proton Spectroscopy and Coherence-Pathway Filtering with Gradients. *J. Mag. Res. Series B* 101, 165-171 (1993).
  28. Sotak CH, Freeman DM. A Method for Volume-Localized Editing Using Zero-Quantum Coherence Created in a Stimulated-Echo Pulse Sequence. *J. Mag. Res.* 77, 382-388 (1988).
  29. Barkhuijsen H, de Beer R, Bovee WMMJ, van Ormondt D. Retrieval of Frequencies, Amplitudes, Damping Factors, and Phases from Time-Domain Signals Using a Linear Least-Squares Procedure. *J. Mag. Res.* 61, 465-481 (1985).
  30. de Beer R, van Ormondt D. Analysis of NMR Data Using Time Domain Fitting Procedures. *NMR Basic Principles and Progress* 26, 201-248 (1992).
  31. Golub GH, Pereyra V. The Differentiation of Pseudo-inverses and Nonlinear Least Squares Problems whose Variables Separate. *SIAM J. Numer. Anal.* 10, 413 (1973).
  32. Brown TR, Stoyanova R. NMR Spectral Quantitation by Principal-Component Analysis II. Determination of Frequency and Phase Shifts. *J. Mag. Res. Series B* 112, 32-43 (1996).

- 
33. Barone P, Guidoni L, Ragona R, Viti V, Furman E, Degani H. Modified Prony Method to Resolve and Quantify in-Vivo  $^{31}\text{P}$  NMR Spectra of Tumors. *J. Mag. Res. Series B* 105, 137-146 (1994).
34. Serrai H, Nadal L, Le Floch M, Leray G, Senhadji L, Le Tallec N, de Certaines JD. Wavelet Transform in Magnetic Resonance Data Processing: Application to Subtraction of Broad Resonances, Resolution of Overlapping Peaks and Quantification. *J. Magn. Reson. Anal* 3, 79-86 (1997).
35. Wishart DS, Bigam CG, Yao J, Abildgaard F, Dyson HJ, Oldfield E, Markley JL, Sykes BD.  $^1\text{H}$ ,  $^{13}\text{C}$  and  $^{15}\text{N}$  Chemical Shift Referencing in Biomolecular NMR. *Journal of Biomolecular NMR*. 6, 135-140 (1995).
36. Kip AF. Fundamentals of Electricity and Magnetism, Second Edition. Toronto, On: McGraw-Hill Book Company, 1969.
37. Narayana PA, Fotedar LK, Jackson EF, Bohan TP, Butler IJ, Wolinsky JS. Regional in Vivo Proton Magnetic Resonance Spectroscopy of Brain. *J. Mag. Res.* 83, 44-52 (1989).
38. Miller BL, Moats RA, Shonk T, Ernst T, Woolley S, Ross BD. Alzheimer Disease: Depiction of Increased Cerebral Myo-Inositol with Proton Spectroscopy. *Radiology* 187, 433-437 (1993).
39. Ross BD, Jacobson S, Villamil F, Korula J, Kreis R, Ernst T, Shonk T, Moats RA. Subclinical Hepatic Encephalopathy: Proton MR Spectroscopic Abnormalities. *Radiology* 193, 457-463 (1994).
40. Wittsack H-J, Kugel H, Roth B, Heindel W. Quantitative Measurements with Localized  $^1\text{H}$  MR Spectroscopy in Children with Canavan's Disease. *J. Mag. Res. Imaging* 6, 889-893 (1996).

- 
41. Bomsdorf H, Helzel T, Kunz D, Roschmann P, Tschendel O, Wieland J. Spectroscopy and Imaging with a 4 Tesla Whole Body MR System. *NMR in Biomedicine* 1, 151-158 (1988).
  42. Barfuss H, Fischer H, Hentschel D, Ladebeck R, Oppelt A, Wittig R, Duerr W, Oppelt R. In Vivo Magnetic Resonance Imaging and Spectroscopy of Humans with a 4 T Whole-body Magnet. *NMR in Biomedicine* 3, 31-45 (1990).
  43. Petroff OAC, Ogino T, Alger JR. High-Resolution Proton Magnetic Resonance Spectroscopy of Rabbit Brain: Regional Metabolite Level and Postmortem Changes. *J. Neurochem.* 51, 163-171 (1988).
  44. Fan TW-M, Higashi RM, Lane AN, Jardetzky O. Combined use of  $^1\text{H}$ -NMR and GC-MS for Metabolite Monitoring and In Vivo  $^1\text{H}$ -NMR Assignments. *Biochimica et Biophysica Acta.* 882, 154-167 (1986).
  45. Hoult DI, Chen C-N, Sank VJ. The Field Dependence of NMR Imaging II. Arguments Concerning an Optimal Field Strength. *Magn. Reson. Med.* 3, 730-746 (1986).
  46. Frahm J, Hanicke W. Comparative Study of Pulse Sequences for Selective Excitation in NMR Imaging. *J Mag Res.* 60, 320-332 (1984).
  47. Prost RW, Mark L, Mewissen M, Li S-J. Detection of Glutamate/Glutamine Resonances by  $^1\text{H}$  Magnetic Resonance Spectroscopy at 0.5 Tesla. *Magn. Reson. Med.* 37, 615-618 (1997).
  48. Nishimura DG. Principles of Magnetic Resonance Imaging. Stanford University, 1996.

- 
49. Beckmann N, Muller S, Seelig J. Comparison of the Signal-to-Noise Ratio at 1.5 and 2.0 T Using a Whole-Body System. *Magn. Reson. Med.* 9, 391-394 (1989).
  50. Posse S, Cuenod CA, Risinger R, Le Bihan D. Anomalous Transverse Relaxation in <sup>1</sup>H Spectroscopy in Human Brain at 4 Tesla. *Magn. Reson. Med.* 33, 246-252 (1995).
  51. Riddle WR, Gibbs SJ, Willcott MR. Removing Effects of Eddy Currents in Proton MR Spectroscopy. *Med. Phys.* 19, 501-509 (1992).
  52. Klose U. In Vivo Proton Spectroscopy in Presence of Eddy Currents. *Magn. Reson. Med.* 14, 26-30 (1990).
  53. Evelhoch JL, Crowley MG, Ackerman JJH. Signal-to-Noise Optimization and Observed Volume Localization with Circular Surface Coils. *J. Mag. Res.* 56, 110-124 (1984).
  54. Ordidge RJ, Connelly A, Lohman JAB. Image-Selected in Vivo Spectroscopy (ISIS). A New Technique for Spatially Selective NMR Spectroscopy. *J. Mag. Res.* 66, 283-294 (1986).
  55. Singh S, Rutt BK, Henkelman RM. Projection Presaturation: A Fast and Accurate Technique for Multidimensional Spatial Localization. *J. Mag. Res.* 87, 567-583 (1990).
  56. Bottomley PA. Point Resolved Spectroscopy. *Ann. N.Y. Acad. Sci.* 508, 333 (1987).
  57. Frahm J, Merboldt KD, Hanicke W. Localized Proton Spectroscopy Using Stimulated Echoes. *J. Mag. Res.* 72, 502-508 (1987).
  58. Moonen CTW, von Kienlin M, van Zijl PCM, Cohen J, Gillen J, Daly P, Wolf G. Comparison of Single-shot Localization Methods (STEAM and PRESS)

- 
- for In Vivo Proton NMR Spectroscopy. *NMR in Biomedicine* 2, 201-208 (1989).
59. Frahm J, Michaelis T, Merboldt KD, Bruhn H, Gyngell ML, Hanicke W. Improvements in Localized Proton NMR Spectroscopy of Human Brain: Water Suppression, Short Echo Times, and 1 ml Resolution. *J. Mag. Res.* 90, 464-473 (1990).
60. de Graaf AA, van Dijk JE, Bovee WMMJ. QUALITY: Quantification Improvement by Converting Lineshapes to the Lorentzian Type. *Magn. Reson. Med.* 13, 343-357 (1990).
61. Robertson S, Hughes DG, Liu Q, Allen PS. Analysis of the Temporal and Spatial Dependence of the Eddy Current Fields in a 40-cm Bore Magnet. *Magn. Reson. Med.* 25, 158-166 (1992).
62. Jehenson P, Syrota A. Correction of Distortions due to the Pulsed Magnetic Field Gradient-Induced Shift in  $B_0$  Field by Postprocessing. *Magn. Reson. Med.* 12, 253-256 (1989).
63. Perdidge RJ, Cresshull ID. The Correction of Transient  $B_0$  Field Shifts following the Application of Pulsed Gradients by Phase Correction in the Time Domain. *J. Mag. Res.* 69, 151-155 (1986).
64. Ernst T, Kreis R, Ross BD. Absolute Quantitation of Water and Metabolites in the Human Brain. I. Compartments and Water. *J. Mag. Res. Series B* 102, 1-8 (1993).
65. Danielsen ER, Henriksen O. Absolute Quantitative Proton NMR Spectroscopy based on the Amplitude of the Local Water Suppression Pulse. Quantification of Brain Water and Metabolites. *NMR in Biomedicine* 7, 311-318 (1994).

- 
66. Hennig J, Pfister H, Ernst T, Ott D. Direct Absolute Quantification of Metabolites in the Human Brain with *In Vivo* Localized Proton Spectroscopy. *NMR in Biomed.* 5, 193-199 (1992).
67. van den Boogaart A, Ala-Korpela M, Jokisaari J, Griffiths JR. Time and Frequency Domain Analysis of NMR Data Compared: An Application to 1D  $^1\text{H}$  Spectra of Lipoproteins. *Magn. Reson. Med.* 31, 347-358 (1994).
68. Barkhuijsen H, de Beer R, van Ormondt D. Improved Algorithm for Noniterative Time-Domain Model Fitting to Exponentially Damped Magnetic Resonance Signals. *J. Mag. Res.* 73, 553-557 (1987).
69. Arfken G. *Mathematical Methods for Physicists*, Third Edition. San Diego, CA: Academic Press Inc., 1985.
70. Press WH, Flannery BP, Teukolsky SA, Vetterling WT. *Numerical Recipes in C*. New York, NY: Cambridge University Press, 1988.
71. Barker PB, Soher BJ, Blackband SJ, Chatham JC, Mathews VP, Bryan RN. Quantification of Proton NMR Spectra of the Human Brain Using Tissue Water as an Internal Concentration Reference. *NMR in Biomedicine* 6, 89-94 (1993).
72. Christiansen P, Henriksen O, Stubgaard M, Gideon P, Larsson HBW. *In Vivo* Quantification of Brain Metabolites by  $^1\text{H}$ -MRS Using Water as an Internal Standard. *Magn. Reson. Imaging* 11, 107-118 (1993).

## Chapter 2

# Factors Affecting the Quantification of Short Echo In-Vivo $^1\text{H}$ Spectra: Prior-Knowledge, Peak Elimination, Filtering<sup>1</sup>

*By Robert Bartha, Dick J Drost, Peter C Williamson*

### 2.0 Introduction

With short TE (20 ms)  $^1\text{H}$  in-vivo brain MR spectroscopy (MRS), biologically important metabolites such as glutamate, glutamine, and  $\gamma$ -aminobutyric acid can be detected with minimal distortions due to J-coupling effects (1). Differences in the levels of these metabolites, as well as others (1, 2, 3, 4), may help determine the pathophysiology involved in illnesses like schizophrenia, obsessive compulsive disorder, and Alzheimer's disease. However, the quantification of many of these metabolites has been difficult resulting in coefficients of variation (CV, metabolite standard deviation divided by mean metabolite level x 100 %) ranging from 10 - 50% and sometimes even larger (2, 3, 4). Sources of variance

---

<sup>1</sup> A version of this chapter has been accepted for publication

Bartha R, Drost DJ, Williamson PC. Factors Affecting the Quantification of Short Echo In-Vivo  $^1\text{H}$  Spectra: Prior-Knowledge, Peak Elimination, Filtering. *NMR in Biomedicine* (in press).

include, voxel placement (partial volume error), the stability of the data acquisition (eddy currents and frequency drift), the method of correcting for lineshape distortions, incorrect prior knowledge (especially regarding the spectral baseline), the method of referencing (to water or metabolite), patient motion, patient mental activity, and normal biological variation. The low precision of metabolite measures means that subtle metabolite level differences that may exist between patients and matched controls can go unnoticed. Therefore, improvements in the precision of current quantification techniques are required to observe subtle changes in brain chemistry between patients and controls and to monitor metabolite level changes over time due to disease progression or drug treatments. This work is an extension of the quantification methodology previously developed in our lab for short echo  $^1\text{H}$  MRS data (2). Both techniques utilize prior knowledge from parameterized in-vitro metabolite spectra. However, current improvements include the development of data quantification in the time domain (vs. frequency domain), the elimination of user interactive zero and first order phasing (phase and delay time are incorporated as fit parameters in the model function), the elimination of Lorentzian-to-Gaussian resolution enhancement, the inclusion of macromolecule resonances in the prior knowledge, and the modeling of resonances outside the spectral region of interest.

Short TE in-vivo  $^1\text{H}$  MR spectra are difficult to quantify precisely at low field (1.5 Tesla) for several reasons. The most obvious is that the chemical similarity of metabolites like glutamate, glutamine, and  $\gamma$ -aminobutyric acid lead to broad, overlapping resonances which are difficult to distinguish. Historical methods such as area integration or simple curve fitting (5) do not work because these



methods are unable to resolve overlapping metabolites. Linear prediction algorithms which incorporate Lorentzian model functions have been used in an attempt to improve the accuracy and precision of metabolite level estimates (6, 7, 8, 9) in simple spectra. However, these algorithms are unable to include prior knowledge to help resolve overlapping resonances with low signal to noise ratio (S/N) making them inappropriate for the quantification of short echo  $^1\text{H}$  MR spectra. In contrast, non-linear iterative fitting procedures (10, 11, 12, 13) can incorporate prior knowledge to aid in the distinction of overlapping resonances. Therefore, the use of a non-linear iterative procedure can lead to more accurate and precise metabolite level estimates, provided the included prior knowledge is correct.

Non-linear algorithms can be implemented in either the time (measurement) domain or the frequency domain (after Fourier transform). Quantification of short TE spectra using prior knowledge from in-vitro metabolite spectra has been demonstrated in the frequency domain by several groups with varying degrees of success (2, 3). Quantification in the time domain has also been demonstrated (14, 15), and will give the same results as quantification in the frequency domain if both are done correctly (15, 16). However, one significant advantage to time domain quantification is the simplicity with which a Gaussian damping component that incorporates phase and delay time as fit parameters can be added to the model function to create the Voigt function (17). Such a function can only be *approximated* in the frequency domain (16, 17, 18) or must be calculated by numerical integration. This limitation makes the inclusion of a Gaussian damping component (with delay time as a fit parameter) impractical in

the frequency domain model function, therefore we chose to do quantification in the time domain.

Prior knowledge for the quantification of multi-subject data sets must include information describing all resonances present in the in-vivo spectrum. Failure to represent all metabolites in the spectrum model (prior-knowledge) will reduce the quantification accuracy and precision of the included metabolites. Factors such as the domain used for fitting or whether in-vitro spectra are used outright (3) rather than first mathematically modeled (1, 2) to obtain prior knowledge are secondary to the *completeness* of the spectrum model. The spectrum model must accurately represent all resonances both inside and adjacent to the spectral region of interest (SRI) which extended from 1.9 - 3.5 ppm (with  $\text{NAA}_{\text{CH}_3}$  referenced to 2.01 ppm) in this study. This region was chosen to avoid spectral distortions occasionally visible in spectra acquired near tissue/bone interfaces (at frequencies greater than 3.5 ppm), and to avoid uncertainty in the spectral baseline outside this region due to inadequately characterized macromolecule resonances. Previous short echo quantification has failed to include specific information about macromolecule resonances in the in-vivo spectral model leading to misfitting. These macromolecule resonances have been partially characterized by Behar *et al* (19) using extracts from human cytosol. In addition, resonances adjacent to the SRI must be accounted for unless they are well separated from the SRI (20). Failing to model outside resonances which overlap with the SRI will lead to the overestimation of resonance areas within the SRI by an amount proportional to the degree of overlap.

The objective of this study was to determine whether modeling both macromolecule resonances inside the SRI and resonances outside the SRI, using various model functions and following the application of different filters, would improve in-vivo quantification precision. Metabolite precision was used to compare fitting strategies instead of accuracy, since 'correct' absolute metabolite levels are unknown. To this end, in-vivo repeated data from a single individual were quantified to eliminate inter-subject variability. Therefore, the variance observed in these measurements can be attributed to the quantification techniques, and not inter-subject metabolite level differences, although some variance also arises from subject motion, possible changes in brain function, and hardware drift.

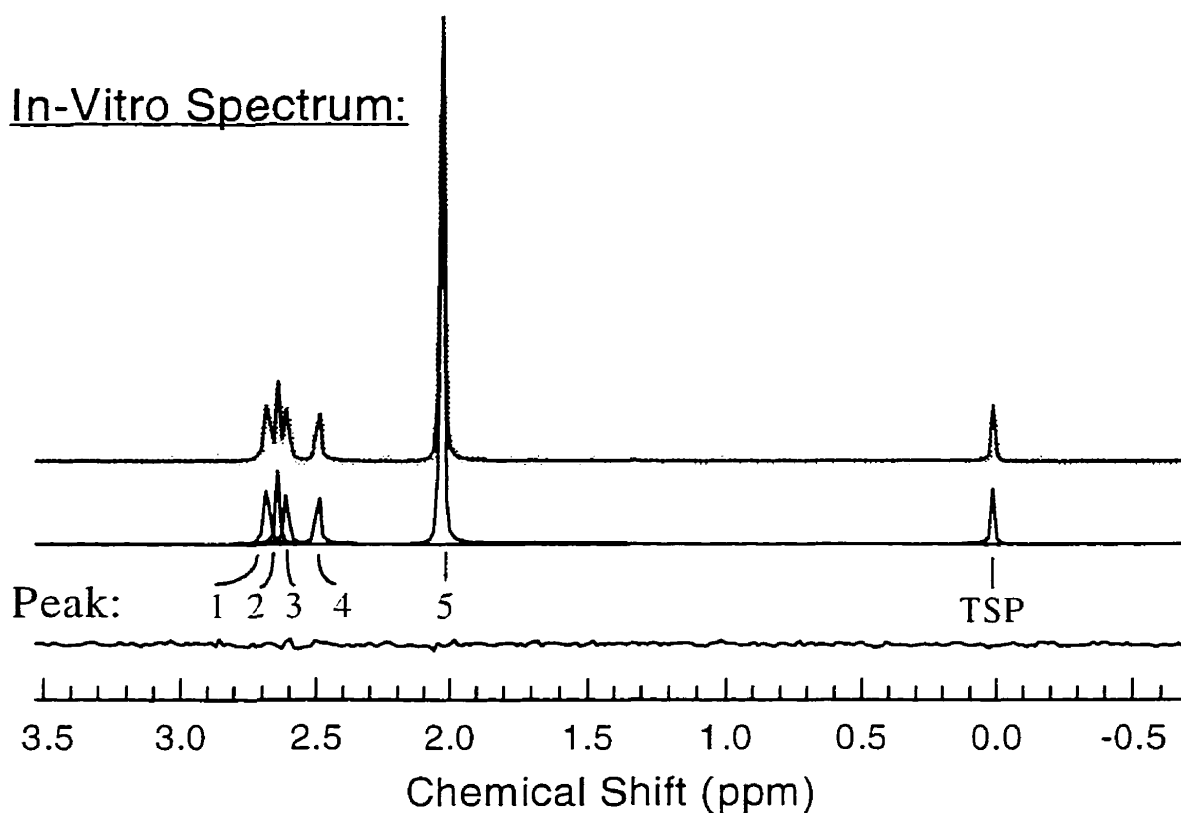
## **2.1 Experimental**

### 2.1.1 Data Acquisition

Prior knowledge was determined from water suppressed (256 averages) and unsuppressed (80 averages) in-vitro metabolite data (2, 3, 14, 21, 22) acquired on a Siemens SP4000 Helicon 1.5 Tesla magnet using a stimulated echo acquisition mode (STEAM) sequence (23) (TR=1500 ms, TE=20 ms, TM=30 ms, 4096 complex points, 250  $\mu$ s dwell time). Solutions of N-acetyl-aspartate (NAA) (Figure 2-1), glutamate (Glu), glutamine (Gln),  $\gamma$ -aminobutyric acid (GABA), taurine (Tau), myo-inositol (Myo), glucose (Glc), aspartate (Asp), N-acetylaspartyl-glutamate (NAAG), and scyllo-inositol (Syl) were prepared as described in detail elsewhere (2). Each metabolite solution contained sodium 3-trimethylsilyl-propionic acid (TSP) as a reference for chemical shift ( $\omega$ ) and

Lorentzian damping ( $\alpha$ ) (24). In-vitro spectra (NAA is shown in Figure 2-1) had sufficient resolution ( $< 1$  Hz full width at half maximum (FWHM) for unsuppressed water) to accurately determine prior knowledge about the relative chemical shifts ( $\omega$ ), relative Lorentzian dampings ( $\alpha$ ), and relative amplitudes ( $c$ ) of individual metabolite resonances. The chemical shift ( $\omega_k$ ) and Lorentzian damping ( $\alpha_k$ ) of each resonance was calculated relative to the TSP resonance ( $\omega_{TSP}, \alpha_{TSP}$ ) before being added to the template of prior knowledge (Figure 2-1). This allowed the chemical shifts ( $\omega_k$ ) and Lorentzian dampings ( $\alpha_k$ ) of all metabolites to be fixed relative to a common 'spectrum' parameter ( $\omega, \alpha$ ), while relative resonance amplitudes ( $c_k$ ) were fixed relative to a common 'metabolite' parameter ( $c_{NAA}$ ). Gaussian widths ( $\beta$ ) were set to zero for all metabolites. Phase and delay time were also constrained by a common 'spectrum' parameter ( $\phi_0, t_0$  respectively).

Eight in-vivo water suppressed (25) STEAM spectra (TR=1500 ms, TE=20 ms, TM=30 ms, 4096 complex points, 250  $\mu$ s dwell time, 200 averages) were acquired from a 2 x 2 x 2 cm<sup>3</sup> volume in the medial parietal lobe (containing mostly white matter) of a single subject without repositioning the subject between acquisitions. Following the acquisition of each water suppressed spectrum a water unsuppressed spectrum (30 averages) was also obtained. Prior to data collection, magnetic field homogeneity was optimized manually over the entire head using linear (X, Y, and Z) and Z<sup>2</sup> shim sets, and within the volume studied using the linear shims. The medial parietal region was chosen because of its homogeneity yielding in-vivo spectra with good resolution ( $4.34 \pm 0.02$  Hz, FWHM for unsuppressed water).



Constraints:

Peak #	Chemical Shift	Exponential Width	Area	Phase	Delay Time	Gaussian Width
1	$\omega + (\omega_{TSP} - \omega_1)$	$\alpha + (\alpha_{TSP} - \alpha_1)$	$c_{NAA} \cdot c_1 / c_5$	$\phi_0$	$t_0$	$\beta$
2	$\omega + (\omega_{TSP} - \omega_2)$	$\alpha + (\alpha_{TSP} - \alpha_2)$	$c_{NAA} \cdot c_2 / c_5$	$\phi_0$	$t_0$	$\beta$
3	$\omega + (\omega_{TSP} - \omega_3)$	$\alpha + (\alpha_{TSP} - \alpha_3)$	$c_{NAA} \cdot c_3 / c_5$	$\phi_0$	$t_0$	$\beta$
4	$\omega + (\omega_{TSP} - \omega_4)$	$\alpha + (\alpha_{TSP} - \alpha_4)$	$c_{NAA} \cdot c_4 / c_5$	$\phi_0$	$t_0$	$\beta$
5	$\omega + (\omega_{TSP} - \omega_5)$	$\alpha + (\alpha_{TSP} - \alpha_5)$	$c_{NAA} \cdot c_5 / c_5$	$\phi_0$	$t_0$	$\beta$

**Figure 2-1: In-Vitro Spectrum of NAA and Template of Prior Knowledge**

NAA portion of the template of prior-knowledge. The top of this figure illustrates the in-vitro NAA spectrum (light trace) along with the resulting fit (dark trace) and individual metabolite components (numbered 1-5) and TSP reference peak. The residual is shown beneath. The bottom of this figure illustrates the constraint of prior knowledge regarding NAA (described in text).

### 2.1.2 Spectral Processing and Fitting

Initial pre-processing of all data consisted of either a QUALITY deconvolution (26) or an eddy current correction (27) to remove eddy current distortions and in the case of the QUALITY deconvolution, to restore the Lorentzian lineshape. When QUALITY was used, data was also exponentially filtered with the decay constant set equal to the Lorentzian damping of the unsuppressed water resonance to restore the original linewidth of the spectrum which is reduced by QUALITY deconvolution. Any remaining unsuppressed water was then removed from each spectrum using a Hankel Lanczos Singular Value Decomposition (HLSVD) (7, 15) which required no prior knowledge. Resonances between 4.1 and 5.1 ppm (water ~ 4.7 ppm) as determined by the HLSVD algorithm were subtracted from the data.

A Levenberg-Marquardt non-linear minimization routine (28, 29) was then employed to fit the lineshapes incorporated in the template of prior knowledge (detailed in the next section) to the data. Initial parameter values were set so that the template of prior knowledge closely resembled the data to be fit. The model function shown in equation 2-1 was used in the time domain.

$$\hat{y}(n) = \sum_{k=1}^K c_k \cdot e^{i(2\pi \omega_k (n \cdot \Delta t + t_0) + \varphi_k)} \cdot e^{-\pi \alpha_k |n \cdot \Delta t + t_0|} \cdot e^{-\left(\frac{\pi^2}{4 \cdot \log 2}\right) \beta_k^2 \cdot (n \cdot \Delta t + t_0)^2} \quad [2-1]$$

$\hat{y}(n)$   $\equiv$  Sampled points along the estimated time domain signal at points  $n$  ( $n = 1, 2, \dots, N$ ).

$K$   $\equiv$  Maximum number of resonances.

$N$   $\equiv$  Maximum number of discrete samples.

$k$   $\equiv$  Resonance index ( $k = 1, 2, \dots, K$ ).

$\omega_k$   $\equiv$  Chemical shift (frequency) of resonance  $k$ .

$c_k$   $\equiv$  Amplitude of resonance  $k$ .

$\alpha_k$   $\equiv$  Lorentzian damping of resonance  $k$ .

$\beta_k$   $\equiv$  Gaussian damping of resonance  $k$ .

$\varphi_k$   $\equiv$  Phase of resonance  $k$  (allows peaks outside the SRI to have independent phase).

$t_0$   $\equiv$  Delay time (time between center of stimulated echo and first readout point).

$\Delta t$   $\equiv$  Dwell time.

Following the completion of the minimization routine (tolerance = 0.001%), estimated metabolite levels were scaled using the unsuppressed water as an internal standard (30, 31, 32). This yielded relative metabolite level estimates in arbitrary units. A further adjustment for  $T_1$  and  $T_2$  relaxation effects and partial volume would be necessary to convert metabolite levels to units of mM/L. This

was not done since  $T_1$  and  $T_2$  values were not easily available for each metabolite nor is there a consensus as to the relative metabolite levels present in white and gray matter for all the metabolites measured in this study. The estimated concentration of internal  $H_2O$  (55.12 M/L) was corrected for the cerebral spinal fluid/gray matter/white matter partial volume (using equation 2 in reference 2) assuming a ratio of 2%/18%/80%, prior to metabolite scaling.

### 2.1.3 Prior Knowledge

Prior knowledge (2, 3, 10, 12, 21, 22) obtained from the in-vitro metabolite samples was incorporated into the non-linear fitting routine to increase the degrees of freedom (number of points modeled minus total number of parameters) when in-vivo data were fit. This information stabilized the fitting routine and reduced fitting times. By using prior knowledge obtained from in-vitro samples it was assumed that in-vitro metabolite resonances had the same chemical shifts ( $\omega$ ), relative Lorentzian dampings ( $\alpha$ ), and relative amplitudes ( $c$ ), as corresponding in-vivo metabolite resonances.

In-vitro metabolite spectra had sufficient resolution for the manual identification of individual resonances (Figure 2-1). Accurate parameterization of each resonance (used to construct the spectrum template) was obtained by fitting the manually identified resonances to the in-vitro spectrum using a non-linear Levenberg-Marquardt minimization (4096 points and no exponential filter). Initial parameter values were manually chosen so that each modeled resonance closely resembled its counterpart in the in-vitro spectrum. The high resolution of each in-vitro spectrum enabled most resonances to be fit with separate chemical



shift ( $\omega$ ), amplitude ( $c$ ), and Lorentzian damping ( $\alpha$ ) parameters. However, when fitting most in-vitro spectra including myo-inositol, glucose, glutamate and glutamine, some low amplitude resonances were forced to have the same Lorentzian damping as nearby higher amplitude resonances to ensure convergence of the fit. This restriction was imposed on resonances that did not converge when initially fit with a separate Lorentzian damping constant. The zero order phase ( $\varphi_0$ ) and delay time ( $t_0$ ) of all resonances in a spectrum were each forced to have the same value. The Gaussian damping ( $\beta$ ) was set to 0 Hz for all in-vitro metabolite resonances because including the Gaussian damping as an additional parameter did not significantly improve in-vitro metabolite fits.

The information describing resonance characteristics obtained from the individual in-vitro metabolite spectra was used to constrain metabolite lineshapes in the template of prior knowledge (Figure 2-1). First the chemical shift and Lorentzian damping of each resonance in a metabolite spectrum was determined relative to the TSP (24) resonance. Peak amplitudes were also calculated relative to the largest resonance in the spectrum. These relative values were then used as offsets to relate each resonance's chemical shift and Lorentzian damping to the common 'spectrum' parameters  $\omega$  and  $\alpha$ , while resonance amplitudes were fixed relative to a common 'metabolite' parameter such as  $c_{\text{NAA}}$  in Figure 2-1. Zero order phase and delay time were also each constrained by the common 'spectrum' parameters  $\varphi_0$  and  $t_0$ , while Gaussian damping was fixed at 0 Hz for each peak. Metabolite amplitude parameters were not fixed relative to other metabolites since relative metabolite levels vary between individuals and subject groups. Constraining metabolites in this way, the fitting routine only varied one

parameter for Lorentzian damping, phase, delay time, and chemical shift, as well as a separate parameter for the amplitude of *each* metabolite when minimizing the difference between the data and lineshapes within the template of prior knowledge. Resonances representing Cho and PCr/Cr were easily resolved *in vivo*; therefore, the chemical shifts and Lorentzian dampings of these two metabolites were not constrained relative to the other metabolites. In clinical cases where Cho and PCr/Cr have low levels and are not easily resolved, the chemical shifts and Lorentzian dampings of these metabolites should be constrained using prior knowledge as described above.

Prior knowledge regarding macromolecule resonances was also incorporated into the template of prior knowledge. Behar *et al* (19) have partially characterized these macromolecules and found distinct resonances to occur at 2.05 ppm (M 2.05), 2.29 ppm. (M 2.29), and 3.00 ppm (M 3.00), within the spectral region of interest. The dampings of these resonances were determined experimentally in the time domain by fixing resonances at the three chemical shifts listed above and leaving both the Lorentzian and Gaussian dampings unrestricted. The resonance at 3.00 ppm was fit most reliably; therefore, all macromolecule widths were based on its results. Its Lorentzian damping term was fit as 0 Hz in more than 50% of spectra and therefore set to zero, while its Gaussian damping term averaged to 22.4 Hz. These damping values ( $\alpha = 0$  Hz,  $\beta = 22.4$  Hz) were fixed in the template of prior knowledge for each macromolecule.

Finally, the template of prior knowledge was made to reflect the manner in which resonances outside the SRI were handled. When required, resonances outside

the SRI were modeled using six resonances with shifts less than 1.9 ppm and four resonances with shifts greater than 3.5 ppm. All parameters describing these resonances (including Gaussian damping, and phase) were unconstrained except for delay time ( $t_0$ ), which was forced to have the same value as metabolites within the SRI.

#### 2.1.4 Optimization of Fitting Strategy

Repeated in-vivo data were used to determine the optimum fitting strategy. A comparison was made between data post-processed using ECC correction and QUALITY deconvolution to determine whether such post-processing could affect quantified metabolite levels.

The optimum method for handling resonances adjacent to the SRI was then determined using the first 512 ms (1-2048 points) of data (there was no signal remaining after 512 ms) with no exponential filter. Two distinct methods were tested: the first involved the removal of these resonances concurrent with the removal of residual water using the results of a fit with HLSVD; the second entailed modeling these resonances using Lorentzian, Gaussian, or Voigt lineshapes as described in the section on prior-knowledge.

Since the total amplitude that macromolecule resonances contribute to the in-vivo spectrum has yet to be determined, metabolite level estimates following the modeling of macromolecules using Lorentzian and Gaussian lineshapes were compared to metabolite level estimates made without macromolecule resonances included in the spectrum template.

Finally, exponential and rectangular filters were applied to the data prior to quantification to assess the effect of these filters on metabolite level estimates. Seven different exponential filter strengths (dampings,  $D$ ) ( $\infty$  ms, 637 ms, 318 ms, 212 ms, 159 ms, 106 ms, and 64 ms) were applied at each of five rectangular filter strengths (widths) (1024 ms, 512 ms, 256 ms, 128 ms, and 64 ms). The following function was used to apply the exponential filter in the time domain:

$$f(n) = e^{-\frac{n \cdot \Delta t}{D}} \quad [2-2]$$

Where

- $f(n)$      $\equiv$  applied exponential filter
- $n$          $\equiv$  point index ( $n = 1, 2, \dots, N$ )
- $D$          $\equiv$  exponential filter damping
- $\Delta t$       $\equiv$  Dwell time.

In these tests, Gaussian macromolecule resonances were included in the spectrum template, and resonances outside the SRI were modeled concurrently with resonances inside.

In all experiments, metabolite levels were compared using two-tailed t-tests (assuming equal variances) and two-tailed paired t-tests. Metabolite variances were also compared using one-tailed f-tests. When making multiple comparisons at the 0.05 level, a significant result will be found in 5% of comparisons by chance. Although considered conservative (33), the Bonferroni correction

reduces the risk of finding a significant result due to chance by multiplying the significance level obtained for a test (t-test, f-test, correlation (34)) by the number of tests. Therefore, in this study  $p$ -values of less than 0.05 following the appropriate Bonferroni based correction (for 15 comparisons) were considered significant for all statistical tests. However, it must be recognized that increasing Type-1 error protection (by Bonferroni correction) decreases Type-2 error protection.

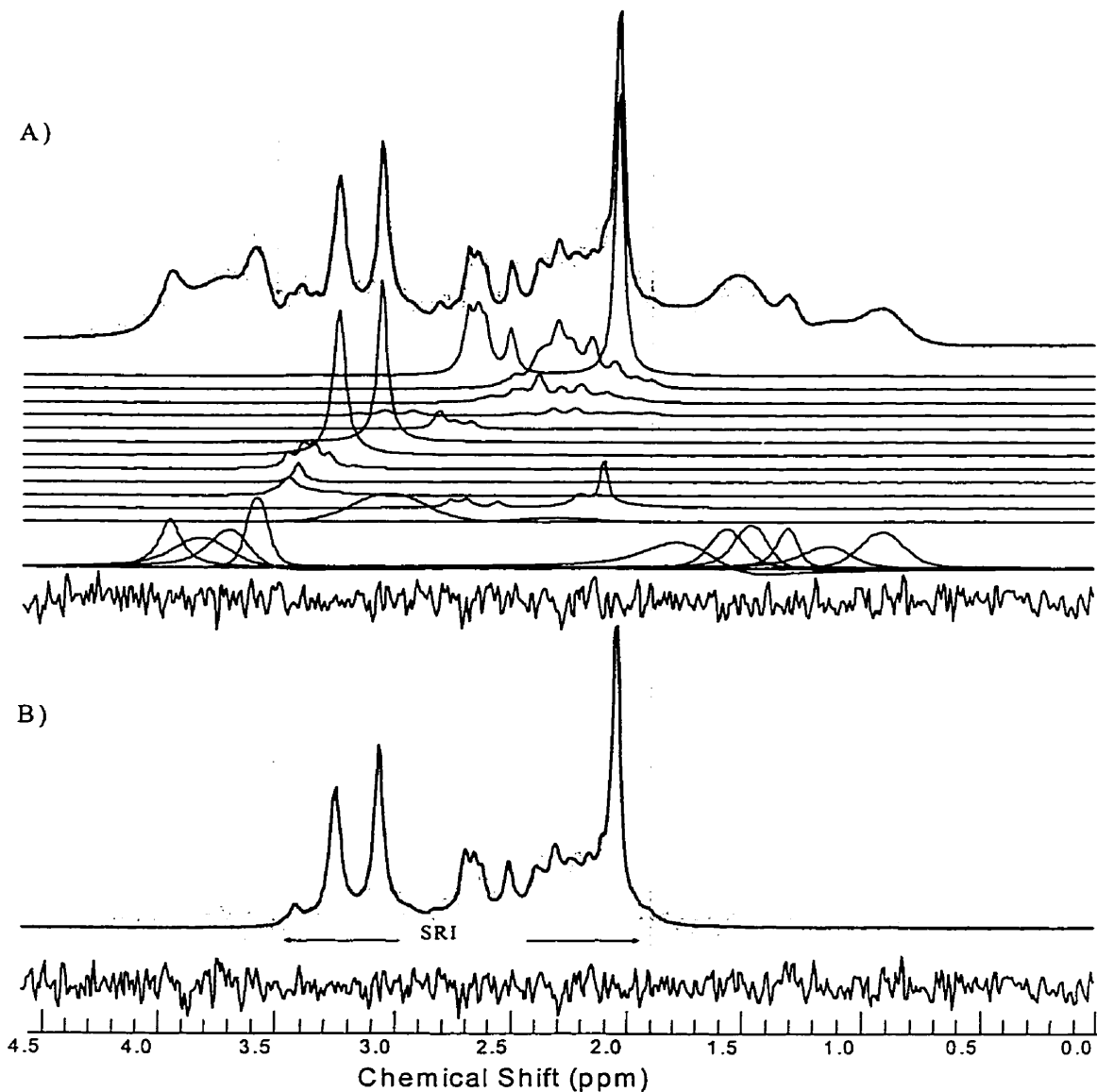
## **2.2 Results**

Table 2-1 shows the results of fitting repeated in-vivo data from the parietal lobe in the time domain following QUALITY deconvolution (26) (Figure 2-2a) and ECC correction (27). The S/N of this data was  $6.0 \pm 0.4$  calculated as the NAA amplitude divided by the root mean square of the noise in the time domain signal. Metabolite level estimates (Table 2-1) were within expected limits based on previous metabolite level reports (2, 3, 4). Paired t-test showed a significant increase in NAA and Cho following ECC correction compared with QUALITY deconvolution ( $p < 0.05$ ,  $DF=7$ ) after Bonferroni correction. There were no significant differences in variance.

Metabolite	Post-Processing Method	
	QUALITY	ECC
NAA	13.7 ± 3.5% <sup>E</sup>	14.2 ± 3.4% <sup>Q</sup>
Glu	9.5 ± 11.4	9.5 ± 10.5
Gln	4.9 ± 19.2	4.9 ± 23.6
GABA	1.4 ± 66.4	1.4 ± 74.5
Asp	3.2 ± 20.7	3.2 ± 20.6
NAAG	2.0 ± 23.0	2.0 ± 24.6
Tau	2.4 ± 19.9	2.4 ± 18.9
Glc	1.6 ± 61.9	1.9 ± 57.3
Cho	2.9 ± 6.5 <sup>E</sup>	3.0 ± 4.9 <sup>Q</sup>
PCr/Cr	9.3 ± 6.4	9.6 ± 7.5
Syl	0.3 ± 80.9	0.4 ± 72.4
Myo	5.4 ± 52.1	2.9 ± 60.2
M 3.00	24.5 ± 18.0	24.5 ± 20.1
M 2.05	0.5 ± 282.8	0.4 ± 282.8
M 2.29	10.3 ± 31.5	11.1 ± 31.4

**Table 2-1 : Metabolite Levels Following QUALITY Deconvolution and ECC Correction**

Relative metabolite levels (arbitrary units) ± CV for repeated (N=8) in-vivo data acquired on a single subject. Data were analyzed in the time domain following post-processing using QUALITY deconvolution and ECC correction as listed. Resonances outside the spectral region of interest (SRI) and macromolecules were modeled using Voigt and Gaussian lineshapes respectively. Data was fit to 512 ms (1-2048 points) with no exponential filter in all cases. Superscript letters indicate significant difference (paired t-test,  $p < 0.05$  following Bonferroni correction, DF=7) from Q (QUALITY post-processed data), or E (ECC post-processed data).



### Figure 2-2: In-Vivo 1.5 Tesla Spectra and Fit Results

The results of fitting in-vivo data in the time domain (512 ms, 1-2048 points) following QUALITY deconvolution, modeling macromolecules with Gaussian lineshapes, and resonances outside the SRI (dotted lines) with Voigt lineshapes. Data is shown in the frequency domain for interpretation. Figure 2-2a shows the raw data (light trace) with corresponding fit result (dark trace), the individual metabolite components (described within the text), and the residual. Figure 2-2b shows the raw data (light trace) following subtraction of resonances outside the SRI with corresponding fit (dark trace) and residual (shown beneath).

Figure 2-2a shows the results of fitting a single spectrum when resonances outside the SRI were modeled with the Voigt lineshape, while Figure 2-2b shows the same data and corresponding fit result after resonances outside the SRI were first subtracted. Fit metabolite spectra are shown in the following order. The first line shows NAA (*N*-acetyl-aspartate) followed by Glu (glutamate), Gln (glutamine), GABA ( $\gamma$ -amino-butyrac acid), Asp (aspartate), PCr/Cr (phosphocreatine /creatine), Cho (choline), Tau (taurine), Syl (scyllo-inositol), Myo (myo-inositol), NAAG (*N*-acetyl-aspartyl-glutamate), macromolecules (M 3.00 and M 2.29), and finally the resonances fit outside the SRI. Glc (glucose) and M 2.05 (macromolecule) are not shown in Figure 2-2 as they were both quantified with a value of zero. Examination of the residuals produced after fitting each spectrum suggests that both methods of handling resonances outside the SRI produced reasonable looking fits. However, some differences in average metabolite levels and CV were observed as a consequence of the different methods of handling resonances outside the SRI (Table 2-2). Paired t-tests ( $p < 0.05$ ,  $DF = 7$ ) showed numerous differences (following Bonferroni based correction) between metabolite levels when different lineshapes were used to model resonances outside the SRI. Unpaired t-tests ( $p < 0.05$ ,  $DF = 14$ ) also showed significant differences (following Bonferroni based correction) in Tau, Myo, and M 3.00, when comparing modeling techniques with the elimination technique. M 2.05 showed a significant decrease in variance following Bonferroni based correction ( $p < 0.05$ ,  $DF = 7$ ) when outside resonances were subtracted, accompanied by a dramatic shift in value from 0.4 to 7.3 arbitrary units.



Metabolite	Model Function used Outside SRI			Subtracted
	Lorentzian	Gaussian	Voigt	
<b>NAA</b>	13.4 ± 3.3% <sup>G</sup>	14.0 ± 4.0% <sup>VL</sup>	13.7 ± 3.5% <sup>G</sup>	13.2 ± 9.2%
<b>Glu</b>	9.3 ± 12.7	9.7 ± 1.9	9.5 ± 11.4	8.6 ± 17.2
<b>Gln</b>	4.3 ± 25.8 <sup>VG</sup>	5.5 ± 19.1 <sup>VL</sup>	4.9 ± 19.2 <sup>LG</sup>	4.5 ± 43.9
<b>GABA</b>	1.1 ± 77.7 <sup>G</sup>	1.6 ± 53.1 <sup>L</sup>	1.4 ± 66.4	2.7 ± 64.9
<b>Asp</b>	2.9 ± 28.0 <sup>VG</sup>	3.6 ± 20.4 <sup>VL</sup>	3.2 ± 20.7 <sup>LG</sup>	2.7 ± 61.0
<b>NAAG</b>	2.0 ± 21.6	2.0 ± 21.9 <sup>V</sup>	2.0 ± 23.0 <sup>G</sup>	1.4 ± 55.0
<b>Tau</b>	2.2 ± 23.7 <sup>SG</sup>	2.7 ± 16.6 <sup>VLS</sup>	2.4 ± 19.9 <sup>SG</sup>	0.8 ± 94.6 <sup>VLG</sup>
<b>Glc</b>	0.8 ± 93.2 <sup>VG</sup>	2.5 ± 41.7 <sup>VL</sup>	1.6 ± 61.9 <sup>LG</sup>	1.2 ± 144.1
<b>Cho</b>	2.9 ± 6.3	2.9 ± 7.0	2.9 ± 6.5	2.7 ± 10.4
<b>PCr/Cr</b>	9.2 ± 7.6	9.3 ± 6.9	9.3 ± 6.4	9.4 ± 4.2
<b>Syl</b>	0.4 ± 69.3 <sup>V</sup>	0.3 ± 81.2 <sup>L</sup>	0.3 ± 80.9 <sup>L</sup>	0.2 ± 81.2
<b>Myo</b>	3.5 ± 76.7 <sup>S</sup>	7.0 ± 37.5 <sup>S</sup>	5.4 ± 52.1 <sup>S</sup>	1.0 ± 282.8 <sup>VLG</sup>
<b>M 3.00</b>	23.9 ± 19.0 <sup>S</sup>	26.2 ± 15.8 <sup>VS</sup>	24.5 ± 18.0 <sup>SG</sup>	13.5 ± 26.9 <sup>VLG</sup>
<b>M 2.05</b>	0.4 ± 282.8	0.4 ± 282.8	0.5 ± 282.8	7.3 ± 80.1
<b>M 2.29</b>	11.5 ± 36.9	9.8 ± 32.6	10.3 ± 31.5	5.0 ± 112.5

**Table 2-2 : Effect of Model Functions for Region Outside the Spectral Region of Interest**

Relative metabolite levels (arbitrary units) ± CV for repeated (N=8) in-vivo data acquired on a single subject following use of different functions to model resonances outside the spectral region of interest (SRI). All data was fit to 512 ms (1-2048 points) in the time domain with no exponential filter. Lorentzian refers to the Lorentzian model function, Gaussian refers to the Gaussian model function, Voigt refers to the Voigt model function, and Subtracted refers to the case when outside resonances were subtracted (using the results from an HLSVD fit) prior to quantification. Superscripts indicate significant difference (paired t-test,  $p < 0.05$  following Bonferroni correction, DF=7) from G (Gaussian), V (Voigt), S (subtracted), or L (Lorentzian).

Table 2-3 summarizes the results of fitting the repeated in-vivo data when macromolecules within the SRI were fit with Gaussian lineshapes, Lorentzian lineshapes, or not modeled. The results showed large changes in estimated metabolite levels (>30 %) for several metabolites including GABA, Asp, Glc, PCr/Cr, and Myo.

Metabolite	Model Function			Difference
	Gaussian	Lorentzian	None	
<b>NAA</b>	13.7 ± 3.5%	12.9 ± 3.2%	13.7 ± 3.7%	0 %
<b>Glu</b>	9.5 ± 11.4 <sup>N</sup>	9.5 ± 15.4	8.5 ± 12.7 <sup>G</sup>	-11%
<b>Gln</b>	4.9 ± 19.2 <sup>L</sup>	3.2 ± 18.2 <sup>NG</sup>	5.7 ± 20.0 <sup>L</sup>	16%
<b>GABA</b>	1.4 ± 66.4 <sup>N</sup>	1.2 ± 37.8 <sup>N</sup>	5.0 ± 20.2 <sup>GL</sup>	247%
<b>Asp</b>	3.2 ± 20.7 <sup>NL</sup>	1.7 ± 56.3 <sup>NG</sup>	4.4 ± 11.9 <sup>GL</sup>	32%
<b>NAAG</b>	2.0 ± 23.0 <sup>N</sup>	1.9 ± 26.8	1.7 ± 25.5 <sup>G</sup>	-13%
<b>Tau</b>	2.4 ± 19.9 <sup>N</sup>	2.0 ± 37.9	1.7 ± 34.0 <sup>G</sup>	-25%
<b>Glc</b>	1.6 ± 61.9 <sup>N</sup>	1.8 ± 51.2 <sup>N</sup>	0.5 ± 108.1 <sup>GL</sup>	-70%
<b>Cho</b>	2.9 ± 6.5	2.8 ± 5.2 <sup>N</sup>	3.0 ± 5.4 <sup>L</sup>	3%
<b>PCr/Cr</b>	9.3 ± 6.4 <sup>N</sup>	9.6 ± 4.6 <sup>N</sup>	12.2 ± 7.2 <sup>GL</sup>	32%
<b>Syl</b>	0.3 ± 80.9	0.3 ± 76.7	0.3 ± 83.6	0%
<b>Myo</b>	5.4 ± 52.1 <sup>L</sup>	3.2 ± 101.0 <sup>G</sup>	12.1 ± 30.0 <sup>L</sup>	108%
<b>M 3.00</b>	24.5 ± 18.0 <sup>L</sup>	41.3 ± 26.8 <sup>G</sup>	-	-
<b>M 2.05</b>	0.5 ± 282.8	6.4 ± 73.3	-	-
<b>M 2.29</b>	10.3 ± 31.5 <sup>L</sup>	24.0 ± 42.1 <sup>G</sup>	-	-

**Table 2-3 : Modeling of Macromolecule Resonances in the In-Vivo Spectrum Template**

Relative metabolite levels (arbitrary units) ± CV for repeated (N=8) in-vivo data acquired on a single subject following various methods of modeling the macromolecules within the SRI. Macromolecule chemical shifts were fixed at 2.05 ppm (M 2.05), 2.29 ppm (M 2.29), and 3.00 ppm (M 3.00)<sup>19</sup>, while dampings were fixed at 22.4 Hz (based on experimental results). Both Lorentzian model functions (Lorentzian) and Gaussian model functions (Gaussian) were attempted as well as the complete omission (None) of any macromolecule resonances from the template of prior knowledge. Superscripts indicate significant difference (paired t-test,  $p < 0.05$  following Bonferroni correction, DF=7) from G (Gaussian), L (Lorentzian), or N (none).

To determine whether the macromolecules interacted significantly with overlapping metabolite resonances bivariate correlations were calculated for metabolite measures following quantification with resonances outside the SRI modeled using the Voigt lineshape and macromolecule resonances inside the SRI modeled using a Gaussian lineshape. There were no significant correlations following Bonferroni based correction. Correlations were distributed both positively and negatively.

Figure 2-3 describes the observed changes in metabolite levels and standard deviations as a function of exponential filter strength for five of the quantified metabolites (NAA, Glu, Gln, Cho, PCr/Cr) using a rectangular filter which extended to 512 ms. Although not shown here, other metabolites showed similar trends. These results indicate that metabolite levels change as a function of exponential filter strength, although some change substantially more than others (Gln level changed by ~90 % following application of a 64 ms exponential filter, while NAA level changed only ~ 5 %). Figure 2-3 (bottom) also shows a general increase in the standard deviations of metabolite level estimates proportional to the applied exponential filter (inversely proportional to the total exponential damping). Similar changes in metabolite levels and standard deviations were observed when the experiment was repeated using different rectangular filter strengths.

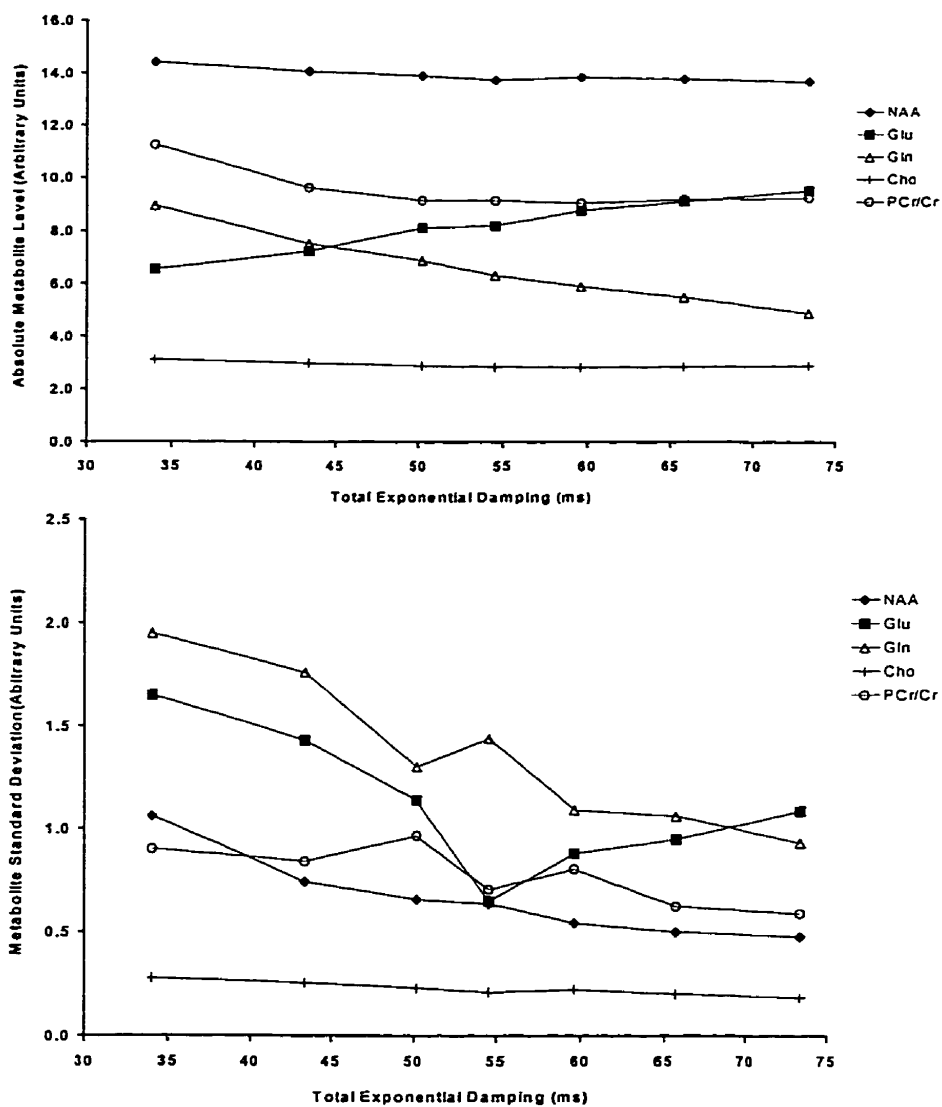


**Figure 2-3: Effect of Exponential Damping on Metabolite Quantification**

Absolute metabolite levels (arbitrary units, top plot) and standard deviations (arbitrary units, bottom plot) are shown for the metabolites NAA, Glu, Gln, Cho, and PCr/Cr as a function of total exponential damping (natural damping of unsuppressed water plus applied exponential filter in ms). Data were fit in the time domain to 512 ms (1-2048 points) following QUALITY deconvolution, modeling macromolecules (Gaussian lineshape) and resonances outside the SRI (Voigt lineshape). Although not shown here, other metabolites also changed significantly with exponential filter.

Figure 2-4 describes the observed change in metabolite levels and standard deviations as a function of rectangular filter strength for five of the quantified metabolites (NAA, Glu, Gln, Cho, PCr/Cr) using data with no additional exponential filter applied (natural damping = 73.3 ms). Although not shown here, other metabolites showed similar trends. These results indicate that metabolite levels remain constant after applying a rectangular filter until the filter begins to truncate real signal (instead of noise). In this data set signal truncation first occurred using a rectangular filter with a width of 256 ms. Figure 2-4 (bottom) also shows an increase in the standard deviation of metabolite level estimates following severe rectangular filter, especially for the metabolites Glu and Gln. Similar changes in metabolite levels and standard deviations were observed when this experiment was repeated following the application of additional exponential filtering.

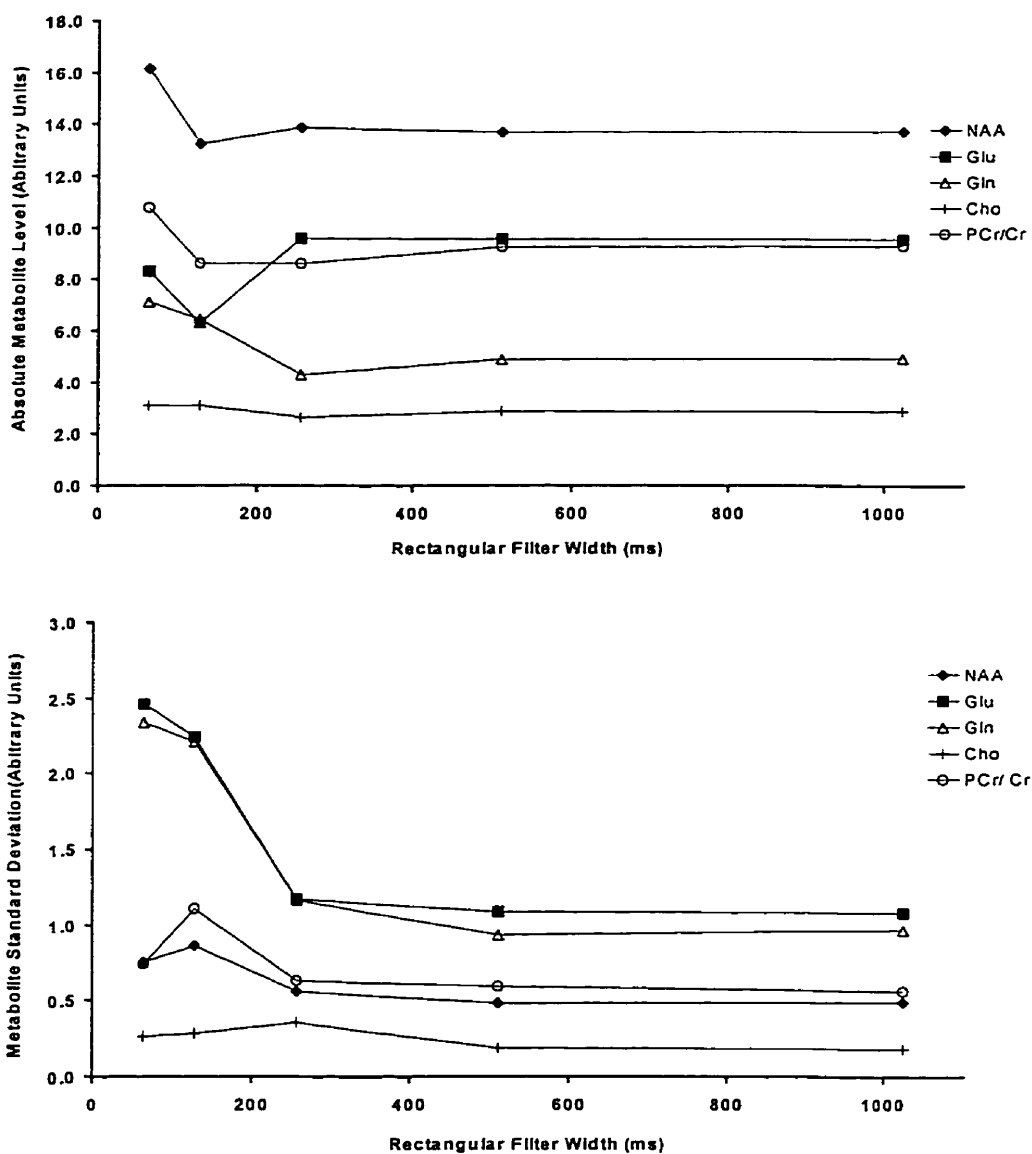


**Figure 2-4: Effect of Rectangular Filter on Metabolite Quantification**

Absolute metabolite levels (arbitrary units, top plot) and standard deviations (arbitrary units, bottom plot) are shown for the metabolites NAA, Glu, Gln, Cho, and PCr/Cr as a function of rectangular filter width (ms). Data was fit in the time domain with no additional exponential filter applied following QUALITY deconvolution, modeling macromolecules (Gaussian lineshape) and resonances outside the SRI (Voigt lineshape). Although not shown here, other metabolites also changed significantly as a function of rectangular filter.

### **2.3 Discussion**

Prior knowledge to fit in-vivo data can be obtained by modeling and parameterizing in-vitro metabolite data (2), or using the in-vitro data directly (3). In either case the in-vitro data must be free from artifacts and lineshape distortions. In this study, in-vitro data were modeled with Lorentzian lineshapes, while macromolecules and resonances outside the SRI were modeled with Lorentzian, Gaussian, or Voigt lineshapes. Since all model functions incorporated phase and delay time as fit parameters there was no operator interaction when quantifying spectroscopic data, which was necessary with some past analysis techniques (1, 2, 4, 32, 35).

With regard to resonances outside the SRI, optimal results (lowest standard deviations) were obtained in 13 of 15 metabolites when resonances adjacent to the SRI were included in the spectrum model as opposed to removing these resonances using HLSVD prior to quantification. When included in the spectral model, resonances adjacent to the SRI were fit concurrently with resonances inside the SRI allowing both groups to interact and reach the best fit. Three different lineshapes were used to fit resonances outside the SRI (Gaussian, Lorentzian, and Voigt). The use of the Gaussian lineshape caused almost all metabolite levels to be quantified with values slightly higher than what was obtained using Lorentzian or Voigt lineshapes. In many cases, this was significant following Bonferroni correction (Table 2-2). Both the Gaussian and Voigt lineshapes resulted in lower metabolite CVs for 11 of 15 metabolites compared to the Lorentzian lineshape. Since the use of the Voigt lineshape did not significantly change the precision of metabolite estimates compared to the



Gaussian lineshape, it may be the best choice for in-vivo modeling of resonances outside the SRI as it allows the maximum lineshape flexibility.

The inclusion of macromolecule resonances in the spectrum model was based on work by Behar *et al* (19). This method was attempted because it is not practical to reduce the effects of macromolecules by not fitting the initial part of the FID. This is because the macromolecules are only about 6 Hz broader than most metabolites ( $T_2 \cong 44$  ms (19) vs.  $T_2 \cong 300$  ms (35)). Therefore, in this data set, to eliminate macromolecule contributions (assuming macromolecule  $T_2^* \cong 36$  ms and waiting  $5 \times T_2^*$  for signal to decay) would require that the initial  $\sim 180$  ms of data be ignored. This would decrease metabolite S/N by a factor of  $(1 - e^{-180/115}) = 0.80$  (assuming metabolite  $T_2^* \cong 115$  ms) for most metabolites, which is a significant amount of signal for metabolites that are already at the limit of S/N for reliable quantification. The macromolecule at 3.00 ppm was consistently fit with CV < 30% (Table 2-3). The omission of these macromolecules in the quantification led to significant changes in most metabolite areas. Most notable was the increase in area to GABA (247%) and PCr/Cr (32%) which overlap with M 3.00. Comparing the ratios of GABA : Cho and PCr/Cr : Cho (Cho remains relatively constant regardless of how the macromolecules are modeled) to estimates made by others (2, 3, 4), it is clear that the omission of the macromolecules leads to an overestimation of GABA and PCr/Cr. Further evidence for the overestimation of GABA comes from the ratio of Glu : GABA which is  $\sim 1.7:1$  when macromolecules are omitted. However, biochemical studies have shown the ratio of Glu : GABA to be closer to 4-5:1 (36, 37). The increase in GABA levels to account for spectral area previously occupied by M 3.00 will influence the estimated level of other amino acids in the 2.05 to 2.40

ppm range. The two other macromolecules at 2.05 ppm and 2.29 ppm had smaller areas and were not quantified as consistently as M 3.00 in this data set. Since there were no significant correlations between metabolite and macromolecule levels, the inclusion of the macromolecule resonances did not cause inconsistent misfitting of other metabolites, which would be indicated by significant negative correlations.

Exponential filtering of data produced changes in metabolite level estimates and a decrease in precision (Figure 2-3). It was expected that exponential filtering would not affect metabolite level estimates, as this type of filtering does not alter metabolite amplitudes in the spectrum. However, for in-vivo spectra where there is heavy overlap between metabolites, the lost resolution after filtering leads to a decrease in the ability of the fitting algorithm to resolve each metabolite. This was observed (Figure 2-3, top) as a progressively worsening misfit of metabolite amplitudes proportional to the applied exponential filter strength. This result suggests that caution must be taken when comparing results obtained from spectra with different resolution (due to shim), and stresses the importance of good in-vivo shims. It was also expected that some exponential filtering of the data would increase precision due to an increase in S/N following the filter application. However, the failure to produce this result suggests that where peaks are heavily overlapped, the negative effect of decreasing resolution from filtering outweighs the benefits in S/N gain.

Rectangular filtering of data also produced changes in metabolite level estimates and a decrease in precision (Figure 2-4), although the changes tended to be less dramatic than those observed with exponential filtering. Metabolite levels were

mostly affected following severe rectangular filter (64 ms, and 128 ms), although the same trends that were seen following exponential filter (Figure 2-3, top) were visible. This is not unexpected as rectangular filtering also reduces spectral resolution. Metabolite precision was optimal when using a rectangular filter of 512 ms or 1024 ms, and decreased following heavier rectangular filtering. In this in-vivo data set, signal extended past 256 ms suggesting that to achieve optimal precision the rectangular filter imposed on the data should be minimized to the point where signal truncation begins.

Two further observations can be made as a result of these comparisons. First, with regards to the use of ECC correction vs. QUALITY deconvolution: our results showed little difference in metabolite levels (except for NAA and Cho) and precision between techniques. Since NAA and Cho are dominated by single peaks, this result suggests there may have been a lineshape distortion present in the spectrum which was uncorrected by the ECC procedure. Although QUALITY deconvolution may theoretically be the best technique for eddy current correction because it also restores the Lorentzian lineshape, in our experience ECC may be the preferred technique on data with low resolution and S/N. This is because data points may become corrupted (“blow up”) at the end of the time domain signal following QUALITY deconvolution due to the division of this signal by noise at the end of the reference signal. To reduce the effect of these corrupted points, extra exponential filtering can be used. However, we have shown that exponential filtering changes estimated metabolite levels, therefore this should be avoided. As ECC does not divide one signal by another, this problem never occurs and an extra filter need never be applied. Therefore, ECC may be considered a better technique for data with low S/N when lineshape distortion is

not a dominant concern. In the future, it may be possible to combine these two techniques by applying QUALITY deconvolution to the initial part of the time domain signal, followed by ECC correction to the last part. Data processed in this way would have partially restored Lorentzian lineshapes and avoid data corruption at the end of the time domain signal.

Second, although the use of HLSVD to subtract resonances adjacent to the SRI was not as reliable as fitting these resonances as discussed above, this technique may be a valuable tool for handling more severe spectral distortions. The residual of the HLSVD fit to the resonances adjacent to the SRI was small, indicating an accurate fit, but because there were no restrictions on peak parameters during HLSVD fitting, the values obtained for phase and delay time parameters may not make physical sense. This unrestricted fitting of peaks resulted in erroneous subtraction of resonances adjacent to the SRI corrupting resonances within the SRI. However, during the course of clinical research in our lab (38) (using the method described in this paper), cases have arisen in which spectra contained large distortions in the region from 0.75 - 1.75 ppm most likely due to susceptibility artifacts. It was found that these distortions were difficult to model with Lorentzian or Gaussian lineshapes concurrent with the fitting of data within the SRI. However the use of HLSVD to remove these distortions prior to fitting allowed these spectra to be reliably quantified.

This time domain quantification technique has been successfully implemented in a clinical study of schizophrenia (38). In this clinical study in-vivo data from the medial prefrontal cortex (4.5 cm<sup>3</sup>) was quantified following ECC correction

showing differences in Gln levels between never treated schizophrenic patients and controls.

### 2.3.1 Limitations

The precision and level of metabolite estimates is highly dependent on the accuracy of the prior knowledge used by the quantification technique. The relative parameter values found in-vitro were assumed valid in-vivo since in-vivo pH conditions were simulated. Although this assumption is probably valid in terms of chemical shift, phase, and relative resonance amplitudes, it may not be a good assumption in terms of relative Lorentzian dampings. Recent work (39) has shown a large discrepancy in apparent  $T_2$  values obtained from metabolites in-vitro, and in-vivo, especially at high field strengths. Therefore, the relative Lorentzian dampings of one metabolite may not be correct compared to the relative Lorentzian dampings of other metabolites in the prior knowledge causing small systematic errors in quantification. An attempt was made to leave the Lorentzian dampings of some in-vivo metabolites unrestricted, however this resulted in erroneous metabolite level estimates and increased standard deviations. Future improvements to the prior knowledge should include unconstraining the zero order phase of individual resonances within a metabolite during in-vitro fitting to account for J-coupling *phase* modulations.

## 2.4 Conclusion

The quantification of short echo  $^1\text{H}$  MR spectra was optimized in the time domain exploiting the simplicity of the Gaussian damping term in this domain to model

macromolecules and resonances outside the spectral region of interest without operator interaction. Optimal precision was achieved when macromolecules within the spectral region of interest were modeled with the Gaussian lineshape and resonances adjacent to the spectral region of interest were modeled with the Gaussian or Voigt lineshape. When processing data prior to fitting, data truncation and exponential filtering should be minimized. Using this approach reliable metabolite level estimates were obtained without the need for arbitrary baseline fitting.

## 2.5 References

---

1. Hennig J, Pfister H, Ernst T, Ott D. Direct Absolute Quantification of Metabolites in the Human Brain with *In Vivo* Localized Proton Spectroscopy. *NMR in Biomed.* 5, 193-199 (1992).
2. Stanley JA, Drost DJ, Williamson PC, Thompson RT. The Use of *a Priori* Knowledge to Quantify Short Echo *in Vivo*  $^1\text{H}$  MR Spectra. *Magn. Reson. Med.* 34, 17-24 (1995).
3. Provencher SW. Estimation of Metabolite Concentrations from Localized *in-vivo* Proton NMR Spectra. *Magn. Reson. Med.* 30, 672-679 (1994).
4. Michaelis T, Merboldt K, Bruhn H, Hanicke W, Frahm J. Absolute Concentrations of Metabolites in the Adult Human Brain *in Vivo*: Quantification of Localized Proton MR Spectra. *Radiology* 187, 219-227 (1993).
5. Tofts PS, Wray S. A Critical Assessment of Methods of Measuring Metabolite Concentrations by NMR Spectroscopy. *NMR in Biomed.* 1, 1-10 (1988).

- 
6. Barkhuijsen H, de Beer R, Bovee WMMJ., van Ormondt D. Retrieval of Frequencies, Amplitudes, Damping Factors, and Phases from Time-Domain Signals Using a Linear Least-Squares Procedure. *J. Mag. Res.* 61, 465-481 (1985).
  7. Barkhuijsen H, de Beer R, van Ormondt D. Improved Algorithm for Noniterative Time-Domain Model Fitting to Exponentially Damped Magnetic Resonance Signals. *J. Mag. Res.* 73, 553-557 (1987).
  8. Ho EK-Y, Snyder RE, Allen PS. Accuracy and Precision in the Estimation of *in Vivo* Magnetic-Resonance Spectral Parameters. *J. Mag. Res.* 99, 590-595 (1992).
  9. Diop A, Kolbel W, Michel D, Briguet A, Graveron-Demilly D. Full Automation of Quantification of *in Vivo* NMR by LPSVD (CR) and EPLPSVD. *J. Mag. Res.* 103, 217-221 (1994).
  10. de Graaf AA, Bovee WMMJ. Improved Quantification of *in Vivo* <sup>1</sup>H NMR Spectra by Optimization of Signal Acquisition and Processing and by Incorporation of Prior Knowledge into the Spectral Fitting. *Magn. Reson. Med.* 15, 305-319 (1990).
  11. van der Veen JWC, de Beer R, Luyten PR, van Ormondt D. Accurate Quantification of *in Vivo* <sup>31</sup>P NMR Signals Using the Variable Projection Method and Prior Knowledge. *Magn. Reson. Med.* 6, 92-98 (1988).
  12. van Dijk JE, Mehlkopf AF, van Ormondt D, Bovee WMMJ. Determination of Concentrations by Time Domain Fitting of Proton NMR Echo Signals Using Prior Knowledge. *Magn. Reson. Med.* 27, 76-96 (1992).

- 
13. Golub GH, Pereyra V. The Differentiation of Pseudo-inverses and Nonlinear Least Squares Problems whose Variables Separate. *SIAM J. Numer. Anal.* 10, 413 (1973).
  14. van Dijk JE, Mehlkopf AF, van Ormondt D, Bovee WMMJ. Determination of Concentrations by Time Domain Fitting of Proton NMR Echo Signals Using Prior Knowledge. *Magn. Reson. Med.* 27, 76-96 (1992).
  15. van den Boogaart A, Ala-Korpela M, Jokisaari J, Griffiths JR. Time and Frequency Domain Analysis of NMR Data Compared: An Application to 1D  $^1\text{H}$  Spectra of Lipoproteins. *Magn. Reson. Med.* 31, 347-358 (1994).
  16. Joliot M, Mazoyer BM, Huesman RH. In Vivo NMR Spectral Parameter Estimation: A Comparison between Time and Frequency Domain Methods. *Magn. Reson. Med.* 18, 358-370 (1991).
  17. Marshall I, Higinbotham J, Bruce S, Freise A. Use of Voigt Lineshape for Quantification of In-Vivo  $^1\text{H}$  Spectra. *Magn. Reson. Med.* 37, 651-657 (1997).
  18. de Beer R, van Ormondt D. Analysis of NMR Data Using Time Domain Fitting Procedures. *NMR Basic Principles and Progress* 26, 201-248 (1992).
  19. Behar KL, Rothman DL, Spencer DD, Petroff OAC. Analysis of Macromolecule Resonances in the  $^1\text{H}$  NMR Spectra of Human Brain. *Magn. Reson. Med.* 32, 294-302 (1994).
  20. Knijn A, de Beer R, van Ormondt D. Frequency Selective Quantification in the Time Domain. *J. Mag. Res.* 97, 444-450 (1992).
  21. Ernst Th, Hennig J. Coupling Effects in Volume Selective  $^1\text{H}$  Spectroscopy of Major Brain Metabolites. *Magn. Reson. Med.* 21, 82-96 (1991).



- 
22. Bovee WMMJ. Quantification of Glutamate, Glutamine, and other Metabolites in *In Vivo* Proton NMR Spectroscopy. *NMR in Biomed.* 4, 81-84 (1991).
  23. Frahm J, Merboldt KD, Hanicke W. Localized Proton Spectroscopy using Stimulated Echoes. *J. Mag. Res.* 72, 502-508 (1987).
  24. Wishart DS, Bigam CG, Yao J, Abildgaard F, Dyson HJ, Oldfield E, Markley JL, Sykes BD.  $^1\text{H}$ ,  $^{13}\text{C}$ ,  $^{15}\text{N}$  Chemical Shift Referencing in Biomolecular NMR. *J. Biomol. NMR* 6, 135-140 (1995).
  25. Frahm J, Michaelis T, Merboldt KD, Bruhn H, Gyngell ML, Hanicke W. Improvements in Localized Proton NMR Spectroscopy of Human Brain: Water Suppression, Short Echo Times, and 1 ml Resolution. *J. Mag. Res.* 90, 464-473 (1990).
  26. de Graaf AA, van Dijk JE, Bovee WMMJ. QUALITY: Quantification Improvement by Converting Lineshapes to the Lorentzian Type. *Magn. Reson. Med.* 13, 343-357 (1990).
  27. Klose U. In Vivo Proton Spectroscopy in Presence of Eddy Currents. *Magn Reson Med.* 14, 26-30 (1990).
  28. Marquardt DW. An Algorithm for Least-Squares Estimations of Non-Linear Parameters. *J. Soc. Indust. Appl. Math.* 11, 431-441 (1963).
  29. Ferrige AG, Lindon JC. Resolution Enhancement in FT NMR Through the Use of a Double Exponential Function. *J. Mag. Res.* 31, 337-340 (1978).
  30. Barker PB, Soher BJ, Blackband SJ, Chatham JC, Mathews VP, Bryan RN. Quantification of Proton NMR Spectra of the Human Brain Using Tissue Water as an Internal Concentration Reference. *NMR in Biomed.* 6, 89-94 (1993).

- 
31. Christiansen P, Henriksen O, Stubgaard M, Gideon P, Larsson HBW. In Vivo Quantification of Brain Metabolites by <sup>1</sup>H-MRS Using Water as an Internal Standard. *Magn. Reson. Imaging* 11, 107-118 (1993).
  32. Kreis R, Ernst T, Ross BD. Absolute Quantification of Water and Metabolites in the Human Brain. II. Metabolite Concentrations. *J. Mag. Res. Series B* 102, 9-19 (1993).
  33. Hirsch RP, Riegelman RK. Statistical First Aid. Interpretation of Health Research Data. Cambridge, MA: Blackwell Scientific Publications, 1992.
  34. Larzelere RE, Mulaik SA. Single sample tests for many comparisons. *Psychol. Bul.* 4: 557 – 569 (1977).
  35. Frahm J, Bruhn H, Gyngell ML, Merboldt KD, Hanicke W, Sauter R. Localized Proton NMR Spectroscopy of the Human Brain *in Vivo*. Relaxation Times and Concentrations of Cerebral Metabolites. *Magn. Reson. Med.* 11, 47-63 (1989).
  36. Petroff OAC, Agino T, Alger JR. High-Resolution Proton Magnetic Resonance Spectroscopy of Rabbit Brain: Regional Metabolite Levels and Postmortem Changes. *Journal of Neurochemistry* 51, 163-171 (1988).
  37. Erecinska M, Silver I. Metabolism and Role of Glutamate in Mammalian Brain. *Progress in Neurobiology.* 35, 245-296 (1990).
  38. Bartha R, Williamson PC, Drost DJ, Malla A, Carr TJ, Cortese L, Canaran G, Rylett RJ, Neufled RWJ. Measurement of Glutamate and Glutamine in the Medial Prefrontal Cortex of Never Treated Schizophrenic Patients and Healthy Controls by Proton Magnetic Resonance Spectroscopy. *Arch. Gen. Psychiatry* 54, 959-965 (1997).

- 
39. Posse S, Cuenod CA, Risinger R, Le Bihan D, Balaban RS. Anomalous Transverse Relaxation in  $^1\text{H}$  Spectroscopy in Human Brain at 4 Tesla. *Magn. Reson. Med.* 33, 246-252 (1995).

## Chapter 3

### Quantification and Precision of Short Echo $^1\text{H}$ Spectra at 1.5 and 4.0 Tesla

*By Robert Bartha, Dick J Drost, Ravi S Menon, and Peter C Williamson*

#### **3.0 Introduction**

Short echo  $^1\text{H}$  in-vivo magnetic resonance spectroscopy (MRS) can be used to measure a variety of biologically important metabolites including *N*-acetylaspartate, glutamate, glutamine, phosphocreatine and creatine, choline containing compounds, and myo-inositol. Clinical investigation of a number of illnesses (1), especially mental illnesses (2, 3), would benefit from the precise determination of in-vivo levels of cerebral metabolites, especially glutamate and glutamine. Glutamate and glutamine are involved in the cycle of excitatory neurotransmission (4), however the severe overlap of multiplet resonances from these metabolites (as well as  $\gamma$ -aminobutyric acid, and macromolecule resonances) at 1.5 Tesla (T) has limited their precise quantification (5, 6, 7). Despite this limitation a previous study by our group at 1.5 T found elevated levels of glutamine in the medial prefrontal cortex of schizophrenic patients (2). Improving the precision of glutamate and glutamine quantification, as well as other metabolites, may result in the detection of more pronounced metabolite level differences between normal and diseased tissue leading to new findings

and facilitating the observation of statistically significant differences in studies with limited participants.

The acquisition of short echo  $^1\text{H}$  data at high fields (4.0 T) has two immediate advantages over acquisition at lower fields (1.5 T). First, the signal to noise ratio (S/N) of the magnetic resonance experiment increases approximately linearly with field strength (8). The extra signal to noise at higher fields may be used to reduce the volume from which data is collected while still maintaining adequate S/N for reliable quantification. This is a significant advantage for the study of specific cerebral structures (i.e. caudate, putamen, thalamus), which often have volumes under  $1.5\text{ cm}^3$ , since typical in-vivo 1.5 T volumes range from  $4.5 - 8\text{ cm}^3$  (2, 3, 5, 6, 7). Second, chemical shift dispersion increases with field strength (9) (although resonances split by J-coupling are unaffected). Therefore, multiplet groups will be better resolved in spectra acquired at high fields compared to spectra acquired at low fields, which should increase the quantification precision of overlapped metabolites such as glutamate and glutamine.

There are also potential problems with high field in-vivo spectroscopy that could negate the gains described above. First, although eddy currents induced directly by the dB/dt of the gradients will be the same at both field strengths, an additional mechanism for causing eddy currents is gradient coil motion. In addition to eddy currents on the cryostat, gradient coil motion may also result in time dependant fluctuations of zero order and higher order magnetic fields in the sample if the room temperature shim coils are placed inside the gradient coil. At high field strengths, increased torque and thrust on the gradient coil increases

gradient coil motion leading to more severe spectral artifacts from this mechanism compared to low field strengths. Although spectral postprocessing may be used to remove the spectral distortion caused by dB/dt (10, 11) and gradient coil motion artifacts, postprocessing will not recover lost S/N from signal dephasing caused by these processes. Second, magnetic field homogeneity within the sample will decrease at high fields because magnetic susceptibility differences between tissue, bone, air, and blood will be augmented (12). This will reduce S/N in the frequency domain and  $T_2^*$  (12) and cause spectral line broadening (decrease resolution) partially offsetting the gain in resonance dispersion described in the paragraph above. Third,  $T_1$  relaxation times increase for some metabolites at high fields (12), therefore, to maintain the same level of saturation the acquisition repetition time (TR) must be lengthened, increasing total acquisition times or decreasing signal averaging in the same total acquisition time. Fourth,  $T_2$  relaxation times may decrease for some metabolites at high fields (12), reducing S/N. Fifth, the RF voltage required to produce a 90 degree tip increases linearly with field strength (assuming a constant length pulse) (8), consequently RF power and specific absorption ratio (SAR) increase as a function of the field strength squared. This is less of a concern for in-vivo stimulated echo acquisition mode (STEAM) or point resolved (PRESS) spectroscopy compared to imaging due to the small number of RF pulses applied during these localized spectroscopy sequences (13, 14, 15). The STEAM (13) sequence used at 4.0 T for this study had an estimated SAR equal to 0.14 W/Kg (assuming a 5 Kg head). Finally, when frequency selective localization is used to acquire data from specific tissue volumes, the chemical shift artifact (16) is directly proportional to the spectrometer field strength (assuming a fixed gradient strength). Therefore, if all other variables are held constant, the chemical shift

artifact can only be maintained at higher fields by using larger gradients, which will increase spectral artifacts due to eddy currents and gradient coil motion.

Despite these problems, we hypothesized that the quantification precision of all metabolites (especially glutamate and glutamine) would increase at 4.0 T due to increased chemical shift dispersion and S/N. The purpose of this study was to provide a direct comparison of metabolite quantification precision between data collected at 1.5 T and 4 T, and to determine the reproducibility of data acquired from 1.5 cm<sup>3</sup> volumes in the left anterior cingulate and left thalamus at 4.0 T. These regions are being investigated in our lab for their possible involvement in schizophrenia.

Direct comparison of spectra acquired at two different field strengths on two different systems can be difficult due to a large number of subtle differences between systems. We have endeavored to reduce differences by studying the same brain region on both systems with similar hardware (gradient coils, gradient drivers, and shim sets), using voxels of the same size and same total acquisition time, and STEAM sequences which use the same mixing time (TM) and echo time (TE). Parameters such as repetition time (TR) and receiver bandwidth were optimized at each field strength.

### **3.1 Experimental**

#### **3.1.0 Data Acquisition**

In-vitro data (for the prior knowledge template) and in-vivo data were acquired separately at 1.5 T (Siemens Vision) and 4.0 Tesla (Varian/Siemens Unity Inova). At 1.5 T, data were acquired using a stimulated echo acquisition mode (STEAM) (13) sequence (TR=1500 ms, TE=20 ms, TM=30 ms, 1K complex points, 1000  $\mu$ s dwell time, 1 KHz receiver bandwidth). At 4.0 T, data were also acquired using a STEAM sequence (TR=2000 ms, TE=20 ms, TM=30 ms, 3K complex points, 500  $\mu$ s dwell time, 2 KHz receiver bandwidth). Sequence repetition time (TR) and receiver bandwidth were optimized at each field strength (1 KHz was the narrowest bandwidth available at 1.5 T). A repetition time of two seconds was chosen at 4.0 T following the acquisition of data from two individuals with repetition times ranging from 0.5 s to 5.0 s keeping total acquisition time constant. The results showed optimal signal to noise for the metabolites *N*-Acetylaspartate, phosphocreatine and creatine, and choline between two and three seconds. Although the same shielded gradient set was used by both systems, the sequences differed slightly in terms of gradient amplitudes and RF pulse shapes. At 1.5 T fixed 3 mT/m slice selection gradients were used while the RF pulse bandwidth was adjusted to achieve a desired slice thickness (RF pulse duration was fixed at 5.12 ms). In contrast, at 4.0 T, fixed bandwidth RF pulses were used (3 ms, 7 lobe sinc pulse) while gradient amplitudes were varied to achieve a desired slice thickness. The slew rate for the gradients at 4.0 T was 5.7 mT/m/ms, compared to 3 mT/m/ms at 1.5 T, therefore, increased eddy current artifacts were expected at 4.0 T. Water suppressed (17) and unsuppressed data were collected for each acquisition.



Three CHESS pulses were used at both fields for water suppression (17). Water unsuppressed data were acquired by setting the RF amplitude of the CHESS water suppression pulses to zero. Shim settings were optimized for each in-vitro and in-vivo spectrum. The global shim settings were obtained by automated MAP shim (18) at 1.5 T using all linear and second order shims and manually using linear and  $Z^2$  shims at 4.0 T. Local shim settings were optimized manually using only linear shims at 1.5 T and 4.0 T.

Spectroscopic data acquired at 1.5 and 4.0 T were compared in terms of S/N, spectral resolution, and quantification precision. For these comparisons eight spectra were acquired consecutively from a  $2.0 \times 2.0 \times 2.0 \text{ cm}^3$  volume in the parietal lobe of one subject using the sequences described above at 1.5 T (200 averages) and 4.0 T (150 averages) within the same total acquisition time (5 minutes/spectrum).

Metabolite quantification test-retest reproducibility was determined at 4.0 T, using spectra acquired on 10 different subjects. For this characterization, spectra were collected twice from  $1.5 \times 1.0 \times 1.0 \text{ cm}^3$  volumes (transverse orientation) in the left anterior cingulate (mostly gray matter) and left thalamus (gray matter) of each subject (Figure 3-1). Subjects were completely removed from the magnet between acquisitions. To separate the biological variance from the quantification variance in these measures two additional data sets with similar S/N were acquired, each consisting of eight consecutive spectra from the parietal lobe of one individual. The first set of eight spectra was obtained using a  $2.0 \times 2.0 \times 2.0 \text{ cm}^3$  volume (16 averages) while the second set was obtained using a  $1.5 \times 1.0 \times 1.0 \text{ cm}^3$  volume (256 averages).

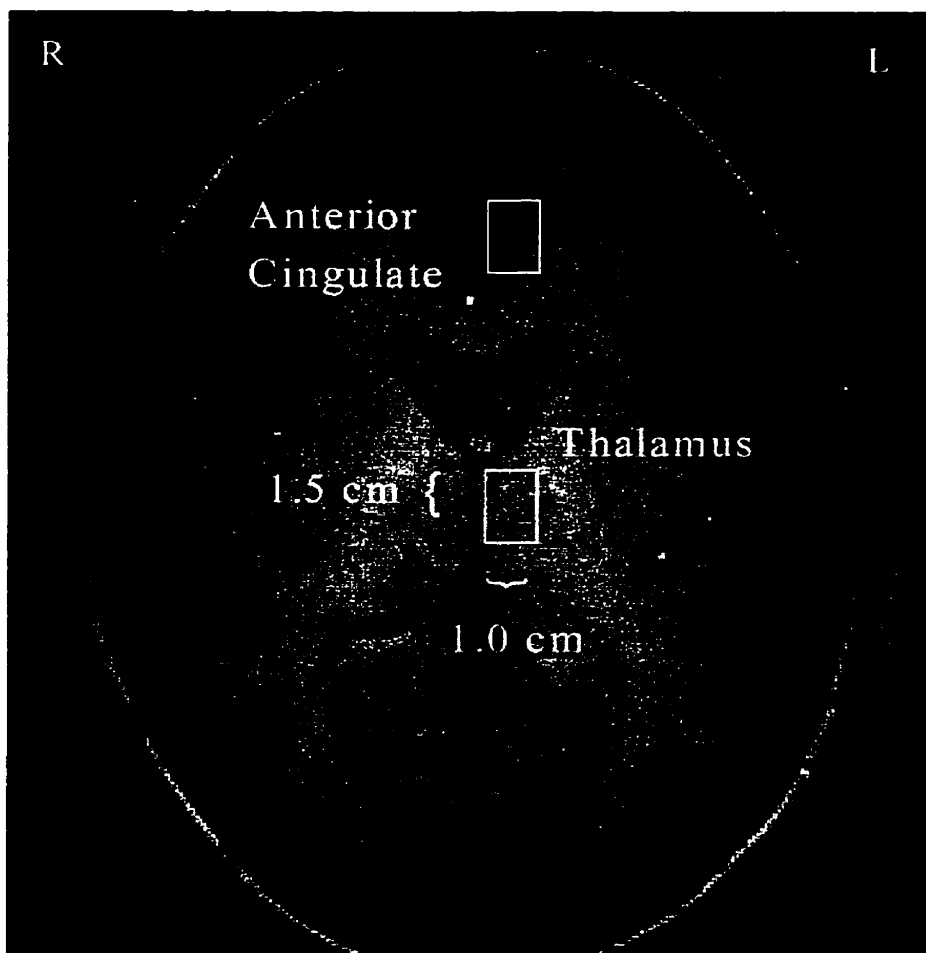


**Figure 3-1: Anatomical Regions used for 4.0 T Reproducibility Testing**

Transverse slice tilted 15 degrees towards the coronal direction. The 1.5 cm<sup>3</sup> volumes in the left cingulate and left thalamus are outlined by white boxes.

### 3.1.1 Spectral Post Processing

Raw spectroscopic data contains artifacts caused by temporal and spatial variations in  $B_0$ , which must be corrected prior to quantification. Variations in  $B_0$  can be grouped into three distinct categories; those which are time dependent but spatially invariant ( $B_0(t)$ ), time varying  $B_0$  offset which could be compensated

by a  $B_0$  coil), those which are spatially dependant but time invariant ( $\Delta B_0(x, y, z)$ , magnetic field inhomogeneities), and those which have both temporal and spatial dependence ( $\Delta B_0(x, y, z, t)$ , motion of shim coils and diffusion). Signal dephasing during echo formation and data acquisition due to  $\Delta B_0(x, y, z, t)$  will lead to reduced S/N, while dephasing due to  $B_0(t)$  will lead to a frequency dependant phase shift at the echo maximum. Signal dephasing caused by  $\Delta B_0(x, y, z)$  will be refocused at the time of echo formation, but will reduce S/N during data acquisition. All three categories will cause signal distortion during data acquisition.

However, raw spectroscopic data can be processed using information from a single peak reference spectrum that has undergone the same pattern of distortions. In  $^1\text{H}$  spectroscopy it is convenient to use the unsuppressed water spectrum for this purpose. Two methods of post processing are widely used in the literature today, eddy current correction (ECC, 10) and QUALITY deconvolution (11). QUALITY deconvolution involves dividing the data by the single peak reference spectrum in the time domain. This technique is effective for removing spectral distortions caused by all three types of field variation and restoring the Lorentzian peak lineshape, although lost S/N is not recovered. However spectra processed using this technique may contain corrupted data points near the end of the time domain signal because the water reference signal used for the correction has a shorter  $T_2$  than most metabolites (11) leading to a 'division by zero' at the end of the time domain data. On the other hand the simple ECC correction involves subtracting the phase of the reference spectrum from the phase of the data in the time domain. This technique avoids corruption of data points near the end of the time domain signal, but only corrects lineshape

distortions caused by  $B_0(t)$ . Data collected at 4.0 T in this study deviated significantly from the Lorentzian lineshape following simple ECC correction. This is an important consideration if resonance lines are modeled with Lorentzian lineshapes (19). Therefore, in this study, data were processed using a hybrid approach that exploits the advantages of both techniques, leaving the time domain signal without corrupted data points and mostly restored to the Lorentzian lineshape. QUALITY deconvolution was performed on the initial time domain points (100 ms at 1.5 T and 4.0 T) followed by the ECC correction on the remaining points.

The division of the data signal by the reference signal in the time domain following QUALITY deconvolution reduces the linewidth of the data by the linewidth of the reference. This requires exponential filtering by an amount equal to the linewidth of the reference to restore the original spectral linewidth (11, 19). The reference linewidth is usually estimated by the full width at half maximum (FWHM) of the reference peak. However, severe spectral distortions on the reference caused incorrect linewidth estimation resulting in discontinuities at the junction between the QUALITY and ECC corrected signal. An alternative approach is to estimate the magnitude of the exponential damping constant (LB) according to equation 3-1 following the application of the combined correction to the reference signal using *itself* as the reference. Acquisition delay time ( $t_0$ ) must be accounted for in the estimate of the exponential damping (LB).

$$FID(t_a) \cdot e^{-\pi \cdot LB \cdot |P_q \cdot \Delta t + t_0|} = FID(t_b) \quad [3-1]$$

Where

- $FID(t_a)$  = value of the last point used in QUALITY
- $FID(t_b)$  = value of the first point used in ECC
- $LB$  = exponential line broadening (filter)
- $\Delta t$  = dwell time
- $t_0$  = delay time
- $P_q$  = number of points where QUALITY has been applied

Following this correction, the remaining unsuppressed water was removed from each suppressed water spectrum using a Hankel Lanczos Singular Value Decomposition (HLSVD) (20, 21, 22, 23) which requires no prior knowledge. Resonances between 4.1 and 5.1 ppm (water ~ 4.7 ppm) as determined by the HLSVD algorithm were subtracted from the data.

### 3.1.2 Spectral Fitting and Prior Knowledge

Spectra were fit in the time domain using a Levenberg-Marquardt minimization routine (24) incorporating prior knowledge as described below. There was no operator interaction necessary for zero or first order phase correction as the zero order phase and delay time were incorporated as parameters in the spectral fitting (19). There was also no baseline correction required since the macromolecule resonances on the baseline were modeled using Gaussian functions (19, 25). Modeling of macromolecule resonances with Gaussian instead of Lorentzian lineshapes increased the precision of other metabolites as

described elsewhere (19). Spectra were fit using the first 1024 (0.5 second) and 512 (0.5 seconds) points at 4.0 T and 1.5 T respectively as signal had fully decayed into the noise by this time. Metabolite levels were normalized to the unsuppressed water amplitude within the voxel (26, 27, 28). Group means were corrected for the gray matter/white matter/cerebral spinal fluid content within the volumes studied (5) estimated as 15%/80%/5% in the parietal lobe, 70%/25%/5% in the anterior cingulate, and 95%/3%/2% in the thalamus. Therefore normalized metabolite values represent absolute levels uncorrected for  $T_1$  and  $T_2$  relaxation in both the metabolites and the unsuppressed water.

High resolution (< 1 Hz FWHM) in-vitro spectra for prior knowledge determination (5, 6, 7, 19, 23) were acquired separately at each field strength from solutions of *N*-acetyl-aspartate (NAA), glutamate (Glu), glutamine (Gln),  $\gamma$ -aminobutyric acid (GABA), taurine (Tau), myo-inositol (Myo), glucose (Glc), aspartate (Asp), *N*-acetylaspartyl-glutamate (NAAG), scyllo-inositol (Syl), creatine (Cr), and choline (Cho). The methodology for the acquisition of prior knowledge is described in detail elsewhere (19). It was assumed that prior knowledge obtained from in-vitro metabolite samples had the same chemical shifts ( $\omega$ ), relative Lorentzian dampings ( $\alpha$ ), relative amplitudes ( $c$ ), and phase modulations ( $\phi$ , due to J-coupling) as corresponding in-vivo metabolite resonances. In this study, resonances within the spectral region of interest (SRI, defined as 1.9-3.5 ppm with  $\text{NAA}_{\text{CH}_3}$  referenced to 2.0 ppm) were constrained as described elsewhere (19). Metabolite information outside these limits was included in the fit although this information was not constrained to resonances within the SRI except for delay time (Figure 3-2). Myo was the only exception; its shift, amplitude, phase, and width were also appropriately constrained to resonances within the SRI.

Myo was treated this way because the inclusion of its dominant resonance, which lies outside the SRI (~ 3.6 ppm), resulted in a significant increase in the precision associated with this metabolite. Prior knowledge regarding macromolecule resonances (25) was also incorporated into the fitting template as described elsewhere (19). Two additional peaks were added at 3.15 ppm and 2.6 ppm to account for the presence of area in the spectrum not due to other metabolites contained in the template of prior knowledge. The phase and delay time of these macromolecule resonances were fixed relative to all other metabolites. Initial guesses for all parameters were determined by visual inspection.

Finally, seven resonances less than 1.9 ppm and four resonances greater than 3.5 ppm were added to the template of prior knowledge to account for other resonances outside the SRI (19). These resonances were unlinked to resonances inside the SRI except for delay time. The resonances outside the SRI described above and the macromolecules described by Behar *et al* (25), are sometimes fit by other groups as a separate 'baseline' component of the spectrum (6).

### 3.1.3 Statistical Analysis

The average S/N ratio for a particular spectrum was calculated as the NAA fitted intensity divided by the RMS noise in the frequency domain. Metabolite precision values were compared using F-tests and corrected for multiple comparisons using the Bonferroni based correction (29), which is considered conservative but

maintains Type-1 error protection (see section 2.1.4). Test-retest reliability at 4.0 Tesla was established using repeated measures analysis of variance.

### 3.2 Results

Figure 3-2 shows the results of fitting in-vivo data from the parietal lobe in the time domain at 1.5 T and 4.0 T. Individual metabolite components are also shown for the 4.0 T data. The first line of metabolite components shows NAA (*N*-acetyl-aspartate) followed by NAAG (*N*-acetyl-aspartyl-glutamate), Glu (glutamate), Gln (glutamine), GABA ( $\gamma$ -amino-butyric acid), Aspartate (Asp), PCr/Cr (phosphocreatine /creatine), Cho (choline), Tau (taurine), Myo (myo-inositol), Syl (scyllo-inositol), macromolecules (at 2.05, 2.29, 2.58, 3.00 and 3.15 ppm), and finally the resonances fit outside the spectral region of interest (SRI). Glc (glucose) is not shown in Figure 3-2 as it was quantified with a value of zero. The S/N ratio (NAA fitted signal intensity divided by RMS noise – to 0.5 s in the time domain) and FWHM (unsuppressed water) for all data at 4.0 T and 1.5 T are summarized in Table 3-1. The third column of Table 3-1 contains the S/N ratio of all experiments normalized to a voxel size of  $2.0 \times 2.0 \times 2.0 \text{ cm}^3$ , total acquisition time of 5.0 minutes, while the fourth column includes normalization to a FWHM of 8.0 Hz. The FWHM normalization involves scaling the S/N of the data by the ratio of the FWHM of data to the FWHM of the reference (30). These results show a factor of 2.5 gain in S/N ratio at 4.0 T compared to 1.5 T for the  $8 \text{ cm}^3$  and  $1.5 \text{ cm}^3$  voxels respectively. Comparison of FWHM shows a 1.5 fold increase at 4.0 T; however, this is still less than the 2.7-fold increase in spectral dispersion.



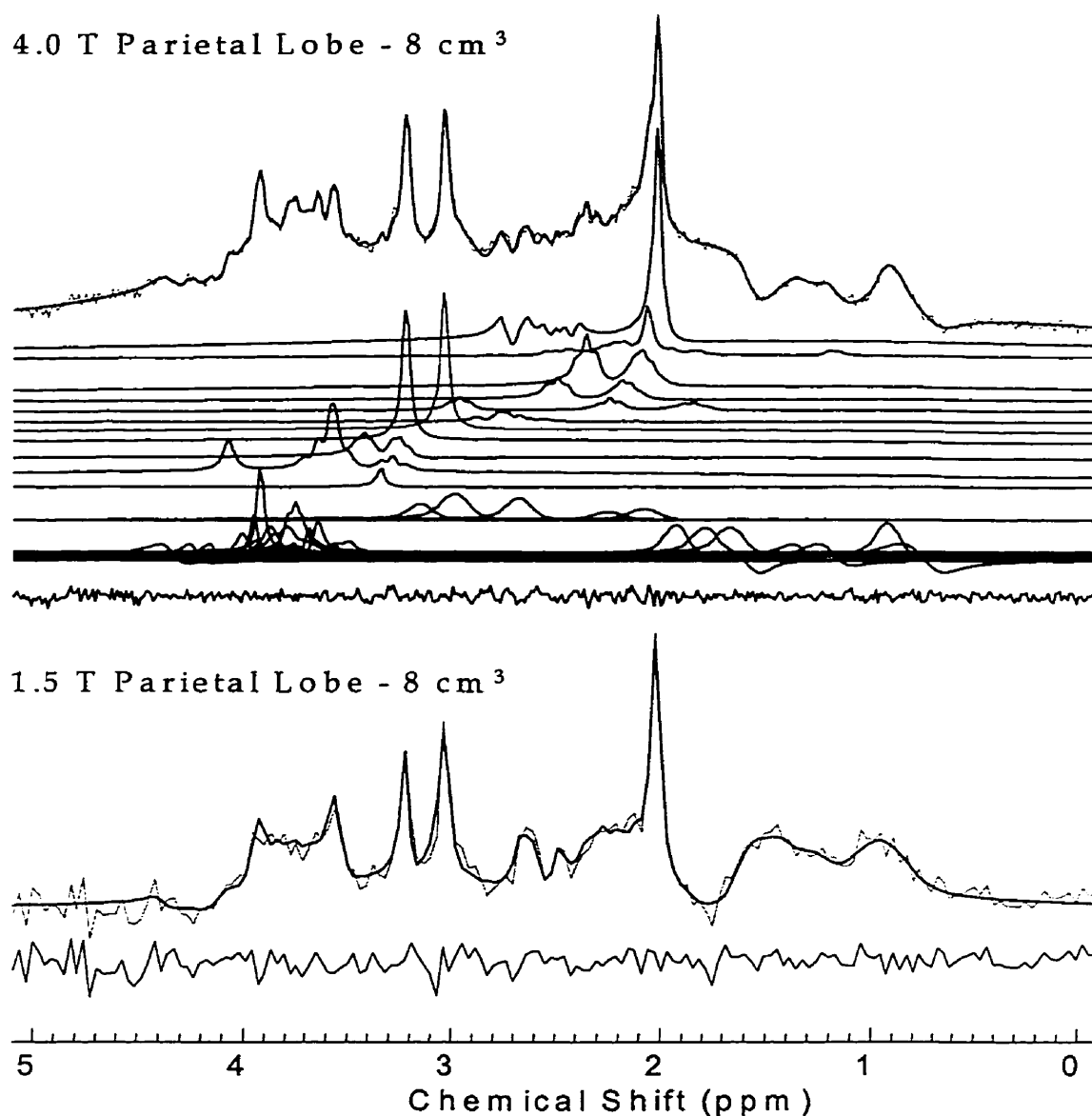


**Figure 3-2: 4.0 T and 1.5 T Parietal Lobe Data used for S/N Comparison**

The results of fitting 1.5 T and 4.0 T in-vivo data from an 8 cm<sup>3</sup> volume the parietal lobe. Although displayed in the frequency domain for interpretation, data was fit in the time domain (0-500 ms) following combined QUALITY deconvolution / ECC correction and subtraction of residual water. 4.0 T data (light trace) with corresponding fit result (dark trace) are shown at the top, followed by the individual metabolite components (described in the text) and residual. 1.5 T data (light trace) with corresponding fit result (dark trace) and residual are shown at the bottom.

Acquisition	RAW	Norm	FWHM	FWHM	Norm
	S/N	S/N	Norm	(Hz)	FWHM
	Mean $\pm$ SD	Mean $\pm$ SD	Mean $\pm$ SD	Mean $\pm$ SD	Mean $\pm$ SD
1.5 T : Parietal Lobe (8 cm <sup>3</sup> , 300 s) N=1, n=8	30.0 $\pm$ 3.5	30.0 $\pm$ 3.5	19.5 $\pm$ 2.8	5.2 $\pm$ 0.1	5.2 $\pm$ 0.1
4.0 T : Parietal Lobe (8 cm <sup>3</sup> , 300 s) N=1, n=8	75.4 $\pm$ 8.9	75.4 $\pm$ 8.9	75.4 $\pm$ 8.9	8.0 $\pm$ 0.5	3.0 $\pm$ 0.2
4.0 T : Parietal Lobe (8 cm <sup>3</sup> , 32 s) N=1, n=8	27.9 $\pm$ 3.4	85.4 $\pm$ 10.4	76.9 $\pm$ 9.4	7.2 $\pm$ 0.1	2.7 $\pm$ 0.04
4.0 T : Parietal Lobe (1.5 cm <sup>3</sup> , 512 s) N=1, n=8	18.4 $\pm$ 1.4	75.1 $\pm$ 5.7	75.1 $\pm$ 5.7	8.0 $\pm$ 0.1	3.0 $\pm$ 0.04
4.0 T : Cingulate (Trial 1) (1.5 cm <sup>3</sup> , 512 s) N=10, n=1	17.3 $\pm$ 4.0	70.6 $\pm$ 16.3	65.3 $\pm$ 15.1	7.4 $\pm$ 0.9	2.7 $\pm$ 0.3
4.0 T : Cingulate (Trial 2) (1.5 cm <sup>3</sup> , 512 s) N=10, n=1	16.6 $\pm$ 3.8	67.8 $\pm$ 15.5	63.6 $\pm$ 14.5	7.5 $\pm$ 0.6	2.8 $\pm$ 0.2
4.0 T : Thalamus (Trial 1) (1.5 cm <sup>3</sup> , 512 s) N=10, n=1	17.3 $\pm$ 3.3	70.6 $\pm$ 13.5	82.1 $\pm$ 15.7	9.3 $\pm$ 2.3	3.4 $\pm$ 0.9
4.0 T : Thalamus (Trial 2) (1.5 cm <sup>3</sup> , 512 s) N=10, n=1	16.0 $\pm$ 3.8	65.3 $\pm$ 15.5	87.3 $\pm$ 20.7	10.7 $\pm$ 0.9	4.0 $\pm$ 0.3

**Table 3-1: Signal to Noise and Resolution at 1.5 and 4.0 Tesla**

The first column lists specific details regarding data acquisition including the volume and total acquisition time in brackets. N refers to the number of individuals studied, while n refers to the number of spectra acquired per individual. The second column lists the signal to noise ratio (fitted NAA signal intensity divided by RMS noise in the frequency domain) and standard deviation. The third column represents the signal to noise ratio normalized to a total acquisition time of 5 minutes, and a volume size of 8 cm<sup>3</sup>. The fourth column represents the S/N ratio normalized to an average FWHM ( $T_2^{*-1}$ ) of 8.0 Hz. The fifth column gives the average full width at half maximum (FWHM) for the unsuppressed water spectra, while the sixth column gives the FWHM values normalized to the spectral dispersion at 1.5 T.

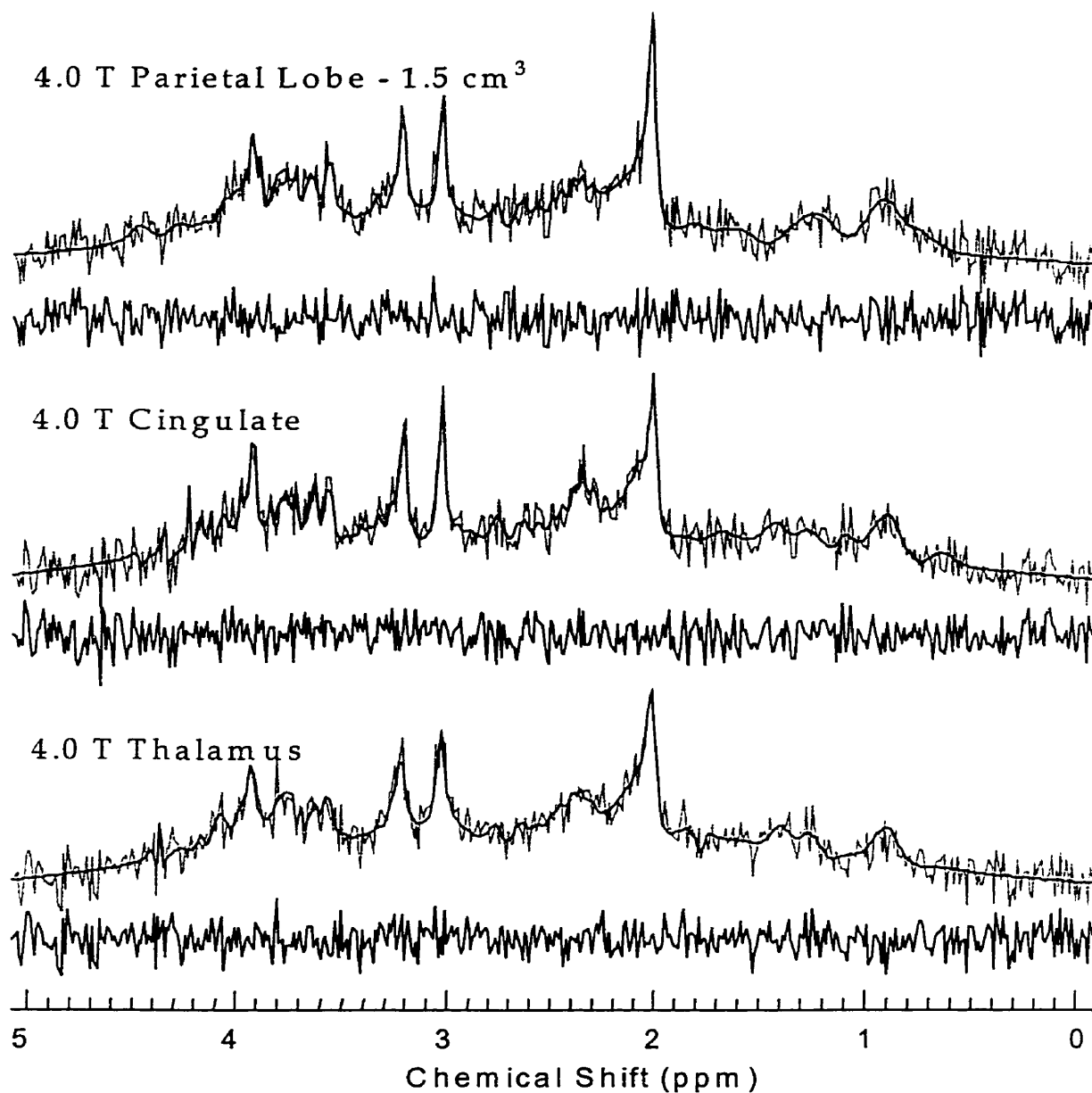
Table 3-2 contains the results of the comparison of quantification precision at 1.5 T (column a) and 4.0 T (column d) in the parietal lobe. The same total acquisition time was used at both field strengths. The results indicate that the coefficients of variation (CV) were less for metabolites quantified at 4.0 T compared to 1.5 T (Table 3-2). Notable improvements included Gln, which decreased to 9.3% CV from 39%, and GABA, which decreased to 22% CV from 88%.

Figure 3-3 illustrates typical spectra and fits obtained from 1.5 cm<sup>3</sup> volumes in the left parietal lobe (top), left thalamus (middle) and left anterior cingulate (bottom). Mean metabolite levels used to determine the overall experimental reproducibility at 4.0 T (trial 1 and trial 2) are reported in Table 3-3 for the anterior cingulate and Table 3-4 for the thalamus. The unsuppressed water area was 18% higher in the thalamus than the cingulate. Repeated measures analysis of variance showed no significant differences before or after Bonferroni based correction.

Metabolite	1.5 Tesla 8 cm <sup>3</sup>	4.0 Tesla 1.5 cm <sup>3</sup>	4.0 Tesla 8 cm <sup>3</sup>	4.0 Tesla 8 cm <sup>3</sup>
	Averages = 200 S/N = 30.0 FWHM = 5.2 (a)	Averages = 256 S/N = 18.4 FWHM = 8.0 (b)	Averages = 16 S/N = 27.9 FWHM = 7.2 (c)	Averages = 150 S/N = 75.4 FWHM = 8.0 (d)
NAA	11.9 ± 4.9%	14.9 ± 2.8%	14.9 ± 5.6%	16.0 ± 3.9%
Glu	7.6 ± 9.6	9.0 ± 13.7	10.0 ± 14.8	10.1 ± 6.8
Gln	3.2 ± 38.8	3.9 ± 42.8 <sup>d</sup>	4.0 ± 21.3	4.8 ± 9.3 <sup>b</sup>
GABA	1.4 ± 87.5	1.0 ± 106	3.0 ± 51.4	3.1 ± 22.0
Asp	0 ± 0	3.7 ± 55.4	2.6 ± 85.1	3.3 ± 26.0
NAAG	1.5 ± 27.0	1.9 ± 43.2	2.1 ± 25.6	2.5 ± 13.7
Tau	0.8 ± 54.1	5.6 ± 23.0	2.2 ± 50.6	2.9 ± 39.9
Glc	0 ± 0	0.2 ± 37.0 <sup>cd</sup>	0.4 ± 132 <sup>b</sup>	0.8 ± 62.0 <sup>b</sup>
PCr/Cr	9.5 ± 3.4	9.4 ± 4.4	10.0 ± 3.8	9.7 ± 4.4
Cho	2.0 ± 8.9	2.3 ± 8.0	3.2 ± 4.9	3.3 ± 5.2
Syl	0.1 ± 125 <sup>bc</sup>	1.0 ± 26.0 <sup>a</sup>	0.4 ± 83.7 <sup>a</sup>	0.6 ± 24.7
Myo	9.1 ± 22.2	6.7 ± 20.6	7.6 ± 17.6	7.0 ± 10.7
M 3.00	14.3 ± 14.1	8.9 ± 27.3	10.2 ± 31.3	11.2 ± 10.5
M 2.29	9.7 ± 13.2	8.1 ± 27.5	6.8 ± 50.3 <sup>d</sup>	4.1 ± 25.3 <sup>c</sup>
M 2.05	10.0 ± 11.0 <sup>bc</sup>	5.1 ± 94.0 <sup>a</sup>	6.3 ± 64.0 <sup>a</sup>	3.1 ± 58.2

**Table 3-2: Quantified Metabolite Levels and Precision at 1.5 and 4.0 Tesla**

The first column lists the metabolites and macromolecules that were quantified. Columns 2, 3, 4, 5 are labeled a, b, c, d respectively. These columns give mean metabolite levels normalized to the unsuppressed water resonance and CV (100% x standard deviation/mean) for the acquisitions described in the first row. Superscript letters indicate the column from which the reported variance is significantly different (one-tailed F-test) following Bonferroni based correction (29).



**Figure 3-3: 4.0 T Short Echo  $^1\text{H}$  Spectra from 1.5 cm<sup>3</sup> Voxels**

The results of fitting 4.0 T in-vivo data (1.5 cm<sup>3</sup> volume) following combined QUALITY deconvolution / ECC correction and subtraction of residual water. Although data is displayed in the frequency domain for interpretation, spectra were fit in the time domain (0-500 ms). Data (light trace) with corresponding fit result (dark trace) and residual from the left parietal lobe, left anterior cingulate, and left thalamus are shown at the top, middle, and bottom of this figure respectively.

<b>4.0 Tesla Cingulate</b>			
<b>Metabolite</b>	<b>Trial 1 S/N = 17.3 (Mean ± CV)</b>	<b>Trial 2 S/N = 16.6 (Mean ± CV)</b>	<b>Repeated Measures p-value</b>
NAA	14.1 ± 16.8%	14.2 ± 11.7%	0.97
Glu	13.4 ± 10.3	14.3 ± 13.7	0.11
Gln	7.7 ± 35.1	7.4 ± 19.5	0.78
GABA	1.7 ± 112	1.4 ± 84.5	0.71
Asp	1.9 ± 90.6	4.2 ± 72.9	0.06
NAAG	0.7 ± 111	0.6 ± 129	0.73
Tau	4.5 ± 61.6	6.9 ± 38.3	0.10
Glc	0.5 ± 162	0.2 ± 124	0.27
PCr/Cr	12.4 ± 9.2	12.9 ± 5.0	0.31
Cho	3.5 ± 9.7	3.3 ± 12.9	0.08
Syl	0.6 ± 74.9	1.0 ± 46.0	0.06
Myo	10.0 ± 18.5	9.2 ± 26.7	0.44
M 3.00	6.1 ± 55.6	6.8 ± 63.7	0.59
M 2.29	9.6 ± 48.8	7.7 ± 52.9	0.39
M 2.05	5.8 ± 70.4	4.8 ± 84.2	0.57

**Table 3-3: Cingulate Test-Retest Reliability at 4.0 Tesla**

Column 1 lists the metabolites that were quantified from spectra (1.5 cm<sup>3</sup> volume, 8.5 minute acquisition) in the left anterior cingulate of a group of 10 normal subjects. Columns 2 and 3 give the mean metabolite levels and CV (100% x standard deviation/mean) for trials 1 and 2 respectively. Repeated measures p-values are shown in column 4 for each metabolite.

<b>4.0 Tesla Thalamus</b>			
<b>Metabolite</b>	<b>Trial 1 S/N = 17.3 (Mean ± CV)</b>	<b>Trial 2 S/N = 16.0 (Mean ± CV)</b>	<b>Repeated Measures p-value</b>
NAA	18.9 ± 8.9%	18.1 ± 8.6%	0.41
Glu	14.4 ± 17.3	14.7 ± 8.7	0.71
Gln	8.1 ± 26.1	8.6 ± 21.2	0.55
GABA	1.5 ± 106	2.9 ± 46.9	0.07
Asp	4.0 ± 74.4	3.4 ± 80.2	0.62
NAAG	0.9 ± 105	1.2 ± 64.0	0.56
Tau	6.0 ± 44.1	6.2 ± 20.1	0.81
Glc	1.1 ± 171	0.2 ± 105	0.20
PCr/Cr	14.6 ± 9.9	14.4 ± 7.9	0.32
Cho	3.7 ± 25.8	3.4 ± 9.0	0.37
Syl	1.0 ± 34.1	0.9 ± 35.2	0.32
Myo	8.9 ± 15.6	9.0 ± 13.6	0.89
M 3.00	9.7 ± 39.0	9.6 ± 41.3	0.99
M 2.29	11.8 ± 32.4	8.9 ± 28.6	0.11
M 2.05	6.9 ± 41.7	5.1 ± 89.9	0.30

**Table 3-4: Thalamus Test-Retest Reliability at 4.0 Tesla**

Column 1 lists the metabolites that were quantified from spectra (1.5 cm<sup>3</sup> volume, 8.5 minute acquisition) in the left thalamus of a group of 10 normal subjects. Columns 2 and 3 give the mean metabolite levels and CV (100% x standard deviation/mean) for trials 1 and 2 respectively. Repeated measures *p*-values are shown in column 4 for each metabolite.

### **3.3 Discussion**

The use of combined QUALITY deconvolution and ECC correction to partially restore the Lorentzian linewidth, and avoid corrupted data points at the end of the time domain signal, was implemented successfully. This method of spectral post-processing is an effective compromise between these two techniques. The point at which QUALITY deconvolution ends and ECC correction begins is somewhat arbitrary, however, this point should be chosen to maximize the Lorentzian lineshape restoration and minimize data point corruption from 'division by zero' errors.

The increase in FWHM at 4.0 T was expected due to increased susceptibility within the tissue at higher  $B_0$  (12), and decreased  $T_2$  (12). However, the increase in FWHM was a factor of 1.8 less than the increase in chemical shift dispersion. Therefore, there is a net gain of multiplet resolution (Table 3-1, column 5), although the resolution of fine structure within multiplets due to J-coupling is decreased. The FWHM of data acquired in the anterior cingulate was lower than that acquired in the parietal lobe or thalamus. It is not surprising that the thalamus would have a shorter  $T_2^*$  compared to regions within the cortex due to an increased concentration of iron (31), however we expected the anterior cingulate to have a greater FWHM than the parietal lobe due to its proximity to the skull and orbital bone. Also surprisingly, decreasing the voxel size in the parietal lobe from 8 cm<sup>3</sup> to 1.5 cm<sup>3</sup> at 4.0 T did not result in an improvement in FWHM. This suggests that decreased  $T_2$  may contribute substantially to the increased FWHM observed at 4.0 T.



There are several obvious discrepancies in absolute metabolite levels: the increased level of NAA, PCr/Cr, and Cho in the parietal lobe (white matter) at 4.0 T compared to 1.5 T; the increased level of Glu, Gln, and PCr/Cr in the gray matter volumes (anterior cingulate and thalamus) compared to the white matter volume (parietal lobe); and the increased level of NAA in the thalamus compared to the anterior cingulate at 4.0 T. These issues will be addressed separately. First, the increased level of NAA and other metabolites in white matter volumes at 4.0 T compared to 1.5 T may be the result of decreased signal saturation.  $T_1$  values reported by Posse *et al* (12) at 4.0 T and Frahm *et al* (32) at 1.5 T suggest that the chosen TR of 2.0 s at 4.0 T would have reduced signal saturation by 11% for NAA and PCr/Cr and 8% for Cho compared to a TR of 1.5 s at 1.5 T. This corresponds to the observed increases.

The increased level of Glu, Gln, and PCr/Cr in the gray matter compared to white matter at 4.0 T is not unexpected. Previous reports have indicated that Glu and Gln (5, 7), as well as PCr/Cr (1, 5, 7) are increased in gray matter compared to white matter. Stanley *et al* (5) reported a 20% increase in both glutamate and glutamine, and a 7% increase in PCr/Cr corresponding to a 20% increase in voxel gray matter content. This would suggest a 70-80% increase in Glu and Gln, and a 25% increase in PCr/Cr should be expected in our study due to the increased specificity for gray and white matter within the voxels studied. This was observed. Comparison of NAA and Cho levels in the white matter and gray matter showed no differences, although NAAG levels were increased in gray matter as expected (7).

The minor increase of Glu, Gln, and PCr/Cr in the thalamus compared to the cingulate can be attributed to increased gray matter content within the voxel. The larger increase in NAA likely represents a true regional difference, however anomalous relaxation effects can not be discounted. The unsuppressed water signal from the thalamus showed a significant increase in linewidth suggesting decreased  $T_2$  or  $T_2^*$  probably resulting from increased iron content in this region of the brain (31, 33). Increased iron content may also be responsible for a decrease in the  $T_1$  of NAA and consequently reduced saturation of NAA accounting for the increase in measured NAA levels.

The comparisons made between short echo  $^1\text{H}$  spectroscopy data collected at 1.5 T and 4.0 T for the same voxel size and same total acquisition time indicate that quantification precision is higher at 4.0 T as anticipated. The average decrease in relative error is 47% for all metabolites, excluding glucose because it was quantified with a value of zero at 1.5 T. This is important for the detection of subtle metabolite level differences that may exist in diseased tissue or following drug treatments. There are two possible explanations for this increased precision. The first is that the S/N ratio of the data collected at 4.0 T is greater (factor of 2.5 for data collected from the  $8\text{ cm}^3$  voxels in the parietal lobe) compared to similar data acquired at 1.5 T. Comparing the CV of metabolite estimates from columns b, c, and d in Table 3-2, it is clear that metabolite precision increases as a function of S/N for most metabolites. The second reason is the increase in chemical shift dispersion, which spreads multiplet resonance groups out along the frequency axis. Presumably this increase in chemical shift dispersion may allow multiplets which are mostly overlapped at 1.5 T ( $\gamma$ -multiplets of Glu and Gln) to be resolved at 4.0 T. Comparison of columns a,

b, and c in Table 3-2 would indicate that this may also be a factor. The 4.0 T data presented in columns b and c of Table 3-2 have a similar S/N ratio than the 1.5 T data in column a, however the precision of some metabolites (glutamine and  $\gamma$ -aminobutyric acid) is higher than at 1.5 T. This suggests that multiplet resolution (FWHM/ field strength) is also an important factor in spectral quantification.

The increased S/N ratio obtained at 4.0 T enabled data collection from 1.5 cm<sup>3</sup> volumes placed in the gray matter of the left anterior cingulate and left thalamus. It is worth noting that data acquisition was also attempted from a 1.5 cm<sup>3</sup> volume at 1.5 T however no peaks were visible. The spectra obtained at 4.0 T were consistently good quality. Test-retest reproducibility results indicated that metabolite levels were reproducible between trials (no significant differences in repeated measures ANOVA before or after Bonferroni based correction). Comparison of the precision between group measures (Tables 3-3 and 3-4) and measures made on a single subject at a comparable S/N ratio (Table 3-2 – column b) indicate that the CV associated with measurements on a single individual are usually less for the metabolites NAA, Cho, and PCr/Cr. However, this is not true for most other metabolites suggesting the precision is limited by the quantification process and low S/N, not biological variation or voxel placement.

### 3.3.0 Limitations

The S/N comparisons between 1.5 T and 4.0 T were sensitive to the quantified level of NAA, which may be affected by differences in prior-knowledge and T<sub>1</sub>

and/or  $T_2$  relaxation. Increasing the acquisition TR at 4.0 T from 1.5 s to 2.0 s may have reduced  $T_1$  saturation effects but at the cost of less averaging. Fully relaxed unsuppressed water global FIDs acquired on the same phantom at both field strengths showed a 2.7-fold increase in S/N as expected. However, localized spectra had reduced S/N due to signal dephasing caused by gradient coil vibration and dB/dt eddy currents from gradient switching.

The frequency selective nature of the STEAM sequence results in frequency dependent localization errors (16). The severity of this displacement is directly proportional to the field strength, assuming a constant gradient strength is applied. The 1.5 T sequence used in this study used fixed gradient amplitudes (3 mT/m) and varied the bandwidth of the RF pulse to achieve the desired slice thickness. This resulted in a fixed chemical shift artifact of 0.5 mm for peaks separated by 1 ppm (or 64 Hz). The 4.0 T sequence used in this study used fixed RF pulses (3ms, 7 lobe sinc) and varied the gradient strength to achieve the desired slice thickness. In this case the chemical shift artifact is a function of the slice thickness: 0.6 mm for a 1 cm slice and 1.2 mm for a 2 cm slice. The use of slightly different RF pulse shapes at the two field strengths may cause some difference in slice selection profiles. However, this would have minimal effect on S/N measures unless out of volume NAA levels were significantly different than within volume levels. Since the 8 cm<sup>3</sup> voxel used for comparisons was placed in the center of the parietal lobe white matter, this possibility is unlikely.

Data collected from volumes smaller than 1.5 cm<sup>3</sup> may be possible at 4.0 T. However, data from smaller volumes may not have adequate S/N for the quantification of metabolites like Glu and Gln with precision that will facilitate

observation of metabolite level differences between normal and diseased tissue. The measurement of NAA, Cho, or PCr/Cr would be possible from volumes less than 1.5 cm<sup>3</sup>. However an acquisition sequence with a longer TE should be used to eliminate short T<sub>2</sub> signals from the spectral baseline (macromolecule signals), reduce the signal from highly J-coupled metabolites (Glu and Gln), and reduce eddy current distortions.

### **3.4 Conclusion**

Increased S/N and chemical shift dispersion at 4.0 T compared to 1.5 T resulted in metabolite level estimates with higher precision (47% increase on average for all metabolites excluding glucose) for in-vivo data collected from the same volume size (8 cm<sup>3</sup>) in the same total acquisition time. Specifically, 12 metabolites including GABA and NAAG were quantified with CVs ≤ 30% in data from a single individual. Data acquired from 1.5 cm<sup>3</sup> volumes in the anterior cingulate and thalamus of multiple subjects were quantified successfully (CV ≤ 35% consistently for 6 metabolites including Glu and Gln) which is not possible at 1.5 T. Therefore, the acquisition of in-vivo data at 4.0 T is advantageous over 1.5 T because volume size may be decreased to reduce partial volume contamination while maintaining adequate S/N ratio for reliable quantification.

### **3.5 References**

- 
1. Ross B, Michaelis T. Clinical Applications of Magnetic Resonance Spectroscopy. *Magnetic Resonance Quarterly* 10, 191-247 (1994).

- 
2. Bartha R, Williamson PC, Drost DJ, Malla A, Carr TJ, Cortese L, Canaran G, Rylett RJ, Neufeld RWJ. Measurement of glutamate and glutamine in the medial prefrontal cortex of never treated schizophrenic patients and healthy controls using proton magnetic resonance spectroscopy. *Arch. Gen. Psychiatry* 54, 959-965 (1997).
  3. Stanley JA, Williamson PC, Drost DJ, Rylett J, Carr T, Malla A, Thompson RT. An in-vivo proton magnetic resonance spectroscopy study of schizophrenic patients. *Schizophr. Bull.* 22, 597-609 (1996).
  4. Erecinska M, Silver I. Metabolism and Role of Glutamate in Mammalian Brain. *Progress in Neurobiology* 35, 245-296 (1990).
  5. Stanley JA, Drost DJ, Williamson PC, Thompson RT. The Use of a Priori Knowledge to Quantify Short Echo in Vivo 1H MR Spectra. *Magn. Reson. Med.* 34, 17-24 (1995).
  6. Provencher SW. Estimation of Metabolite Concentrations from Localized in-vivo Proton NMR Spectra. *Magn. Reson. Med.* 30, 672-679 (1994).
  7. Michaelis T, Merboldt K, Bruhn H, Hanicke W, Frahm J. Absolute Concentrations of Metabolites in the Adult Human Brain in Vivo: Quantification of Localized Proton MR Spectra. *Radiology* 187, 219-227 (1993).
  8. Hoult DI, Chen C-N, Sank VJ. The Field Dependence of NMR Imaging II. Arguments Concerning an Optimal Field Strength. *Magn. Reson. Med.* 3, 730-746 (1986).
  9. Bomsdorf H, Helzel T, Kunz D, Roschmann P, Tschendel O, Wieland J. Spectroscopy and Imaging with a 4 Tesla Whole-body MR System. *NMR in Biomedicine* 1, 151-158 (1988).

- 
10. Klose U. In Vivo Proton Spectroscopy in Presence of Eddy Currents. *Magn. Reson. Med.* 14, 26-30 (1990).
  11. de Graaf AA, van Dijk JE, Bovee WMMJ. QUALITY: Quantification Improvement by Converting Lineshapes to the Lorentzian Type. *Magn. Reson. Med.* 13, 343-357 (1990).
  12. Posse S, Cuenod CA, Risinger R, Le Bihan D. Anomalous Transverse Relaxation in <sup>1</sup>H Spectroscopy in Human Brain at 4 Tesla. *Magn. Reson. Med.* 33, 246-252 (1995).
  13. Frahm J, Merboldt KD, Hanicke W. Localized Proton Spectroscopy using Stimulated Echoes. *J. Mag. Res.* 72, 502-508 (1987).
  14. Bottomley PA. Point Resolved Spectroscopy. *Ann. N.Y. Acad. Sci.* 508, 333 (1987).
  15. Ordidge RJ, Connelly A, Lohman JAB. Image-Selected in Vivo Spectroscopy (ISIS). A New Technique for Spatially Selective NMR Spectroscopy. *J. Mag. Res.* 66, 283-294 (1986).
  16. van Zijl PCM, Moonen CTW, Alger JR, Cohen JS, Chesnick SA. High Field Localized Proton Spectroscopy in Small Volumes: Greatly Improved Localization and Shimming Using Shielded Strong Gradients. *Magn. Reson. Med.* 10, 256-265 (1989).
  17. Frahm J, Michaelis T, Merboldt KD, Bruhn H, Gyngell ML, Hanicke W. Improvements in Localized Proton NMR Spectroscopy of Human Brain: Water Suppression, Short Echo Times, and 1 ml Resolution. *J. Mag. Res.* 90, 464-473 (1990).
  18. Liu Z, Javaid T, Hu J, Brown TR. CSI—Autoshim Procedures for Body and Surface Coil. In: Proceedings of the Society of Magnetic Resonance 2nd

---

Annual Meeting; August 6-12, 1994; San Francisco, California; Page 1174.  
Abstract.

19. Bartha R, Drost DJ, Williamson PC. Factors Affecting the Quantification of Short Echo In-Vivo  $^1\text{H}$  MR Spectra: Prior Knowledge, Peak Elimination, Filtering. *NMR in Biomedicine* (in press).
20. van den Boogaart A, Ala-Korpela M, Jokisaari J, Griffiths JR. Time and Frequency Domain Analysis of NMR Data Compared: An Application to 1D  $^1\text{H}$  Spectra of Lipoproteins. *Magn. Reson. Med.* 31, 347-358 (1994).
21. Barkhuijsen H, de Beer R, Bovee WMMJ, van Ormondt D. Retrieval of Frequencies, Amplitudes, Damping Factors, and Phases from Time-Domain Signals Using a Linear Least-Squares Procedure. *J. Mag. Res.* 61, 465-481 (1985).
22. Barkhuijsen H, de Beer R, van Ormondt D. Improved Algorithm for Noniterative Time-Domain Model Fitting to Exponentially Damped Magnetic Resonance Signals. *J. Mag. Res.* 73, 553-557 (1987).
23. de Beer R, van Ormondt D. Analysis of NMR Data Using Time Domain Fitting Procedures. *NMR Basic Principles and Progress* 26, 201-248 (1992).
24. Marquardt DW. An Algorithm for Least-Squares Estimations of Non-Linear Parameters. *J. Soc. Indust. Appl. Math.* 11, 431-441 (1963).
25. Behar KL, Rothman DL, Spencer DD, Petroff OAC. Analysis of Macromolecule Resonances in the  $^1\text{H}$  NMR Spectra of Human Brain. *Magn. Reson. Med.* 32, 294-302 (1994).
26. Barker PB, Soher BJ, Blackband SJ, Chatham JC, Mathews VP, Bryan RN. Quantification of Proton NMR Spectra of the Human Brain Using Tissue



- 
- Water as an Internal Concentration Reference. *NMR in Biomed.* 6, 89-94 (1993).
27. Christiansen P, Henriksen O, Stubgaard M, Gideon P, Larsson HBW. In Vivo Quantification of Brain Metabolites by <sup>1</sup>H-MRS Using Water as an Internal Standard. *Magn. Reson. Imaging* 11, 107-118 (1993).
28. Kreis R, Ernst T, Ross BD. Absolute Quantification of Water and Metabolites in the Human Brain. II. Metabolite Concentrations. *J. Mag. Res. Series B.* 102, 9-19 (1993).
29. Ingelfinger JA, Mosteller F, Thibodeau LA, Ware JH. Biostatistics in Clinical Medicine. New York, NY: Macmillan Publishing Co., 1983.
30. Canet D. Nuclear Magnetic Resonance Concepts and Methods. New York, NY: John Wiley & Sons Inc., 1996.
31. Ye FQ, Martin WRW, Allen PS. Estimation of the Iron Concentration in Excised Gray Matter by Means of Proton Relaxation Measurements. *Magn. Reson. Med.* 35, 285-289 (1996).
32. Frahm J, Bruhn H, Gyngell ML, Merboldt KD, Hanicke W, Sauter R. Localized Proton NMR Spectroscopy in Different Regions of the Human Brain In Vivo. Relaxation Times and Concentrations of Cerebral Metabolites. *Magn. Reson. Med.* 11, 47-63 (1989).
33. Vymazal J, Brooks RA, Baumgarner C, Tran V, Katz D, Bulte JWM, Bauminger ER, Di Chiro G. The Relation Between Brain Iron and NMR Relaxation Times: An in Vitro Study. *Magn. Reson. Med.* 35, 56-61 (1996).

## Chapter 4

### **<sup>1</sup>H Magnetic Resonance Spectroscopy in Mental Illness**

#### ***4.0 Clinical Application of Short Echo <sup>1</sup>H MRS to Mental Illness***

##### 4.0.1 A Neurochemical Basis for Mental Illness?

Magnetic resonance spectroscopy (MRS) can be used to measure levels of in-vivo metabolites (1, 2, 3), information which is unobtainable using other imaging techniques such as positron emission tomography (PET) (4) or single photon emission computed tomography (SPECT) (5, 6). Therefore it is natural to consider MRS as a tool for studying illnesses within the brain which likely have a neurochemical basis. Proton (<sup>1</sup>H) MRS is particularly useful as it provides information about several metabolites such as glutamate and glutamine (7, 8) which are involved in the process of neurotransmission (9).

The concept of mental illness has evolved over the past several decades. It is now believed that most mental illness like schizophrenia and obsessive-compulsive disorder (OCD) are caused by neurochemical (10, 11) and/or structural (12) abnormalities within the brain. However, brain chemistry, structure, and physiology is complex, making it difficult to determine the exact location of such abnormalities in each illness. In fact, each mental illness likely

involves the interaction of multiple brain regions (13), and patients may have abnormalities in one or more regions each leading to a similar symptomatology.

Within this thesis, subjects with symptoms of two different mental illnesses were investigated; schizophrenia and obsessive-compulsive disorder. Several hypotheses have been made regarding the causality of each illness (11, 14, 15, 16). These will not be discussed. However, one possible explanation for both illnesses is the malfunctioning of specific neuronal circuits within the basal ganglia - thalamocortical pathway (17).

#### 4.0.2 The Basal-Ganglia Thalamocortical Pathway

The basal-ganglia thalamocortical pathway describes a group of neuronal circuits, which connect several anatomically and functionally distinct regions within the brain, as shown in Figure 4-1.

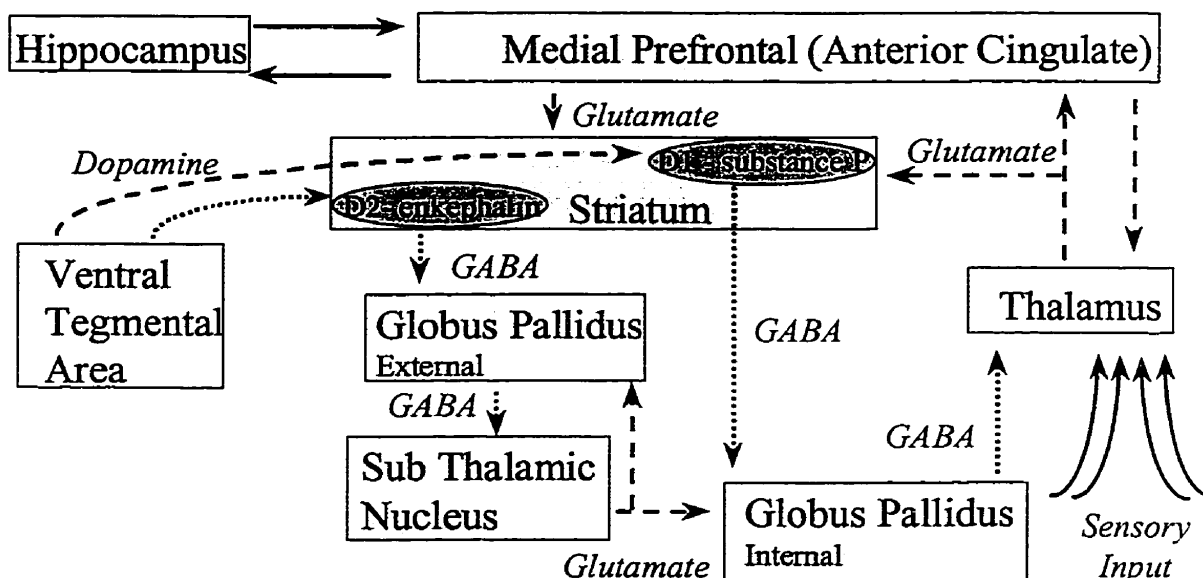


**Figure 4-1: Basal Ganglia – Thalamocortical Neuronal Circuit**

A schematic representation of the connections within the basal ganglia – thalamocortical neuronal circuits, adapted from the paper by Alexander *et al* (17). Boxes indicate functionally distinct regions within the circuit. The dashed lines indicate excitatory projections while the dotted lines indicate inhibitory projections. The basic functioning of this circuit is described within the text.

This circuit acts as a feedback loop controlling the degree of cortical activity gated by the thalamus. The activity of the thalamus is tonically inhibited by projections from the internal component of the globus pallidus. Two competing pathways to the internal globus pallidus, which originate in the striatum, modulate the degree of inhibition of the thalamus. Excitatory projections from specific areas within the cerebral cortex, which are modulated by the thalamus, regulate the activity of each striatal channel. Many other regions within the brain also participate in the modulation of activity within this circuit. Perhaps of note is the

effect of dopaminergic input to the striatum from the ventral tegmental area and the interaction between the hippocampus and cortical regions.

Many imaging and post-mortem studies have shown differences between schizophrenic patients and controls in the prefrontal cortex (18, 19, 20). Schizophrenia has also been associated with abnormalities in cognition (21), an activity that involves the dorsolateral prefrontal and medial prefrontal cortex (17). However, the prefrontal cortex does not act in isolation. It receives afferent connections from the thalamus and hippocampus, and sends efferent connections to the striatum. Therefore, it is possible that the abnormalities observed in schizophrenia in this region may result from a malfunction of one or more basal ganglia thalamocortical circuits (22).

Similarly, previous studies of OCD have shown abnormalities in the striatum and prefrontal cortex, as well as abnormalities in sensorimotor gating (23) an activity involving the thalamus. These regions are all components of the basal ganglia thalamocortical circuits. Therefore it is also reasonable to suspect the involvement of this circuitry in OCD.

Therefore,  $^1\text{H}$  MRS was used to determine whether differences in metabolite levels were measurable within one or more components of the basal ganglia - thalamocortical neuronal circuit in schizophrenic patients, OCD patients, and control subjects. Specifically, the left medial prefrontal cortex and left striatum were studied in both subject groups and controls. The results of the investigation of the left medial prefrontal cortex showed an increase in glutamine levels in never treated schizophrenic patients compared to controls (Chapter 5) which was

not observed in obsessive-compulsive patients. The results of the investigation of the left striatum showed a decrease in NAA in obsessive-compulsive patients compared to controls (Chapter 6) which was not observed in the schizophrenic patients.

#### **4.1 Physiological Interpretation of $^1\text{H}$ Magnetic Resonance Spectroscopy**

##### 4.1.1 Physiological Interpretation of Measured Metabolites

The use of  $^1\text{H}$  MRS to study and interpret in-vivo physiology is based on the measurement of several different metabolites which are listed in Section 1.0.1 of Chapter 1. The relevance of each metabolite is described in this section. An in depth account of the processes in which each metabolite is involved is omitted; instead a brief description is given of the main role that each metabolite has within the brain.

Some metabolites are localized within neurons or glial cells making them convenient markers of neuronal or glial integrity. For example, the most prominent in-vivo peak arises from the second most abundant amino acid in the brain (24), *N*-Acetylaspartate, which is almost exclusively localized within neurons (24, 25). Therefore *N*-acetylaspartate levels indicate neuronal density within the volume studied (24, 25). This metabolite may also be involved in many specific cellular functions although these have not been positively identified and are the subject of some debate (25). Some possible functions include osmoregulation and the storage of acetyl groups for myelin synthesis (25). Another metabolite, *N*-acetylaspartyl-glutamate, is a precursor of *N*-acetylaspartate and glutamate and is also present in neurons (24, 26). However

the concentration of this metabolite is small, and its resonances severely overlap with other higher concentration metabolites (*N*-acetylaspartate, glutamate, glutamine), making *N*-acetylaspartyl-glutamate difficult to quantify precisely in-vivo (3). In contrast to *N*-acetylaspartate, both myo-inositol and scyllo-inositol (sugar alcohols) are contained mostly within astrocytes and therefore are considered astrocytic markers (1). These sugars are involved in many metabolic pathways (27) and may also be breakdown products of myelin (1).

Three metabolites involved in energy metabolism can be detected using  $^1\text{H}$  MRS: glucose, creatine and phosphocreatine. Glucose, the major source of energy for the brain, is broken down in the formation of adenosine triphosphate (ATP). This process ensures that adequate energy (in the form of high energy phosphate bonds) is present in the brain for normal functioning (28). ATP may also be formed by the direct phosphorylation of ADP; a reaction catalyzed by the enzyme creatine kinase. The energy and inorganic phosphate for this reaction come from the breakdown of PCr. Therefore measurement of glucose, phosphocreatine, and creatine can yield important information regarding cerebral energy metabolism. Phosphocreatine and creatine (PCr + Cr), which are indistinguishable in the in-vivo  $^1\text{H}$  MR spectrum at low field strengths may also fluctuate in concentration in response to osmotic changes (levels increase in hyperosmolar states) (1). Phosphocreatine levels are also extremely sensitive to oxygenation levels and may be involved in regulating mitochondrial activity (28).

Several measurable metabolites are directly or indirectly involved with the process of neurotransmission: glutamate, glutamine,  $\gamma$ -aminobutyric acid, aspartate, and taurine. The amino acid  $\gamma$ -aminobutyric acid is the principle

inhibitory neurotransmitter in the brain (29, 30). Glutamate, the most abundant amino acid in the brain, is the principle excitatory neurotransmitter. It is found in two distinct compartments, one compartment is involved in neurotransmission, while a second compartment has more general functions including protein synthesis (31, 32). Although the concentration of glutamate in the brain is tightly controlled, the concentration of glutamine may fluctuate (7). Glutamine is also an amino acid, and is both a precursor and breakdown product of glutamate. Together glutamate, glutamine,  $\gamma$ -aminobutyric acid, aspartate, and taurine may provide important insights regarding abnormalities in neurotransmission related to mental illness (Figure 4-1).

The resonance due to choline is composed of mainly phosphorylcholine, glycerophosphocholine, and free choline (1). The concentration of choline is almost equal in white and gray matter and represents components of membrane phospholipid metabolism (1). Therefore, increased levels of choline are expected following the breakdown of myelin as seen in multiple sclerosis.

The in-vivo spectrum also contains a major contribution from macromolecule resonances. These macromolecule signals likely arise from hydrogen atoms in glutamate, glutamine, and other amino acids that have been incorporated into medium sized protein molecules (33).

Chapter 5 and Chapter 6 illustrate specific examples of the use of in-vivo  $^1\text{H}$  MRS to investigate mental illness. Chapter 5 reports the results of an investigation of the medial prefrontal cortex in first episode, never treated schizophrenic patients, while Chapter 6 reports the results of an investigation of the striatum in



obsessive-compulsive patients. In both cases metabolite level differences were found between the patient and control groups. Metabolite differences were consistent with previous findings and theories, yet provided unique information regarding these illnesses.

## 4.2 References

---

1. Ross B, Michaelis T. Clinical Applications of Magnetic Resonance Spectroscopy. *Magnetic Resonance Quarterly* 10, 191-247 (1994).
2. Provencher SW. Estimation of Metabolite Concentrations from Localized *in-vivo* Proton NMR Spectra. *Magn. Reson. Med.* 30, 672-679 (1994).
3. Stanley JA, Drost DJ, Williamson PC, Thompson RT. The Use of *a Priori* Knowledge to Quantify Short Echo *in Vivo*  $^1\text{H}$  MR Spectra. *Magn. Reson. Med.* 34, 17-24 (1995).
4. Tamminga CA, Thaker GK, Buchanan R, Kirkpatrick B, Alphas LD, Chase TN, Carpenter WT. Limbic System Abnormalities Identified in Schizophrenia using Positron Emission Tomography with Fluorodeoxyglucose and Neocortical Alterations with Deficit Syndrome. *Arch. Gen. Psychiatry* 49, 522-529 (1992).
5. Tsui BMW, Zhao X, Frey EC, McCartney WH. Quantitative Single Photon Emission Computed Tomography: Basics and Clinical Considerations. *Seminars in Nuclear Medicine* 24, 38-65 (1994).
6. Ebmeier KP, Blackwood DHR, Murray C, Souza V, Walker M, Dougall N, Moffoot APR, O'Carroll RE, Goodwin GM. Single-photon emission computed

- 
- tomography with  $^{99m}\text{Tc}$  exametazime in unmedicated schizophrenic patients. *Biol. Psychiatry* 33, 487-495 (1993).
7. Chamuleau RAFM, Bosman DK, Bovee WMMJ, Luyten PR, den Hollander JA. What the Clinician Can Learn from MR Glutamine/Glutamate Assays. *Magn. Reson. Med.* 34, 17-24 (1995).
  8. Prost RW, Mark L, Mewissen M, Li S-J. Detection of Glutamate/Glutamine Resonances by  $^1\text{H}$  Magnetic Resonance Spectroscopy at 0.5 Tesla. *Magn. Reson. Med.* 37, 615-618 (1997).
  9. Erecinska M, Silver IA. Metabolism and Role of Glutamate in Mammalian Brain. *Prog. Neurobiol.* 35, 245-296 (1990).
  10. Carlsson M, Carlsson A. Schizophrenia: A Subcortical Neurotransmitter Imbalance Syndrome? *Schiz. Bull.* 16, 425-432 (1990).
  11. Deutsch SI, Mastropaolo J, Schwartz BL, Rosse RB, Morihisa JM. A "Glutamatergic Hypothesis" of Schizophrenia. *Clinical Neuropharmacology* 12, 1-13 (1989).
  12. Breier A, Buchanan RW, Elkashef A, Munson RC, Kirkpatrick B, Gellad F. Brain Morphology and Schizophrenia: A Magnetic Resonance Imaging Study of Limbic, Prefrontal Cortex, and Caudate Structures. *Arch. Gen. Psychiatry* 49, 921-926 (1992).
  13. Hoffman RE, McGlashan TH. Parallel Distributed Processing and the Emergence of Schizophrenic Symptoms. *Schiz. Bull.* 19, 119-136 (1993).
  14. Sedvall G, Farde L. Chemical Brain Anatomy in Schizophrenia. *Lancet* 346, 743-749 (1995).
  15. Javitt DC, Zukin SR. Recent Advances in the Phencyclidine Model of Schizophrenia. *Am. J. Psychiatry* 148, 1301-1308 (1991).

- 
16. Olney JW, Farber NB. Glutamate Receptor Dysfunction and Schizophrenia. *Arch. Gen. Psychiatry* 52, 998-1007 (1995).
  17. Alexander GE, Crutcher MD, DeLong MR. Basal Ganglia – Thalamocortical Circuits: Parallel Substrates for Motor, Oculomotor, “Prefrontal” and “Limbic” Functions. *Progress in Brain Research* 85, 119-146 (1990).
  18. Tamminga CA, Thaker GK, Buchanan R, Kirkpatrick B, Alphas LD, Chase TN, Carpenter WT. Limbic system abnormalities identified in schizophrenia using positron emission tomography with fluorodeoxyglucose and neocortical alternations with deficit syndrome. *Arch. Gen. Psychiatry* 49, 522-529 (1992).
  19. Benes FM, Sorensen I, Vincent SL, Bird ED. Increased density of glutamate-immunoreactive vertical process in superficial laminae in cingulate cortex of schizophrenic brain. *Cerebral Cortex* 2, 503-512 (1992).
  20. Nishikawa T, Takashima M, Toru M. Increased [<sup>3</sup>H] kainic acid binding in the prefrontal cortex in schizophrenia. *Neuroscience Letters* 40, 245-250 (1983).
  21. Buckley PF, Moore C, Long H, Larkin C, Thompson P, Mulvany F, Redmond O, Stack JP, Ennis JT, Waddington JL. <sup>1</sup>H-Magnetic Resonance Spectroscopy of the Left Temporal and Frontal Lobes in Schizophrenia: Clinical, Neurodevelopmental, and Cognitive Correlates. *Biol. Psychiatry* 36, 792-800 (1994).
  22. Insel TR, Winslow JT. Neurobiology of Obsessive Compulsive Disorder. *Psychiatric Clinics of North America* 15, 813-824 (1992).
  23. Swerdlow NR, Benbow CH, Zisook S, Geyer MA, Braff DL: A preliminary assessment of sensorimotor gating in patients with obsessive compulsive disorder. *Biol. Psychiatry* 33: 298-301 (1993).

- 
24. Tsai G, Coyle JT. *N*-Acetylaspartate in Neuropsychiatric Disorders. *Progress in Neurobiology* 46, 531-540 (1995).
  25. Miller BL. A Review of Chemical Issues in  $^1\text{H}$  NMR Spectroscopy: *N*-Acetyl-L-aspartate, Creatine and Choline. *NMR in Biomedicine* 4, 47-52 (1991).
  26. Pouwels PJ, Frahm J. Differential Distribution of NAA and NAAG in Human Brain as Determined by Quantitative Localized Proton MRS. *NMR in Biomedicine* 10, 73-78 (1997).
  27. Miller BL, Moats RA, Shonk T, Ernst T, Woolley S, Ross BD. Alzheimer Disease: Depiction of Increased Cerebral Myo-Inositol with Proton MR Spectroscopy. *Radiology* 187, 433-437 (1993).
  28. Clarke DD, Sokoloff L. Circulation and Energy Metabolism of the Brain. In: Basic Neurochemistry: Molecular, Cellular, and Medical Aspects: eds Siegel GJ, Agranoff BW, Albers RW, Molinoff PB. *Raven Press*. New York, NY (1994).
  29. Ross BD, Bluml S. New Aspects of Brain Physiology. *NMR in Biomedicine* 9, 279-296 (1996).
  30. Nicholls DG. Release of Glutamate, Aspartate, and  $\gamma$ -Aminobutyric Acid from Isolated Nerve Terminals. *Journal of Neurochemistry* 52, 331-341 (1989).
  31. Erecinska M, Silver IA. Metabolism and Role of Glutamate in Mammalian Brain. *Progress in Neurobiology* 35, 245-296 (1990).
  32. Hamberger AC, Chiang GH, Nysten ES, Scheff SW, Cotman CW. Glutamate as a CNS Transmitter. I. Evaluation of Glucose and Glutamine as Precursors for the Synthesis of Preferentially Released Glutamate. *Brain Research* 168, 513-530 (1979).

- 
33. Behar KL, Rothman DL, Spencer DD, Petroff OAC. Analysis of Macromolecule Resonances in the  $^1\text{H}$  NMR Spectra of Human Brain. *Magn. Reson. Med.* 32, 294-302 (1994).

## Chapter 5

### **Measurement of Glutamate and Glutamine in the Medial Prefrontal Cortex of Never Treated Schizophrenic Patients and Healthy Controls by Proton Magnetic Resonance Spectroscopy<sup>2</sup>**

*By Robert Bartha, Peter C Williamson, Dick J Drost, Ashok Malla, Tom J Carr, Len Cortese, Gita Canaran, R Jane Rylett, Richard WJ Neufeld*

#### **5.0 Introduction**

The medial prefrontal and anterior cingulate cortical regions have been implicated in the pathophysiology of schizophrenia by a number of *in vivo* and post-mortem investigations. Recent in-vivo studies using positron emission tomography (PET) and single photon emission computed tomography (SPECT) have shown decreased cerebral blood flow or glucose uptake in these regions in both medicated and unmedicated schizophrenic patients compared to controls (1,

---

<sup>2</sup> A version of this chapter has been published.

**Bartha R, Williamson PC, Drost DJ, Malla A, Carr TJ, Cortese L, Canaran G, Rylett RJ, Neufeld RWJ. Measurement of Glutamate and Glutamine in the Medial Prefrontal Cortex of Never Treated Schizophrenic Patients and Healthy Controls by Proton Magnetic Resonance Spectroscopy. *Archives of General Psychiatry*, October 1997, 54: 959-965.**

Copyright: 1997, American Medical Association.

2, 3, 4, 5, 6). Other investigators have reported deficits only for patients with negative symptoms (7, 8) or have failed to confirm these findings (9, 10).

Increased cerebral blood flow in the right anterior cingulate cortex has also been observed in schizophrenic patients (11) with PET in association with verbal reports of auditory hallucinations.

Post-mortem studies of schizophrenic brains have found abnormalities in cell populations including increased glutamate-immunoreactive vertical axons and decreased small interneurons and neurons (12, 13). Other post-mortem studies have found conflicting evidence implicating glutamatergic function in schizophrenia. For example, studies have shown increased kainate receptor binding (14) (Brodmann's areas 9 and 10), decreased prefrontal glutamate (Glu) levels and N-acetyl- $\alpha$ -linked-acidic dipeptidase activity, and increased prefrontal N-acetylaspartyl-glutamate (NAAG) (15) suggesting reduced glutamatergic activity in schizophrenics, while other findings of increased binding of D-[ $^3\text{H}$ ] aspartate to glutamate uptake sites and [ $^3\text{H}$ ] kainate to postsynaptic glutamate receptors (16) suggest an overabundant glutamatergic innervation in the same region.

The medial prefrontal cortex and anterior cingulate regions receive glutamatergic afferents from the thalamus as well as other cortical regions which have also been implicated in schizophrenia (17). Therefore, it would be of interest to examine levels of glutamate and its metabolites in the medial prefrontal region (including anterior cingulate) of living patients. Levels of Glu and metabolites such as glutamine (Gln), NAAG, and aspartate (Asp) can be measured simultaneously in-vivo using short echo  $^1\text{H}$  magnetic resonance spectroscopy

(MRS) (18, 19, 20), which is not possible with PET or SPECT. Abnormalities in Gln have been observed with in-vivo short echo  $^1\text{H}$  MRS in other diseases (21, 22). An earlier  $^1\text{H}$  MRS study of the dorsolateral prefrontal region by our group found increased Gln levels in chronic but not in never-treated schizophrenic patients compared to controls (23). However, a decrease in Gln was observed in these patients after neuroleptic therapy. As Gln is a precursor of the neurotransmitter Glu, this decrease in Gln suggests increased levels of glutamate available for neurotransmission after treatment with neuroleptics.

We hypothesised that in the medial prefrontal and anterior cingulate region (including portions of Brodmann's areas 24, 32, and 9), schizophrenic patients would show altered metabolite levels suggesting decreased glutamatergic activity compared to controls. In this study, we report preliminary short echo  $^1\text{H}$  MRS medial prefrontal (including anterior cingulate) findings in ten never-treated schizophrenic patients compared to ten healthy controls of comparable age, sex, handedness, education and parental education levels.

## **5.1 Method**

### **5.1.1 Subjects**

Fourteen never treated, first episode schizophrenic patients and ten control subjects participated in the study which was approved by the Review Board for Health Sciences Research Involving Human Subjects of the University of Western Ontario. Patients were referred for evaluation by their treating psychiatrist in the community who was aware of the study. All participants gave



their informed written consent. However, two subjects withdrew consent during the study and were not included. One patient was excluded due to the acquisition of data which was of insufficient quality for accurate quantification. Another was excluded because of the discovery of a large temporal lobe cyst on clinical MRI. Eight of the remaining ten were in-patients and two were out-patients. None of these patients participated in our previous study (23). Clinical information for subjects is provided in Table 5-1. Subject classification as schizophrenic patient (DSM-III-R criteria) or control was established by a psychiatrist (P.W.) and a psychometrist (G.C.) using the Structured Clinical Interview for DSM-III-R (SCID) (24). Both interviewers had to agree with the diagnosis for the subject to be included. Six were classified as paranoid, and four as undifferentiated subtype. A follow-up SCID interview six months after the study by a psychiatrist (P.W.) confirmed the diagnosis of schizophrenia in eight patients (one had committed suicide and one could not be located). Along with the SCID, schizophrenic patients were also evaluated immediately prior to the imaging procedure by a psychiatrist (P.W.) using the Scale for the Assessment of Negative Symptoms (SANS) (25) and the Scale for the Assessment of Positive Symptoms (SAPS) (26), based on symptoms experienced over the previous week.

<b>Group</b>	<b>Controls</b>	<b>Never-treated Schizophrenics</b>
	<b>(N = 10)</b>	<b>(N = 10)</b>
<b>Age (years)</b>	26.3 ± 6.4	24.4 ± 5.1
<b>Gender</b>	8 Male, 2 Female	8 Male, 2 Female
<b>Hand</b>	9 Right, 1 Left	10 Right
<b>Education Level</b>	2.7 ± 0.7	2.7 ± 0.9
<b>Parental Education Level</b>	3.0 ± 0.8	2.5 ± 0.9
<b>SANS</b>	n/a	32.2 ± 16.0
<b>SAPS</b>	n/a	24.4 ± 9.5

**Table 5-1: Subject Characteristics**

Except for gender and hand, demographic data is given as mean ± standard deviation. N represents the number of participants in each group; SANS is Scale for the Assessment of Negative Symptoms (25); SAPS is Scale for the Assessment of Positive Symptoms (26). The age was that at time of MR spectroscopy examination. Handedness was rated by a questionnaire (27). Education levels are rated as 1, ≤ grade 10; 2, grade 11 to grade 13; 3, 1 to 3 years of college; 4, > 3 years of college.

Schizophrenic patients ranged in age from 17 - 33 years with an average age of 24 ± 5 years. Eight of ten schizophrenic patients experienced their first positive symptoms one year or less before imaging. One schizophrenic patient had positive symptoms for seventeen months before imaging. One heard voices occasionally for seven years but did not develop other symptoms of

schizophrenia until three months before imaging. Six schizophrenic patients received between 1 and 4 mg of lorazepam in the 24 hours before scanning. None of these subjects had been exposed to any antipsychotic medication prior to the MR exam. The education level of each subject was rated on a four point scale (1,  $\leq$  grade 10; 2, grade 11 - 13; 3, 1-3 years of college or university; 4,  $\geq$  4 years of college or university). Parental education ratings were also evaluated as above for the most educated parent. The handedness of each subject was defined by a handedness questionnaire (27).

Ten control subjects were chosen from a pool of subjects recruited by advertisement. Subjects were chosen to minimize demographic differences between the patient and control groups (Table 5-1). The criteria used included gender, age, education, parental education, and handedness assessed in the same manner as for patients. A SCID interview was also conducted on each control by the same two interviewers who conducted patient interviews; the absence of psychiatric symptoms in these subjects was confirmed by consensus. Five control subjects had participated in previous studies which included a magnetic resonance imaging (MRI) and MRS exam.

No patients or controls had a history of head injury, drug or alcohol abuse, or serious medical illness based on the information provided during the SCID interview. As part of the MR study, routine clinical images were collected and viewed by a radiologist (T.C.) who detected no gross abnormalities on any scans of the twenty subjects who were included in the data analysis.

### 5.1.2 $^1\text{H}$ MR Spectroscopy

Each subject was positioned within a Siemens SP4000 Helicon 1.5 Tesla whole body MR imager and taped under the chin and across the forehead to reduce motion. The same Siemens circularly polarized head coil was used to obtain all images and spectra. Every study began with an iterative computer algorithm (28) that directly set the currents in 12 resistive shim coils to improve magnetic field homogeneity over the entire head and thereby improve spectral quality. A series of sagittal and coronal images were then acquired for placing a  $15 \times 15 \times 20 \text{ mm}^3$  volume of interest (VOI) in the medial prefrontal region of the brain (Figure 5-1). In Talairach co-ordinates (29), the VOI was placed to lie within the region between  $x = 0$  to  $-15$ ,  $y = 30$  to  $50$ , and  $z = 0$  to  $20$ . This volume encompassed parts of Brodmann's areas 24, 32, and 9. After placing the VOI, a STEAM (30) localized manual shim was done to further increase magnetic field homogeneity within the VOI. Both water suppressed (31) and water unsuppressed spectroscopy data were acquired using a STEAM sequence (TR=1500 ms, TE=20 ms, TM=30 ms, 4096 points, 250  $\mu\text{s}$  dwell time, 550 and 30 suppressed and unsuppressed averages respectively).

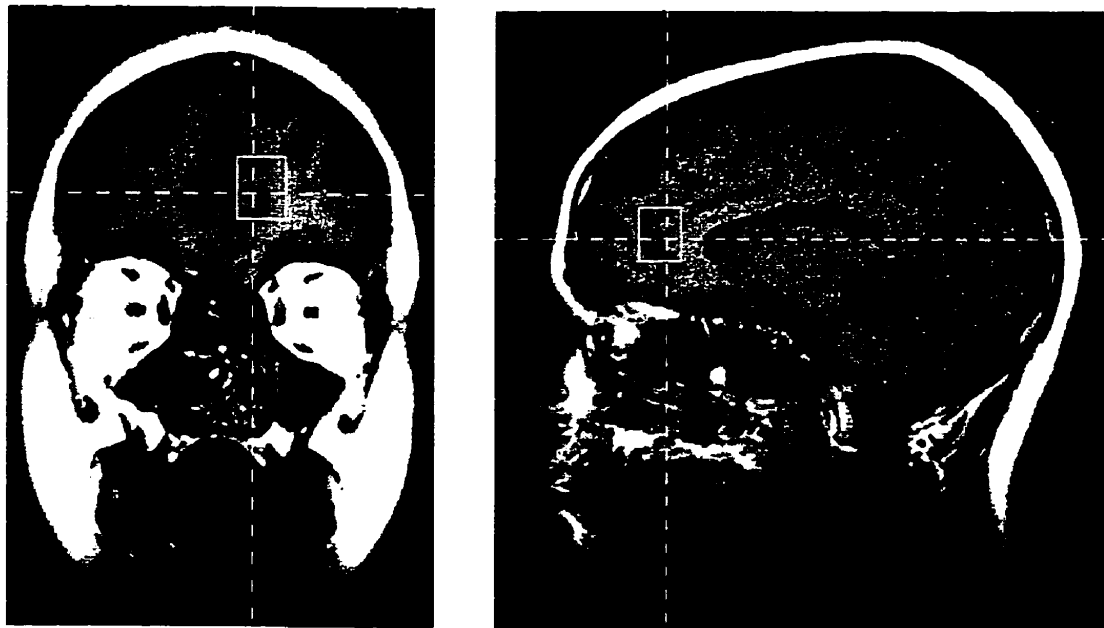


### Figure 5-1: Coronal and Sagittal Localizer Images

Coronal (a) and Sagittal (b)  $^1\text{H}$  MR images showing the placement of the volume of interest (VOI) in one subject. The  $15 \times 15 \times 20 \text{ mm}^3$  VOI is outlined by a white box positioned in the left medial prefrontal cortex and anterior cingulate regions (Brodmann areas and Talairach coordinates are specified in the text). The vertical dotted line in the coronal image gives the position of the sagittal slice. The vertical dotted line in the sagittal image gives the position of the coronal slice. The horizontal lines in both images give the position of a transverse slice also used for positioning but not shown here.

#### 5.1.3 Spectral Processing

All spectra were processed identically without operator interaction using our own software (32). Each spectrum was eddy current corrected (33), using the water unsuppressed spectrum as a reference. Residual water was then subtracted

using the results of an initial fit of the data in the time domain (34) (0.0 - 0.512 seconds) using a singular value decomposition algorithm, HLSVD (35). The resulting spectrum was then fit in the time domain (0.0 - 0.512 seconds) using a non-linear Marquardt algorithm (36) to a complete spectrum model composed of twelve metabolites (18, 19, 20) and three macromolecules (37) with resonances between 1.9 ppm and 3.5 ppm. The metabolites *N*-acetyl-aspartate (NAA), glutamate (Glu), glutamine (Gln),  $\gamma$ -aminobutyric acid (GABA), taurine (Tau), myo-inositol (Myo), glucose (Glc), aspartate (Asp), *N*-acetylaspartyl-glutamate (NAAG), phosphocreatine + creatine (PCr + Cr), choline containing compounds including mostly phosphorylcholine, glycerophosphorylcholine, and free choline (20, 38) (Cho), and scyllo-inositol (Syl) were all modeled with exponentially damped sinusoids. Macromolecule resonances at 3.00 ppm (M 3.00), 2.29 ppm (M 2.29), and 2.05 ppm (M 2.05) (37) were modeled with Gaussian damped sinusoids. The full width half maximum (FWHM) of these macromolecule peaks was fixed at 24 Hz. Six resonances with shifts < 1.9 ppm and four resonances with shifts > 3.5 ppm were included in the spectrum model to account for minor baseline distortions and resonances adjacent to our spectral region of interest (1.9 - 3.5 ppm with  $\text{NAA}_{\text{CH}_3}$  referenced to 2.01 ppm). These ten resonances were unrestricted in amplitude, shift, width, and phase, and independent of the modeled metabolites except in delay time which was linked.

By adjusting the amplitude parameters of each metabolite as well as the overall width, shift, zero order phase, and delay time, the computer fitting algorithm minimized the difference between the complete spectrum model and the original data. Metabolite amplitudes were then scaled by the total NMR visible water (39) obtained from the unsuppressed water spectrum (corrected for 3% cerebral

spinal fluid (18) (CSF)), and the approximate concentration of water in the VOI ( $[H_2O] = 55.12 \text{ mM/ml}$ , corrected for 41 % gray matter and 56 % white matter) (18), to yield relative metabolite levels in arbitrary units. This measure represents the average metabolite level in the volume studied uncorrected for the NMR relaxation parameters  $T_1$  and  $T_2$  (since these parameters are unavailable for each metabolite in each individual).

#### 5.1.4 Statistical Analysis

All statistical tests were performed using SPSS (SPSS Inc.) release 6.0 (40). The subject characteristics age, education level, and parental education were comparable between subject groups according to a two tailed t-test ( $p > 0.10$ ). These variables were covariates for all statistical comparisons to reduce the extraneous variance in error terms, without removing genuine group effects (41, 42).

Although there were twelve metabolites and three macromolecules modeled for each data set, some metabolites and macromolecules had very large standard deviations. Therefore, we decided that only metabolites and macromolecules with CV of less than 75 % should be included in between group comparisons. As Glu and Gln comprised the focus of hypothesized differences, values of these metabolites were compared using analysis of covariance (ANCOVA); the remaining metabolites were compared using multivariate analysis of covariance (MANCOVA).  $P$ -values of  $\leq 0.05$  were considered statistically significant.

To establish if estimated metabolite levels were correlated (due to physiology or quantification artifact), bivariate correlations were made between all metabolites included in the analysis as well as between each metabolite and the SANS and SAPS scores for the schizophrenic patients. These correlations were carried out on each subject group independently. *P*-values for significance were determined using a Bonferroni based correction (42, 43) as no prior hypotheses were made.

## **5.2 Results**

A typical spectrum (after water removal) from one subject is shown in Figure 5-2. It is displayed in the frequency domain after Fourier transform although all quantification was done in the time domain. Metabolite components are shown in the following order. The first line shows NAA (*N*-acetyl-aspartate, solid), PCr + Cr (phosphocreatine and creatine, dotted), and Cho (choline containing compounds, dashed). The second line shows NAAG (*N*-acetyl-aspartyl-glutamate, solid), Glu (glutamate, dashed), and Glc (glucose, dotted). The third line shows Gln (glutamine, solid), Asp (aspartate, dashed), Tau (taurine, dotted). The fourth line shows GABA ( $\gamma$ -amino-butyric acid, solid), Myo (myo-inositol, dashed), and Syl (scyllo-inositol, dotted). The fifth line shows the macromolecules, while the sixth line shows the resonances fit outside the spectral region of interest (<1.9 ppm and > 3.5 ppm). The average SNR (32) for all data prior to preprocessing was  $20 \pm 5 : 1$ . The average FWHM of the unsuppressed water spectra was  $5.74 \pm 1.02$  Hz.



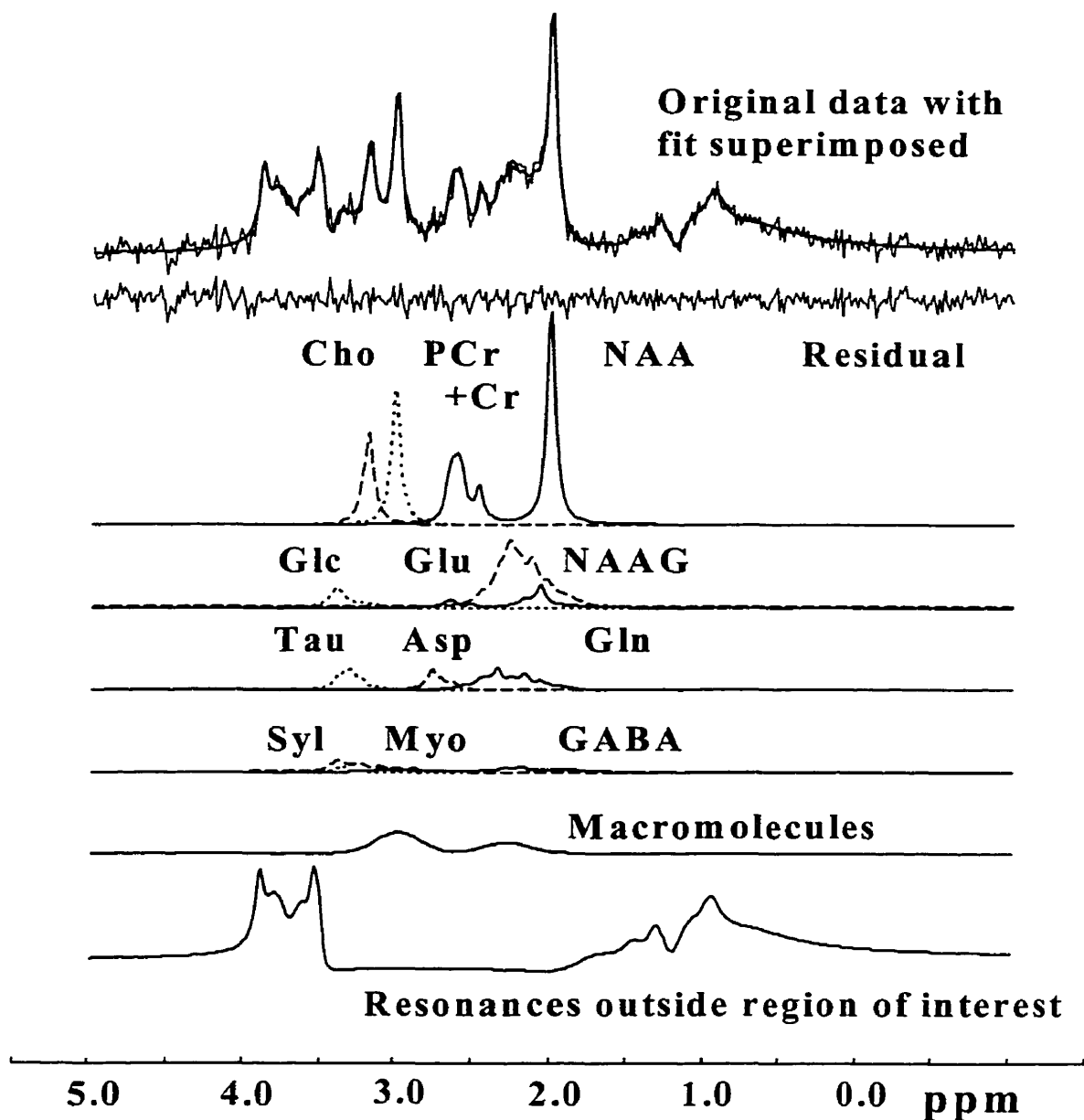


**Figure 5-2: In-vivo Spectrum and Components from Left Medial Prefrontal Cortex**

Typical in vivo  $^1\text{H}$  data is shown after water subtraction in top trace (light line) with corresponding fit result superimposed (dark line). The difference between the two is shown beneath (residual). The individual metabolite components (described within the text) are displayed beneath the residual. This spectrum was fit in the time domain but is shown in the frequency domain for interpretation.

Five of the twelve quantified metabolites (NAA, Glu, Gln, PCr + Cr, and Cho ) had CVs less than 75 % and were included in the statistical analysis. Figure 5-3 shows the average estimated metabolite levels  $\pm$  standard deviation for each group. These metabolite levels represent average resting levels from the entire volume under investigation and are uncorrected for the NMR relaxation parameters  $T_1$  and  $T_2$ , or changes in CSF, gray matter, and white matter ratios.

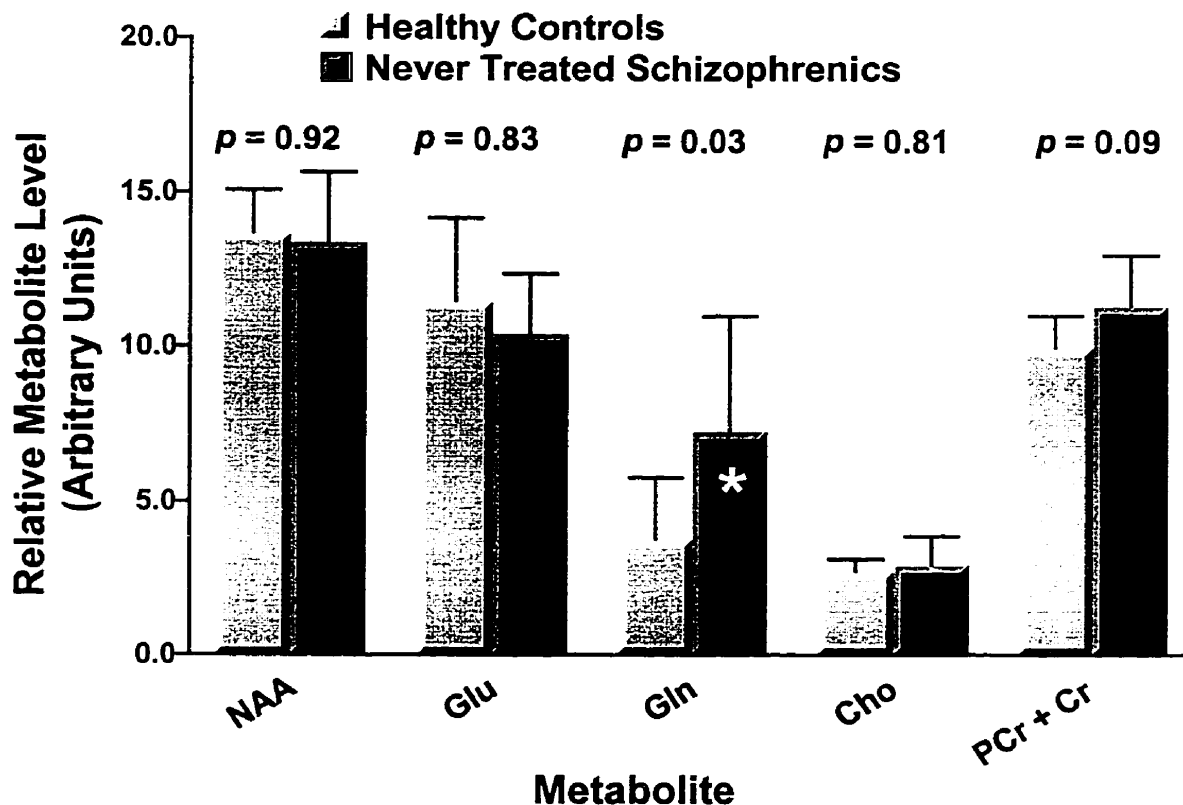


**Figure 5-3: Mean Metabolite Levels**

Mean metabolite levels are given in arbitrary units after normalization to total NMR visible water for the medial prefrontal cortex (encompassing portions of Brodmann's areas 24, 32, and 9) of healthy control subjects (N=10) and never treated schizophrenic patients (N=10). Errors represent  $\pm$  one standard deviation. NAA represents N-acetyl-aspartate, Glu represents glutamate, Gln represents glutamine, Cho represents choline containing compounds (phosphorylcholine, glycerophosphorylcholine, and free choline (20, 38)), and PCr + Cr represents phosphocreatine and creatine. Single asterisks mark statistically significant ANCOVA's ( $p$  values shown on plot), covariates comprising age, education, and parental education.

A significant increase was observed in the level of Gln among never treated schizophrenic patients as compared to controls ( $7.2 \pm 3.7$  vs.  $3.7 \pm 2.0$  arbitrary units,  $N=10$ ,  $DF=15$ ,  $F=6.1$ ,  $p = 0.026$ ), while no differences were observed in Glu. The MANCOVA on the three remaining metabolites did not show a statistically significant difference between never treated schizophrenic patients and controls ( $p = 0.420$ ). The ANCOVA's on individual metabolite groups gave the  $p$ -values shown in Figure 5-3. Never treated schizophrenics showed a trend towards higher PCr + Cr levels ( $11.3 \pm 1.7$  vs.  $9.9 \pm 1.1$  arbitrary units,  $N=10$ ,  $DF=15$ ,  $F=3.4$ ,  $p = 0.085$ ) compared with controls. Patients on ( $N = 6$ ) and off ( $N = 4$ ) lorazepam had Gln levels of  $6.0 \pm 4.1$  and  $9.1 \pm 2.5$  arbitrary units respectively, and PCr + Cr levels of  $10.9 \pm 1.7$  and  $11.9 \pm 1.7$  arbitrary units respectively. These metabolite levels were not significantly different between patients on and off lorazepam using a 2-tailed t-test ( $p=0.21$  and  $p=0.40$  for Gln and PCr + Cr respectively; the power of this test was necessarily low, but the *direction* of differences was contrary to lorazepam being the agent of elevated patient values).

Bivariate correlations between measured metabolites and clinical symptoms (SANS (25) and SAPS (26)) were done separately for healthy controls and never treated schizophrenic patients.  $P$ -values  $< 0.020$  and  $< 0.014$  were considered statistically significant for the healthy control and never treated schizophrenic groups respectively. One significant positive correlation was found between the metabolites Gln and Cho in the control group ( $r = 0.753$ ,  $p = 0.012$ ). Pearson correlation coefficients for the correlation of clinical symptoms with metabolite levels are summarized in Table 5-2. No significant correlations were found between estimated metabolite levels and SANS scores. SAPS scores correlated

negatively with NAA levels ( $p = 0.016$ ) however, this correlation was not significant after Bonferroni correction.

Metabolite	SANS	SAPS
	Pearson Correlation	Pearson Correlation
NAA	0.304	-0.730*
Glu	0.358	0.104
Gln	-0.261	-0.507
Cho	-0.334	-0.037
PCr + Cr	-0.345	0.181

\*  $p = 0.016$ , not significant after Bonferroni-based correction

### Table 5-2: Metabolite Correlations with Symptom Scores

The following abbreviations are used in Table 5-2: SANS represents the Scale for the assessment of negative symptoms (25), SAPS represents the Scale for the assessment of positive symptoms (26), NAA represents *N*-acetyl-aspartate, Glu represents glutamate, Gln represents glutamine, Cho represents choline containing compounds (phosphorylcholine, glycerophosphorylcholine, and free choline (20, 38)), PCr + Cr represents phosphocreatine + creatine. Correlations were performed based on the results from all 10 never treated schizophrenic subjects. The significance of all correlations were above the 0.05 level except the correlation of NAA with SAPS ( $p = 0.016$ ). However, this was not significant after Bonferroni based correction.

### 5.3 Comment

Although these results must be considered preliminary, this study showed a significant glutamine increase in the medial prefrontal cortex (encompassing

portions of Brodmann's areas 24, 32, and 9) of never treated schizophrenic patients compared to healthy controls. It has been estimated that 80% of stimulus released glutamate is derived from glutamine (44). In this cycle, stimulus released glutamate is taken up by astrocytes and converted to glutamine which is transported back to the presynaptic neuron and reconverted to glutamate (45, 46). This small neurotransmitter pool of glutamate does not equilibrate quickly with a larger pool of cellular glutamate (44, 47).

Our observation of increased glutamine in schizophrenic patients may indicate an abnormality in the cycle of conversion of glutamine to glutamate. This would decrease the glutamate available for signal transduction while the overall level of glutamate would appear unchanged since the larger pool of cellular glutamate is unaltered. Thus, higher glutamine levels could suggest decreased glutamatergic activity in the medial prefrontal region of schizophrenic patients. Conversely, increased glutamine could indicate increased glutamatergic activity in keeping with increased D- $^3\text{H}$  aspartate binding (16) (although caution must be taken when comparing the results of this study to previous postmortem studies, since the volume studied here includes several distinct regions of cortex). This possibility seems unlikely as most functional imaging studies have shown decreased metabolic activity in this region (1, 2, 3, 4, 5, 6) and the increase in receptor sites found on post-mortem analysis could be interpreted as a compensatory effect of decreased glutamatergic activity. Increased glial cell volumes could also account for increased glutamine levels in schizophrenic subjects since  $^1\text{H}$  MRS measures glutamine for both neurons and glial cells (48), but recent post-mortem studies have not found increased glial cell volumes in the prefrontal cortex (49).

As some patients received lorazepam in the 24 hours before assessment, there is a possibility that this medication could have affected glutamine levels in patients, accounting for the difference from controls. However, this does not appear to be the case as glutamine levels tended to be lower in the patients who had received lorazepam compared to the patients who had not received lorazepam.

If the finding of increased glutamine levels reflects decreased glutamatergic activity, this would be consistent with N-methyl-D-aspartate (NMDA) receptor hypofunction which has been hypothesized in schizophrenia (50, 51). Olney and Farber (50) suggest that any mechanism that impairs the functional status of NMDA receptors of GABAergic neurons could result in widespread damage to the limbic system. This damage would be expected to be associated with decreased NAA levels in the medial prefrontal region in keeping with reports of decreased NAA levels in the temporal regions of schizophrenic patients (52, 53). No differences were observed but neuronal loss by this process could be subtle and not detectable by this technique. Differences in levels of  $\gamma$ -aminobutyric acid cannot be ruled out as this metabolite is poorly resolved at this field strength.

The anterior cingulate cortex receives inputs from many parts of the brain so it is impossible to determine the origin of glutamatergic projections which could account for the increase in glutamine in patients. However, it is of note that the anterior cingulate cortex receives glutamatergic afferents from the thalamus via basal ganglia-thalamocortical pathways (54, 55). It is possible that excitatory glutamatergic thalamic afferents to the anterior cingulate and medio-orbital cortex

could be damaged early in brain development. Early neurodevelopmental lesions to the mediodorsal thalamus (56) or ventral hippocampus (57) in rats results in behaviors associated with dopaminergic supersensitivity in the nucleus accumbens at maturity, by a mechanism likely involving glutamatergic afferents to the medial prefrontal region. Our findings of increased glutamine in never-treated patients could result from either type of neurodevelopmental lesion.

$^1\text{H}$  MRS measures total PCr + Cr (58) although the ratio of PCr:Cr is close to 1:1 in the brain (20). The trend towards an increase in PCr levels in never treated schizophrenics could be the result of an increase in PCr or Cr. The trend to increased PCr + Cr levels could indicate reduced metabolic activity which has been demonstrated with functional imaging studies (1, 2, 3, 4, 5, 6) since PCr is an energy reserve used to produce ATP. However, measurements of PCr with  $^{31}\text{P}$  magnetic resonance spectroscopy have not shown increased PCr levels in never treated schizophrenic patients in frontal regions (59, 60, 61). Buckley *et al* (62), the only other  $^1\text{H}$  MRS study in the prefrontal region that we are aware of, did not find differences in PCr + Cr levels between schizophrenic patients and controls. However, differences in patient medications, brain region studied, data acquisition parameters, and quantification technique, makes it difficult to compare these results with those presented here.

Increased Gln and PCr + Cr levels in never-treated schizophrenic patients would be expected to be associated with functional deficits in the cingulate cortex. This region is believed to be important in the regulation of affect, motivation, selective attention, social interactiveness, and rational thought processes, functions which are impaired in schizophrenic patients (63). Although none of the metabolite



levels were significantly correlated with symptom scores, SAPS scores were inversely correlated with NAA levels before Bonferroni correction. While NAA levels did not differ between groups in this study, patients with positive symptoms may have a change in neuronal integrity in this region reflected in NAA levels. However, a larger study is necessary to confirm this correlation.

### 5.3.1 Limitations

Although the volume used was small ( $4.5 \text{ cm}^3$ ) and positioning was done with the aid of images to place the volume in gray matter, there was still a significant amount of white matter present in each volume which could decrease the sensitivity of measurements. To exclude partial volume effects as the cause of metabolite level changes, the partial volume must be equal in controls and schizophrenics. Studies comparing metabolite levels in gray and white matter have generally shown increased PCr + Cr and Glu, and decreased Cho levels in gray matter compared to white matter (18, 20, 38). Although a trend towards increased PCr + Cr levels was observed, this increase was not accompanied by a corresponding increase in Glu, and decrease in Cho. Therefore, it is unlikely that the changes reported here are the result of increased gray matter in the schizophrenic volume.

Changes in NMR relaxation properties can not be ruled out as the cause for increased glutamine levels. For example, decreased  $T_1$  or increased  $T_2$  relaxation for glutamine would result in an increased level of this metabolite in the spectrum. However, this would still indicate an abnormality related to glutamine and implicate glutamatergic transmission in this brain region. Altered water

relaxation would cause a change in all metabolite levels, not a specific increase in glutamine level.

The inclusion of prior knowledge reduced the uncertainty of metabolite level estimates, but the overlapping resonances in the region of the spectrum containing Glu, Gln, and GABA were difficult to resolve. This lack of resolution lead to metabolite estimates with high standard deviations for some metabolites (i.e. ~ 53% for Gln); although the standard deviations of other metabolites (NAA ~14%, Glu ~21%) were comparable to those obtained from post-mortem analysis (NAA ~20%, Glu ~40%) (15) and larger volume spectroscopy studies (NAA+NAAG ~9%, Glu ~14%) (19). Future studies may show more pronounced results due to improvements in equipment and quantification which lead to decreased metabolite standard deviations. Although one positive correlation between Gln and Cho was observed in the control group, the lack of negative correlations between Gln and any other metabolite, as well as PCr + Cr and any other metabolite in either subject group suggests that the changes seen in these metabolites are not the result of misfitting one or more of the other metabolites.

#### **5.4 Conclusion**

Increased levels of glutamine were observed in the medial prefrontal and anterior cingulate regions (including Brodmann's areas 24, 32, and 9) of never treated schizophrenic patients compared to controls. These findings most likely reflect reduced glutamatergic activity in this part of the brain in schizophrenic patients.

## 5.5 References

---

1. Tamminga CA, Thaker GK, Buchanan R, Kirkpatrick B, Alphas LD, Chase TN, Carpenter WT. Limbic system abnormalities identified in schizophrenia using positron emission tomography with fluorodeoxyglucose and neocortical alternations with deficit syndrome. *Arch. Gen. Psychiatry* 49, 522-529 (1992).
2. Ebmeier KP, Blackwood DHR, Murray C, Souza V, Walker M, Dougall N, Moffoot APR, O'Carroll RE, Goodwin GM. Single-photon emission computed tomography with  $^{99m}\text{Tc}$  exametazime in unmedicated schizophrenic patients. *Biol. Psychiatry* 33, 487-495 (1993).
3. Kawasaki Y, Maeda Y, Suzuki M, Urata K, Higaskima M, Kiba K, Yamaguchi N, Matsuda H, Hisada K. SPECT analysis of regional cerebral blood flow changes in patients with schizophrenia during the Wisconsin Card Sorting Test. *Schiz. Res.* 10, 109-116 (1993).
4. Siegel BV, Buchsbaum MS, Bunney WE, Gottschalk LA, Haier RJ, Lohr JB, Lottenberg S, Najafi A, Nuechterlein KH, Potkin SG, Wu JC. Cortical-striatalthalamic circuits and brain glucose metabolic activity in 70 unmedicated male schizophrenic patients. *Am. J. Psychiatry*. 150, 1325-1336 (1993).
5. Ebmeier KP, Lawrie SM, Blackwood DHR, Johnstone EC, Goodwin GM. Hypofrontality revisited: a high resolution single photon emission computed tomography study in schizophrenia. *J. Neurol. Neurosurg. Psychiatry* 58, 452-456 (1995).
6. Dolan RJ, Fletcher P, Frith CD, Friston KJ, Frackowiak RSJ, Grasby PM. Dopaminergic modulation of impaired cognitive activation in the anterior

- 
- cingulate cortex in schizophrenia. *Nature* 378, 180-194 (1995). Letter to the Editor.
7. Liddle PF, Friston KJ, Frith CD, Hirsch SR, Jones T, Frackowiak SJ. Patterns of cerebral blood flow in schizophrenia. *Brit. J. Psychiatry* 160, 179-186 (1992).
  8. Andreasen NC, Rezai K, Alliger R, Swayze VW, Flaum M, Kirchner P, Cohen G, O'Leary DS. Hypofrontality in neuroleptic-naïve patients and in patients with chronic schizophrenia. *Arch. Gen. Psychiatry* 49, 943-958 (1992).
  9. Gur RE, Mozley D, Resnick SM, Harper Mozley L, Shtasl DL, Gallacher F, Arnold SE, Karp JS, Alavi A, Reivich M, Gur RC. Resting cerebral glucose metabolism in first-episode and previously treated patients with schizophrenia relates to clinical features. *Arch. Gen. Psychiatry* 52, 657-667 (1995).
  10. Frith CD, Friston KJ, Herold S, Silbersweig D, Fletcher P, Cahill C, Dolan RJ, Frackowiak RSJ, Liddle PF. Regional brain activity in chronic schizophrenic patients during the performance of a verbal fluency task. *Brit. J. Psychiatry* 167, 343-349 (1995).
  11. Silbersweig DA, Stern E, Frith C, Cahill C, Holmes A, Grootenk S, Seaward J, McKenna P, Chua SE, Schnorr L, Jones T, Frackowiak RSJ. A functional neuroanatomy of hallucinations in schizophrenia. *Nature* 378, 176-179 (1995). Letter to the Editor.
  12. Benes FM, Sorensen I, Vincent SL, Bird ED. Increased density of glutamate-immunoreactive vertical process in superficial laminae in cingulate cortex of schizophrenic brain. *Cerebral Cortex* 2, 503-512 (1992).

- 
13. Benes FM, McSparren J, Bird ED, SanGiovanni JP, Vincent SL. Deficits in small interneurons in prefrontal and cingulate cortices of schizophrenic and schizoaffective patients. *Arch. Gen. Psychiatry* 48, 996-1001 (1991).
  14. Nishikawa T, Takashima M, Toru M. Increased [<sup>3</sup>H] kainic acid binding in the prefrontal cortex in schizophrenia. *Neuroscience Letters* 40, 245-250 (1983).
  15. Tsai G, Passani LA, Slusher BS, Carter R, Baer L, Kleinman JE, Coyle JT. Abnormal excitatory neurotransmitter metabolism in schizophrenic brains. *Arch. Gen. Psychiatry* 52, 829-836 (1995).
  16. Deakin JFW, Slater P, Simpson MDC, Gilchrist AC, Skan WJ, Royston MC, Reynolds GP, Cross AJ. Frontal cortical and left temporal glutamatergic dysfunction in schizophrenia. *J. Neurochem.* 52, 1781-1786 (1989).
  17. Vogt BA. Structural organization of cingulate cortex: areas, neurons, and somatodendritic transmitter receptors. In: Vogt BA, Gabriel M, eds. *Neurobiology of Cingulate Cortex and Limbic Thalamus*. Boston, USA: Birkhauser, 19-70 (1993).
  18. Stanley JA, Drost DJ, Williamson PC, Thompson RT. The use of *a priori* knowledge to quantify short echo in vivo <sup>1</sup>H MR spectra. *Magn. Reson. Medicine* 34, 17-24 (1995).
  19. Provencher SW. Estimation of metabolite concentrations from localized *in-vivo* proton NMR spectra. *Magn. Reson. Medicine* 30, 672-679 (1994).
  20. Michaelis T, Merboldt K, Bruhn H, Hanicke W, Frahm J. Absolute concentrations of metabolites in the adult human brain in vivo: quantification of localized proton MR spectra. *Radiology* 187, 219-227 (1993).
  21. Ernst T, Ross BD, Flores R. Cerebral MRS in infants with suspected Reyes syndrome. *The Lancet* 340, 486 (1992).

- 
22. Kreis R, Ross BD, Farrow NA, Ackerman Z. Metabolic disorders of the brain in chronic hepatic encephalopathy detected with H-1 MR spectroscopy. *Neuroradiology* 182, 19-27 (1992).
  23. Stanley JA, Williamson PC, Drost D J, Rylett J, Carr T, Malla A, Thompson RT. An In vivo proton magnetic resonance spectroscopy study of schizophrenic patients. *Schizophrenia Bull.* 22, 597-609 (1996).
  24. Spitzer R, and Williams J, Structured Clinical Interview for DSM-III-R. New York: New York Psychiatric Institute (1985).
  25. Andreasen, N. Scale for the Assessment of Negative Symptoms (SANS). Iowa City: The University of Iowa (1994).
  26. Andreasen, N. Scale for the Assessment of Positive Symptoms (SAPS). Iowa City: The University of Iowa (1994).
  27. Bryden P. Measuring handedness with questionnaires. *Neuropsychologia* 15:617-624 (1977).
  28. Liu Z, Javaid T, Hu J, Brown TR, CSI - Autoshim procedures for body and surface coil. Proceedings of the Society of Magnetic Resonance 2<sup>nd</sup> Annual Meeting, San Francisco, CA , USA. 1174 (1994). Abstract.
  29. Talairach J, Tournoux P. Co-Planar Stereotaxic Atlas of the Human Brain. New York, NY, USA: Thieme Medical Publishers Inc (1988).
  30. Frahm J, Merboldt KD, Hanicke W. Localized proton spectroscopy using stimulated echoes. *J. Mag. Res.* 72, 502-508 (1987).
  31. Frahm J, Michaelis T, Merboldt KD, Bruhn H, Gyngell ML, Hanicke W. Improvements in localized proton NMR spectroscopy of human brain. Water suppression, short echo times, and 1 ml resolution. *J Mag Res.* 90, 464-473 (1990).

- 
32. Bartha R, Drost DJ, Stanley J, Williamson PC. A comparison between time and frequency domain quantification of short echo  $^1\text{H}$  MR spectra. Proceeding of the 3<sup>rd</sup> Society of Magnetic Resonance Meeting, Nice France 1946 (1995). Abstract
  33. Klose U. In vivo proton spectroscopy in presence of eddy currents. *Magn. Reson. Medicine* 14, 26-30 (1990).
  34. de Beer R, van Ormondt D. Analysis of data using time domain fitting procedures. *NMR Basic Principles and Progress* 26, 201-248 (1992).
  35. van den Boogaart A, Ala-Korpela M, Jokisaari J, Griffiths JR. Time and frequency domain analysis of NMR data compared: an application to 1D  $^1\text{H}$  spectra of lipoproteins. *Magn. Reson. Medicine*. 31, 347-358 (1994).
  36. Marquardt DW. An Algorithm for least-squares estimations of non-linear parameters. *J. Soc. Indust. Appl. Math* 11, 431-441 (1963).
  37. Behar KL, Rothman DL, Spencer DD, Petroff OAC. Analysis of macromolecule resonances in  $^1\text{H}$  NMR spectra of human brain. *Magn. Reson. Medicine* 32, 294-302 (1994).
  38. Ross B, Michaelis T. Clinical applications of magnetic resonance spectroscopy. *Mag. Res. Quarterly* 10, 191-247 (1994).
  39. Christiansen P, Henriksen O, Stubgaard M, Gideon P, Larsson HBW. In vivo quantification of brain metabolites by 1H-MRS using water as an internal standard. *Magn. Reson. Imaging* 11, 107-118 (1993).
  40. SPSS for Windows: Release 6.0. SPSS Inc, (1993).
  41. Cochran WG. Analysis of covariance: its nature and uses. *Biometrics* 13, 261-281 (1957).

- 
42. Lees MC, Neufeld RWJ. Matching the limits of clinical inference to the limits of quantitative methods: A formal appeal to practice what we persistently preach. *Canadian Psychology* 35, 268-282 (1994).
  43. Larzelere RE, Mulaik SA. Single sample tests for many comparisons. *Psychol. Bul.* 4: 557 – 569 (1977).
  44. Bradford HF, Ward HK, Thomas AJ. Glutamine - a major substrate for nerve endings. *J. Neurochem.* 30, 1453–1459 (1978).
  45. Erecinska M, Silver IA. Metabolism and role of glutamate in mammalian brain. *Prog. Neurobiol.* 35, 245-296 (1990).
  46. Ross B. Biochemical considerations in <sup>1</sup>H spectroscopy. Glutamate and glutamine; myo-inositol and related metabolites. *NMR in Biomedicine* 4, 59-63 (1991).
  47. Hamberger AC, Chiang GH, Nylén ES, Scheff SW, Cotman CW. Glutamate as a CNS transmitter I. Evaluation of glucose and glutamine as precursors for the synthesis of preferentially released glutamate. *Brain Res.* 168, 513 – 530 (1979).
  48. Urenjak J, Williams SR, Gadian DG, Noble M. Proton nuclear magnetic resonance spectroscopy unambiguously identifies different neural cell types. *J. Neuroscience* 13, 981 – 989 (1993).
  49. Selemon LD, Rajkowska G, Goldman-Rakic PS. Abnormally high neuronal density in the schizophrenic cortex. *Arch. Gen. Psychiatry* 53, 805-818 (1995).
  50. Olney JW, Farber NB. Glutamate receptor dysfunction in schizophrenia. *Arch. Gen. Psychiatry* 52, 998-1007 (1995).



- 
51. Javitt DC, Zukin SR. Recent advances in the phencyclidine model of schizophrenia. *Am. J. Psychiatry* 148, 1301-1308 (1991).
  52. Nasrallah PM. In vivo proton magnetic resonance spectroscopy of the hippocampal amygdala region in schizophrenics. *Schiz. Research* 6, 150 (1992).
  53. Renshaw PF, Yurgelum-Todd DA, Tohen M, Gruber S, Cohen BM. Temporal lobe proton magnetic resonance spectroscopy of patients with first-episode psychosis. *Am. J. Psychiatry* 152, 444-446 (1995).
  54. Alexander GE, De Long MR, Strick PL. Parallel organization of functionally segregated circuits linking basal ganglia and cortex. *Annual Review of Neuroscience* 9, 357-381 (1986).
  55. Alexander EA, Crutcher MD, DeLong MR. Basal ganglia-thalamocortical circuits: Parallel substrates for motor, oculomotor, "prefrontal" and "limbic" functions. In: Uylings HBM, Van Eden CG, De Bruin JPC, Corner MA, Feenstra MGP eds. *Progress in Brain Research*. New York, NY, USA: Elsevier Science Publishers, 85, 119-146 (1990).
  56. Rajakumar N, Williamson P, Stoessl J, Flumerfelt B. Neurodevelopmental pathogenesis of schizophrenia. *Proc. Soc. for Neuroscience Meeting*, Washington, DC, USA, 2, 1187 (1996).
  57. Lipska BK, Jaskiw GE, Chrapasta S, Karoum F, Weinberger DR. Ibotenic acid lesion of the ventral hippocampus differentially affects dopamine and its metabolites in the nucleus accumbens in prefrontal cortex. *Brain Res.* 585, 1-6 (1992).
  58. Miller BL. A review of chemical issues in  $^1\text{H}$  NMR spectroscopy: N-acetyl-L-aspartate, creatine, and choline. *NMR in Biomedicine* 4, 47-52 (1991).

- 
59. Pettegrew JW, Keshavan MS, Panchalingam K, Strychor S, Kaplan DB, Tretta MG, Allen M. Alternations in brain high-energy phosphate and membrane phospholipid metabolism in first-episode, drug-naïve schizophrenics: a pilot study of the dorsal prefrontal cortex by in vivo phosphorus 31 nuclear magnetic resonance spectroscopy. *Arch. Gen. Psychiatry* 48, 563-568 (1991).
60. Potwarka J, Drost DJ, Williamson PC. A study of schizophrenia using 2D <sup>31</sup>P chemical shift imaging with <sup>1</sup>H decoupling. Proceedings of the Society of Magnetic Resonance Meeting, New York, NY, USA, 998 (1996). Abstract.
61. Stanley JA, Williamson PC, Drost DJ, Carr TJ, Rylett RJ, Malla A, Thompson RT. An in vivo study of the prefrontal cortex of schizophrenic patients at different stages of illness via phosphorus magnetic resonance spectroscopy. *Arch. Gen. Psychiatry* 52, 399-406 (1995).
62. Buckley PF, Moore C, Long H, Larkin C, Thompson P, Mulvany F, Redmond O, Stack JP, Ennis JT, Waddington JL. <sup>1</sup>H-magnetic resonance spectroscopy of the left temporal and frontal lobes in schizophrenia: clinical, neurodevelopmental, and cognitive correlates. *Biol. Psychiatry* 36, 792-800 (1994).
63. Benes FM. Relationship of cingulate cortex to schizophrenia and other psychiatric disorders. In: Vogt BA, Gabriel M eds. *Neurobiology of Cingulate Cortex and Limbic Thalamus*. Boston, USA: Birkhauser; 581-605 (1993).

## Chapter 6

### **A Short Echo $^1\text{H}$ Spectroscopy and Volumetric MR Imaging Study of the Corpus Striatum in Patients with Obsessive-Compulsive Disorder and Comparison Subjects<sup>3</sup>**

*By Robert Bartha, Murray B Stein, Peter C Williamson, Dick J Drost, Richard WJ Neufeld, Tom J Carr, Gita Canaran, M Densmore, Geri Anderson, Abdur R Siddiqui*

#### **6.0 Introduction**

Obsessive-compulsive disorder (OCD) is a prevalent, serious neuropsychiatric disorder (1) of unknown etiology. Several lines of investigation into the cause(s) of OCD have suggested that it is characterized by dysfunction within a basal ganglia-thalamocortical neuronal circuit (2, 3). In particular, the corpus striatum has shown abnormalities in OCD patients compared to comparison subjects in

---

<sup>3</sup> A version of this chapter has been published.

Bartha R, Stein MB, Williamson PC, Drost DJ, Neufeld RWJ, Carr TJ, Canaran G, Densmore M, Anderson G, Siddiqui AR. A Short Echo  $^1\text{H}$  Spectroscopy and Volumetric MR Imaging Study of the Corpus Striatum in Patients with Obsessive-Compulsive Disorder and Comparison Subjects. *American Journal of Psychiatry* 155, 1584-1591, 1998.

Copyright 1998, the American Psychiatric Association. Reprinted by permission.

several imaging studies (4, 5, 6). Positron emission tomography (PET) and functional magnetic resonance imaging (fMRI) studies (7, 8) during symptom provocation have revealed activation within the corpus striatum (specifically in the caudate) along with other brain regions (medial orbitofrontal cortex, anterior cingulate, amygdala). Studies of OCD patients following treatment with either pharmacotherapy or behavior therapy indicate that functional abnormalities in the corpus striatum normalize as a correlate of symptom reduction (5, 6). Additional support for the involvement of the basal ganglia-thalamocortical neuronal circuit in OCD comes from the finding of neurosensory “gating” abnormalities in patients with OCD. These gating deficits are consistent with dysfunction within this neuronal circuit (9, 10).

Several investigators have attempted to delineate a neuroanatomic abnormality in OCD by measuring the size or assessing the structural integrity of presumably critical central nervous system (CNS) structures. In particular, the corpus striatum has been the focus of a series of computerized tomographic (CT) and, more recently structural MRI studies (11, 12, 13, 14, 15, 16). These studies have been remarkably inconsistent with some finding reduced caudate size, (13, 16) another finding increased caudate size (12) and some finding no differences (14, 15).

Short echo proton magnetic resonance spectroscopy ( $^1\text{H}$ -MRS) can be used to obtain information about several metabolites which are highly relevant to our understanding of the mechanisms of dysfunction within neuronal circuits in OCD and other neuropsychiatric disorders (17, 18). N-acetylaspartate (NAA) which is readily measured using  $^1\text{H}$ -MRS, has become a well accepted neuronal marker

(17, 18, 19, 20). In fact, it is believed that N-acetylaspartate may decline in neuronal tissue prior to neuronal loss being detectable using conventional MRI morphometric methods (21, 22). Glutamate (Glu) and glutamine (Gln) which are also reliably measured using short echo  $^1\text{H-MRS}$  are involved in the cycle of excitatory neurotransmission (17, 18) and as such may yield additional information regarding OCD.

In this study of patients with OCD and matched comparison subjects,  $^1\text{H-MRS}$  and volumetric MR imaging were used to further delineate a role for corpus striatum dysfunction in the pathophysiology of OCD. Maintaining a tolerable total study time for these subject (1.5–2 hours) precluded the acquisition of data from the left and right striatum. We elected to focus on the left side because previous studies had shown bilateral abnormalities, and for comparison to data acquired in never treated schizophrenic patients on the left side. We hypothesized that OCD patients and comparison subjects would show different N-acetylaspartate levels in the left corpus striatum based on previous reports of volumetric and functional anomalies in this region. To the best of our knowledge this is the first study to combine short echo  $^1\text{H-MRS}$  and volumetric imaging of the caudate in OCD. Caudate volumes were measured in these same subjects in the hope that the simultaneous examination of these volumes and N-acetylaspartate levels might shed light on the inconsistent volumetric findings which have emerged from prior studies.

## **6.1 Method**

### **6.1.1 Subjects**

Thirteen patients with DSM-IV OCD and 13 healthy comparison subjects were studied. Patients with OCD were recruited from among persons seeking treatment at either the Department of Psychiatry, St. Boniface General Hospital, Winnipeg, Manitoba (N=10), or the Department of Psychiatry, London Health Sciences Centre, London, Ontario (N=3). Comparison subjects were chosen from a pool of subjects recruited from the London area by advertisement. Subjects were chosen in such a way as to minimize demographic differences (gender, age, education, parental education, and handedness) between the patient and comparison groups (Table 6-1).

Subjects with OCD were diagnosed by an experienced clinician-researcher (MBS) using a semi-structured interview (SCID) (23). Comorbidity, family history, and other illness parameters (e.g., age at onset) were assessed at this time as part of the clinical interview, as was the patient's medical and prior treatment history. This same experienced interviewer (MBS) determined the severity of OCD symptomatology using the Yale-Brown Obsessive-Compulsive Scale (YBOCS) (24, 25), Clinical Global Impression Scale (CGI) (26) and the National Institute of Mental Health Obsessive Compulsive Scale (NIMH-OCS) (27). One patient had clinical depression at the time of the study. All OCD subjects were outpatients and had no other current comorbidity including tics.

Group	Age (years)	Gender	Hand	Education Level	Parental Education Level
Comparison Subjects (N=13)	32.4 ± 9.7	7 Male, 6 Female	12 Right, 1 Left	3.0 ± 0.7	2.3 ± 1.1
OC Patients (N=13)	34.9 ± 8.8	7 Male, 6 Female	10 Right, 3 Left	3.0 ± 0.8	2.5 ± 1.1
Group	YBOCS Obsessive	YBOCS Compulsive	YBOCS Total	CGI	NIMH - OCS
Comparison Subjects (N=13)	n/a	n/a	n/a	n/a	n/a
OC Patients (N=13)	11.6 ± 4.0	14.3 ± 2.8	25.9 ± 5.2	4.9 ± 1.0	9.5 ± 1.8

**Table 6-1: Subject Demographics**

Except for gender and hand, data are given as mean ± SD. N represents the total participants included in a group; YBOCS is the Yale-Brown Obsessive-Compulsive Scale (24, 25), CGI is the Clinical Global Impression Scale (26), and NIMH-OCS is the National Institute of Mental Health Obsessive Compulsive Scale (27). The age was that at time of MR spectroscopy examination. Handedness was determined by questionnaire (28). Education levels are rated as 1, ≤ grade 10; 2, grade 11 to grade 13; 3, 1 to 3 years of college; 4, ≥ 4 years of college.

Subjects with OCD and healthy comparison subjects were required to be medication free for a minimum of six weeks prior to the day of scanning (nine patients had *never* received antidepressant medication), to be otherwise in good physical health, and to have no history of significant head injury or seizures. One subject had a history of neuroleptic exposure two years before this study. None

of the OCD subjects were participating in formal behavior or cognitive therapy during the time of study participation, nor were they involved in any form of self-help cognitive or behavioral therapy for their condition. As part of the MR study, routine clinical images were collected for each subject and viewed by a radiologist (TC) who detected no gross abnormalities on any scans. In addition to the aforementioned criteria, healthy comparison subjects underwent a routine clinical interview and were screened with the SCID by another experienced clinician-researcher (PCW) to ensure they did not satisfy criteria for any Axis I or Axis II psychiatric disorders.

The education level of each subject was rated on a four point scale (1,  $\leq$  grade 10; 2, grade 11 - 13; 3, 1-3 years of college or university; 4,  $\geq$  4 years of college or university). Parental education ratings were also evaluated as above for the most educated parent. The handedness of each subject was defined by a handedness questionnaire (28). The height and weight of each subject was also recorded so that these characteristics could be used as covariates in the statistical analysis of the volumetric data.

After complete description of the study to each subject, written informed consent was obtained. This study was approved by the Faculty of Medicine Human Subjects Committee of the University of Manitoba and the Review Board for Health Sciences Research Involving Human Subjects of the University of Western Ontario.



### 6.1.2 $^1\text{H}$ MR Spectroscopy

Spectroscopy data were acquired as described in detail elsewhere (29). Spectra were acquired from a  $15 \times 20 \times 15 \text{ mm}^3$  volume of interest (VOI) in the left corpus striatum (Figure 6-1). Although the images used to position the VOI were not transformed to Tailairach space (30) the VOI studied was approximately positioned within the volume defined by the following Tailairach coordinates:  $x = 0$  to  $-15$ ,  $y = -10$  to  $20$ , and  $z = 0$  to  $15$ . Both water suppressed (31) and water unsuppressed spectra were acquired using a stimulated echo acquisition mode (STEAM) (32) sequence (TR=1500 ms, TE=20 ms, TM=30 ms, 4096 complex points, 250  $\mu\text{s}$  dwell time, 550 and 30 averages respectively).

### 6.1.3 Spectral Processing

Spectral processing is also described in detail elsewhere (29, 33). Each spectrum was fit to a complete spectrum model composed of twelve metabolites (19, 29, 34, 35, 36) and three macromolecules (37) with resonances between 1.9 ppm. and 3.5 ppm (NAA<sub>CH3</sub> referenced to 2.01 ppm). The caption to Figure 6-2 contains a complete list of the metabolites and macromolecules included in the spectrum model.

Metabolite levels were normalized to the unsuppressed water signal following correction for the partial volume effect (29, 35) of cerebral spinal fluid (CSF), gray matter, and white matter ratio (estimated as 1%/60%/39%). Therefore, metabolite levels represent the average metabolite level ( $\pm$  SD) in the volume

studied uncorrected for the NMR relaxation parameters  $T_1$  and  $T_2$ , (since accurate values were unavailable for each metabolite).

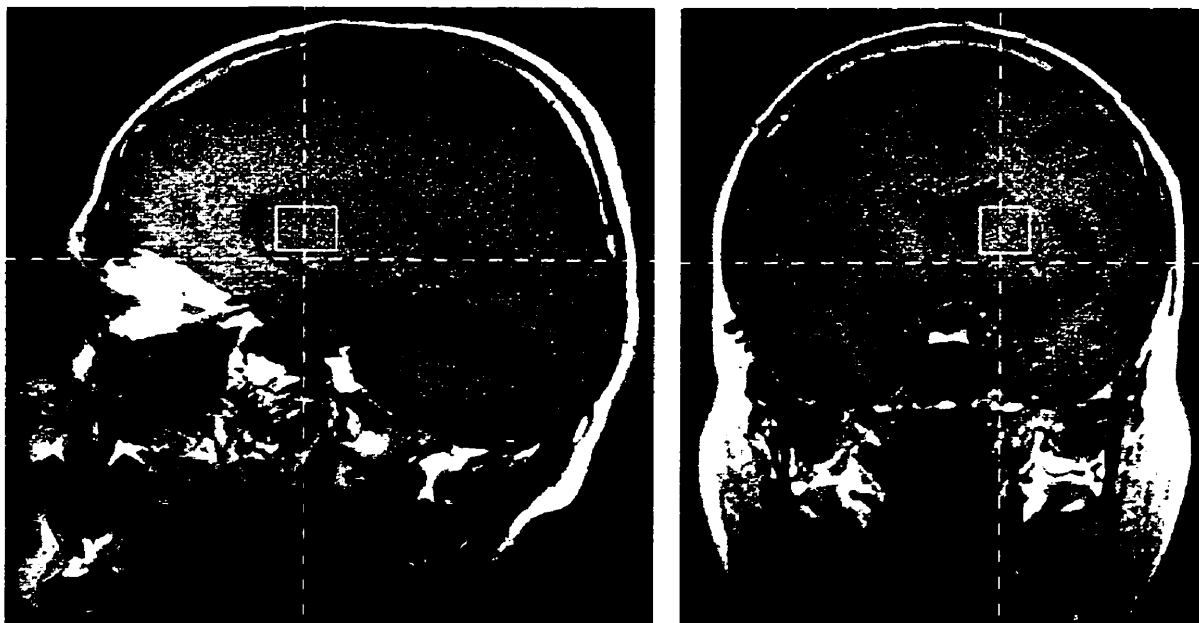


**Figure 6-1: Location of Volume of Interest in Left Corpus Striatum**

Sagittal and coronal  $^1\text{H}$  MR localizer images showing the placement of the volume of interest (VOI) in the left corpus striatum. The projection of the  $15 \times 20 \times 15 \text{ mm}^3$  VOI in the corpus striatum is outlined by the white rectangle in each slice. Approximate Talairach co-ordinates for this volume are given in the methods section. The vertical dotted lines in the coronal image give the position of the corresponding sagittal slice. The vertical dotted lines in the sagittal image give the position of the corresponding coronal slice. The horizontal lines in all images show the position of the most inferior transverse slices that were also used for positioning but are not shown here.

#### 6.1.4 Volumetric Imaging

The entire brain of each subject was imaged on the same MR scanner and same day as  $^1\text{H}$ -MRS data were acquired. Volumetric images consisted of 128 contiguous 1.56 mm thick coronal slices (0.94 mm x 0.94 mm in plane resolution) acquired using a 3D FLASH (38) sequence (TR = 30 ms, TE = 10 ms). To measure consistent volumes of the head of the caudate nucleus ANALYZE software (39) was used to reformat the coronal slices into slices perpendicular to a plane joining the most inferior margin of the splenium with the most inferior margin of the genu of the corpus callosum. The head of the caudate nucleus bordered by a plane parallel to the anterior portion of the pons (13), a plane parallel to the anterior commissure, the frontal horn of the lateral ventricle, and the anterior limb of the internal capsule (14) was segmented using a semi-automated histogram technique in Xstatpack (40). Ten subjects had volumes calculated twice on the same scan to determine test-retest reliability. All volume measurements were performed by the same rater (MD) without knowledge of diagnosis or MRS measures.

#### 6.1.5 Statistical Analysis

All statistical tests were performed using SPSS (SPSS Inc.) release 6.0 (41). The subject characteristics age, education level, parental education, height, and weight were comparable between subject groups according to a two tailed t-test ( $p > 0.50$ , DF=24). The use of these variables as covariates therefore allowed for the reduction of extraneous variance in error terms, without risking removal of genuine group effects (42, 43).

Although twelve metabolites and three macromolecules were modeled for each spectrum only metabolites quantified with coefficient of variation (CV) < 75% were considered reliable and included in between group comparisons. As N-acetylaspartate was the focus of hypothesized differences, values of this metabolite were submitted to analysis of covariance (ANCOVA); the remaining measures were analyzed using multivariate analysis of covariance (MANCOVA). Age, education, and parental education were used as covariates in these tests. *P*-values of  $\leq 0.05$  (two-tailed) were considered statistically significant.

Caudate volume repeated measure stability was assessed with intra class correlation coefficients (44). Caudate volumes of OCD patients and comparison subjects were compared using ANCOVA, covarying for age, height, and weight. *P*-values of  $\leq 0.05$  (two-tailed) were considered statistically significant.

To establish if estimated metabolite levels were related (due to physiology or quantification artifact), bivariate correlations were made between reliably quantified metabolites (CV < 75%). Bivariate correlations were also made between metabolites which showed group differences and caudate volumes, and between these metabolites and symptom scores (YBOCS, CGI, and NIMH-OCS). Correlations were made independently for each subject group. *P*-values for significance of all correlations were determined using a Bonferroni based correction (45) as no prior hypotheses were made.

## 6.2 Results

Spectra from all thirteen OCD patients and all thirteen comparison subjects were quantified. A typical spectrum (after water removal) acquired from the left corpus striatum of one OCD patient is shown in Figure 6-2. It is displayed in the frequency domain after Fourier transform although all quantification was done in the time domain. Individual metabolite spectra are also shown. The first line below the residual shows *N*-acetylaspartate (solid), phosphocreatine + creatine (dotted), and choline containing compounds including mostly phosphorylcholine, glycerophosphorylcholine, and free choline (19, 36) (dashed). The second line shows *N*-acetylaspartyl-glutamate (solid), glutamate (dashed), and glucose (dotted). The third line shows glutamine (solid), aspartate (dashed), taurine (dotted). The fourth line shows  $\gamma$ -aminobutyric acid (solid), and myo-inositol (dashed). The fifth line shows the macromolecule resonances at 3.00 ppm (M 3.00), and 2.29 ppm (M 2.29) (37), while the sixth line shows the resonances fit outside the spectral region of interest ( <1.9 ppm and > 3.5 ppm). Scyllo-inositol and the macromolecule at 2.05 ppm are not shown in Figure 6-2 because they were fit with amplitudes of zero in this spectrum. The average signal to noise ratio (mean  $\pm$  SD) measured as the *N*-acetylaspartate area divided by the root-mean-squared noise level in the time domain was  $8.6 \pm 1.2 : 1$  (N=13) for comparison subject spectra and  $8.0 \pm 1.6 : 1$  (N=13) for OCD spectra. The average full-width at half-maxima (FWHM) of the unsuppressed water spectra (mean  $\pm$  SD) were  $6.2 \pm 0.7$  Hz for comparison subjects and  $6.7 \pm 0.5$  Hz for OCD patients.

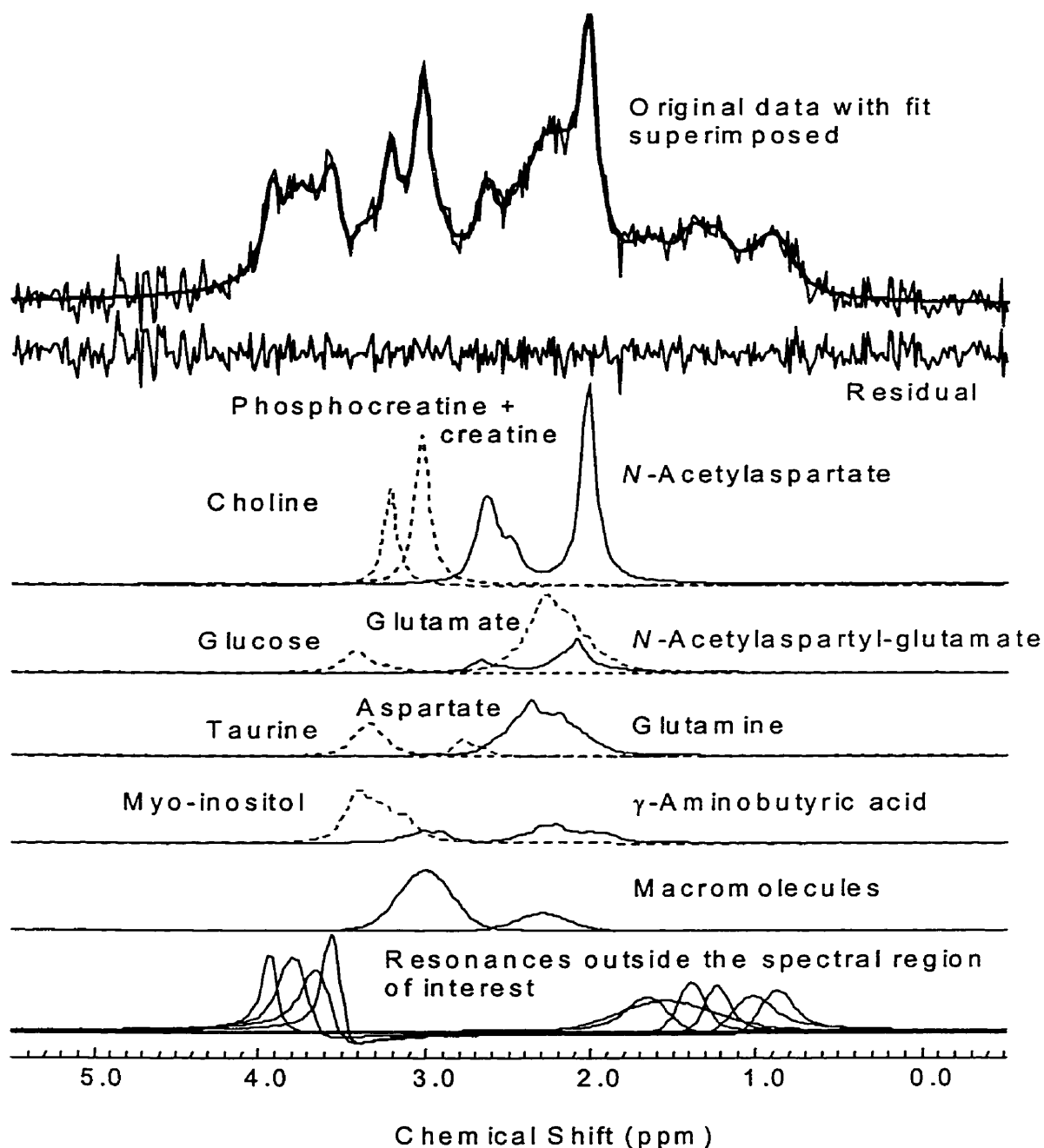


**Figure 6-2: In-vivo Spectrum and Components from Left Corpus Striatum**

Typical in vivo  $^1\text{H}$  data from the corpus striatum (after water removal) for one OCD patient. Data (light trace) was fit in the time domain, but is shown here in the frequency domain along with the fit result (dark trace) for interpretation. The difference between the data and fit result is shown beneath (residual) followed by the individual metabolite components (described within the text).

### 6.2.1 Spectroscopy Results

Seven of the twelve quantified metabolites and two macromolecules had CVs less than 75% and were included in the statistical analysis. These included N-acetylaspartate, glutamate, glutamine, N-acetylaspartyl-glutamate, taurine, choline containing compounds, and phosphocreatine + creatine, as well as the macromolecules at 2.29 ppm and 3.00 ppm. The metabolites  $\gamma$ -aminobutyric acid, aspartate, glucose, scyllo-inositol, myo-inositol, and the macromolecule at 2.05 ppm were quantified with CVs greater than 75%, and therefore considered unreliable and excluded from the statistical analysis. Figure 6-3 shows the estimated metabolite and macromolecule levels of the metabolites included in the statistical analysis for each subject group. Groups differed with respect to N-acetylaspartate which was significantly lower in OCD patients compared to comparison subjects (mean  $\pm$  SD,  $14.7 \pm 1.6$  vs.  $16.1 \pm 1.1$  arbitrary units,  $N=13/\text{group}$ ,  $DF=(1, 21)$ ,  $F=6.1$ ,  $p = 0.022$ ). The MANCOVA for the remaining six metabolites and two macromolecules listed above did not show an overall statistically significant difference between OCD patients and comparison subjects ( $N=13/\text{group}$ ,  $DF=(8, 14)$ ,  $F= 0.22$ ,  $p = 0.982$ ).

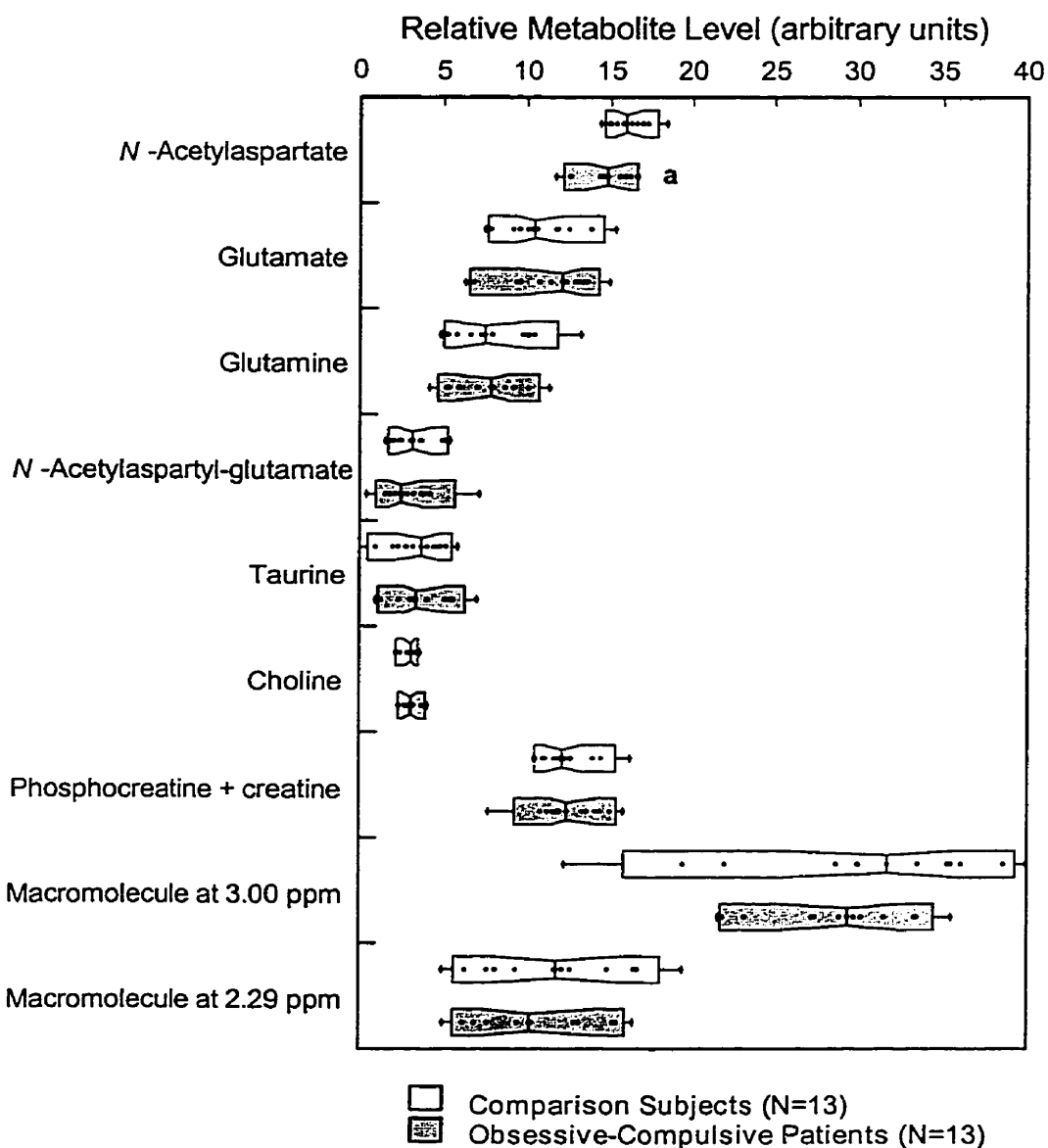


**Figure 6-3: Quantified Metabolite Levels from Left Corpus Striatum**

Box and whisker plot showing metabolite levels after normalization to total NMR visible water in the corpus striatum of healthy comparison subjects (N=13) and OCD patients (N=13). Whiskers indicate 5 and 95 percentiles, box indicates 10 and 90 percentiles, notch indicates 25 and 75 percentiles, and line indicates 50 percentile. Each box-whisker plot contains 13 metabolite measures (points), although some points are difficult to distinguish because they are co-incident with other points. Letter 'a' indicates significant ANCOVA.



### 6.2.2 Volumetric Imaging Results

Intra class correlation coefficients for test-retest reliability were 0.86 and 0.90 for left and right caudate volumes respectively. ANCOVA showed no differences between patients with OCD and comparison subjects in left (mean  $\pm$  SD,  $4.6 \pm 0.7$  vs.  $4.4 \pm 0.5$  cm<sup>3</sup>, N=13/group, DF=(1, 21), F=1.76,  $p = 0.20$  ) or right (mean  $\pm$  SD,  $4.8 \pm 0.7$  vs.  $4.6 \pm 0.4$  cm<sup>3</sup>, N=13/group, DF=(1, 21), F=0.95,  $p = 0.34$ ) caudate volume.

### 6.2.3 Bivariate Correlations

Plots of each correlation (available from the first author) were visually inspected and showed no evidence of outliers or anomalies which could give rise to false correlations. The correlations reported here were significant after Bonferroni based correction (45). Metabolite correlations in the comparison subject group showed that glutamate was inversely correlated with glutamine ( $r = -0.703$ , DF=11,  $p = 0.007$ ) and phosphocreatine + creatine was positively correlated with the macromolecule at 2.29 ppm ( $r = 0.760$ , DF=11,  $p = 0.003$ ). In the OCD group N-acetylaspartate was positively correlated with glutamate ( $r = 0.750$ , DF=11,  $p = 0.003$ ), phosphocreatine + creatine was positively correlated with choline ( $r = 0.827$ , DF=11,  $p < 0.001$ ) and with the macromolecule at 2.29 ppm ( $r = 0.763$ , DF=11,  $p = 0.002$ ). There were no significant correlations between N-acetylaspartate levels and symptom scores or left and right caudate volumes.

### **6.3 Discussion**

We found decreased levels of N-acetylaspartate in the left corpus striatum of OCD patients compared to comparison subjects without a corresponding decrease in caudate volume. Recently Ebert *et al* (46) have also independently reported decreased N-acetylaspartate levels in the *right* striatum of OCD patients compared to comparison subjects. Reduced N-acetylaspartate levels are often reported in disorders such as Alzheimer's disease (47) which are associated with neuronal loss. In the absence of caudate volume differences between groups in this study, lower N-acetylaspartate levels in OCD patients may indicate a greater sensitivity of this metabolite compared to measurement of tissue volume for the detection of neuronal loss (21). Our finding would be consistent with this interpretation and might explain the discrepancy among prior studies in the detection of caudate volume differences in OCD patients, since small scale volume loss might not have been detectable. It remains to be determined if age at onset, severity and duration of illness, or etiology might explain this apparent heterogeneity in caudate volumes among subjects. If replicated, however, our findings would support the notion that reduced neuronal density in the corpus striatum - albeit of a magnitude which is not readily detectable using conventional imaging techniques - is a feature of many cases of OCD.

Since N-acetylaspartate is found primarily within neurons in the brain (20), reduced N-acetylaspartate levels suggest decreased neuronal density within the volume studied. What pathophysiologic processes might lead to this state? One attractive hypothesis is that neuronal loss leading to reduced N-acetylaspartate levels could result from an excitotoxic process caused by an increase in activity of afferent glutamatergic neurons from the prefrontal cortex. A recent fMRI study

showed increased activation in the corpus striatum during symptom provocation of patients with OCD (8), suggesting that increased afferent input to this region - much of which is glutamatergic (48) - may be an important factor in the pathophysiology of OCD symptomatology. However, previous PET and single photon emission computed tomography (SPECT) neutral state studies have not consistently shown increased activity in the corpus striatum (4, 5). In interpreting the functional brain literature in OCD, however, one must consider that the interpretation of relative differences in either blood flow or glucose utilization in the corpus striatum might be confounded by actual differences in neuronal density between patients and comparison subjects. In fact, if reduced corpus striatum N-acetylaspartate is replicated in other studies of patients with OCD, an argument could be made in favor of correcting for neuronal density in functional studies of the corpus striatum in OCD.

There are undoubtedly several alternatives to a glutamatergic excitotoxic explanation for reduced corpus striatum neuronal density in OCD. Most promising among these explanations is the possibility that OCD may be caused by an auto-immune process (49, 50, 51, 52). Antibodies directed against B-hemolytic streptococcus cross-react with corpus striatum neurons (53, 54). Damage to the corpus striatum caused by such a process could lead to decreased neuronal density and decreased N-acetylaspartate levels as were observed in this study. This damage, unless extensive, would not necessarily lead to volume changes that could be detected with conventional MR morphometry.

### 6.3.1 Limitations

There are a number of alternative explanations for our findings, as well as a number of unanswered questions. It is possible, for example, that changes in OCD occur selectively or predominantly in particular striatal structures (e.g. caudate, putamen), (16, 55, 56) rather than generally throughout the corpus striatum. Our voxel size and positioning were such that both caudate and putamen were sampled, perhaps to differing degrees in different patients, leaving us unable to discern whether low N-acetylaspartate levels were confined to one or both of these structures. This possibility bears more careful scrutiny in future studies. Another possible explanation for the variability in caudate findings across the literature, and for the reduction of N-acetylaspartate in our particular patient sample, may be that our patients lacked tic symptoms (55, 57). As others have suggested (15), heterogeneity within and among samples for the presence of tic symptoms may lie at the heart of the inconsistent caudate volume findings in OCD. This issue could be resolved by conducting a study where two groups of patients with OCD are included: one group with, and one group without significant tic symptomatology.

Ramifications of technical limitations must also be considered. Although the volume studied was small ( $4.5 \text{ cm}^3$ ) and positioning was done with the aid of images to sample only the caudate (gray matter), all voxels contained partial volumes of internal capsule (white matter) and putamen (gray matter). Since N-acetylaspartate levels measured by MR spectroscopy are slightly higher in gray matter than white matter a decrease in the ratio of gray matter to white matter within a VOI would result in a measured decrease of N-acetylaspartate level. As we observed no change in caudate volume in this group of subjects it is unlikely

that decreased gray matter content within the VOI studied in OCD patients is the cause of observed differences in N-acetylaspartate levels. Furthermore, assuming N-acetylaspartate levels are 25% higher in gray matter compared to white matter (35), and that the average comparison subject volume contained 60% gray matter and 40% white matter, if partial volume were the sole reason for the observed decrease in N-acetylaspartate levels (9%) in OCD patients, the average OCD volume would have contained only 20% gray matter and 80% white matter, a highly unlikely scenario.

#### **6.4 Conclusion**

We found decreased levels of N-acetylaspartate in the left corpus striatum in the absence of volumetric changes of the left or right head of the caudate nucleus in OCD patients compared to comparison subjects. These findings suggest there is decreased neuronal density within this region and support the view of OCD as a neuropsychiatric disorder involving an alteration in neural architecture within one or more components of a basal ganglia-thalamocortical neuronal circuit.

Subsequent studies using spectroscopic techniques which permit more precise regional localization will be required to determine whether or not specific corpus striatum structures are selectively involved in the disorder. Such studies would benefit from careful attention to diagnostic subtype classification (tics, family history, age of onset, autoimmune etiology) which may serve to reduce patient heterogeneity and improve the precision of metabolite measurements.

#### **6.5 Reference**

- 
1. Koran LM, Thienemann ML, Davenport R. Quality of life for patients with obsessive-compulsive disorder. *Am. J. Psychiatry* 153, 783-788 (1996).
  2. Modell JG, Mountz JM, Curtis GC, Greden JF. Neurophysiologic dysfunction in basal ganglia/limbic striatal and thalamocortical circuits as a pathogenetic mechanism of obsessive-compulsive disorder. *J. Neuropsychiatry Clin. Neurosci.* 1, 27-36 (1989).
  3. Insel TR. Toward a neuroanatomy of obsessive-compulsive disorder. *Arch. Gen. Psychiatry* 49, 739-744 (1992).
  4. Hoehn-Saric R, Benkelfat C. Structural and functional brain imaging in obsessive-compulsive disorder. in *Current Insights in Obsessive-Compulsive Disorder*, pp 183-211. Edited by Hollander E, Zohar J, Marazziti D, Olivier B. New York, NY, John Wiley & Sons Inc, (1994).
  5. Baxter LR Jr., Schwartz JM, Bergman KS, Szuba MP, Guze BH, Mazziotta JC, Alazraki A, Selin CE, Ferng HK, Munford P, Phelps ME. Caudate glucose metabolic rate changes with both drug and behavior therapy for obsessive-compulsive disorder. *Arch. Gen. Psychiatry* 49, 681-689 (1992).
  6. Schwartz JM, Stoessel PW, Baxter LR Jr., Martin KM, Phelps ME. Systematic changes in cerebral glucose metabolic rate after successful behavior modification treatment of obsessive-compulsive disorder. *Arch. Gen. Psychiatry* 53, 109-113 (1996).
  7. Rauch SL, Jenike MA, Alpert NM, Baer L, Breiter HCR, Savage CR, Fischman AJ. Regional cerebral blood flow measured during symptom provocation in obsessive-compulsive disorder using oxygen 15-labeled carbon dioxide and positron emission tomography. *Arch. Gen. Psychiatry* 51, 62-70 (1994).

- 
8. Breiter HC, Rauch SL, Kwong KK, Baker JR, Weisskoff RM, Kennedy DN, Kendrick AD, Davis TL, Jiang A, Cohen MS, Stem CE, Belliveau JW, Baer L, O'Sullivan RL, Savage CR, Jenike MA, Rosen BR. Functional magnetic resonance imaging of symptom provocation in obsessive-compulsive disorder. *Arch. Gen. Psychiatry* 53, 595-606 (1996).
  9. Swerdlow NR, Benbow CH, Zisook S, Geyer MA, Braff DL: A preliminary assessment of sensorimotor gating in patients with obsessive compulsive disorder. *Biol. Psychiatry* 33: 298-301 (1993).
  10. Enright SJ, Beech AR. Reduced cognitive inhibition in obsessive-compulsive disorder. *Br. J. Clin. Psychology* 32, 67-74 (1993).
  11. Kellner CH, Jolley RR, Holgate RC, Austin L, Lydiard RB, Laraia M, Ballenger JC. Brain MRI in obsessive-compulsive disorder. *Psychiatry Res.* 36, 45-49 (1991).
  12. Scarone S, Colombo C, Livian S, Abbruzzese M, Ronchi P, Locatelli M, Scotti G. Increased right caudate size in obsessive-compulsive disorder: Detection with magnetic resonance imaging. *Psychiatry Res.: Neuroimaging* 45, 115-121 (1992).
  13. Robinson D, Wu H, Munne RA, Ashtari M, Alvir JM, Lerner G, Koreen A, Cole K, Bogerts B. Reduced caudate nucleus volume in obsessive-compulsive disorder. *Arch. Gen. Psychiatry* 52, 393-398 (1995).
  14. Aylward EH, Harris GJ, Hoehn-Saric R, Barta PE, Machlin SR, Pearlson GD. Normal caudate nucleus in obsessive-compulsive disorder assessed by quantitative neuroimaging. *Arch. Gen. Psychiatry* 53, 577-584 (1996).
  15. Jenike MA, Breiter JC, Baer L, Kennedy DN, Savage CR, Olivares MJ, O'Sullivan RL, Shera DM, Rauch SL, Keuthen N, Rosen BR, Caviness VS,

- 
- Filipek PA. Cerebral structural abnormalities in obsessive-compulsive disorder: a quantitative morphometric magnetic resonance imaging study. *Arch. Gen. Psychiatry* 53, 625-632 (1996).
16. Rosenberg DR, Keshavan MS, O'Hearn KM, Dick EL, Bagwell WW, Seymour AB, Montrose DM, Pierri JN, Birmaher B. Fronto-striatal morphology in treatment-naïve pediatric obsessive compulsive disorder. *Arch. Gen. Psychiatry* 54, 824-830 (1997).
17. Dager SR, Steen RG. Applications of magnetic resonance spectroscopy to the investigation of neuropsychiatric disorders. *Neuropsychopharmacology* 6, 249-266 (1992).
18. Stanley JA, Drost DJ, Williamson PC, Carr TJ. In vivo proton MRS study of glutamate in schizophrenia. in *NMR Spectroscopy in Psychiatric Brain Disorders*, pp 21-44. Edited by Nasrallah HA, Pettegrew JH. Washington, DC, American Psychiatric Press, (1995).
19. Michaelis T, Merboldt K-D, Bruhn H, Hanicke W, Math D, Frahm J. Absolute concentrations of metabolites in the adult human brain in vivo: quantification of localized proton MR spectra. *Radiology* 187, 219-227 (1993).
20. Urenjak J, Williams SR, Gadian DG, Noble M. Specific expression of N-acetylaspartate in neurons, oligodendrocyte type 2 astrocyte progenitors, and immature oligodendrocytes in vitro. *J. Neurochem.* 59, 55-61 (1992).
21. Ebisu T, Rooney WD, Graham SH, Weiner MW, Maudsley AA. N-Acetylaspartate as an in vivo marker of neuronal viability in kainate-induced status epilepticus: <sup>1</sup>H magnetic resonance spectroscopic imaging. *J. Cereb. Blood Flow Metab.* 14, 373-382 (1994).



- 
22. Cendes F, Andermann F, Preul MC, Arnold DL. Lateralization of temporal lobe epilepsy based on regional metabolic abnormalities in proton magnetic resonance spectroscopic images. *Ann. Neurol.* 35, 211-216 (1994).
  23. First MB, Spitzer RL, Williams JBW, Gibbon M. Structured Clinical interview for DSM-IV – Patient Edition (SCID-P). Washington, D.C., American Psychiatric Press Inc (1995).
  24. Goodman WK, Price LH, Rasmussen SA, Mazure C, Fleischmann RL, Hill CL, Heninger GR, Charney DS. The Yale-Brown Obsessive-Compulsive Scale (YBOCS), I: development, use, and reliability. *Arch. Gen. Psychiatry* 46, 1006-1011 (1989).
  25. Goodman WK, Price LH, Rasmussen SA, Mazure C, Delgado P, Heninger GR, Charney DS. The Yale-Brown Obsessive-Compulsive Scale (YBOCS), II: validity. *Arch. Gen. Psychiatry* 46, 1012-1016 (1989).
  26. Guy W. ECDEU Assessment Manual for Psychopharmacology. Publication 76 - 338, Washington D.C., US. Department of Health, Education, and Welfare (1976).
  27. Murphy DL, Pickar D, Alterman IS. Methods for the quantitative assessment of depressive and manic behavior. in *The Behavior of Psychiatric Patients*, pp 355-391. Edited by Burdock EI, Sudilovsky A, Gershon S. New York, NY, Marcel Dekker Inc (1982).
  28. Bryden P: Measuring handedness with questionnaires. *Neuropsychologia* 15, 617-624 (1977).
  29. Bartha R, Williamson PC, Drost DJ, Malla A, Carr TJ, Cortese L, Canaran G, Rylett RJ, Neufeld RWJ. Measurement of glutamate and glutamine in the medial prefrontal cortex of never treated schizophrenic patients and healthy

- 
- controls using proton magnetic resonance spectroscopy. *Arch. Gen. Psychiatry* 54, 959-965 (1997).
30. Tailairach J, Tournoux P. Co-Planar Stereotaxic Atlas of the Human Brain. New York, NY, USA, Thieme Medical Publishers Inc (1988).
31. Frahm J, Michaelis T, Merboldt KD, Bruhn H, Gyngell ML, Hanicke W. Improvements in localized proton NMR spectroscopy of human brain. Water suppression, short echo times, and 1 ml resolution. *J. Mag. Res.* 90, 464-473 (1990).
32. Frahm J, Merboldt KD, Hanicke W. Localized proton spectroscopy using stimulated echoes. *J. Mag. Res.* 72, 502-508 (1987).
33. Bartha R, Drost DJ, Stanley J, Williamson PC. A comparison between time and frequency domain quantification of short echo  $^1\text{H}$  MR spectra. Proceedings of the 3<sup>rd</sup> Society of Magnetic Resonance Meeting, Nice, France, 1946 (1995). Abstract
34. Provencher SW. Estimation of metabolite concentrations from localized in-vivo proton NMR spectra. *Magn. Reson. Medicine* 30, 672-679 (1994).
35. Stanley JA, Drost DJ, Williamson PC, Thompson RT. The use of a priori knowledge to quantify short echo in vivo  $^1\text{H}$  MR spectra. *Magn. Reson. Medicine* 34, 17-24 (1995).
36. Ross B, Michaelis T. Clinical applications of magnetic resonance spectroscopy. *Mag. Res. Quarterly* 10, 191-247 (1994).
37. Behar KL, Rothman DL, Spencer DD, Petroff OAC. Analysis of macromolecule resonances in  $^1\text{H}$  NMR spectra of human brain. *Magn. Reson. Medicine* 32, 294-302 (1994).

- 
38. Haase A, Frahm J, Matthaei KD. FLASH imaging: Rapid NMR imaging using low flip angles. *J. Magn. Reson.* 67, 258-266 (1986).
  39. Robb RA. A software system for interactive and quantitative analysis of biomedical images. in 3D imaging in medicine NATO ASI Series Volume F60, pp 333-361. Edited by Hohne KH, Fuchs H, Pizer SM. Berlin, Springer-Verlag (1990).
  40. Davis J. Xstatpack (copyright symbol) is a multi-purpose image quantification utility for use by medical imagers (1998).
  41. SPSS for Windows: Release 6.0. SPSS Inc (1993).
  42. Cochran WG. Analysis of covariance: its nature and uses. *Biometrics* 13, 261-281 (1957).
  43. Lees MC, Neufeld RWJ. Matching the limits of clinical inference to the limits of quantitative methods: A formal appeal to practice what we persistently preach. *Canadian Psychology* 35, 268-282 (1994).
  44. Fleiss, J. in The design and analysis of clinical experiments. New York, NY, John Wiley & Sons Inc (1988).
  45. Larzelere RE, Mulaik SA. Single sample tests for many comparisons. *Psychol. Bul.* 4, 557-569 (1977).
  46. Ebert D, Speck O, Konig A, Berger M, Hennig J, Hohagen F. <sup>1</sup>H-magnetic resonance spectroscopy in obsessive-compulsive disorder: evidence for neuronal loss in the cingulate gyrus and the right striatum. *Psychiatry Res.: Neuroimaging* 74, 173-176 (1997).
  47. MacKay S, Ezekiel F, Di Sclafani V, Meyerhoff DJ, Gerson J, Norman D, Fein G, Weiner MW. Alzheimer disease and subcortical ischemic vascular

- 
- dementia: evaluation by combining MR imaging segmentation and H-1 MR spectroscopic imaging. *Radiology* 198, 537-545 (1996).
48. Alexander GE, Crutcher MD, DeLong MR. Basal ganglia-thalamocortical circuits: Parallel substrates for motor, oculomotor, "prefrontal" and "limbic" functions. in *Progress in Brain Research*, pp 119-146. Edited by Uylings HBM, Van Eden CG, De Bruin JPC, Feenstra MGP. New York, NY, Elsevier Science Publishers (1990).
49. Swedo SE, Leonard HL, Kiessling LS. Speculations on antineuronal antibody mediated neuropsychiatric disorders of childhood. *Pediatrics* 93, 323-326 (1994).
50. Kiessling LS, Marcotte AC, Culpepper L. Antineuronal antibodies: tics and obsessive-compulsive symptoms. *J. Dev. Behav. Pediatr.* 15, 421-425 (1994).
51. Swedo SE, Leonard HL, Mittleman BB, Allen AJ, Rapoport JL, Dow SP, Kanter ME, Chapman F, Zabriskie J. Identification of children with pediatric autoimmune neuropsychiatric disorders associated with streptococcal infections by a marker associated with rheumatic fever. *Am. J. Psychiatry* 154, 110-112 (1997).
52. Murphy TK, Goodman WK, Fudge MW, Williams RC, Ayoub EM, Dalal M, Lewis MH, Zabriskie JB. B lymphocyte antigen D8/17: A peripheral marker for childhood-onset obsessive-compulsive disorder and Tourette's syndrome? *Am. J. Psychiatry* 154, 402-407 (1997).
53. Bronze MS, Dale JB. Epitopes of streptococcal M proteins that evoke antibodies that cross-react with human brain. *J. Immunol.* 151, 2820-2828 (1993).

- 
54. Husby G, van de Rijn I, Zabriskie JB, Abdin ZH, Williams RC Jr. Antibodies reacting with cytoplasm of subthalamic and caudate nuclei neurons in chorea and acute rheumatic fever. *J. Exp. Med.* 144, 1094-1110 (1976).
55. Peterson B, Riddle MA, Cohen DJ, Katz LD, Smith JC, Hardin MT, Leckman JF. Reduced basal ganglia volumes in Tourette's syndrome using three-dimensional reconstruction techniques from magnetic resonance images. *Neurology* 43, 941-949 (1993).
56. Singer HS, Reiss AL, Brown JE, Aylward EH, Shih B, Chee E, Harris EL, Reader MJ, Chase GA, Bryan RN, Denckla MB. Volumetric MRI changes in basal ganglia of children with Tourette's syndrome. *Neurology* 43, 950-956 (1993).
57. Holzer JC, Goodman WK, McDougle CJ, Baer L, Boyarsky BK, Leckman JF, Price LH. Obsessive-compulsive disorder with and without a chronic tic disorder. A comparison of symptoms in 70 patients. *Br. J. Psychiatry* 164, 469-473 (1994).

## Chapter 7

### Summary and Future Work

#### *7.0 Summary*

##### 7.0.1 Acquisition, Processing, and Quantification

$^1\text{H}$  magnetic resonance spectroscopy – specifically short echo spectroscopy – is gaining in use and usefulness as a tool for the clinical investigation of cerebral disease processes (1). In the early 1990's, this technique was used by our group to study cerebral volumes as small as  $8\text{ cm}^3$  (2). However, to reduce the partial volume effect associated with sampling gray and white matter simultaneously, and because pathology is likely localized to volumes smaller than  $8\text{ cm}^3$ , data collection for this thesis was attempted from volumes as small as  $4.5\text{ cm}^3$  at 1.5 T and  $1.5\text{ cm}^3$  at 4.0 T. But signal to noise ratio is directly proportional to volume (3), therefore data acquired from volumes less than  $8\text{ cm}^3$  at 1.5 T were difficult to quantify using existing quantification techniques. As a result, the goals of this thesis were to improve data quantification and collection techniques so that reliable measures could be made from volumes smaller than  $8\text{ cm}^3$ .

The first step in this process was the development of automated software for the post-processing and quantification of short echo  $^1\text{H}$  MR spectra. This has removed human interaction and bias from the spectral analysis. This software

was then used to develop an optimized approach to spectral fitting for use on clinical data using good quality data acquired from a single individual (Chapter 2).

During the course of these experiments, several interesting observations were made. First, in regards to lineshape correction following data acquisition, it is best to combine the QUALITY deconvolution correction technique (4) with the simple eddy current correction technique (5) to yield data which is both lineshape corrected and free from corrupted data points at the end of the time domain signal. Second, the common use of exponential filtering to enhance signal to noise leads to a decrease in quantification precision and altered metabolite levels. Therefore for short echo  $^1\text{H}$  spectra, which contain heavily overlapped resonances, exponential filtering prior to data quantification should be avoided.

The template of prior knowledge used for in-vivo spectral quantification must include accurate prior knowledge about all metabolites within the spectral region of interest. This includes macromolecule resonances, which contribute a significant amount of signal to the short echo  $^1\text{H}$  spectrum (6). Also resonances outside the spectral region of interest must be included if they overlap with resonances inside the spectral region of interest. Failure to include outside resonances will lead to the overestimation of inside resonances.

Finally, data acquisition and quantification was tested at 4.0 Tesla and compared to 1.5 Tesla in terms of quantification precision (Chapter 3). The results showed that there was an increase in the precision of metabolite quantification due to increased signal to noise ratio and increased chemical shift dispersion. This enabled the acquisition and quantification of glutamate and glutamine (with CV

less than 35 %) from 1.5 cm<sup>3</sup> volumes in the anterior cingulate and thalamus in a group of control subjects, which was not possible at 1.5 T.

### 7.0.2 In-Vivo Application to Schizophrenia

Short echo <sup>1</sup>H magnetic resonance spectroscopy was used to study a 4.5 cm<sup>3</sup> volume in the left medial prefrontal cortex of schizophrenic patients and matched control subjects (Chapter 5). The optimized approach to data quantification developed using data from a single individual was used to measure metabolite levels from all subjects. An increase in the amino acid glutamine was measured. As glutamine is a precursor of the neurotransmitter glutamate, this finding suggests abnormal glutamatergic transmission in this region.

### 7.0.3 In-Vivo Application to Obsessive-Compulsive Disorder

Short echo <sup>1</sup>H magnetic resonance spectroscopy was used to measure a 4.5 cm<sup>3</sup> volume in the left striatum in obsessive-compulsive patients and matched control subjects using the same method described above (Chapter 6). A decrease in *N*-acetylaspartate was measured. Since *N*-acetylaspartate is found only within neurons, decreased *N*-acetylaspartate suggests these patients may have a reduction in neuronal density in this region.



## **7.1 Limitations**

### 7.1.1 Quantification Limitations

Three factors continue to limit the precision of in-vivo spectral quantification: poor spectral resolution, low signal to noise ratio, and unknown spectral baseline components. Spectral resolution is partially determined by the hardware used and the location in the body that is being studied. However, some improvements by shimming are possible. The system at 4.0 Tesla does not yet have an automated shimming package available (such as the one used at 1.5 Tesla (7)) which calculates the global shims sets for all shims (including higher order shim sets). Such an automated shimming package improved spectral linewidth consistency at 1.5 T and should do the same at 4.0 T when it is implemented.

Signal to noise ratio is limited by the size of the volume studied and the total time of the experiment. Since it is desirable to acquire data from increasingly smaller volumes (to reduce partial volume effects), and data collection time does not increase, the signal to noise ratio of our experiments is continuously decreasing. The acquisition of data at 4.0 Tesla partially alleviated both resolution and signal to noise problems. This is due to the gain in signal to noise ratio, as well as the increase in chemical shift dispersion, which occurs when data is collected at higher fields (8). The use of magnetic field strengths higher than 4.0 T may increase S/N and chemical shift dispersion and further improve quantification precision.

Finally, the dominant factor that contributes to imprecise metabolite quantification is the uncharacterized macromolecule resonances that occur on the spectral

baseline. The main macromolecule components (3.00 ppm, 2.15 ppm, and 2.05 ppm) were modeled with Gaussian lineshapes, however this characterization is only an approximation based on experimental results. Therefore, inaccurate characterization of these resonances will undoubtedly decrease the precision of other metabolites.

### 7.1.2 In-Vivo Application Limitations

The in-vivo studies of schizophrenia and obsessive-compulsive disorder suffered from several limitations which must be emphasized. First, due to the severe selection criteria which was placed on the patient groups –schizophrenic patients were first episode and never treated – the number of patients studied was small. Second, some metabolite levels were quantified with high standard deviations due to a combination of low S/N, poor resolution, and biological variation. Therefore care must be taken when these results are interpreted.

Many metabolites also have multiple roles within the sampled tissue. For example, glutamine is both a precursor and a breakdown product of glutamate. Therefore, there is an inherent ambiguity in the physiological interpretation of changes in the level of this metabolite. Similarly, changes in the PCr/Cr resonance can not be definitively attributed to changes in either PCr or Cr or both. Finally, changes in measured metabolite levels are usually attributed to changes in concentration. However, metabolite level changes will also occur due to changes in  $T_1$  and/or  $T_2$  relaxation. Therefore, in the absence of relaxation measurements, this possibility should be considered for the physiological interpretation of results.

## 7.2 Future Work

### 7.2.1 Future Work in Short Echo $^1\text{H}$ Quantification

Two questions in regards to the quantification of short echo  $^1\text{H}$  spectra must be answered. First, would the acquisition of a metabolite nulled spectrum (as proposed by Behar *et al* (6) and described in Chapter 1, Section 1.3.8) in addition to the normally collected spectrum significantly increase quantification precision and reproducibility? Since the collection of such a spectrum requires a considerable amount of time, the gain in quantification precision must be significant to warrant this approach for clinical studies. Second, spectral editing techniques have been proposed to measure several metabolites including taurine, glucose, and  $\gamma$ -aminobutyric acid (9, 10, 11). Editing techniques may improve the quantification precision of these metabolites by simplifying the acquired spectrum, although other metabolite information is lost. However, spectral editing techniques must be evaluated in vivo to determine whether this approach would lead to increased quantification precision for the edited metabolite compared to short echo  $^1\text{H}$  MRS.

There are also potential signal to noise gains to be made through the use of other coil designs such as smaller head coils (since less noise would be detected), and phased array coils (12). Phased array coils may provide a significant advantage for the acquisition of data near the surface of the brain (i.e. anterior cingulate). If such coils increased the signal to noise ratio of acquired data, this would improve quantification precision both at 1.5 T and at 4.0 T.

The simultaneous acquisition of multiple spectra should also be considered. Chemical shift imaging (CSI, (13)) is one approach that could be used. The advantages of this technique are that multiple voxels could be acquired simultaneously from an oblique slice passing through the prefrontal cortex and subcortical regions (including the thalamus), and that voxel positions within the slice could be finalized following data acquisition. The disadvantages include signal bleedthrough (14) and inconsistent water suppression due to magnetic field inhomogeneity. Another approach would be the acquisition of multiple single voxels during the same repetition time (TR) interval. Since the in-vivo  $^1\text{H}$  MR signal at 4.0 T has decayed to the level of noise (due to  $T_2^*$  relaxation) by 0.5 seconds, and the acquisition TR is 2.0 seconds, four different voxels could be excited during one TR interval. This would result in the acquisition of four spectra from different locations, without the signal bleedthrough effects present in CSI techniques, during the same acquisition time that is currently used to acquire data from a single location.

### 7.2.2 Future Applications to Schizophrenia and Obsessive-Compulsive Disorder

The investigation of mental disorders such as schizophrenia and obsessive-compulsive disorder is an ongoing process which will likely continue for many years. The application of short echo  $^1\text{H}$  spectroscopy to the investigation of these illnesses has already contributed important information to the puzzle. However, this technique should be applied to other brain regions that have yet to be studied including the ventral tegmental region and the thalamus.

Finally, future studies must be aimed at the replication of previous work. For example, the finding of increased glutamine in the left medial prefrontal cortex of never treated schizophrenic patients must be replicated by other groups and by ourselves at 4.0 Tesla.

### 7.3 Reference

---

1. Ross B, Michaelis T. Clinical Applications of Magnetic Resonance Spectroscopy. *Magnetic Resonance Quarterly* 10, 191-247 (1994).
2. Stanley JA, Drost DJ, Williamson PC, Thompson RT. The Use of a *Priori* Knowledge to Quantify Short Echo *in Vivo*  $^1\text{H}$  MR Spectra. *Magn. Reson. Med.* 34, 17-24 (1995).
3. Hoult DI, Chen C-N, Sank VJ. The Field Dependence of NMR Imaging II. Arguments Concerning an Optimal Field Strength. *Magn. Reson. Med.* 3, 730-746 (1986).
4. de Graaf AA, van Dijk JE, Bovee WMMJ. QUALITY: Quantification Improvement by Converting Lineshapes to the Lorentzian Type. *Magn. Reson. Med.* 13, 343-357 (1990).
5. Klose U. In Vivo Proton Spectroscopy in Presence of Eddy Currents. *Magn. Reson. Med.* 14, 26-30 (1990).
6. Behar KL, Rothman DL, Spencer DD, Petroff OAC. Analysis of Macromolecule Resonances in the  $^1\text{H}$  NMR Spectra of Human Brain. *Magn. Reson. Med.* 32, 294-302 (1994).
7. Liu Z, Javaid T, Hu J, Brown TR. CSI—Autoshim Procedures for Body and Surface Coil. In: *Proceedings of the Society of Magnetic Resonance 2<sup>nd</sup>*

---

*Annual Meeting; August 6-12; San Francisco, California; Page 1174.*

Abstract. (1994).

8. Barfuss H, Fischer H, Hentschel D, Ladebeck R, Oppelt A, Wittig R, Duerr W, Oppelt R. In Vivo Magnetic Resonance Imaging and Spectroscopy of Humans with a 4T Whole-body Magnet. *NMR in Biomed.* 3, 31-45 (1990).
9. Hardy DL, Norwood TJ. Spectral Editing Technique for the In-Vitro and In-Vivo Detection of Taurine. *J Magn. Reson.* 133, 70-78 (1998).
10. Keltner JR, Wald LL, Ledden PJ, Chen YC, Matthews RT, Kuestermann EH, Baker JR, Rosen BR, Jenkins BG. A Localized Double-Quantum Filter For the In Vivo Detection of Brain Glucose. *Magn. Reson. Med.* 39, 651-656 (1998).
11. Keltner JR, Wald LL, Frederick BD, Renshaw PF. In Vivo Detection of GABA in Human Brain Using a Localized Double-Quantum Filter Technique. *Magn. Reson. Med.* 37, 366-371 (1997).
12. Wright SM, Wald LL. Theory and Application of Array Coils in MR Spectroscopy. *NMR in Biomed.* 10, 394-410 (1997).
13. Brown TR, Kincaid BM, Ugurbil K. NMR Chemical Shift Imaging in Three Dimensions. *Proc. Natl. Acad. Sci. USA* 79, 3523-3526 (1982).
14. Brown TR. Practical Applications of Chemical Shift Imaging. *NMR in Biomedicine.* 5, 238-243 (1992).

## Appendix A: Post Processing by Eddy Current Correction

Post processing of MR spectroscopy data by eddy current correction (ECC) utilizes a reference signal to determine time dependent phase shifts. In the experiments described within this thesis, an unsuppressed water spectrum was always used as the reference signal. The water suppressed time domain signal has the form given by equation A-1.

$$\hat{y}_j(t, r) = c_j \cdot e^{i(2\pi\omega_j(r,t)t + \phi_j)} \cdot e^{-\pi\alpha_j t} \quad [\text{A-1}]$$

Where  $\hat{y}_j(t, r) \equiv$  Sampled points at time  $t$  and position  $r$  from resonance  $j$ .

- $c_j \quad \equiv$  Amplitude of resonance  $j$ .
- $\omega_j \quad \equiv$  Chemical shift (frequency) of resonance  $j$ .
- $\alpha_j \quad \equiv$  Lorentzian damping of resonance  $j$ .
- $\phi_j \quad \equiv$  Phase of resonance  $j$ .

Similarly, water unsuppressed data has the form given by equation A-2.

$$y_w(t, r) = c_w \cdot e^{i(2\pi\omega_w(r,t)t + \phi_w)} \cdot e^{-\pi\alpha_w t} \quad [\text{A-2}]$$

Where  $\hat{y}_w(t, r) \equiv$  Sampled points at time  $t$  and position  $r$  from resonance  $w$ .

- $c_w \quad \equiv$  Amplitude of resonance  $w$ .
- $\omega_w \quad \equiv$  Chemical shift (frequency) of resonance  $w$ .
- $\alpha_w \quad \equiv$  Lorentzian damping of resonance  $w$ .
- $\phi_w \quad \equiv$  Phase of resonance  $w$ .

If we make the assumptions that  $\sigma_j \times \Delta B_{0,D} \ll 1$ ,  $\sigma_j \times \Delta B_{0,V} \ll 1$ ,  $B_0 \times \sigma_j = 0$  (reference is on resonance) and  $\Delta B_{0,S}(r) = 0$  in Chapter 1 equation [1-6] then the reference precession frequency is described by equation A-3.

$$\omega_w(r,t) = -\gamma \cdot (\Delta B_{0,D} \cdot e^{-(t\alpha_D)} + \Delta B_{0,V} \cdot \sin(t \cdot f_V + \phi_V) \cdot e^{-(t\alpha_V)}) \quad [A-3]$$

These time dependent frequency shifts, which also exist in the suppressed signal, can be considered as time dependent phase shifts of a single frequency (the reference). Therefore a subtraction of the water reference signal phase removes the effects of  $\Delta B_{0,D}$  and  $\Delta B_{0,V}$  from the suppressed data.



## Appendix B: Post Processing by QUALITY Deconvolution

The signal acquired from the MR experiment can be written in the form of equation B-1. The symbols used are described in Appendix A.

$$\hat{y}_j(t, r) = c_j \cdot e^{i(2\pi\omega_j(r,t) \cdot t + \phi_j)} \cdot e^{-\pi\alpha_j \cdot t} \quad [\text{B-1}]$$

For the QUALITY deconvolution it is assumed that  $\sigma_j \times \Delta B_{0,D} \ll 1$ ,  $\sigma_j \times \Delta B_{0,V} \ll 1$ , and  $B_0 \times \sigma_j = 0$  (reference is on resonance) for equation [1-6] in Chapter 1.

However, it is not assumed that  $\Delta B_{0,S}(r) = 0$ . Therefore the MR signal over the entire volume of interest is given by equation B-2.

$$y_j(t) = \int_r c_j \cdot e^{i(2\pi\omega_j(r,t) \cdot t + \phi_j)} \cdot e^{-\pi\alpha_j \cdot t} \cdot d^3 r \quad [\text{B-2}]$$

Substituting equations 1-5 and 1-6 from Chapter 1 gives equation B-3.

$$y_j(t) = \int_r c_j \cdot e^{-2\pi i \gamma (B_0 + \Delta B_{0,D} \cdot e^{-t/\alpha_D} + \Delta B_{0,V} \cdot \sin(t \cdot f_V + \phi_V) \cdot e^{-t/\alpha_V} + \Delta B_{0,S}(r))(1 - \sigma_j) \cdot t + \phi_j / \gamma} \cdot e^{-\pi\alpha_j \cdot t} \cdot d^3 r \quad [\text{B-3}]$$

The portion of the equation with dependence on  $r$  can be separated as follows assuming  $\sigma_j \times \Delta B_{0,D} \ll 1$ ,  $\sigma_j \times \Delta B_{0,V} \ll 1$ , and  $\sigma_j \times \Delta B_{0,S} \ll 1$ :

$$y_j(t) = c_j \cdot e^{-2\pi i \gamma \cdot t (B_0(1 - \sigma_j) + \Delta B_{0,D} \cdot e^{-t/\alpha_D} + \Delta B_{0,V} \cdot \sin(t \cdot f_V + \phi_V) \cdot e^{-t/\alpha_V} + \phi_j / \gamma \cdot t)} \cdot e^{-\pi\alpha_j \cdot t} \cdot \int_r e^{-2\pi i \gamma (\Delta B_{0,S}(r) \cdot t)} \cdot d^3 r \quad [\text{B-4}]$$

Now consider a reference signal that consists of a single peak on resonance:

$$y_w(t) = c_w \cdot e^{-2\pi i \gamma \cdot t (B_0(1-\sigma_w) + \Delta B_{0,D}) \cdot e^{-t(\alpha_D)} + \Delta B_{0,V} \cdot \sin(t \cdot f_V + \phi_V) \cdot e^{-t(\alpha_V)} + \phi_w / \gamma \cdot t} \cdot e^{-\pi \alpha_w \cdot t} \cdot \int_r e^{-2\pi i \gamma (\Delta B_{0,w}(r) \cdot t)} \cdot d^3 r$$

[B-5]

Following normalization of the reference signal (divide by  $c_w$ )

$$y_w(t) = e^{-2\pi i \gamma \cdot t (B_0(1-\sigma_w) + \Delta B_{0,D}) \cdot e^{-t(\alpha_D)} + \Delta B_{0,V} \cdot \sin(t \cdot f_V + \phi_V) \cdot e^{-t(\alpha_V)} + \phi_w / \gamma \cdot t} \cdot e^{-\pi \alpha_w \cdot t} \cdot \int_r e^{-2\pi i \gamma (\Delta B_{0,w}(r) \cdot t)} \cdot d^3 r$$

[B-6]

Now deconvolution of the data is done as a division in the time domain.

Therefore simply divide the data spectrum by the reference spectrum, assuming the reference is on resonance ( $\sigma_w = 0$ ) and the experiment and reference signals have the same phase ( $\phi_j = \phi_w$ ).

$$y_c(t) = \frac{y_j(t)}{y_w(t)} = c_j \cdot e^{-2\pi i \gamma \cdot t (B_0(1-\sigma_j))} \cdot \frac{e^{-\pi \alpha_j \cdot t}}{e^{-\pi \alpha_w \cdot t}}$$

[B-7]

Finally multiplication by the damping term of the reference restores the original spectral linewidth.

$$y_c(t) = c_j \cdot e^{-2\pi i \gamma \cdot t (B_0(1-\sigma_j))} \cdot e^{-\pi \alpha_j \cdot t}$$

[B-8]

The corrected signal has had all spatially dependant and time dependant variations in  $B_0$  removed and is therefore purely Lorentzian.

## Appendix C: Singular Value Decomposition of MR Spectra

The linear fitting routine described in Chapter 1 employs a singular value decomposition of a data matrix and interprets the results assuming the data is composed of a series of exponentially damped sinusoids according to the following formulation in equation C-1.

$$\hat{x}_n = \sum_{k=1}^K C_k \cdot Z_k^n \quad [C-1]$$

Such that  $Z_k = e^{(-b_k + i\omega_k) \cdot \Delta t}$

- Where
- $k \equiv 1, 2 \dots K$  are defined as signal poles
  - $C_k \equiv$  complex amplitude in which the phase has been absorbed
  - $b_k \equiv$  damping factors of sinusoid  $k$
  - $\omega_k \equiv$  angular frequency of sinusoid  $k$
  - $\Delta t \equiv$  dwell time

Equation C-1 can be rewritten in matrix form as given by equation C-2.

$$\hat{x}_n = \tilde{e} \cdot Z^n \cdot C \quad [C-2]$$

- Where
- $\tilde{e} \equiv$  a row vector with entries equal to 1
  - $Z^n \equiv$  a  $K \times K$  diagonal matrix with entries equal to  $Z_k$
  - $C \equiv$  a column vector with entries equal to the amplitudes  $C_k$

The data may be arranged in matrix form as shown in equation C-3.

$$X = \begin{bmatrix} x_0 & x_1 & x_2 & x_3 & \cdots & x_M \\ x_1 & x_2 & x_3 & x_4 & \cdots & x_{M+1} \\ x_2 & x_3 & x_4 & x_5 & \cdots & x_{M+2} \\ \vdots & \vdots & \vdots & \vdots & & \vdots \\ x_L & x_{L+1} & x_{L+2} & x_{L+3} & \cdots & x_{N-1} \end{bmatrix} \quad [\text{C-3}]$$

This data matrix is decomposed into a left and right singular matrix by singular value decomposition (SVD). The SVD result is related to specific resonances by substituting equation C-1 above into equation C-3.

$$X = \begin{bmatrix} \sum_{k=1}^K C_k \cdot Z_k^0 & \sum_{k=1}^K C_k \cdot Z_k^1 & \sum_{k=1}^K C_k \cdot Z_k^2 & \sum_{k=1}^K C_k \cdot Z_k^3 & \cdots & \sum_{k=1}^K C_k \cdot Z_k^M \\ \sum_{k=1}^K C_k \cdot Z_k^1 & \sum_{k=1}^K C_k \cdot Z_k^2 & \sum_{k=1}^K C_k \cdot Z_k^3 & \sum_{k=1}^K C_k \cdot Z_k^4 & \cdots & \sum_{k=1}^K C_k \cdot Z_k^{M+1} \\ \sum_{k=1}^K C_k \cdot Z_k^2 & \sum_{k=1}^K C_k \cdot Z_k^3 & \sum_{k=1}^K C_k \cdot Z_k^4 & \sum_{k=1}^K C_k \cdot Z_k^5 & \cdots & \sum_{k=1}^K C_k \cdot Z_k^{M+2} \\ \vdots & \vdots & \vdots & \vdots & & \vdots \\ \sum_{k=1}^K C_k \cdot Z_k^L & \sum_{k=1}^K C_k \cdot Z_k^{L+1} & \sum_{k=1}^K C_k \cdot Z_k^{L+2} & \sum_{k=1}^K C_k \cdot Z_k^{L+3} & \cdots & \sum_{k=1}^K C_k \cdot Z_k^{N-1} \end{bmatrix} \quad [\text{C-4}]$$

This can be factored into two separate matrices as follows:

$$X = \begin{bmatrix} 1 & 1 & 1 & \cdots & 1 \\ Z_1 & Z_2 & Z_3 & \cdots & Z_k \\ Z_1^2 & Z_2^2 & Z_3^2 & \cdots & Z_k^2 \\ \vdots & \vdots & \vdots & & \vdots \\ Z_1^L & Z_2^L & Z_3^L & \cdots & Z_k^L \end{bmatrix} \cdot \begin{bmatrix} C_1 & C_1 Z_1 & C_1 Z_1^2 & \cdots & C_1 Z_1^M \\ C_2 & C_2 Z_2 & C_2 Z_2^2 & \cdots & C_2 Z_2^M \\ C_3 & C_3 Z_3 & C_3 Z_3^2 & \cdots & C_3 Z_3^M \\ \vdots & \vdots & \vdots & & \vdots \\ C_k & C_k Z_k & C_k Z_k^2 & \cdots & C_k Z_k^M \end{bmatrix} \quad [\text{C-5}]$$

The left matrix above has the special characteristic of a Vandermonde matrix: each row is equal to the previous one postmultiplied by Z. Therefore, we can write the relation C-6.

$$U_b \cdot Z' = U_t$$

[C-6]

Where  $U_b$  and  $U_t$  stand for the left matrix above where the bottom and top row, respectively, have been removed. Calculation and diagonalization of the matrix  $Z'$  using the left hand singular matrix following SVD of the data matrix for  $U_b$  and  $U_t$  yields the signal poles  $Z$ . This in turn yields the frequencies and damping factors of each resonance. The amplitudes and phases can then be determined directly from the first column of the right matrix in Equation C-5.

## Appendix D: Non-Linear Minimization

The noise in the NMR signal is Gaussian distributed, therefore for purposes of minimization, we choose a merit function  $X^2$  defined by equation D-1.

$$X^2(\bar{a}) = \sum_{i=1}^N \left[ \frac{y_i - y(x_i, \bar{a})}{\sigma_i} \right]^2 \quad [\text{D-1}]$$

Where

$\bar{a}$	≡ vector of parameters
$\sigma_i$	≡ variance at point i
$y_i$	≡ data at point i

Minimization of this  $X^2$  merit function results in parameter values that are the most likely to occur given a particular data set.

A Levenberg-Marquardt minimization routine employs two different approaches to minimize the  $X^2$  merit function depending on the distance of this function from its minimum. The first method, called the 'Method of Steepest Descent', was first proposed by Cauchy in 1847. This method estimates the parameter values which give the minimum value of  $X^2$  based on the current parameter values and the gradient of the  $X^2$  function given in equation D-2.

$$\bar{a}_{\min} = \bar{a}_i - \text{const} \cdot \nabla X^2(\bar{a}_i) \quad [\text{D-2}]$$

Where

- $a_{\min}$              $\equiv$  value of the next guess of parameter a
- $a_i$                   $\equiv$  current value of parameter a
- $\nabla X^2(a_i)$         $\equiv$  value of the derivative of each parameter

The second approach to minimization utilizes the Taylor Series expansion of the  $X^2$  merit function defined by equation D-1.

$$X^2(\bar{a}) = X^2(0) + \sum_i \frac{dX^2}{da_i} \cdot a_i + \frac{1}{2} \cdot \sum_{i,j} \frac{d^2X^2}{da_i \cdot da_j} \cdot a_i \cdot a_j + \dots \quad [\text{D-3}]$$

Which can be approximated as:

$$X^2(\bar{a}) = c - b \cdot \bar{a} + \frac{1}{2} \cdot \bar{a} \cdot [A] \cdot \bar{a} \quad [\text{D-4}]$$

Where

- $c$                   $\equiv X^2(0)$
- $b$                   $\equiv -\nabla X^2(a_i)$
- $[A]$                 $\equiv \frac{d^2X^2}{da_i \cdot da_j}$

Taking the derivative and setting equal to zero (at minimum) gives:

$$[A] \cdot \bar{a}_{\min} = b \quad [\text{D-5}]$$

And at the current point we have:

$$[A] \cdot \bar{a}_i = \nabla X^2(\bar{a}_i) + b \quad [D-6]$$

Subtracting equation D-6 from equation D-5 gives:

$$\bar{a}_{\min} = \bar{a}_i + [A]^{-1} [-\nabla X^2(\bar{a}_i)] \quad [D-7]$$

Therefore, if the quadratic approximation is a good one, then the values of  $a_i$  which yield the minimum  $X^2$  value can be calculated using equation D-7.

Since the model function and hence the derivatives of the model function are known completely and input into the fitting routine, both equations [D-2] and [D-7] can be used at will. Therefore, all that remains is to decide which one to use at any particular time. Marquardt proposed a method of varying between the ‘Steepest Descent Method’ and ‘Quadratic Approximation Method’ based on a suggestion by Levenberg. Thus the Levenberg-Marquardt minimization routine seamlessly approximates the ‘Steepest Descent Method’ when far from minimum, and the ‘Quadratic Approximation Method’ when near the minimum.



## Appendix E: Quantification of Simulated $^1\text{H}$ Short Echo Spectra

In-vivo simulations were created (Figure E-1) to determine the accuracy and precision attainable when fitting in-vivo data utilizing prior knowledge of metabolite lineshapes obtained from in-vitro metabolite spectra. In-vitro spectra were acquired and fully parameterized as described in detail in Chapters one and two. Residual water and resonances outside the region 1.9-3.5 ppm were removed using results from a fit with HLSVD (see Chapter 1). These in-vitro metabolite spectra were scaled and combined (Figure E-1 column A) to create a simulated in-vivo spectrum (Figure E-1 column B) with the following relative metabolite levels (correct values obtained by separately fitting each metabolite spectrum): *N*-acetylaspartate – 6.0, glutamate – 3.38, glutamine – 1.69,  $\gamma$ -aminobutyric acid – 1.88, aspartate – 0.78, *N*-acetylaspartyl-glutamate – 1.00, taurine – 0.44, glucose – 0.38, choline – 2.50, phosphocreatine – 3.00, scyllo-inositol – 1.00, myo-inositol – 0.19, macromolecule at 3.00 ppm – 1.00, and macromolecule at 2.05 ppm – 5.00.

To further reproduce in-vivo conditions, the simulated spectrum was line broadened so that the  $\text{NAA}_{\text{CH}_3}$  peak had a full width at half maximum of 6 Hz (using an exponential damping function in the time domain), simulating the overlap of resonance lines at 1.5 T. The signal to noise ratio (calculated as the intensity of the  $\text{NAA}_{\text{CH}_3}$  resonance (2.0 ppm) divided by the standard deviation of the noise in the frequency domain) of the simulated spectrum was 280:1. To create realistic in-vivo signal to noise ratios, in-vivo noise was acquired by setting the RF voltages to zero in the same acquisition sequence as that used to obtain all in-vitro and in-vivo spectra (STEAM, TE=20 ms, TM=30 ms) and added to the simulated spectrum. Eight different in-vivo noise representations were acquired

(Figure E-1 column C). Therefore, eight simulated spectra were created, each one containing identical metabolite information with different noise at a single signal to noise ratio (Figure E-1 column D). This process was repeated for twelve different signal to noise ratios (280:1, 140:1, 120:1, 107:1, 90:1, 78:1, 69:1, 62:1, 52:1, 41:1, 29:1, 23:1). The signal to noise ratio of data acquired in the clinical studies of chapter 5 and 6 were approximately 20:1. Quality deconvolution was done with a simulated unsuppressed water FID.

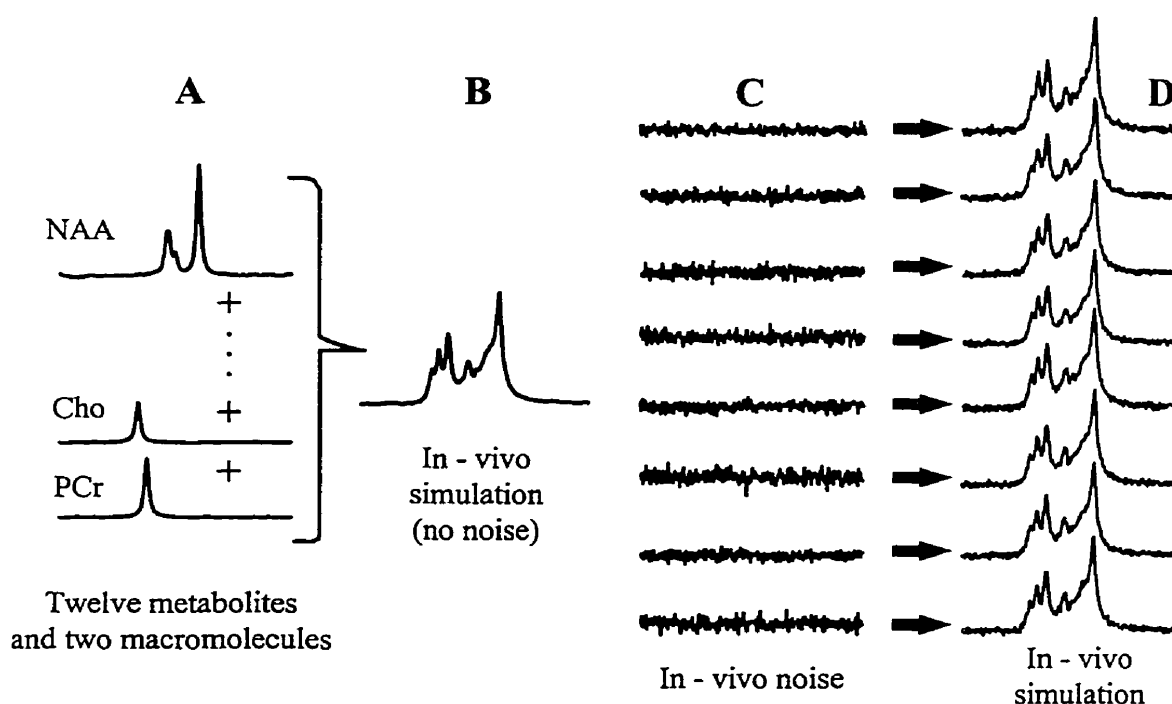


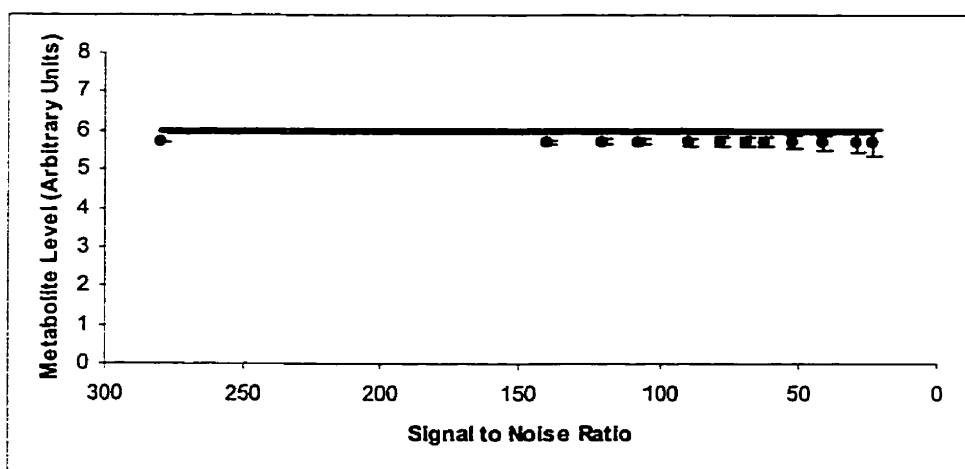
**Figure E-1: The Creation of In-Vivo Simulated Spectra**

Known levels of in-vitro spectra were combined to create an in-vivo simulation. The resulting spectrum was line broadened to simulate conditions of in-vivo overlap. The simulated spectrum was added to eight in-vivo noise representations to create a series of eight simulations each containing identical metabolite information but different noise.

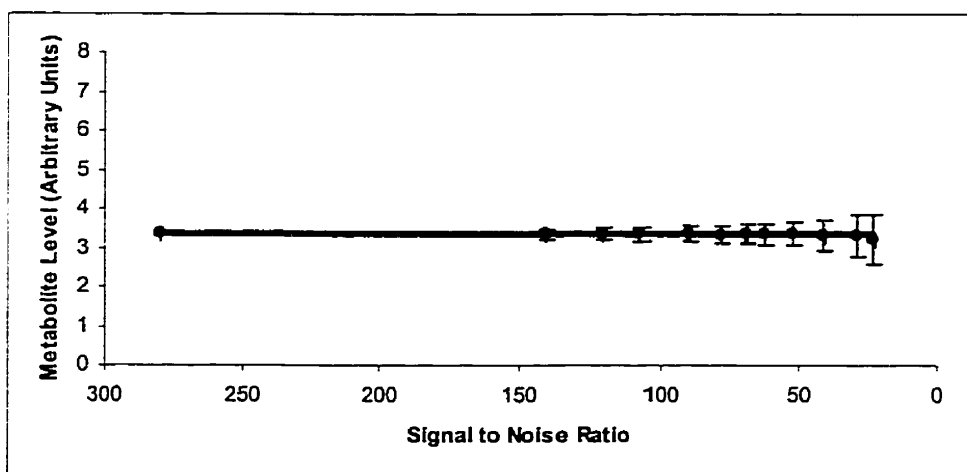
The results of fitting these simulated spectra are summarized in Figure E-2. Each plot within this figure displays the average quantified level and standard deviation of one metabolite as a function of signal to noise ratio, along with the expected value.

Quantified metabolite levels showed various levels of accuracy. The percent difference from expected values ranged from 0.3% for choline to 220% for myo-inositol, although the maximum deviation from the expected value was 0.5 absolute units (*N*-acetylaspartyl-glutamate). *N*-acetylaspartate, glutamate, glutamine, and phosphocreatine + creatine were quantified with the following average % differences from expected values, 4.9%, 1.3%, -2.3%, and -4.9% respectively. The results were highly reproducible across all signal to noise ratios. As expected, metabolite level standard deviations increased as signal to noise decreased. At a signal to noise ratio of 23:1, which is typical of the clinical studies presented in Chapters five and six, *N*-acetylaspartate, glutamate, glutamine, phosphocreatine + creatine, and choline were quantified with the following CV (standard deviation divided by mean X 100%), 5.9%, 19.6%, 14.0%, 5.6%, and 9.8% respectively.

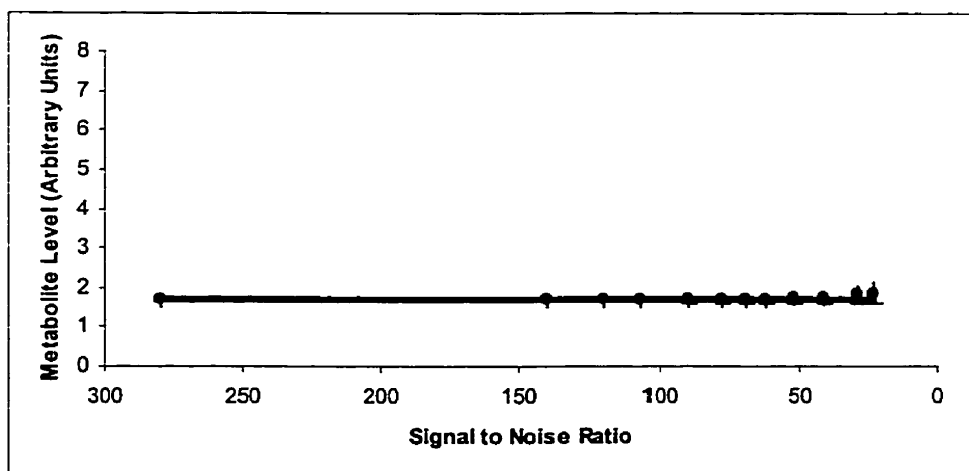
### N-acetylaspartate

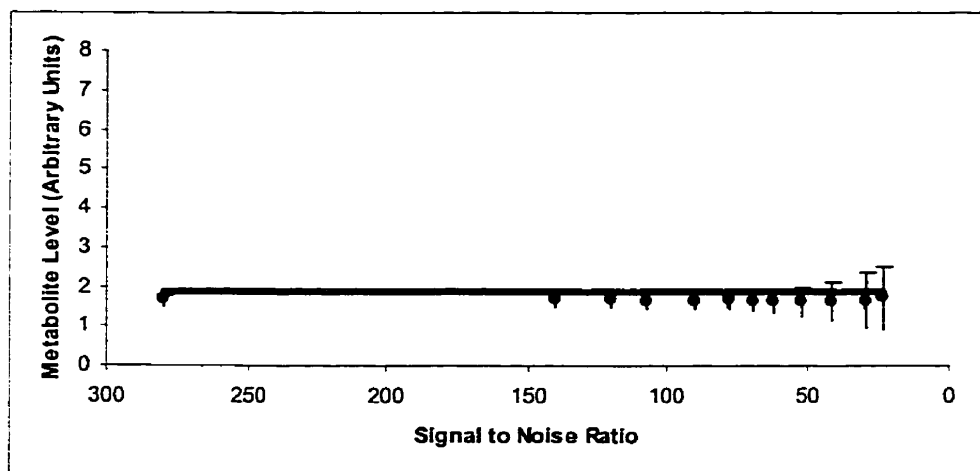


### Glutamate

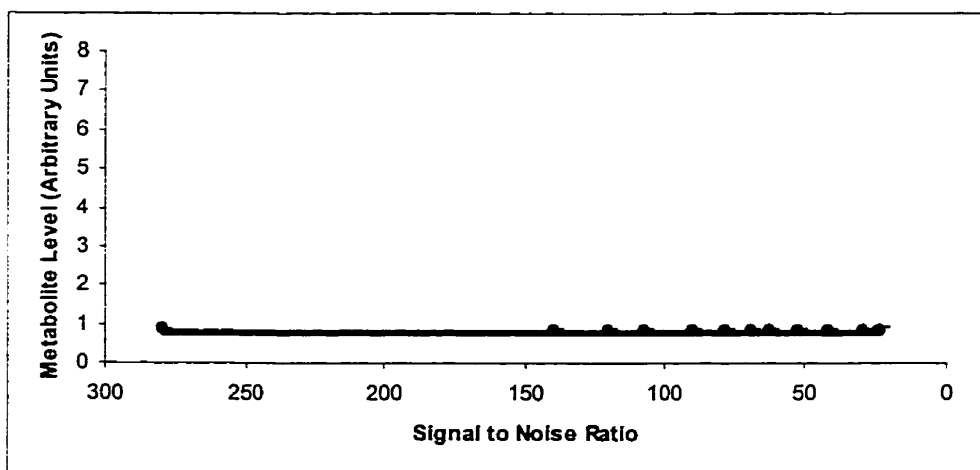
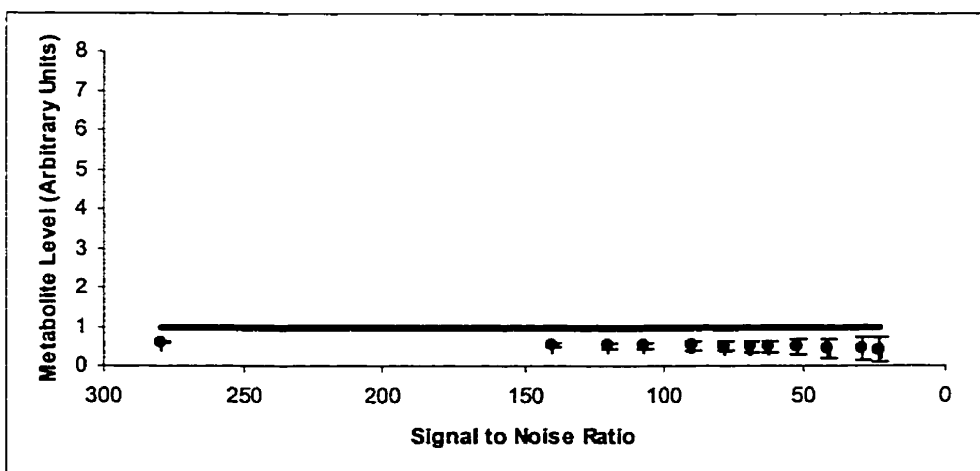


### Glutamine

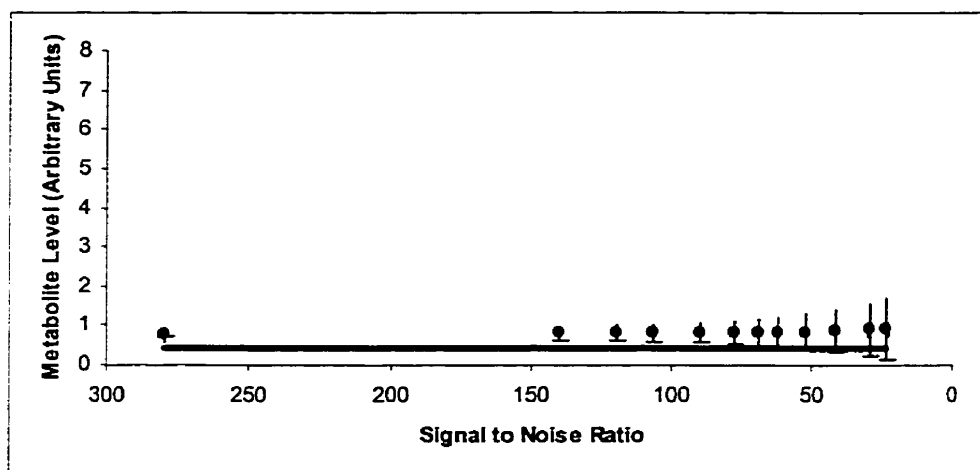


$\gamma$ -aminobutyric acid

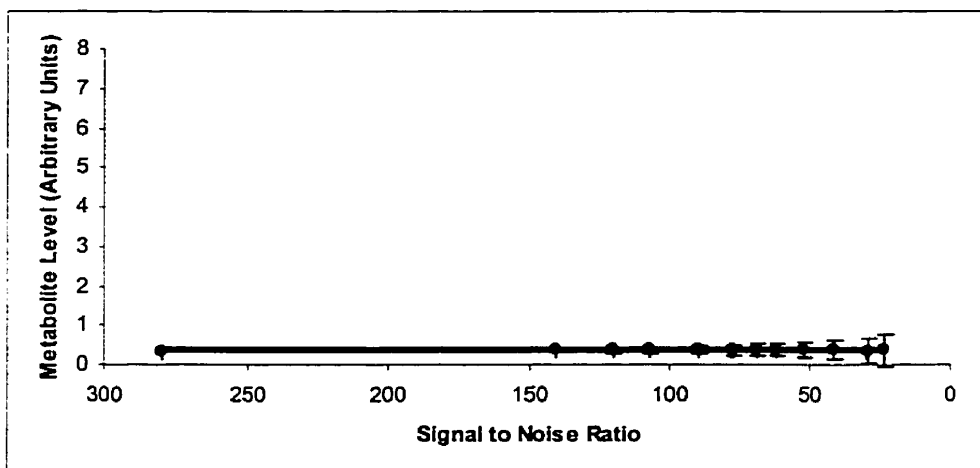
## Aspartate

*N*-Acetylaspartyl-glutamate

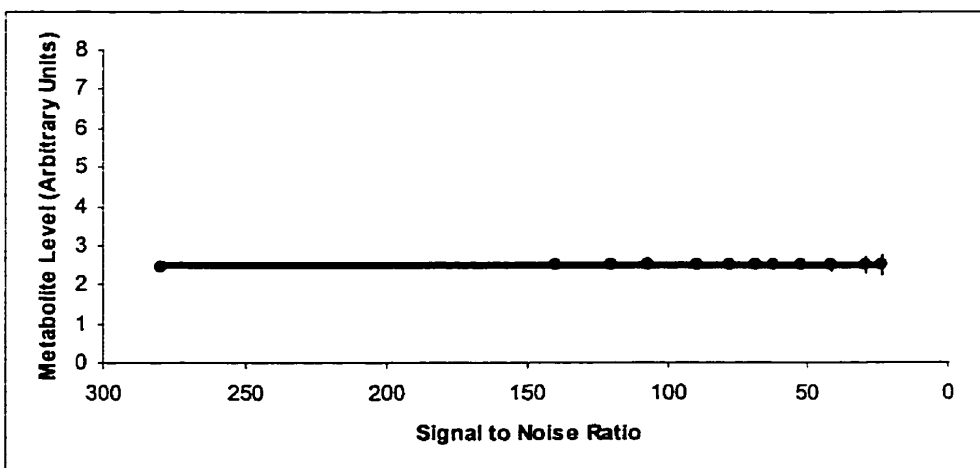
## Taurine



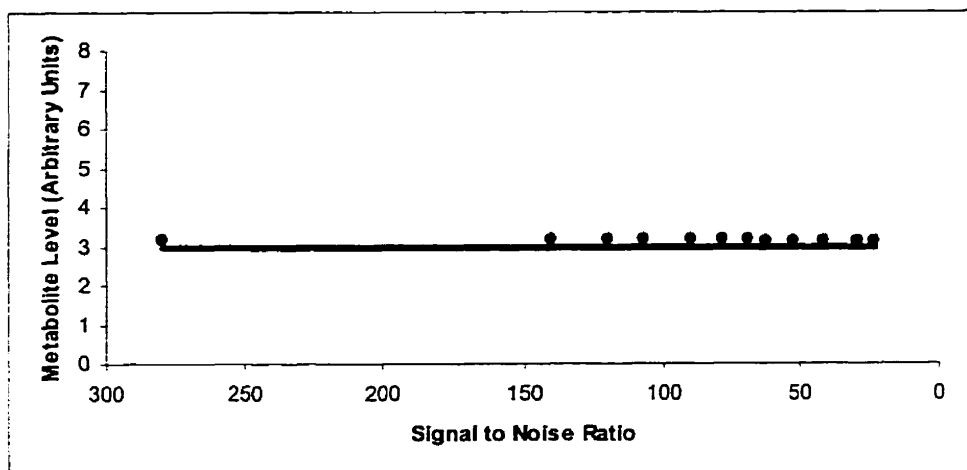
## Glucose



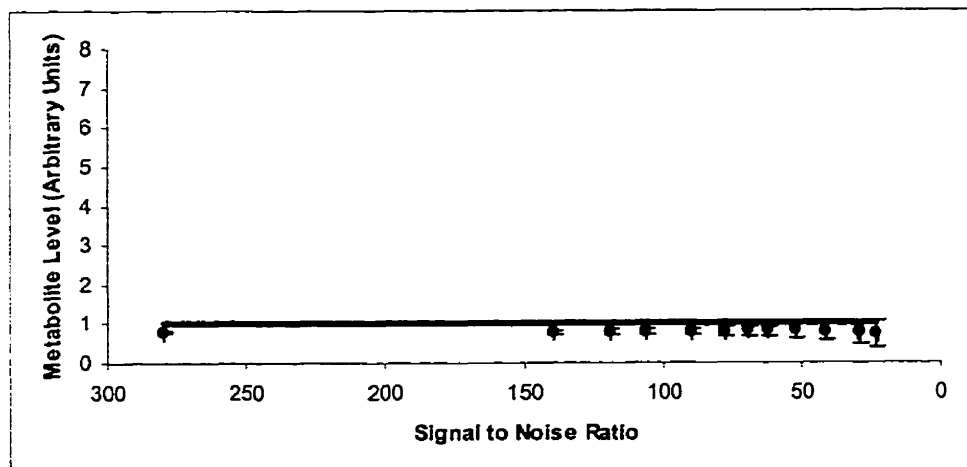
## Choline



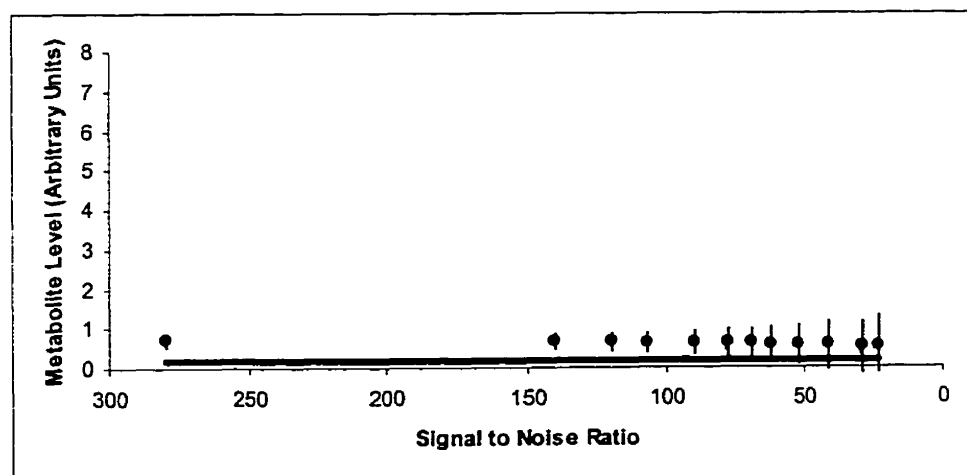
## Phosphocreatine + Creatine



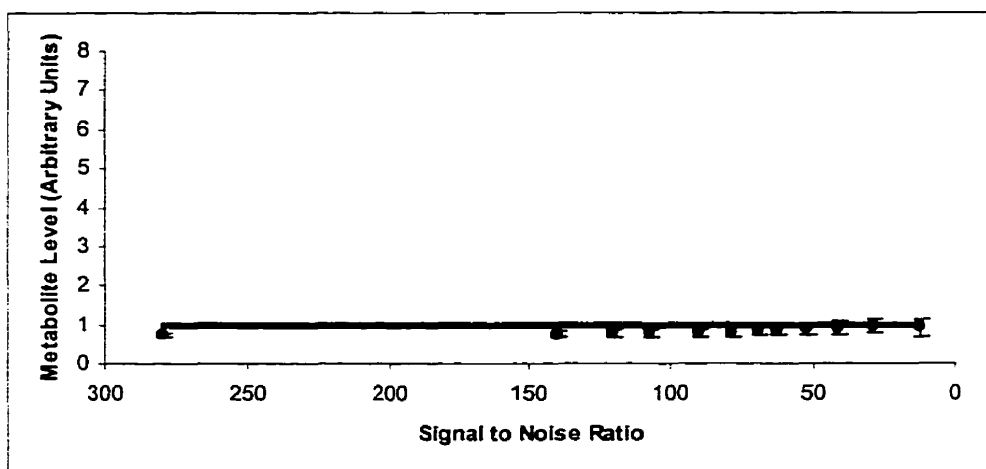
## Scyllo-Inositol



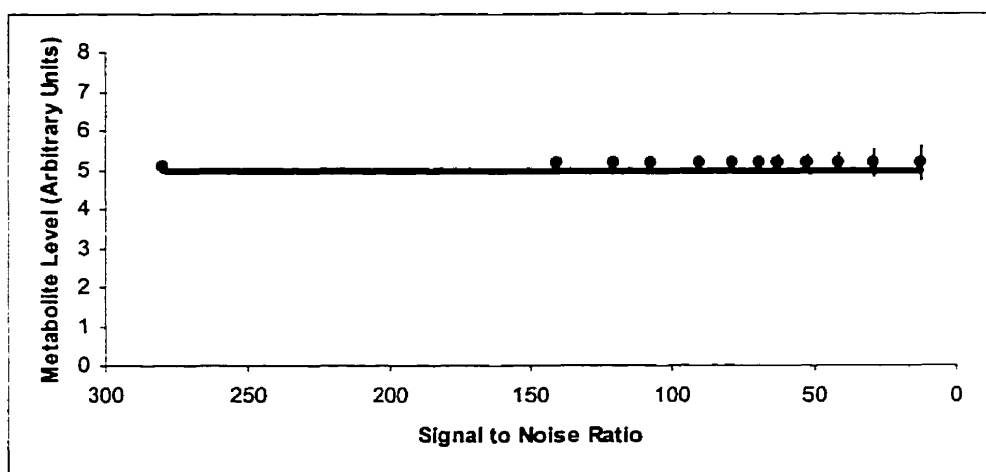
## Myo-Inositol



## Macromolecule at 3.00 ppm



## Macromolecule at 2.05 ppm

**Figure E-2: Results from the Quantification of In-Vivo Simulations**

Metabolite levels were quantified for each metabolite included in the in-vivo simulation. The results are summarized above. Each point represents the average metabolite level across eight simulated spectra at a single signal to noise ratio. The error bars represent one standard deviation. The dark solid line indicates the expected metabolite level. All plots are shown on the same scale.



# Appendix F: Ethics Approval for Studies Involving Human Subjects



## The UNIVERSITY of WESTERN ONTARIO

Vice-Provost • Health Sciences • Health Sciences Centre

REVIEW BOARD FOR HEALTH SCIENCES RESEARCH INVOLVING HUMAN SUBJECTS

### 1992-93 CERTIFICATION OF APPROVAL OF HUMAN RESEARCH

ALL HEALTH SCIENCES RESEARCH INVOLVING HUMAN SUBJECTS AT THE UNIVERSITY OF WESTERN ONTARIO IS CARRIED OUT IN COMPLIANCE WITH THE MEDICAL RESEARCH COUNCIL OF CANADA "GUIDELINES ON RESEARCH INVOLVING HUMAN SUBJECT."

#### 1992-93 REVIEW BOARD MEMBERSHIP

- 1) Dr. B. Borwein, Associate Dean-Research - Medicine (Chairman) (Anatomy/Ophthalmology)
  - 2) Ms. S. Hoddinott, Assistant Director of Research Services (Epidemiology)
  - 3) St. Joseph's Hospital Representative
  - 4) Dr. F. Rutledge, Victoria Hospital Representative (Critical Care - Medicine)
  - 5) Dr. D. Bocking, University Hospital Representative (Physician - Internal Medicine)
  - 6) Dr. M. Lennon, Office of the President Representative (Libraries)
  - 7) Mrs. E. Jones, Office of the President Representative (Community)
  - 8) Mrs. G. Grant, Office of the President Representative (Legal)
  - 9) Dr. D. Freeman, Faculty of Medicine Representative (Medicine)
  - 10) Dr. K. Campbell, Faculty of Medicine Representative (Epidemiology/Biostatistics)
  - 11) Dr. J.T. Hamilton, Faculty of Dentistry Representative (Pharmacology)
  - 12) Dr. H. Laschinger, Faculty of Nursing Representative (Nursing)
  - 13) Dr. J. Stouffer, Faculty of Applied Health Sciences Representative (Comm. Disorders)
  - 14) Dr. A. Taylor, Faculty of Kinesiology Representative (Kinesiology)
  - 15) Dr. L.S. Glowacki, Research Institutes Representative (Nephrology)
  - 16) Mrs. R. Yohnicki, Administrative Officer
- Alternates are appointed for each member.

THE REVIEW BOARD HAS EXAMINED THE RESEARCH PROJECT ENTITLED:  
"H and <sup>31</sup>P magnetic resonance spectroscopy in mental illness."

REVIEW NO: 3596

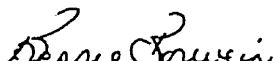
AS SUBMITTED BY: Dr. P.C. Williamson, Psychiatry, UH

AND CONSIDERS IT TO BE ACCEPTABLE ON ETHICAL GROUNDS FOR RESEARCH INVOLVING HUMAN SUBJECTS UNDER CONDITIONS OF THE UNIVERSITY'S POLICY ON RESEARCH INVOLVING HUMAN SUBJECTS.

APPROVAL DATE: 21 October 1992

AGENCY: MRC

TITLE: H and <sup>31</sup>P magnetic resonance spectroscopy in Schizophrenia.

  
Bessie Borwein, Chairman

c.c. Hospital Administration



## The UNIVERSITY of WESTERN ONTARIO

Vice-Provost • Health Sciences • Health Sciences Centre

### REVIEW BOARD FOR HEALTH SCIENCES RESEARCH INVOLVING HUMAN SUBJECTS

#### 1993-94 CERTIFICATION OF APPROVAL OF HUMAN RESEARCH

ALL HEALTH SCIENCES RESEARCH INVOLVING HUMAN SUBJECTS AT THE UNIVERSITY OF WESTERN ONTARIO IS CARRIED OUT IN COMPLIANCE WITH THE MEDICAL RESEARCH COUNCIL OF CANADA "GUIDELINES ON RESEARCH INVOLVING HUMAN SUBJECT."

#### 1993-94 REVIEW BOARD MEMBERSHIP

- 1) Dr. B. Borwein, Assistant Dean-Research - Medicine (Chairman) (Anatomy/Ophthalmology)
  - 2) Ms. S. Hoddinott, Assistant Director of Research Services (Epidemiology)
  - 3) Dr. J.M. Thompson, St. Joseph's Hospital Representative (Rheumatology - Medicine)
  - 4) Dr. F. Rutledge, Victoria Hospital Representative (Critical Care - Medicine)
  - 5) Dr. D. Bocking, University Hospital Representative (Physician - Internal Medicine)
  - 6) Dr. C.L. Murison, Office of the President Representative (Classical Studies)
  - 7) Mrs. E. Jones, Office of the President Representative (Community)
  - 8) Mrs. J. Buckrell, Office of the President Representative (Legal)
  - 9) Dr. D. Freeman, Faculty of Medicine Representative (Clinical Pharmacology - Medicine)
  - 10) Dr. L. Pederson, Faculty of Medicine Representative (Epidemiology/Biostatistics)
  - 11) Dr. J.T. Hamilton, Faculty of Dentistry Representative (Pharmacology)
  - 12) Dr. H. Laschinger, Faculty of Nursing Representative (Nursing)
  - 13) Dr. J. Stouffer, Faculty of Applied Health Sciences Representative (Comm. Disorders)
  - 14) Dr. D.H. Paterson, Faculty of Kinesiology Representative (Kinesiology)
  - 15) Dr. K. Speechley, Research Institutes Representative (Paediatrics)
  - 16) Mrs. R. Yohnicki, Administrative Officer
- Alternates are appointed for each member.

THE REVIEW BOARD HAS EXAMINED THE RESEARCH PROJECT ENTITLED:  
"IH and 31P magnetic resonance spectroscopy in mental illness."

REVIEW NO: 3434

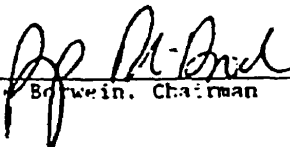
AS SUBMITTED BY: Dr. P.C. Williamson, Psychiatry, LPH

AND CONSIDERS IT TO BE ACCEPTABLE ON ETHICAL GROUNDS FOR RESEARCH INVOLVING HUMAN SUBJECTS UNDER CONDITIONS OF THE UNIVERSITY'S POLICY ON RESEARCH INVOLVING HUMAN SUBJECTS.

APPROVAL DATE: 11 August 1993 (UPDATED APPROVAL)

AGENCY: NATIONAL INSTITUTE OF MENTAL HEALTH ROCKWELL, MARYLAND U.S.A.

TITLE: IH and 31P magnetic resonance spectroscopy in schizophrenia.

  
Bessie Borwein, Chairman

c.c. Hospital Administration



## The UNIVERSITY of WESTERN ONTARIO

Vice-Provost • Health Sciences • Health Sciences Centre

### REVIEW BOARD FOR HEALTH SCIENCES RESEARCH INVOLVING HUMAN SUBJECTS

#### 1995-96 CERTIFICATION OF APPROVAL OF HUMAN RESEARCH

ALL HEALTH SCIENCES RESEARCH INVOLVING HUMAN SUBJECTS AT THE UNIVERSITY OF WESTERN ONTARIO IS CARRIED OUT IN COMPLIANCE WITH THE MEDICAL RESEARCH COUNCIL OF CANADA "GUIDELINES ON RESEARCH INVOLVING HUMAN SUBJECT."

#### 1995-96 REVIEW BOARD MEMBERSHIP

- 1) Dr. B. Borwein, Assistant Dean-Research - Medicine (Chairman) (Anatomy/Ophthalmology)
  - 2) Ms. S. Hoddinott, Assistant Director of Research Services (Epidemiology)
  - 3) Dr. R. Richards, St. Joseph's Hospital Representative (Surgery)
  - 4) Dr. F. Rutledge, Victoria Hospital Representative (Critical Care - Medicine)
  - 5) Dr. D. Bocking, University Hospital Representative (Physician - Internal Medicine)
  - 6) Dr. L. Heller, Office of the President Representative (French)
  - 7) Mrs. E. Jones, Office of the President Representative (Community)
  - 8) Mr. H.E. Fleming, Office of the President Representative (Legal)
  - 9) Dr. D. Freeman, Faculty of Medicine Representative (Clinical)
  - 10) Dr. D. Sim, Faculty of Medicine Representative (Basic) (Epidemiology)
  - 11) Dr. D. Johnston, Faculty of Dentistry Representative (Community Dentistry)
  - 12) Dr. H. Laschinger, Faculty of Nursing Representative (Nursing)
  - 13) Dr. S.J. Spaulding, Faculty of Applied Health Sciences Representative (Occup. Therapy)
  - 14) Dr. G. Leyshon, Faculty of Kinesiology Representative (Kinesiology)
  - 15) Dr. W. Khalil, Research Institutes Representative (Endocrinology & Metabolism)
  - 16) Mrs. R. Yohnicki, Administrative Officer
- Alternates are appointed for each member.

THE REVIEW BOARD HAS EXAMINED THE RESEARCH PROJECT ENTITLED:  
"Candidate neuronal circuits in schizophrenia."

REVIEW NO: 5263

AS SUBMITTED BY: Dr. P. Williamson, Psychiatry, Victoria/University Hospital

AND CONSIDERS IT TO BE ACCEPTABLE ON ETHICAL GROUNDS FOR RESEARCH INVOLVING HUMAN SUBJECTS UNDER CONDITIONS OF THE UNIVERSITY'S POLICY ON RESEARCH INVOLVING HUMAN SUBJECTS.

APPROVAL DATE: 04 April 1996 (UWO Protocol, Letter of Information & Consent)

AGENCY: MEDICAL COUNCIL OF CANADA

TITLE: Same as above

  
Bessie Borwein, Chairman

c.c. Hospital Administration

## Appendix G: Copyright Release Information

10/19/88 17:00 FAX 519 646 6135

NUCL MED ST-JOE'S LONDON

002



Department of Nuclear Medicine &amp; Magnetic Resonance

268 Grosvenor St., London, Ontario N6A 4V2  
Telephone (519) 646-6100 Ext. 4328

October 19, 1998

RE: Arch Gen Psychiatry 1997; 54: 959-965

Ada Walker  
Fax: 312 464 5835

Dear Ada Walker,

During the course of my Ph.D. training, I wrote a paper that was published in the Archives of General Psychiatry in October of 1997. I would like to include this paper in my doctoral thesis. Therefore, I am writing to obtain permission to do so. The thesis will be submitted to the University of Western Ontario in London, Ontario, Canada, through the department of Medical Biophysics. The complete citation of the article is as follows:

R Bartha, PC Williamson, DJ Drost, A Malla, TJ Carr, L Cortese, G Canaran, RJ Rylett, WRJ Neufeld. Measurement of Glutamate and Glutamine in the Medial Prefrontal Cortex of Never Treated Schizophrenic Patients and Healthy Controls using Proton Magnetic Resonance Spectroscopy. *Archives of General Psychiatry* 1997; 54: 959-965.

If you need any other information I would be happy to provide it. My phone number is 519 646 6000 ext 4460, and my fax number is 519 646 6135.

Thank you,

ENGLISH  
ONE EDITION  
IN PRINT

Robert Bartha

**PERMISSION GRANTED: Rights granted herein are nonexclusive.**

Your credit line must include the name of Publication, issue date, volume and page numbers, as well as, "Copyright 1998, American Medical Association."

Owned and Operated by  
St. Joseph's Health Services Association of London, Incorporated  
Affiliated with The University of Western Ontario

*Ada Walker*  
10.21.98

October 30, 1998

AJP-4619

Robert Bartha  
St. Josephs

Dear Dr. Bartha :

Upon satisfaction of the conditions listed below, use of the material indicated on the attached request(s) is approved. Permission is granted for nonexclusive world distribution rights, forthcoming edition only.

The republished material must include a full bibliographic citation in the following format: Title of Publication, Volume Number, Page Numbers, 19\_\_. Copyright 19\_\_, the American Psychiatric Association. Reprinted by permission.

No fee is charged to authors using their own material.

Sincerely,

Spencerita Bellinger  
Copyright Permissions  
Periodical Services Division  
(202) 682-6211  
Email Address: [sbelling@psych.org](mailto:sbelling@psych.org)